UNIVERSITÀ
DEGLI STUDI
DI BRESCIA

Dottorato di ricerca in
Ingegneria Civile, Ambientale,
della Cooperazione Internazionale e di Matematica

Ciclo XXXIII

Settore scientifico-disciplinare:
ICAR/08 Scienza delle Costruzioni

Modeling the electrochemo-poromechanics of ionic polymer metal composites and cell clusters

Dottorando:
Alessandro Leronni

Relatore:
Prof. Lorenzo Bardella

Abstract

In this thesis, we theoretically investigate the electrochemo-poromechanics of ionic polymer metal composites (IPMCs) and cell clusters.

IPMCs are layered micro-devices constituted by an ionic electroactive polymeric membrane sandwiched between metal electrodes. In the membrane, the negatively charged polymeric network is soaked in a fluid phase consisting of cations dispersed in a solvent. The motion of this fluid phase makes the IPMC electroactive. IPMCs can find application as actuators, sensors, and energy harvesters in biomedical engineering, soft robotics, and portable electronics.

Cell clusters are collectives of closely packed cells, held together through anchoring junctions. Their intracellular and extracellular spaces are saturated with water hosting different ion species. Water and ions can move in the intercellular spaces, directly between cells through gap junctions, and across cell membranes through aquaporins and ion channels, respectively. Cell clusters are suitable systems for studies on developmental mechanobioelectricity.

Since IPMCs and cell clusters share common features, their behavior can be investigated through similar continuum multiphysical frameworks. Specifically, we herein illustrate two models. The first one, already present in the IPMC literature, couples the electro-diffusion of ions and the elasticity of the solid network. The second one, which is an original contribution, additionally encompasses the solvent transport, providing also a micromechanical source for the volumetric deformation of the network.

In the context of IPMCs, we specialize the first model to an advanced structural theory featuring a zigzag warping kinematics of the IPMC cross-section. This allows us to study the effect of the membrane shear deformation on the electro-diffusion of ions, triggered by the membrane curvature. We adopt the second model to address the cross-diffusion of solvent and ions in IPMC actuation and sensing. Specifically, in actuation, the solvent counter-diffusion contributes to the relaxation of the IPMC curvature under a fixed voltage; in sensing, the ion counter-diffusion is associated with an electrical discharge under a sustained mechanical load.

With regard to cell clusters, inspired by the first theoretical framework adopted for IPMCs, we augment a numerical code in the literature for the study of bioelectrical dynamics, in order to further account for its coupling with the elasticity of the cluster. We then use this augmented code to explore possible feedback loops elicited by osmotic pressure and mechanosensitive ion channels in morphogenesis. Finally, we employ the second model to investigate the osmotic water fluxes within the cluster, triggered by the bioelectrical activity and responsible of the cluster deformation. This theory, if complemented with a model for biological growth, is expected to provide a contribution toward addressing problems of interest in developmental mechanobioelectricity, such as regeneration and cancer proliferation.

Ultimately, we believe that elucidating the electrochemo-poromechanics underlying both IPMCs and cell clusters may be of paramount importance for fostering bioinspired soft robotics applications.

Sommario

In questa tesi, si studia da un punto di vista teorico il comportamento elettrochemo-poromeccanico degli *ionic polymer metal composites* (IPMC) e degli aggregati cellulari.

Gli IPMC sono compositi laminati alla microscala costituiti da una membrana in polimero elettroattivo ionico racchiusa tra elettrodi metallici. Nella membrana, il reticolo polimerico, carico negativamente, è immerso in una fase fluida costituita da cationi dispersi in un solvente. Il movimento di questa fase fluida rende l'IPMC elettroattivo. Gli IPMC possono trovare applicazione come attuatori, sensori e raccoglitori di energia pulita per l'ingegneria biomedica, la robotica soffice e dispositivi elettronici portatili.

Gli aggregati cellulari sono degli insiemi di cellule prossime le une alle altre, tenute insieme da giunzioni di ancoraggio. In tali aggregati, gli spazi intracellulari ed extracellulari sono saturati da acqua e diverse specie ioniche. L'acqua e gli ioni possono muoversi negli spazi intercellulari, direttamente da una cellula all'altra tramite giunzioni comunicanti e attraverso le membrane cellulari tramite le acquaporine e i canali ionici. Gli aggregati cellulari sono dei modelli utili per lo studio della meccanobioelettricità dello sviluppo.

Poiché gli IPMC e gli aggregati cellulari esibiscono comportamenti che sono regolati da principi fisici di base comuni, è possibile e utile studiare il loro comportamento tramite simili teorie multifisiche alla scala del continuo. In particolare, in questa tesi si illustrano due modelli. Il primo, già presente nella letteratura degli IPMC, accoppia l'elettro-diffusione degli ioni con il comportamento elastico del reticolo solido. Il secondo, che costituisce un contributo originale, tiene conto in aggiunta del trasporto del solvente, che tra l'altro fornisce un modello per descrivere la deformazione volumetrica del reticolo.

Per quanto riguarda gli IPMC, il primo modello viene combinato con una teoria strutturale avanzata che tiene conto di una cinematica lineare a tratti della sezione retta dell'IPMC. Ciò permette di studiare l'effetto della deformazione a taglio della membrana sull'elettro-diffusione degli ioni, innescata dalla flessione della membrana. Il secondo modello viene utilizzato per trattare la diffusione

incrociata del solvente e degli ioni nei comportamenti ad attuatore e a sensore degli IPMC. In particolare, in attuazione, la contro-diffusione del solvente contribuisce al rilassamento della curvatura dell'IPMC a voltaggio costante; nel comportamento a sensore, la contro-diffusione degli ioni è associata a una diminuzione della carica elettrica accumulata sotto carico meccanico mantenuto per un tempo sufficientemente lungo.

Con riferimento agli aggregati cellulari, traendo ispirazione dal primo modello utilizzato per gli IPMC, si estende un codice numerico proposto in letteratura per lo studio delle dinamiche della bioelettricità, in modo tale da tener conto in aggiunta dell'accoppiamento di queste ultime con il comportamento elastico dell'aggregato. Successivamente, si fa uso di questo codice esteso per esplorare possibili fenomeni di retroazione provocati dalla pressione osmotica e dai canali ionici meccanosensitivi nell'ambito della morfogenesi. Infine, il secondo modello viene adoperato per investigare i flussi osmotici dell'acqua all'interno dell'aggregato, innescati dall'attività bioelettrica e responsabili del processo deformativo. Tale teoria, se completata con un modello per la descrizione della crescita biologica, dovrebbe contribuire all'analisi di problemi di reale interesse per la meccanobioelettricità dello sviluppo, quali la rigenerazione e la proliferazione tumorale.

In ultima analisi, si ritiene che lo studio approfondito del comportamento elettrochemo-poromeccanico alla base degli IPMC e degli aggregati cellulari possa essere di fondamentale importanza per promuovere applicazioni di robotica soffice bioispirata.

Contents

Ringraziamenti

Desidero ringraziare il Prof. Lorenzo Bardella per aver creduto in me ed avermi dato l'opportunità di intraprendere il percorso di dottorato. Lo ringrazio in particolare per essere stato sempre presente, per avermi concesso la possibilità di scegliere il mio percorso e per avermi trattato con rispetto. Ringrazio il Prof. Luis Dorfmann per avermi accolto calorosamente alla Tufts University e per essere stato un prezioso riferimento e sostegno anche in seguito al mio ritorno a Brescia. Ringrazio il Prof. Michael Levin e la Dott.sa Alexis Pietak per essere stati disponibili a collaborare con me. Ringrazio anche il Prof. Maurizio Porfiri, la cui collaborazione ha ispirato la mia decisione di iscrivermi al dottorato e di perseguire la carriera accademica. Ringrazio il Prof. Prashant Purohit e il Prof. Thomas Wallmersperger per aver letto attentamente la mia tesi e per avermi fornito suggerimenti utili al suo miglioramento. Infine ringrazio la mia famiglia, chi mi vuole bene e chi me ne ha voluto per essere stati di supporto durante questi anni.

Chapter 1

Introduction

In the recent years, the field of soft robotics has attracted the interest of the engineering community (Trivedi et al., 2008; Kim et al., 2013; Rus and Tolley, 2015). The aim of this line of research is to design and assemble robots capable of undergoing large deformations, endowed with self-integrated sensors, control systems, and power sources. Correspondingly, the field requires the synergistic effort of different specialists, including electrical and mechanical engineers. Moreover, soft robots are typically bioinspired and are required to be biocompatible, as they are of importance for biomedical applications. Therefore, biologists are likewise fundamental in this sector.

Electro-mechanical effects are at the core of soft robotics. Historically, the most studied type of electro-mechanical interaction is represented by piezoelectricity (Yang, 2005). Recent applications include advanced piezo-active composites with advantageous electro-mechanical properties (Topolov et al., 2013) and biodegradable piezoelectric actuators and sensors safely interacting with biological parts (Chorsi et al., 2019). The piezoelectric behavior of some biological tissues, such as the bone tissue, has also long been acknowledged (Bassett, 1967). While uniform strains are responsible for the direct piezoelectric effect, strain gradients trigger the direct flexoelectric effect (Nguyen et al., 2013). Flexoelectricity is particularly relevant in nanoscale systems, including those made of soft biomaterials. Both the theories of piezoelectricity and flexoelectricity are linear; differently, Dorfmann and Ogden (2005) have proposed a nonlinear theory of electroelasticity, useful for the study of the large deformations experienced by dielectric elastomers (Gei et al., 2013; Carpi et al., 2015). Piezoelectricity, flexoelectricity, and nonlinear electroelasticity are all grounded on theoretical frameworks coupling continuum solid mechanics and electrostatics.

In this thesis, we rather focus on a specific sub-field of devices and biological systems whose behavior is governed by *electrochemo-poromechanical* interactions.

Specifically, we use the term *electrochemistry* to refer to the *electro-diffusion* of ions, that is, the transport of ions along both their concentration gradient and an electric field (Rubinstein, 1990). Electro-diffusion is typically described by the Nernst-Planck equation, to be complemented with the Poisson equation for the associated electrostatic problem. We remark that possible electrochemical reactions are not included in our definition of electrochemistry, and they are not considered here. We use the term *poromechanics* to refer to the deformation of a porous medium in the presence of fluid transport within the porous network (Coussy, 2004). Addressing poromechanics requires Cauchy-Navier-like equations for the mechanics of the solid network and the Darcy equation for the description of the fluid flow. Effects of the coupling between electrochemistry and poromechanics, including osmotic pressure, Maxwell stress, electro-osmotic fluid flux, and convective ion flux, are responsible for electro-mechanical actuation and sensing mechanisms.

Therefore, studying electrochemo-poromechanical interactions requires theoretical frameworks accounting for ion and fluid transport, along with electrostatics and mechanics. In the literature, relevant contributions have been given in the fields of polyelectrolyte gels (Hong et al., 2010) and biological tissues (Ateshian, 2007). Specifically, in this thesis we devote our interest to the electrochemo-poromechanics of *ionic polymer metal composites* (IPMCs) and cell clusters.

IPMCs are sandwich structures composed of an ionic electroactive polymeric membrane, a few hundred of micrometers thick, plated with thinner metal electrodes (Shahinpoor and Kim, 2001). The membrane typically consists of a negatively charged polymer network soaked in a solution of solvent and cations. The motion of this solution confers the IPMC its remarkable electroactive properties. Specifically, an applied voltage drop across the electrodes is converted into motion in actuation, whereas an imposed mechanical load is detected electrically in sensing mode, or induces charge accumulation in energy harvesting applications (Shahinpoor and Kim, 2004; Pugal et al., 2010; Jo et al., 2013). Within our terminology, in actuation the electrochemistry drives the poromechanical response, whereas in sensing/energy harvesting the poromechanics elicits the electrochemical response. The foregoing features make IPMCs attractive in the fields of soft robotics, biomedical engineering, and low-power electronics (Shahinpoor and Kim, 2005).

We adopt the term *cell cluster* to refer to biological model systems, similar to epithelia, composed of closely packed cells, joined by anchoring junctions connecting the cytoskeletons of the different cells (Alberts, 1983). Cell clusters comprise both intracellular (IC) spaces and thin extracellular (EC) spaces separating neighboring cells. IC and EC spaces are delimited by cell membranes. These are equipped with ion channels, through which ions electro-diffuse between the IC and the EC spaces, aquaporins, through which water diffuses between the IC and the EC spaces, and gap junctions, through which ions and water are exchanged directly between the IC spaces of neighboring cells. We remark that, in the present investigation, we disregard active transport mechanisms such as ion pumps. Within cell clusters, the electro-diffusion of ions, setting the cell membrane potential, triggers the poromechanical response; in turn, the latter affects the electrochemistry mainly through the activity of mechanosensitive ion channels, responding to the mechanics of the cell membrane. These mechanisms are very similar to those of actuation and sensing in IPMCs, justifying the usage of similar theoretical frameworks for their description. The study of the electro-diffusion of ions and related membrane potential variations in non-excitable cells is usually referred to as *bioelectricity* (Levin et al., 2017). *Mechanobiology* is instead the discipline focusing on the role of mechanics in biological processes (Huang et al., 2012). It has been shown that both bioelectricity and mechanobiology are fundamental in development (McCaig et al., 2005; Mammoto and Ingber, 2010), alongside the more established fields of biochemistry and genetics. In the following, we will adopt the term *mechanobioelectricity* to refer to the aforementioned interactions between mechanical and electrochemical signals. For brevity, we will often refer to cell clusters as a shortcut for "mechanobioelectricity of cell clusters".

Both IPMCs and cell clusters are of interest for bioinspired soft robotics. In particular, IPMCs have already been used for specific applications in the field, such as to propel the locomotion of biomimetic underwater vehicles (Aureli et al., 2010), to design robotic carnivorous plants (Shahinpoor, 2011), and to harvest energy from the beating of a robotic fish tail (Cha et al., 2013). Many more applications will be possible thanks to the rapid progress in IPMC manufacturing, allowed by technologies such as 3D printing (Carrico et al., 2015). Because of their ability to grow, assemble, and repair autonomously guided be electrical, chemical, and mechanical cues, cell clusters hold promise for the design of multicellular engineered living systems (Mustard and Levin, 2014; Kamm et al., 2018), this also being encouraged by the possibility of manipulating ion channels *in vivo* through genetic, pharmacological, and optogenetic techniques (Levin et al., 2017).

The aim of this thesis is to develop continuum electrochemo-poromechanical theories for both IPMCs and cell clusters, and to find analytical and numerical solutions of the proposed theories for specific cases of interest. With the exception of Ch. 8, we employ the finite element commercial software *COMSOL Multiphysics®* for the numerical computations.[1] This a natural and suitable

---

[1] The *COMSOL Multiphysics®* software has been run at the Applied Acoustics Lab - Univeristy of Brescia.

choice, given the multidisciplinarity of the undertaken research. Furthermore, *COMSOL Multiphysics®* has been often employed to develop numerical models for IPMCs (Pugal et al., 2015; Volpini et al., 2017; Porfiri et al., 2018). When integrated by experimental endeavors, we expect this work to help shed light on specific aspects of the complex multiphysical behavior of IPMCs and cell clusters, with the ultimate goal of fostering advancements in their soft robotics applications.

We organize the thesis in two self-consistent parts, separately treating the electrochemo-poromechanics of IPMCs and cell clusters. Before starting, in Ch. 2 we present the notation and the symbols consistently used throughout the thesis. During the dissertation, the sections denoted with the symbol † and written with a smaller font contain mathematical derivations that may be skipped by the uninterested reader.

Part I deals with IPMCs. After introducing them in Ch. 3 with reference to their composition, manufacturing, and underlying physical principles, we recall a purely electrochemo-mechanical theory for IPMCs, disregarding the solvent transport, in Sec. 4.2. This theory, originally proposed by Cha and Porfiri (2014), relies on three coupled governing equations, namely, a momentum balance for the displacement field, a mass balance for the ion concentration, and the Gauss law for the electric potential. It allows one to address both actuation and sensing of IPMCs. Specifically, according to this theory, actuation is triggered by osmotic and Maxwell stresses, entering the momentum balance as *active* stresses (or *eigenstresses*). Sensing is instead promoted by a contribution to the ion flux depending on the gradient of the volumetric deformation. Here, differently from Cha and Porfiri (2014), we explicitly account for the mechanics of the electrodes, but neglect steric effects of ions and the composite polymer-electrode layers at the membrane-electrode interfaces.

This theory, previously employed in its original form neglecting the electrode mechanics to describe the time-dependent actuation of IPMCs (Porfiri et al., 2017, 2018), is specialized in Sec. 4.3 to a structural model for sandwich structures, in order to discuss the role of shear deformation on the sensing response of IPMCs. Specifically, we employ a *zigzag warping* model to describe the kinematics of the IPMC, thus allowing the membrane and electrode cross-sections to undergo independent Timoshenko-like rotations. This advanced structural theory, originally proposed by Yu (1959) and Krajcinovic (1972), leads to a membrane volume ratio that depends, in addition to the curvature, on the shear deformation, thus reflecting on the electro-diffusion of ions, as mathematically described in Sec. 4.4 and quantitatively discussed in Sec. 4.7. Overall, Ch. 4 is adapted from "Leronni and Bardella (2019), Influence of shear on sensing of ionic polymer metal composites, *European Journal of Mechanics-*

A/Solids".

In Sec. 5.2 we present an original electrochemo-poromechanical theory for saturated IPMCs. This framework expands on the Cha and Porfiri (2014) theory by explicitly addressing the transport of the solvent within the membrane porosity network. Within the proposed framework, the *osmotic* stress of the Cha and Porfiri (2014) theory, depending on the redistribution of ions, is replaced by the *solvent* pressure. Therefore, the osmotic pressure does not enter the mechanical equilibrium, but competes with the solvent pressure in establishing the solvent chemical potential. Moreover, we account for the *cross-diffusion* of solvent and ions, that is, on the basis of experimental evidences, we assume that the (electro)chemical potential of each of these species influences the fluxes of both species (Vanag and Epstein, 2009).

In Sec. 5.3 we apply the proposed model to the study of IPMC actuation under a fixed voltage and sensing under a sustained mechanical load. In actuation we uncover that, after initially accumulating near the cathode, the solvent molecules *counter-diffuse*, determining a relaxation of the bending deformation of the IPMC. This is strengthened by the asymmetry of the Maxwell stress in the vicinity of the electrodes, which can even lead to a reversal of the curvature (Porfiri et al., 2017), as observed in experiments (Asaka et al., 1995). In short-circuit sensing, after first being transported toward the cathode with the solvent, ions counter-diffuse, resulting in a decrease of the charge stored at the electrodes (Farinholt and Leo, 2004). Overall, Ch. 5 is adapted from "Leronni and Bardella (2021), Modeling actuation and sensing in ionic polymer metal composites by electrochemo-poromechanics, *Journal of the Mechanics and Physics of Solids*".

Finally, in Ch. 6 we propose a detailed comparison between the electrochemo-mechanical theory of Cha and Porfiri (2014) and the electrochemo-poromechanical theory proposed in this thesis.

In Part II we treat cell clusters. We start by briefly reviewing, in Sec. 7.1, the literature on bioelectricity and its role in important biological processes at the cellular scale, such as the regulation of the cell cycle (Blackiston et al., 2009) and, in particular, of cell proliferation (Sundelacruz et al., 2009). These aspects reflect on tissue-scale processes such as embryonic development, left-right organ asymmetry, wound healing, tissue regeneration, and cancer progression (McCaig et al., 2005). Then, in Sec. 7.1.1 we deal with the very recent subject of mechanobioelectricity, focusing on how bioelectrical and mechanical signals interact to coordinate growth and morphogenesis (Silver and Nelson, 2018; Silver et al., 2020).

In Sec. 7.2 we describe the constituents of cell clusters relevant for mechanobioelectricity. In particular, Sec. 7.2.1 deals with the mechanical constituents of cell clusters, namely, cytoskeletal filaments and anchoring junctions. Sec. 7.2.2

describes cell membranes and tight junctions, acting like barriers between the IC and EC spaces and between the inside and outside of the cluster, respectively. Sec. 7.2.3 presents an overview of the channel proteins involved in passive ion and water transport, that is, ion channels, aquaporins, and gap junctions. Specifically, we focus on mechanosensitive ion channels (MCs), which are important for the following developments.

Among the computational efforts in the field of bioelectricity, Pietak and Levin (2016) have proposed a finite volume code, referred to as the *BioElectric Tissue Simulation Engine* (BETSE), describing the bioelectrical ion fluxes and the related membrane potential variations within cell clusters. In Secs. 8.2 and 8.3 we augment BETSE in order to describe the mechanobioelectricity of cell clusters. The resulting code, named mecBETSE (`https://gitlab.com/betse/mecbetse`), allows one to compute the stress and strain fields resulting from the osmotic pressure gradients due to the bioelectrical activity, and the consequent impact on the opening of MCs, circularly modulating the bioelectrical state of the cluster.

In Sec. 8.4 we employ mecBETSE to explore the feedback loops elicited by osmotic pressure and MCs at both short and long-range, in relation to the cluster geometry, mechanical properties and boundary conditions, and ion channel distribution and selectivity. We also hint at aspects of biological significance, such as the progression and regulation of cancer and the establishment of asymmetries in tissue morphogenesis. The mecBETSE code and the benchmarks discussed in Ch. 8 are the subject of "Leronni et al. (2020), On the coupling of mechanics with bioelectricity and its role in morphogenesis, *Journal of the Royal Society Interface*".

By following the approach adopted in Sec. 5.2 for IPMCs, and inspired by previous efforts for single cells in the literature (Yellin et al., 2018), in Sec. 9.2 we construct an electrochemo-poromechanical theory for cell clusters. The model consists of two Gauss laws for the IC and EC electric potentials, $2n$ mass balances for the IC and EC concentrations of the n mobile ion species involved, two mass balances for the IC and EC water concentrations, and an overall momentum balance for the displacement field. Self-balancing source terms in the mass balances describe the exchange of ions and water between the IC and EC spaces through the cell membrane, simulating the activity of ion channels and aquaporins.

We employ this theory in Sec. 9.3 to accurately describe the osmotic transport of water in the EC spaces separating cells, in the IC spaces through gap junctions, and across the cell membranes through aquaporins. These osmotic phenomena, triggered by the bioelectrical activity, are in turn responsible of the cluster deformation. We examine both drained and undrained conditions, that is, we suppose that water and ions are either allowed or prevented from moving across the cluster boundary, with the latter condition simulating the presence of sealing tight junctions. Overall, Ch. 9 is adapted from "Leronni (2020), Modeling the mechanobioelectricity of cell clusters, *Biomechanics and Modeling in Mechanobiology*".

The proposed model may be further augmented to quantitatively describe the interplay between growth and depolarization (Sundelacruz et al., 2009), such as to actually tackle complex developmental processes, including regeneration and cancer proliferation. We comment on such a possible extension, relying on the theory of kinematic growth (Ambrosi et al., 2019), in Ch. 10.

In the final Ch. 11 we draw the conclusions of our study, by also focusing on the differences between the electrochemo-poromechanics of IPMCs and cell clusters.

Chapter 2

Notation and symbols

In this thesis, we denote scalars with lightface letters, whereas we indicate vectors and tensors with boldface letters.

Except for Ch. 8, limited to small deformations, we distinguish between reference and current configurations, and use uppercase letters for the referential description of geometry-dependent scalars, vectors, and tensors (that is, for the so-called *nominal* quantities), and lowercase letters for the spatial description of the same quantities (that is, for the so-called *current* quantities). Consistently, we use the symbol $\mathbf{X}$ for the coordinates in the reference configuration (that is, the so-called *material* coordinates) and $\mathbf{x}$ for the coordinates in the current configuration (that is, the so-called *spatial* coordinates). As for *mixed* tensors such as the deformation gradient, we use uppercase letters, and indicate their components with one lowercase and one uppercase index.

In the following, we introduce the notation used for differential and algebraic operations. For this purpose, we adopt the symbols A and a to indicate generic nominal and current scalars, $\mathbf{A}$ and $\tilde{\mathbf{A}}$ for generic distinct nominal vectors, $\mathbf{a}$ and $\tilde{\mathbf{a}}$ for generic distinct current vectors, $\mathbf{B}$ and $\tilde{\mathbf{B}}$ for generic distinct nominal second-order tensors, and $\mathbf{b}$ for a generic current second-order tensor.

We use the symbol ∇ to indicate the material gradient operator, such that

$$(\nabla A)_I = \frac{\partial A}{\partial X_I} = A_{,I}\,, \tag{2.1a}$$

$$(\nabla \mathbf{A})_{IJ} = \frac{\partial A_I}{\partial X_J} = A_{I,J}\,, \tag{2.1b}$$

and grad to indicate the spatial gradient operator, such that

$$(\operatorname{grad} a)_i = \frac{\partial a}{\partial x_i} = a_{,i}\,, \tag{2.2a}$$

$$(\mathrm{grad}\,\mathbf{a})_{ij} = \frac{\partial a_i}{\partial x_j} = a_{i,j}\,. \tag{2.2b}$$

We use the symbol Div to refer to the material divergence operator, such that

$$\mathrm{Div}\,\mathbf{A} = \frac{\partial A_I}{\partial X_I} = A_{I,I}\,, \tag{2.3a}$$

$$(\mathrm{Div}\,\mathbf{B})_I = \frac{\partial B_{IJ}}{\partial X_J} = B_{IJ,J}\,, \tag{2.3b}$$

and div to refer to the spatial divergence operator, such that

$$\mathrm{div}\,\mathbf{a} = \frac{\partial a_i}{\partial x_i} = a_{i,i}\,, \tag{2.4a}$$

$$(\mathrm{div}\,\mathbf{b})_i = \frac{\partial b_{ij}}{\partial x_j} = b_{ij,j}\,. \tag{2.4b}$$

We note that, though uncommon, material operators could also be applied to current quantities and, vice versa, spatial operators could also be applied to nominal quantities. In Ch. 8, restricted to small deformations, we adopt the symbols associated with the spatial description.

We use the notation convention that writing two tensors of any order next to each other implies the saturation of one index, such that

$$(\mathbf{BA})_I = B_{IJ}A_J\,, \tag{2.5a}$$

$$(\mathbf{B}\tilde{\mathbf{B}})_{IJ} = B_{IK}\tilde{B}_{KJ}\,. \tag{2.5b}$$

We use the symbol $\cdot$ to indicate the inner product of two tensors of the same order, resulting in a scalar; therefore

$$\mathbf{A}\cdot\tilde{\mathbf{A}} = A_I\tilde{A}_I\,, \tag{2.6a}$$

$$\mathbf{B}\cdot\tilde{\mathbf{B}} = B_{IJ}\tilde{B}_{IJ}\,. \tag{2.6b}$$

We use the symbol $\otimes$ to indicate the tensor product between two vectors, that is

$$(\mathbf{A}\otimes\tilde{\mathbf{A}})_{IJ} = A_I\tilde{A}_J\,. \tag{2.7}$$

Finally, we adopt the standard superscripts $^{\mathrm{T}}$ and $^{-1}$ to indicate the transpose and the inverse operations.

In Tabs. 2.1, 2.2, and 2.3 we list the generic, electrochemical, and poromechanical physical quantities, and related symbols, consistently used throughout the thesis. Finally, in Tab. 2.4 we provide a list featuring all the abbreviations used in this work.

Symbol	Description	Unit
U	Nominal internal energy density	$\mathrm{J/m^3}$
W	Nominal Helmholtz free energy density	$\mathrm{J/m^3}$
W_{mec}	Mechanical contribution to W	$\mathrm{J/m^3}$
W_{mix}	Mixing contribution to W	$\mathrm{J/m^3}$
W_{pol}	Polarization contribution to W	$\mathrm{J/m^3}$
$\mathbf{N}$	Outward unit normal to the reference boundary	–
$\mathbf{n}$	Outward unit normal to the current boundary	–

Table 2.1: Generic physical quantities used throughout the thesis.

Symbol	Description	Unit
C	Nominal molar concentration	$\mathrm{mol/m^3}$
c	Current molar concentration	$\mathrm{mol/m^3}$
D	Diffusivity	$\mathrm{m^2/s}$
F	Faraday constant	$\mathrm{C/mol}$
$\mathcal{R}$	Gas constant	$\mathrm{J/(mol\,K)}$
k_{B}	Boltzmann constant	$\mathrm{J/K}$
T	Absolute temperature	K
$\mathbf{M}$	Mobility tensor	$\mathrm{mol^2/(N\,m^2s)}$
$\mathbf{J}$	Nominal molar flux	$\mathrm{mol/(m^2s)}$
$\mathbf{j}$	Current molar flux	$\mathrm{mol/(m^2s)}$
ψ	Electric potential	V
ε_0	Vacuum permittivity	$\mathrm{F/m}$
ε_{r}	Relative permittivity	–
ε	Absolute permittivity	$\mathrm{F/m}$
$\mathbf{E}$	Nominal electric field	$\mathrm{V/m}$
$\mathbf{e}$	Current electric field	$\mathrm{V/m}$
$\mathbf{D}$	Nominal electric displacement	$\mathrm{C/m^2}$
$\mathbf{d}$	Current electric displacement	$\mathrm{C/m^2}$
Q	Nominal surface charge density	$\mathrm{C/m^2}$
Q_{tot}	Nominal linear charge density	$\mathrm{C/m}$
μ	Chemical potential	$\mathrm{J/mol}$
$\tilde{\mu}$	Electrochemical potential	$\mathrm{J/mol}$

Table 2.2: Electrochemical physical quantities used throughout the thesis.

Symbol	Description	Unit
$\mathbf{u}$	Displacement field	m
E	Young modulus	$\mathrm{N/m^2}$
ν	Poisson ratio	–
λ	First Lamé parameter	$\mathrm{N/m^2}$
G	Second Lamé parameter (shear modulus)	$\mathrm{N/m^2}$
$\mathbf{F}$	Deformation gradient	–
$\mathbf{C}$	Right Cauchy-Green deformation tensor	–
$\mathbf{b}$	Left Cauchy-Green deformation tensor	–
$\boldsymbol{\mathcal{E}}$	Green-Lagrange strain tensor	–
$\boldsymbol{\varepsilon}$	Small strain tensor	–
J	Volume ratio	–
$\mathbf{P}$	Nominal[a] stress tensor	$\mathrm{N/m^2}$
$\boldsymbol{\sigma}$	Cauchy stress tensor	$\mathrm{N/m^2}$
p	Pressure	$\mathrm{N/m^2}$
$\mathbf{T} = \mathbf{PN}$	Nominal traction vector	$\mathrm{N/m^2}$
$\mathbf{t} = \boldsymbol{\sigma}\mathbf{n}$	Current traction vector	$\mathrm{N/m^2}$
M	Nominal bending moment (per unit depth)	N
V	Nominal shear force (per unit depth)	N/m
$\mathbf{P}_{\mathrm{mec}}$ $(\boldsymbol{\sigma}_{\mathrm{mec}})$	Mechanical nominal (Cauchy) stress tensor	$\mathrm{N/m^2}$
$\mathbf{P}_{\mathrm{mix}}$ $(\boldsymbol{\sigma}_{\mathrm{mix}})$	Osmotic nominal (Cauchy) stress tensor	$\mathrm{N/m^2}$
$\mathbf{P}_{\mathrm{pol}}$ $(\boldsymbol{\sigma}_{\mathrm{pol}})$	Maxwell nominal (Cauchy) stress tensor	$\mathrm{N/m^2}$
p_{mec}	Mechanical pressure	$\mathrm{N/m^2}$
p_{mix}	Osmotic pressure	$\mathrm{N/m^2}$
p_{pol}	Electrostatic pressure	$\mathrm{N/m^2}$
p_{w}	Water pressure	$\mathrm{N/m^2}$
v_{w}	Water molar volume	$\mathrm{m^3/mol}$
Φ	Nominal porosity	–

Table 2.3: Poromechanical physical quantities used throughout the thesis.

---

[a] The terminology for this stress tensor, **P**, is very much heterogeneous in the literature. For instance, (i) in Gurtin et al. (2010) it is referred to as the Piola stress, (ii) in Malvern (1969) it is the transpose of the first Piola-Kirchhoff stress, (iii) Ogden (1984) denotes it as the first Piola-Kirchhoff stress (while calling nominal stress the transpose of our **P**), and, finally, (iv) Hong et al. (2010), that we follow, call it the nominal stress.

Abbreviation	Description
ECM	Electrochemo-mechanical
ECPM	Electrochemo-poromechanical
IPMC	Ionic polymer metal composite
EB	Euler-Bernoulli
FOSD	First order shear deformation
ZW	Zigzag warping
FE	Finite element
CONT-FE	Continuum finite element
PVW	Principle of virtual work
PPA	Parallel plate assumption
MPNP	Modified Poisson-Nernst-Planck
MAE	Matched asymptotic expansions
PDE	Partial differential equation
ODE	Ordinary differential equation
BETSE	BioElectric Tissue Simulation Engine
mecBETSE	Mechanical BioElectric Tissue Simulation Engine
IC	Intracellular
EC	Extracellular
MC	Mechanosensitive ion channel
TJ	Tight junction
GJ	Gap junction

Table 2.4: Abbreviations used throughout the thesis.

Part I

Ionic polymer metal composites

Chapter 3

Introduction

Ionic polymer metal composites (IPMCs) are sandwich micro-devices, whose core, denoted as the *membrane* and plated with thin metal electrodes, consists of a negatively charged polymer network soaked in a fluid phase of solvent and cations, referred to as *counterions* (Shahinpoor and Kim, 2001). The IPMC electroactive behavior has to be ascribed to the possibility of these counterions to redistribute within the membrane upon the imposition of an electrical or mechanical stimulus. Owing to their large compliance, low activation voltage, ability to operate in different environmental conditions, and ease of manufacturing and customization, IPMCs hold promise for actuation, sensing, and energy harvesting in soft robotics, biomedical engineering, energy storage, and space applications (Shahinpoor and Kim, 2005; Pugal et al., 2010; Jo et al., 2013; Punning et al., 2014).

In Fig. 3.1 an IPMC in a cantilever configuration with its physical constituents is sketched. The IPMC is subject to either an applied voltage in actuation or an imposed mechanical load in sensing. In Sec. 3.1 we describe in more detail the IPMC composition and manufacturing process, while in Sec. 3.2 we introduce the physics behind actuation and sensing, and briefly overview the related modeling efforts in the literature.

3.1 IPMC composition and manufacturing

In IPMCs, Nafion and Flemion are typically used as ionomers for the membrane (Kim and Shahinpoor, 2003; Shahinpoor, 2015a). An *ionomer* is a polymer that includes electrically neutral units and a small but significant part of ionized units, bonded to the polymer backbone. Ionomers are designed to selectively pass cations or anions across their ionic groups. In particular, Nafion is a synthetic polymer that incorporates perfluorovinyl ether groups terminating with sulfonate groups $SO_3^-H^+$ over a Teflon backbone. Nafion pores allow the transport of

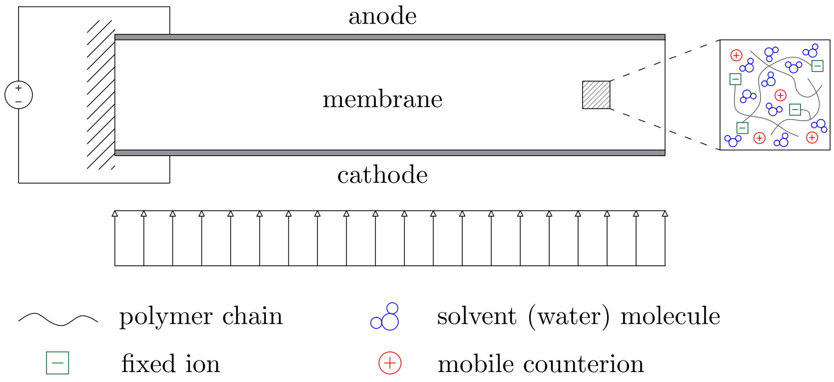

Figure 3.1: Cantilever IPMC subject to either an applied voltage across the electrodes (actuation) or an imposed mechanical load (sensing), with physical constituents highlighted.

cations, but they prevent the movement of anions or electrons. Flemion is an ionomer similar to Nafion, having carboxylate groups COO^-H^+ instead of sulfonate groups. Although thin sheet-like membranes made of commercially available Nafion or Flemion are normally employed, the fused filament 3D printing technique allows the realization of more complex and unconventional geometries (Carrico et al., 2015).

Different cation species, such as lithium, sodium, and potassium, can be used as counterions. These are usually dispersed in water, but other solvents such as ethylene glycol, glycerol, and crown ethers have also been considered (Nemat-Nasser et al., 2006). As for the electrodes, noble metals such as platinum, gold, silver, and palladium are usually employed.

In order to fabricate an IPMC, one of the most common manufacturing techniques is the so-called *impregnation-reduction* process (Kim and Shahinpoor, 2003; Shahinpoor, 2015b). In the following, we refer to the production of a typical IPMC constituted by a Nafion membrane, neutralized by either sodium or lithium counterions dispersed in water and sandwiched between platinum electrodes.

The initial stage consists of immersing the ionomer in a platinum salt solution for a few hours. In this way, the water-saturated ionic polymer is oxidized by the platinum salt. Specifically, the H^+ cations of the sulfonate groups are exchanged with the metallic cations Pt^+ in the oxidation process. Then, the oxidized ionic polymer is placed in a reduction solution composed of $NaBH_4$ or $LiBH_4$. The process reduces the oxidized Pt^+ particles to Pt particles, which are mainly deposited on the membrane surfaces. In parallel, H^+ cations are replaced with

Na^+ or Li^+ cations, which are the so-called mobile counterions neutralizing the fixed anions of the polymeric chains. Finally, additional amounts of Pt are plated on the top of the formerly deposited Pt, to increase the electrode conductivity. The result of the chemical plating is an ionomeric membrane with reduced metal nano-particles accumulated in the proximity and on the top of its surfaces, acting as distributed electrodes.

Alternatively to chemically depositing the metallic electrodes on the membrane, Akle et al. (2007) have proposed the so-called *direct assembly* method, consisting in painting large surface area electrodes on the membrane surfaces. This process allows a better control of the electrode geometry and composition.

In the theoretical models developed in this thesis, we will assume that the electrodes are homogeneous metallic layers forming a perfect interface with the enclosed polymeric membrane, participating to the mechanics of the sandwich IPMC. A similar approach has been undertaken in Schicker and Wallmersperger (2013). We note that the electrode surface roughness and the composite polymer-metal layers have been considered in some other works in the literature, including Porfiri (2009) and Cha et al. (2012).

3.2 Modeling actuation and sensing in IPMCs

As anticipated, the IPMC electroactivity essentially depends on the motion of the positive counterions within the membrane, while the anions are anchored to the polymer chains. Specifically, in actuation, the application of a voltage difference across the electrodes forces counterions to migrate toward the cathode, along the electric field. The redistribution of counterions establishes an osmotic pressure gradient across the membrane thickness, producing a bending deformation toward the anode. Conversely, in short-circuit sensing, the imposition of a mechanical load determines a volumetric deformation gradient across the membrane thickness. This, in turn, causes the diffusion of counterions up the volumetric deformation gradient, and correspondingly the detection of an electric current. According to some authors, accounting for the Maxwell stress due to charge imbalance (Cha and Porfiri, 2014; Schicker and Wallmersperger, 2013) and for the solvent flow (Schicker and Wallmersperger, 2013; Zhu et al., 2013, 2016) is also important for accurately predicting the IPMC response.

Therefore, IPMCs are characterized by an inherently complex physics, resulting from the nonlinear interplay among electrostatics, ion and solvent transport, and mechanics. Importantly, the IPMC behavior is mostly governed by the thin electric double layers (Bard and Faulkner, 2001) originating at the membrane-electrode interfaces (Porfiri, 2008). Indeed, while the membrane bulk remains approximately electroneutral in operating conditions, counterions accumulate in the proximity of the cathode, leaving the membrane region adjacent to the anode ion-depleted. Likewise, strong electric potential gradients are observed in the membrane regions next to the electrodes. Hence, the accurate modeling of such double layers plays a key role in the proper prediction of the IPMC electrochemo-mechanical behavior.

Since the pioneering contributions of Nemat-Nasser and Li (2000) and Shahinpoor and Kim (2004), several models have been proposed for actuation and sensing of IPMCs. In Ch. 4 of this thesis, which is adapted from Leronni and Bardella (2019), we rely on the finite deformation electrochemo-mechanical theory recently developed by Cha and Porfiri (2014), here summarized in Sec. 4.2, in order investigate the role of shear deformation in IPMC sensing.

We note that several studies have already been conducted on the basis of the pivotal contribution of Cha and Porfiri (2014). In particular, Volpini et al. (2017) and Volpini and Bardella (2021) have focused on modeling the short-circuit sensing response elicited by through-the-thickness compression. Porfiri et al. (2017) and Porfiri et al. (2018) have proposed an alternative explanation of the so-called *back-relaxation* phenomenon in actuation, grounded on the competition between osmotic and Maxwell stresses. Recent works on actuation have revealed the importance of considering complex deformation states, with the consequent need for sophisticated structural theories if, toward efficient design and optimization, one wants to avoid cumbersome numerical models of IPMCs treated as continua (Boldini and Porfiri, 2020; Boldini et al., 2020).

In Ch. 5, we elaborate a more comprehensive theory also accounting for the solvent transport within the membrane, and use it to study both IPMC actuation and sensing. In Ch. 6, closing the first part of the thesis, we critically compare this new theory with the Cha and Porfiri (2014) theory.

Chapter 4

The role of shear deformation in the sensing response of ionic polymer metal composites

This chapter is adapted from "Leronni and Bardella (2019), Influence of shear on sensing of ionic polymer metal composites, *European Journal of Mechanics-A/Solids*, 77:103750".

4.1 Introduction

In this chapter, we adopt the Cha and Porfiri (2014) *electrochemo-mechanical* theory, summarized in Sec. 4.2, with the aim of investigating the influence of shear deformation on IPMC sensing. This would in fact seem to be a quite natural issue to address in IPMCs, given their sandwich structure, such that their flexure should be affected by shear (Allen, 1969). A further motivation for this study is provided by Zangrilli and Weiland (2015), whose experiments show some evidence of sensing promoted by shear loading.

This notwithstanding, we are unaware of attempts to model the role of shear in IPMCs under flexure. A reason for this could be that, given the complexity of IPMC modeling, their laminate structure is typically neglected. Indeed, although the electrode layers have been studied in relation to the IPMC electrochemical response (Porfiri, 2009; Akle et al., 2011; Cha et al., 2012), usually they do not explicitly enter the mechanical modeling, thereby hampering the possibility of studying warping. An exception is represented by Schicker and Wallmersperger (2013), which however focus on IPMC actuation.

In particular, the Cha and Porfiri (2014) theory has been initially applied to model the IPMC time-dependent flexure in actuation by assuming the simplest possible kinematics, based on the Euler-Bernoulli theory for homogeneous beams (Porfiri et al., 2017, 2018). Later, the same theory has been employed with reference to more complex beam theories also accounting for the electrode layers, though still restricting attention to actuation (Boldini et al., 2020).

Given that shear deformation directly occurs under transverse mechanical load, here we are mostly concerned with the modeling of IPMCs as sensors. However, we provide a general result showing that even IPMC actuation is not necessarily warping-free.

Accounting for shear deformation may be particularly relevant in short IPMCs with quite stiff electrodes. Short IPMC samples have been tested in Lee et al. (2006) for actuation improvement, and also employed in Abdulsadda and Tan (2012) for the detection of a dipole source in water. Stiff electrodes could be realized through the direct assembly method, as documented in Akle et al. (2011), wherein high surface area electrodes with high particle density and large thickness have been produced, demonstrating an increase in charge accumulation, consistently with the results of Porfiri (2009).

To reach our goal, we model the IPMC mechanical behavior through the Yu-Krajcinovic kinematics, characterized by a zigzag warping (Yu, 1959; Krajcinovic, 1972; Bardella and Tonelli, 2012) in which the cross-sections of both membrane and electrodes are allowed to undergo independent Timoshenko-like rotations. Henceforth, we refer to this structural model, presented in Sec. 4.3, as *zigzag warping* (ZW) model.

By resorting to the principle of virtual work, written in a Lagrangian formulation, we obtain three equilibrium equations to be solved for the transverse displacement v and the membrane and electrode rotations, φ_{m} and φ_{e}. Notably, such equations also involve the Maxwell stress and the osmotic pressure, which, in turn, depend on the electric potential ψ and counterion concentration C.

In the case of linearized kinematics, and by assuming ψ and C as known fields, we provide an analytical solution for v, φ_{m}, and φ_{e}. Then, we demonstrate that disregarding the electrochemical fields in solving the equilibrium equations leads to accurate results for the flexure of IPMCs in sensing, thus confirming the previous results of Volpini et al. (2017) on IPMC through-the-thickness compression sensing.

By following Cha and Porfiri (2014), we establish a modified Poisson-Nernst-Planck (MPNP) system of equations governing the time-dependent electrochemical response. The novelty of this MPNP system, referred to as *modified* because modulated by kinematic fields, is that it nonlinearly involves not only the membrane curvature (as in previous efforts on IPMC flexure based on the Euler-Bernoulli beam kinematics), but also the membrane shear strain. In the following, this resulting electrochemo-mechanical model, presented in Sec. 4.4, is referred to as ZW-MPNP model.

By relying on the parallel plate assumption (PPA) (Pelesko and Bernstein, 2003), we semi-analytically solve the MPNP system for ψ and C, as functions of the membrane curvature and shear strain, through the method of matched asymptotic expansions (Verhulst, 2005). This method, previously employed by Porfiri and his group (Porfiri, 2008; Aureli and Porfiri, 2013; Cha and Porfiri, 2014), allows us to accurately capture the large gradients of ψ and C arising in the membrane regions close to the electrodes, denoted as *boundary layers* and characterizing the IPMC electrochemical response.

By focusing on a cantilever IPMC subject to a uniform transverse load, we show that shear deformation amplifies the electric response, measured in terms of stored charge. We validate the new semi-analytical model by systematic comparison against the results of two-dimensional finite element (FE) analyses of the fully coupled nonlinear system of PDEs governing the IPMC electrochemo-mechanics. These FE analyses are implemented in the commercial software *COMSOL Multiphysics*®, as documented in Sec. 4.6.

In discussing the results in Sec 4.7, we also consider the simpler structural models relying on the Bernoulli-Navier assumption of planar cross-section kinematics, that is, the Euler-Bernoulli (EB) model and the first order shear deformation (FOSD) theory, the latter basically coinciding with the Timoshenko theory for laminate structures (Bert, 1973). According to the foregoing terminology, in the following, we refer to the electrochemo-mechanical models obtained from these structural theories as EB-MPNP and FOSD-MPNP models.

As a further contribution, the availability of the two-dimensional FE implementation allows us to study the influence of the counterion flux along the IPMC axis, thus removing the PPA, which is customary in IPMC modeling (Nemat-Nasser and Li, 2000; Wallmersperger et al., 2007; Chen et al., 2007; Porfiri, 2008; Cha and Porfiri, 2014). Our FE analyses show that the PPA is generally appropriate to evaluate the overall electric response, although a large shear deformation may lead to some discrepancies in the local counterion distribution. Notably, this can be unveiled only by avoiding any linearization of the kinematics.

4.2 Summary of Cha and Porfiri (2014) electrochemo-mechanical theory

Here, we briefly summarize the continuum electrochemo-mechanical theory of Cha and Porfiri (2014), simplified in order to neglect steric effects and composite layers, as also adopted by Boldini and Porfiri (2020) and Boldini et al. (2020).

The equations presented in this section refer to the membrane, while the electrodes enter the modeling solely through their mechanical contribution (see Sec. 4.2.4) and by providing the boundary conditions for the electrochemical problem, to be imposed at the membrane-electrode interfaces, assumed to be perfect (see Secs. 4.4.2 and 4.6). Moreover, this theory disregards the solvent transport within the membrane (considered instead in the theory of Sec. 5.2), while the membrane hydration is taken into account through the Young modulus (see Sec. 4.7.1).

The primal variable for the mechanical description is the deformation gradient

$$\mathbf{F} = \frac{\partial \mathbf{x}}{\partial \mathbf{X}} = \nabla \mathbf{x}\,, \tag{4.1}$$

with $\mathbf{x}(\mathbf{X}, t)$ denoting the current position (at time t) of the material point $\mathbf{X}$ in the reference state, undeformed and electroneutral. Hence, the displacement field reads $\mathbf{u}(\mathbf{X}, t) = \mathbf{x}(\mathbf{X}, t) - \mathbf{X}$.

4.2.1 Balance equations

The balance equations consist of the mechanical equilibrium

$$\operatorname{Div} \mathbf{P} + \mathbf{B} = \mathbf{0}\,, \tag{4.2a}$$

the Gauss law

$$\operatorname{Div} \mathbf{D} = F(C - C_0)\,, \tag{4.2b}$$

and the mass balance of counterions in the absence of sources

$$\frac{\partial C}{\partial t} + \operatorname{Div} \mathbf{J} = 0\,. \tag{4.2c}$$

Here, Div is the material divergence operator, $\mathbf{P}$ is the nominal stress tensor, satisfying $\mathbf{P}\mathbf{F}^{\mathrm{T}} = \mathbf{F}\mathbf{P}^{\mathrm{T}}$, $\mathbf{B}$ is the nominal body force, $\mathbf{D}$ is the nominal electric displacement, F is the Faraday constant, C and C_0 are the nominal molar concentrations of counterions and fixed ions, and $\mathbf{J}$ is the nominal counterion flux.

4.2.2 Constitutive relations

We assume the nominal Helmholtz free energy density W to be dependent on $\mathbf{F}$, $\mathbf{D}$, and C, and to be additively decomposable as follows:

$$W(\mathbf{F},\mathbf{D},C) = W_{\mathrm{mec}}(\mathbf{F}) + W_{\mathrm{pol}}(\mathbf{F},\mathbf{D}) + W_{\mathrm{mix}}(\mathbf{F},C)\,, \tag{4.3}$$

where W_{mec}, W_{pol}, and W_{mix} account for mechanical deformation, dielectric polarization, and mixing of counterions, respectively.

This leads to the determination of three contributions to the stress:

$$\mathbf{P} = \frac{\partial W(\mathbf{F},\mathbf{D},C)}{\partial \mathbf{F}} = \mathbf{P}_{\mathrm{mec}} + \mathbf{P}_{\mathrm{pol}} + \mathbf{P}_{\mathrm{mix}}\,, \tag{4.4a}$$

where

$$\mathbf{P}_{\mathrm{mec}} = \frac{\partial W_{\mathrm{mec}}(\mathbf{F})}{\partial \mathbf{F}}\,, \quad \mathbf{P}_{\mathrm{pol}} = \frac{\partial W_{\mathrm{pol}}(\mathbf{F},\mathbf{D})}{\partial \mathbf{F}}\,, \quad \mathbf{P}_{\mathrm{mix}} = \frac{\partial W_{\mathrm{mix}}(\mathbf{F},C)}{\partial \mathbf{F}} \tag{4.4b}$$

are the mechanical, Maxwell (or electrostatic), and osmotic stresses, respectively.

The nominal electric field $\mathbf{E} = -\nabla\psi$, with ψ denoting the electric potential, is conjugate to the electric displacement (Dorfmann and Ogden, 2005):

$$\mathbf{E} = \frac{\partial W(\mathbf{F},\mathbf{D},C)}{\partial \mathbf{D}} = \frac{\partial W_{\mathrm{pol}}(\mathbf{F},\mathbf{D})}{\partial \mathbf{D}}\,. \tag{4.5}$$

The mixing free energy W_{mix} provides the relation between C and the chemical potential μ, the latter written in terms of the electrochemical potential $\tilde{\mu}$ and the electric potential ψ:

$$\mu = \tilde{\mu} - F\psi = \frac{\partial W(\mathbf{F},\mathbf{D},C)}{\partial C} = \frac{\partial W_{\mathrm{mix}}(\mathbf{F},C)}{\partial C}\,, \tag{4.6}$$

where the term $F\psi$ accounts for the electrophoretic effect, while W_{mix} is specified in such a way as to incorporate Fick's law into the model (see Sec. 4.2.4).

The counterion flux $\mathbf{J}$ is related as follows to $\tilde{\mu}$, thus ensuring non-negative dissipation:

$$\mathbf{J} = -\frac{DC}{\mathcal{R}T}\mathbf{C}^{-1}\nabla\tilde{\mu}\,, \tag{4.7}$$

where D is the diffusivity, $\mathcal{R}$ is the gas constant, T is the absolute temperature, and $\mathbf{C} = \mathbf{F}^{\mathrm{T}}\mathbf{F}$ is the right Cauchy-Green deformation tensor. The second-order tensor $\mathbf{M} = DC/(\mathcal{R}T)\mathbf{C}^{-1}$ in Eq. (4.7) is recognizable as a symmetric mobility tensor within the framework of Gurtin et al. (2010).

By writing Eq. (4.5) in terms of ψ and substituting it into the Gauss law (4.2b), one obtains the modified Poisson equation. Writing $\tilde{\mu}$ as a function of $\mathbf{F}$, ψ, and C and, then, substituting the resulting relation for the flux (4.7) into the mass balance (4.2c) leads to the modified Nernst-Planck equation. The modified Poisson and Nernst-Planck equations constitute the MPNP system of PDEs governing the electrochemistry, where the term *modified* refers to the presence of the mechanical deformation in these PDEs. The MPNP system has to be solved together with the Navier-like vectorial PDE obtained from the combination of equilibrium (4.2a) and constitutive equations (4.4), for five unknown scalar fields consisting of $\psi(\mathbf{X}, t)$, $C(\mathbf{X}, t)$, and the three components of $\mathbf{u}(\mathbf{X}, t)$. We explicit the governing equations in Sec. 4.2.4, after prescribing a specific form for the free energy density in Sec. 4.2.3.

We note that, given the time scale associated with counterion transport, we assume that the electro-diffusion occurs after the whole mechanical load is statically applied.

4.2.3 Prescription of the free energy density contributions

We consider isotropic elasticity governed by the Saint-Venant–Kirchhoff potential:

$$W_{\mathrm{mec}}(\mathbf{F}) = \frac{E_{\mathrm{m}}}{2(1+\nu_{\mathrm{m}})}\left[\frac{\nu_{\mathrm{m}}}{1-2\nu_{\mathrm{m}}}(\operatorname{tr}\boldsymbol{\mathcal{E}})^2 + \operatorname{tr}\boldsymbol{\mathcal{E}}^2\right], \tag{4.8}$$

in which E_{m} and ν_{m} are the Young modulus and Poisson ratio of the membrane and

$$\boldsymbol{\mathcal{E}} = \frac{1}{2}(\mathbf{C} - \mathbf{I}) \tag{4.9}$$

is the Green-Lagrange strain tensor, with $\mathbf{I}$ denoting the second-order identity tensor.

The polarization free energy W_{pol} is chosen in such a way as to provide the simplest relation between $\mathbf{E}$ and $\mathbf{D}$, that is, a linear relationship in the current configuration (Dorfmann and Ogden, 2005):

$$W_{\mathrm{pol}}(\mathbf{F}, \mathbf{D}) = \frac{|\mathbf{FD}|^2}{2\varepsilon J}, \tag{4.10}$$

where ε is the membrane absolute permittivity and

$$J = \det \mathbf{F} \tag{4.11}$$

denotes the Jacobian, or volume ratio.

The mixing free energy W_{mix} accounts for the change in entropy due to counterion mixing, and reads

$$W_{\mathrm{mix}}(\mathbf{F}, C) = \mathcal{R}T\left[C\left(\ln\frac{C}{C_0 J} - 1\right) - C_0\left(\ln\frac{1}{J} - 1\right)\right]. \tag{4.12}$$

With this form of W_{mix}, C may be unbounded in the boundary layer at the cathode, where counterions accumulate. This behavior can be controlled by a material parameter, referred to as *steric coefficient*, that can be introduced by properly extending W_{mix} (Kilic et al., 2007a,b; Porfiri, 2009; Porfiri et al., 2018). This is not a central issue in this investigation on sensing, such that we adopt the simpler form in Eq. (4.12). However, for the sake of completeness, in Sec. 4.5 we provide the relevant equations of the model when steric effects are accounted for.

4.2.4 Governing equations

By combining the balance equations of Sec. 4.2.1, the constitutive relations of Sec. 4.2.2, and the prescriptions for W in Sec. 4.2.3, we obtain the following governing equations, to be solved once assigned proper initial and boundary conditions:

$$\mathrm{Div}\Bigg[\underbrace{\frac{E_{\mathrm{m}}}{1+\nu_{\mathrm{m}}}\mathbf{F}\left(\frac{\nu_{\mathrm{m}}\mathrm{tr}\,\boldsymbol{\mathcal{E}}}{1-2\nu_{\mathrm{m}}}\mathbf{I}+\boldsymbol{\mathcal{E}}\right)}_{\mathbf{P}_{\mathrm{mec}}}+\underbrace{\frac{1}{2\varepsilon J}\Big(2\mathbf{F}(\mathbf{D}\otimes\mathbf{D})-\mathbf{C}\cdot(\mathbf{D}\otimes\mathbf{D})\mathbf{F}^{-\mathrm{T}}\Big)}_{\mathbf{P}_{\mathrm{pol}}}\underbrace{-\mathcal{R}T(C-C_0)\mathbf{F}^{-\mathrm{T}}}_{\mathbf{P}_{\mathrm{mix}}}\Bigg]+\mathbf{B}=\mathbf{0}\,, \tag{4.13a}$$

$$\mathrm{Div}\,\underbrace{\left[-\varepsilon J\mathbf{C}^{-1}\nabla\psi\right]}_{\mathbf{D}}=F(C-C_0)\,, \tag{4.13b}$$

$$\frac{\partial C}{\partial t}+\mathrm{Div}\underbrace{\left[-D\mathbf{C}^{-1}\left(\underbrace{\nabla C-\frac{C}{J}\nabla J}_{J\nabla c}+\frac{F}{\mathcal{R}T}C\nabla\psi\right)\right]}_{\mathbf{J}}=0\,, \tag{4.13c}$$

where $\cdot$ and $\otimes$ denote the inner and tensor products, respectively, and $c=C/J$ is the current counterion concentration. In particular, the counterion flux is driven by the gradient of the nominal concentration (that is, by the gradient of counterion moles, at *fixed* volume), by the gradient of the volume ratio, and by the electric field. The first two contributions represent Fick's law in deformable solids, while the third describes the electrophoretic effect.

In the electrodes the problem is purely mechanical, and reads

$$\mathrm{Div}\underbrace{\left[\frac{E_{\mathrm{e}}}{1+\nu_{\mathrm{e}}}\mathbf{F}\left(\frac{\nu_{\mathrm{e}}\mathrm{tr}\,\boldsymbol{\mathcal{E}}}{1-2\nu_{\mathrm{e}}}\mathbf{I}+\boldsymbol{\mathcal{E}}\right)\right]}_{\mathbf{P}_{\mathrm{mec}}}+\mathbf{B}=\mathbf{0}\,, \tag{4.14}$$

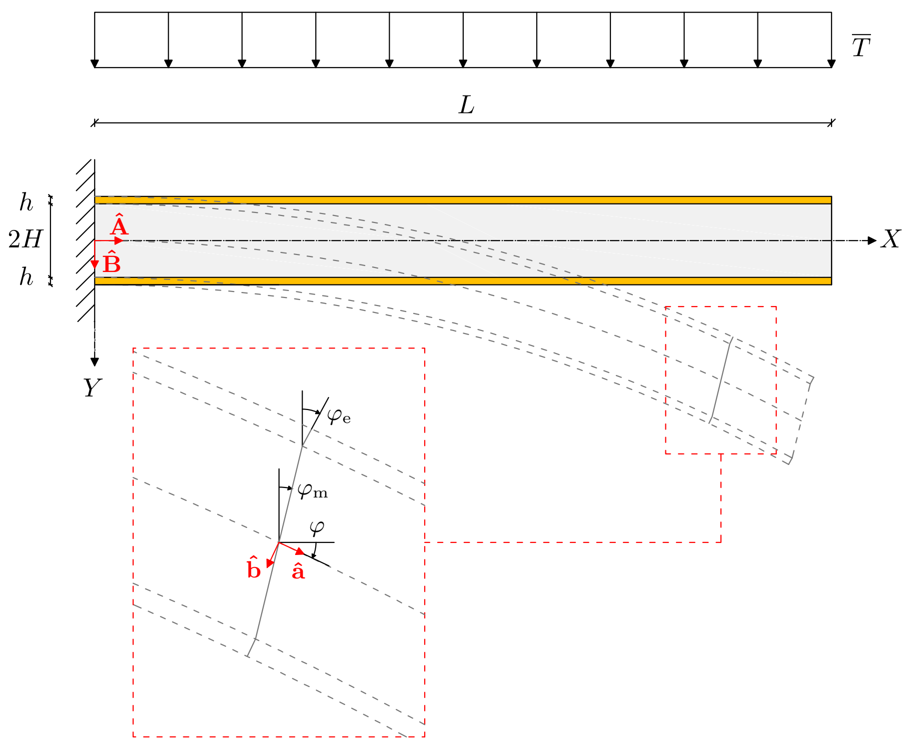

Figure 4.1: Schematics of the IPMC geometry and assumed zigzag warping, displaying both the reference and the current configurations.

where E_e and ν_e are the Young modulus and Poisson ratio of the electrodes.

4.3 The zigzag structural model

We model the IPMC as a sandwich plate, made up of a relatively thick and soft core, that is, the ionomeric membrane, and of two thin and much stiffer skins, that is, the metal electrodes. The membrane has reference thickness $2H$, whereas each electrode has thickness h. We hypothesize that the IPMC plate undergoes cylindrical bending, such that it can be studied like a plane strain beam of unit depth.

4.3.1 Kinematics

We model the IPMC kinematics by adopting the zigzag (piecewise linear) warping (ZW) model developed by Yu (1959), Krajcinovic (1972, 1975), and Bardella and Tonelli (2012) for sandwich beams. More specifically, as illustrated in Fig. 4.1, such a warping consists of allowing the cross-sections of each of the three layers to rotate independently of the mid-axis, with each layer behaving as a

Timoshenko homogeneous beam.

Because of the assumption of perfect interface between membrane and electrodes, three independent kinematic variables are needed: the transverse displacement v (related to the mid-axis rotation φ), the cross-section rotation of the membrane φ_{m}, and the cross-section rotation of the electrodes φ_{e}.

As indicated in Fig. 4.1, in the reference configuration, Y is the through-the-thickness coordinate, normal to the mid-axis X. The unit vectors along the X and Y axes are denoted with $\hat{\mathbf{A}}$ and $\hat{\mathbf{B}}$, respectively, and, in the current configuration, they become $\hat{\mathbf{a}}$ and $\hat{\mathbf{b}}$:

$$\hat{\mathbf{a}}(X,t) = \cos\varphi(X,t)\hat{\mathbf{A}} + \sin\varphi(X,t)\hat{\mathbf{B}}\,, \tag{4.15a}$$

$$\hat{\mathbf{b}}(X,t) = -\sin\varphi(X,t)\hat{\mathbf{A}} + \cos\varphi(X,t)\hat{\mathbf{B}}\,. \tag{4.15b}$$

Since we neglect the mid-axis stretching, the following relations hold:

$$x_0'(X,t) = \cos\varphi(X,t)\,, \quad y_0'(X,t) = \sin\varphi(X,t)\,, \tag{4.16}$$

where x_0 and y_0 are the current positions of the mid-axis material points and the notation $f' = \partial f/\partial X$ has been introduced.

The motion of each material point is described by

$$x(X,Y,t) = \begin{cases} x_0(X,t) - \sin\varphi_{\mathrm{m}}(X,t)\,Y \quad \text{if} \quad Y \in [-H,H]\,, \\ \\ x_0(X,t) - \sin\varphi_{\mathrm{m}}(X,t)\,H\,\mathrm{sgn}(Y) \\ -\sin\varphi_{\mathrm{e}}(X,t)\,[Y - H\ \mathrm{sgn}(Y)] \quad \text{if} \quad |Y| \in [H,H+h]\,, \end{cases} \tag{4.17a}$$

$$y(X,Y,t) = \begin{cases} y_0(X,t) + \cos\varphi_{\mathrm{m}}(X,t)\,Y \quad \text{if} \quad Y \in [-H,H]\,, \\ \\ y_0(X,t) + \cos\varphi_{\mathrm{m}}(X,t)\,H\,\mathrm{sgn}(Y) \\ +\cos\varphi_{\mathrm{e}}(X,t)\,[Y - H\,\mathrm{sgn}(Y)] \quad \text{if} \quad |Y| \in [H,H+h]\,. \end{cases} \tag{4.17b}$$

Hence, the relevant (in-plane) components of the deformation gradient read

$$\mathbf{F} = \begin{cases} \begin{bmatrix} \cos\varphi - \varphi_{\mathrm{m}}' Y \cos\varphi_{\mathrm{m}} & -\sin\varphi_m \\ \sin\varphi - \varphi_{\mathrm{m}}' Y \sin\varphi_{\mathrm{m}} & \cos\varphi_{\mathrm{m}} \end{bmatrix} & \text{if} \quad Y \in [-H, H]\,, \\ \begin{bmatrix} \cos\varphi - \varphi_{\mathrm{m}}' H \operatorname{sgn}(Y) \cos\varphi_{\mathrm{m}} & \\ \quad -\varphi_{\mathrm{e}}' [Y - H \operatorname{sgn}(Y)] \cos\varphi_{\mathrm{e}} & -\sin\varphi_e \\ \sin\varphi - \varphi_{\mathrm{m}}' H \operatorname{sgn}(Y) \sin\varphi_{\mathrm{m}} & \\ \quad -\varphi_{\mathrm{e}}' [Y - H \operatorname{sgn}(Y)] \sin\varphi_{\mathrm{e}} & \cos\varphi_{\mathrm{e}} \end{bmatrix} & \text{if} \quad |Y| \in [H, H+h]\,. \end{cases} \tag{4.18}$$

The volume ratio (4.11) in the membrane, which plays an important role in counterion diffusion, reads

$$J = \cos(\varphi - \varphi_{\mathrm{m}}) - \varphi_{\mathrm{m}}' Y \quad \text{if} \quad Y \in [-H, H]\,. \tag{4.19}$$

Since $\cos(\varphi - \varphi_{\mathrm{m}}) < 1$, the shear deformation is responsible of a local shrinkage, which is uniform over each cross-section.

4.3.2 Structural mechanical balance

We impose the mechanical balance by resorting to the principle of virtual work (PVW). With $\delta a = \dot{a}\delta t$ denoting any admissible variation of the field a, the internal virtual work (per unit depth) reads

$$\mathcal{W}_{\mathrm{int}} = \int_0^L \int_{-H-h}^{H+h} \mathbf{P} \cdot \delta\mathbf{F} \, \mathrm{d}Y \mathrm{d}X\,, \tag{4.20}$$

where the stress in the membrane comprises mechanical, electrostatic, and osmotic contributions, while the stress in the electrodes is purely mechanical (see Sec. 4.2.4).

In the external virtual work (per unit depth) we consider a transverse load per unit length and depth $\overline{T}(X,t)$, conjugate to the displacement $v(X,t)$:

$$\mathcal{W}_{\mathrm{ext}} = \int_0^L \overline{T}\, \delta v \, \mathrm{d}X\,, \tag{4.21}$$

where a relation between v and φ exists on the basis of how the transverse load works.

After integration over the cross-section and by parts, the PVW allows us to obtain

$$\mathcal{W}_{\text{int}} = \int_0^L \left[(M'_{\text{m}} - V_{\text{m}})\delta\varphi_{\text{m}} + (M'_{\text{e}} - V_{\text{e}})\delta\varphi_{\text{e}} + (V_{\text{m}} + V_{\text{e}})\delta\varphi\right]\mathrm{d}X \\ - \left[M_{\text{m}}\delta\varphi_{\text{m}} + M_{\text{e}}\delta\varphi_{\text{e}}\right]_0^L = \mathcal{W}_{\text{ext}}\,, \tag{4.22}$$

where

$$M_{\text{m}} = \int_{-H}^{H} \mathbf{T}\cdot\hat{\mathbf{a}}_{\text{m}}\, Y\,\mathrm{d}Y + 2\int_{H}^{H+h} \mathbf{T}\cdot\hat{\mathbf{a}}_{\text{m}}\, H\,\mathrm{d}Y\,, \tag{4.23a}$$

$$M_{\text{e}} = 2\int_{H}^{H+h} \mathbf{T}\cdot\hat{\mathbf{a}}_{\text{e}}(Y-H)\,\mathrm{d}Y\,, \tag{4.23b}$$

$$V_{\text{m}} = \int_{-H}^{H} \mathbf{T}\cdot\hat{\mathbf{b}}\,\mathrm{d}Y + 2\int_{H}^{H+h} \mathbf{T}\cdot\hat{\mathbf{b}}_{\text{m}}\,\varphi'_{\text{m}} H\,\mathrm{d}Y\,, \tag{4.23c}$$

$$V_{\text{e}} = 2\int_{H}^{H+h} \mathbf{T}\cdot\left(\hat{\mathbf{b}} - \hat{\mathbf{b}}_{\text{m}}\varphi'_{\text{m}}H\right)\,\mathrm{d}Y\,, \tag{4.23d}$$

in which $\mathbf{T} = \mathbf{P}\hat{\mathbf{A}}$ is the nominal traction vector, $\hat{\mathbf{a}}_{\text{m}}$ and $\hat{\mathbf{b}}_{\text{m}}$ are the unit vectors normal and tangent to the deformed membrane cross-section, and $\hat{\mathbf{a}}_{\text{e}}$ and $\hat{\mathbf{b}}_{\text{e}}$ are the unit vectors normal and tangent to the deformed electrode cross-sections.

Specifically, M_{m} is the part of the total bending moment $M = M_{\text{m}} + M_{\text{e}}$ conjugate to $\delta\varphi_{\text{m}}$ and M_{e} is the part of M conjugate to $\delta\varphi_{\text{e}}$. The internal action

$$V = V_{\text{m}} + V_{\text{e}} = \int_{-H-h}^{H+h} \mathbf{T}\cdot\hat{\mathbf{b}}\,\mathrm{d}Y \tag{4.24}$$

is referred to as the *shear force* even if it is not the integral of the shear stress over the cross-section. We note that in the small strain case V_{m} and V_{e} become the integrals over the membrane and the electrodes, respectively, of the shear stress, while M_{m} still includes a contribution from the longitudinal stresses in the electrodes, such that it does not correspond to the bending moment sustained by the membrane. Moreover, we remark that the internal actions in the membrane comprise three contributions, analogously to the stress contributions of the continuum theory, see Eq. (4.4b):

$$V_{\text{m}} = V_{\text{mec,m}} + V_{\text{pol}} + V_{\text{mix}}\,, \quad M_{\text{m}} = M_{\text{mec,m}} + M_{\text{pol}} + M_{\text{mix}}\,. \tag{4.25}$$

In order to analytically solve the electrochemo-mechanical problem, we follow our previous studies (Volpini et al., 2017; Porfiri et al., 2017) and linearize the mechanical balance with respect to the kinematics. We remark that this type of linearization is not applied to the MPNP system (see Sec. 4.4), where the use of the nonlinear expression (4.19) of J is essential to unveil the influence of shear deformation on the electrochemistry.

Hence, we have $\delta v' = \delta\varphi$, such that $V = V_\mathrm{m} + V_\mathrm{e}$ is the force conjugate to δv and the PVW (4.22) becomes

$$\int_0^L \big[(M'_\mathrm{m} - V_\mathrm{m})\delta\varphi_\mathrm{m} + (M'_\mathrm{e} - V_\mathrm{e})\delta\varphi_\mathrm{e} - (V'_\mathrm{m} + V'_\mathrm{e})\delta v\big]\mathrm{d}X \\ + \Big[(V_\mathrm{m} + V_\mathrm{e})\delta v - M_\mathrm{m}\delta\varphi_\mathrm{m} - M_\mathrm{e}\delta\varphi_\mathrm{e}\Big]_0^L = \mathcal{W}_\mathrm{ext} \quad \forall\, \delta v, \delta\varphi_\mathrm{m}, \delta\varphi_\mathrm{e}\,. \tag{4.26}$$

Hence, by using Eq. (4.21), the strong form of the equilibrium equations immediately follows:

$$M'_\mathrm{m} = V_\mathrm{m}\,, \tag{4.27a}$$

$$M'_\mathrm{e} = V_\mathrm{e}\,, \tag{4.27b}$$

$$V' = -\overline{T}\,. \tag{4.27c}$$

By substituting the relations presented in Sec. 4.2 in the foregoing definitions, the internal actions result

$$M_\mathrm{mec,m} = M^{\varphi_\mathrm{m}}_\mathrm{mec}\varphi'_\mathrm{m} + M^{\varphi_\mathrm{m}\varphi_\mathrm{e}}_\mathrm{mec}\varphi'_\mathrm{e} \\ \text{with} \quad M^{\varphi_\mathrm{m}}_\mathrm{mec} = -\frac{2E_\mathrm{m}H^3}{3(1-\nu_\mathrm{m}^2)} - \frac{2E_\mathrm{e}H^2h}{1-\nu_\mathrm{e}^2}\,,\ M^{\varphi_\mathrm{m}\varphi_\mathrm{e}}_\mathrm{mec} = -\frac{E_\mathrm{e}Hh^2}{1-\nu_\mathrm{e}^2}\,, \tag{4.28a}$$

$$M_\mathrm{pol} = -\int_{-H}^{H} \frac{\varepsilon}{2}\left(\frac{\partial\psi}{\partial Y}\right)^2 Y\,\mathrm{d}Y\,, \tag{4.28b}$$

$$M_\mathrm{mix} = M^{\varphi_\mathrm{m}}_\mathrm{mix}\varphi'_\mathrm{m} + M^0_\mathrm{mix} \\ \text{with} \quad M^{\varphi_\mathrm{m}}_\mathrm{mix} = \int_{-H}^{H} -\mathcal{R}T(C-C_0)Y^2\,\mathrm{d}Y\,,\ M^0_\mathrm{mix} = \int_{-H}^{H} -\mathcal{R}T(C-C_0)Y\,\mathrm{d}Y\,, \tag{4.28c}$$

$$M_\mathrm{mec,e} = M^{\varphi_\mathrm{m}\varphi_\mathrm{e}}_\mathrm{mec}\varphi'_\mathrm{m} + M^{\varphi_\mathrm{e}}_\mathrm{mec}\varphi'_\mathrm{e} \quad \text{with} \quad M^{\varphi_\mathrm{e}}_\mathrm{mec} = -\frac{2E_\mathrm{e}h^3}{3(1-\nu_\mathrm{e}^2)}\,, \tag{4.28d}$$

$$V_\mathrm{mec,m} = V^{\gamma_\mathrm{m}}_\mathrm{mec}(v' - \varphi_\mathrm{m}) \quad \text{with} \quad V^{\gamma_\mathrm{m}}_\mathrm{mec} = 2G_\mathrm{m}H\,, \tag{4.28e}$$

$$V_\mathrm{pol} = V^{\gamma_\mathrm{m}}_\mathrm{pol}(v' - \varphi_\mathrm{m}) \quad \text{with} \quad V^{\gamma_\mathrm{m}}_\mathrm{pol} = -\int_{-H}^{H} \frac{\varepsilon}{2}\left(\frac{\partial\psi}{\partial Y}\right)^2 \mathrm{d}Y\,, \tag{4.28f}$$

$$V_\mathrm{mix} = V^{\gamma_\mathrm{m}}_\mathrm{mix}(v' - \varphi_\mathrm{m}) \quad \text{with} \quad V^{\gamma_\mathrm{m}}_\mathrm{mix} = \int_{-H}^{H} \mathcal{R}T(C-C_0)\,\mathrm{d}Y\,, \tag{4.28g}$$

$$V_\mathrm{mec,e} = V^{\gamma_\mathrm{e}}_\mathrm{mec}(v' - \varphi_\mathrm{e}) \quad \text{with} \quad V^{\gamma_\mathrm{e}}_\mathrm{mec} = 2G_\mathrm{e}h\,. \tag{4.28h}$$

Here, $G_\mathrm{m} = E_\mathrm{m}/[2(1+\nu_\mathrm{m})]$ and $G_\mathrm{e} = E_\mathrm{e}/[2(1+\nu_\mathrm{e})]$ are the shear moduli and, by introducing the further condition of vanishing through-the-thickness normal stress, as in standard plate theory, the longitudinal modulus entering the bending stiffness is $E_{\mathrm{i}}/(1-\nu_{\mathrm{i}}^2)$, with $\mathrm{i} = \mathrm{m}, \mathrm{e}$. We note that, in Eqs. (4.28b) and (4.28f), according to the parallel plate assumption (PPA), we have neglected the Maxwell stress contributions proportional to ψ'. Moreover, because of the definition (4.23c), it results that $V_{\mathrm{mix}} \neq 0$, although $\boldsymbol{\sigma}_{\mathrm{mix}}$, that is, the Cauchy stress corresponding to $\mathbf{P}_{\mathrm{mix}}$, is a spherical tensor.

4.3.3 General analytical solution of the structural mechanical balance

By substituting the internal actions (4.28) into the equilibrium Eqs. (4.27), we obtain a system of ODEs to be solved for $v(X)$, $\varphi_{\mathrm{m}}(X)$, and $\varphi_{\mathrm{e}}(X)$. Here, we analytically solve this system by assuming that ψ and C are known, and by neglecting their dependence on X. We remark that our final solution for ψ and C will eventually depend on X, because it will be obtained, in Sec. 4.4, by integrating the MPNP PDEs in Y and t at each X, the latter position along the mid-axis providing the membrane curvature and shear strain modulating the MPNP system. The validity of this strategy will be proved in Sec. 4.7.

The analytical solution of the structural mechanical balance can be obtained by extending the technique proposed by Krajcinovic (1972) (see also Bardella and Tonelli, 2012) to uncouple the three ODEs and integrate them. More details are given at the end of this section for the interested reader. It results that $\varphi_{\mathrm{m}}(X)$, $\varphi_{\mathrm{e}}(X)$, and $v(X)$ can be expressed in terms of an auxiliary function $f(X)$, as follows:

$$\varphi_{\mathrm{m}} = \frac{\beta_1 \alpha_2}{\alpha_1 \beta_2} \left(k^2 f' - f'''\right) + e f''' \,, \tag{4.29a}$$

$$\varphi_{\mathrm{e}} = \frac{\beta_1 \alpha_2}{\alpha_1 \beta_2} \left(k^2 f' - f'''\right) - H(m+1) f''' \,, \tag{4.29b}$$

$$v = \frac{\alpha_2}{\beta_2} f^{IV} - \left(\frac{\beta_3}{\beta_2} + \frac{\beta_1 \alpha_2}{\alpha_1 \beta_2}\right) f'' + \frac{\beta_1 \alpha_2 k^2}{\alpha_1 \beta_2} f \,, \tag{4.29c}$$

in which

$$\alpha_1 = -M_{\mathrm{mec}}^{\varphi_{\mathrm{m}}} - 2M_{\mathrm{mec}}^{\varphi_{\mathrm{m}}\varphi_{\mathrm{e}}} - M_{\mathrm{mix}}^{\varphi_{\mathrm{m}}} - M_{\mathrm{mec}}^{\varphi_{\mathrm{e}}} \,, \tag{4.30a}$$

$$\begin{aligned} \alpha_2 = {} & -(M_{\mathrm{mec}}^{\varphi_{\mathrm{m}}} + M_{\mathrm{mix}}^{\varphi_{\mathrm{m}}}) h^2 + M_{\mathrm{mec}}^{\varphi_{\mathrm{m}}\varphi_{\mathrm{e}}} (m+1) H h \\ & - \frac{M_{\mathrm{mec}}^{\varphi_{\mathrm{m}}} + M_{\mathrm{mec}}^{\varphi_{\mathrm{m}}\varphi_{\mathrm{e}}} + M_{\mathrm{mix}}^{\varphi_{\mathrm{m}}}}{M_{\mathrm{mec}}^{\varphi_{\mathrm{m}}\varphi_{\mathrm{e}}} + M_{\mathrm{mec}}^{\varphi_{\mathrm{e}}}} h \left[-M_{\mathrm{mec}}^{\varphi_{\mathrm{m}}\varphi_{\mathrm{e}}} h + M_{\mathrm{mec}}^{\varphi_{\mathrm{e}}} (m+1) H\right] , \end{aligned} \tag{4.30b}$$

$$\beta_1 = V_{\mathrm{mec}}^{\gamma_{\mathrm{m}}} + V_{\mathrm{pol}}^{\gamma_{\mathrm{m}}} + V_{\mathrm{mix}}^{\gamma_{\mathrm{m}}} + V_{\mathrm{mec}}^{\gamma_{\mathrm{e}}} \,, \tag{4.30c}$$

$$\beta_2 = -(V_{\mathrm{mec}}^{\gamma_{\mathrm{m}}} + V_{\mathrm{pol}}^{\gamma_{\mathrm{m}}} + V_{\mathrm{mix}}^{\gamma_{\mathrm{m}}}) h + V_{\mathrm{mec}}^{\gamma_{\mathrm{e}}} (m+1) H \,, \tag{4.30d}$$

$$\beta_3 = (V^{\gamma_\mathrm{m}}_\mathrm{mec} + V^{\gamma_\mathrm{m}}_\mathrm{pol} + V^{\gamma_\mathrm{m}}_\mathrm{mix})h^2 + \frac{V^{\gamma_\mathrm{e}}_\mathrm{mec}(m+1)Hh(M^{\varphi_\mathrm{m}}_\mathrm{mec} + M^{\varphi_\mathrm{m}\varphi_\mathrm{e}}_\mathrm{mec} + M^{\varphi_\mathrm{m}}_\mathrm{mix})}{M^{\varphi_\mathrm{m}\varphi_\mathrm{e}}_\mathrm{mec} + M^{\varphi_\mathrm{e}}_\mathrm{mec}}\,, \tag{4.30e}$$

$$m = \frac{(M^{\varphi_\mathrm{m}}_\mathrm{mec} + M^{\varphi_\mathrm{m}\varphi_\mathrm{e}}_\mathrm{mec} + M^{\varphi_\mathrm{m}}_\mathrm{mix})h}{(M^{\varphi_\mathrm{m}\varphi_\mathrm{e}}_\mathrm{mec} + M^{\varphi_\mathrm{e}}_\mathrm{mec})H} - 1\,, \tag{4.30f}$$

$$k^2 = \frac{\beta_1\beta_3 - \beta_2^2}{\beta_1\alpha_2}\,, \tag{4.30g}$$

and the auxiliary function $f(X)$ solves the sixth-order ODE

$$f^{VI}(X) - k^2 f^{IV}(X) = -\frac{\beta_2}{\beta_1\alpha_2}\overline{T}(X)\,, \tag{4.31}$$

involving the determination of six integration constants C_i (with $\mathrm{i} = 1, \ldots, 6$). For a uniform applied transverse load $\overline{T}$, $f(X)$ reads

$$f(X) = C_1\sinh(kX) + C_2\cosh(kX) + \overline{T}_0X^4 + C_3X^3 + C_4X^2 + C_5X + C_6\,, \tag{4.32}$$

where

$$\overline{T}_0 = \frac{\beta_2}{24(\beta_1\beta_3 - \beta_2^2)}\overline{T}\,. \tag{4.33}$$

Solution for the cantilever benchmark

We consider the cantilever IPMC of Fig. 4.1, whose kinematic and static boundary conditions read, respectively:

$$v(X=0) = 0\,, \quad \varphi_\mathrm{m}(X=0) = 0\,, \quad \varphi_\mathrm{e}(X=0) = 0\,, \tag{4.34a}$$

and

$$V(X=L) = 0\,, \quad M_\mathrm{m}(X=L) = 0\,, \quad M_\mathrm{e}(X=L) = 0\,. \tag{4.34b}$$

Rewriting the last two static boundary conditions in terms of the kinematic variables reveals an interesting outcome of the adopted structural theory to study IPMC electrochemo-mechanics:

$$\varphi'_\mathrm{m}(X=L) = \gamma_1\,, \quad \varphi'_\mathrm{e}(X=L) = \gamma_2\,, \tag{4.35}$$

where

$$\gamma_1 = -\frac{M^{\varphi_\mathrm{m}\varphi_\mathrm{e}}_\mathrm{mec}(M_\mathrm{pol} + M^0_\mathrm{mix})}{(M^{\varphi_\mathrm{m}\varphi_\mathrm{e}}_\mathrm{mec})^2 - M^{\varphi_\mathrm{e}}_\mathrm{mec}(M^{\varphi_\mathrm{m}}_\mathrm{mec} + M^{\varphi_\mathrm{m}}_\mathrm{mix})}\,, \quad \gamma_2 = -\gamma_1\frac{2h}{3H}\,. \tag{4.36}$$

Hence, at the free end the static boundary conditions (4.35) are not homogeneous, even in the absence of concentrated moments, because of the electrochemical contribution. Therefore, at least theoretically, even IPMC actuation is not free from warping, the latter being proportional, through M_{pol} and M^0_{mix}, to the applied voltage.

Back to our sensing problem, by imposing the boundary conditions (4.34), we obtain the following integration constants:

$$
\begin{aligned}
&C_1 = \frac{24\overline{T}_0 L}{k^3}\,, \quad C_2 = -\frac{24\overline{T}_0}{k^4}\frac{1+kL\sinh(kL)}{\cosh(kL)} + \frac{1}{k^4}\frac{\mathrm{sech}(kL)(\gamma_1-\gamma_2)}{H(m+1)+h}\,,\\
&C_3 = -4\overline{T}_0 L\,, \quad C_4 = \frac{6\overline{T}_0}{k^2}(2+k^2L^2) + \frac{\alpha_1\beta_2}{2(-\beta_2^2+\beta_1\beta_3)}\frac{H(m+1)\gamma_1+h\gamma_2}{H(m+1)+h}\,,\\
&\qquad C_5 = -\frac{24\overline{T}_0 L}{k^2}\,, \quad C_6 = 12\overline{T}_0\Bigg[\frac{2}{k^4}+\frac{L^2}{k^2}+\frac{L^2}{k^2}\frac{\alpha_1\beta_3}{\alpha_2\beta_1}\\
&+\frac{2}{k^4}\frac{\alpha_1\beta_2^2}{\alpha_2\beta_1^2}\Big(1-\mathrm{sech}(kL)-kL\tanh(kL)\Big)\Bigg] + \frac{\alpha_1\beta_2}{[H(m+1)+h](\beta_2^2-\beta_1\beta_3)^2}\\
&\times\Big[(\alpha_2\beta_1+\alpha_1\beta_3)[H(m+1)\gamma_1+h\gamma_2]+\alpha_2\beta_2(\gamma_1-\gamma_2)\,\mathrm{sech}(kL)\Big]\,,
\end{aligned}
\tag{4.37}
$$

in which we note that the second contributions in C_2, C_4, and C_6 vanish in the absence of electro-diffusion (as $\gamma_1 = \gamma_2 = 0$). Finally, by substituting Eq. (4.37) in Eq. (4.32), we obtain the following expression for $f(X)$, to be plugged in Eq. (4.29):

$$
\begin{aligned}
f(X) &= \frac{24\overline{T}_0}{k^4}\frac{1}{1+\exp(-2kL)}\Big[kL[\exp(-2kL+kX)-\exp(-kX)]\\
&\quad -\exp(-kL+kX)-\exp(-kL-kX)\Big] + \frac{1}{k^4}\frac{\gamma_1-\gamma_2}{H(m+1)+h}\\
&\times\frac{\exp(-kL)+\exp(-kL-2kX)}{\exp(-kX)+\exp(-2kL-kX)} + \overline{T}_0X^4 - 4\overline{T}_0LX^3 + \frac{6\overline{T}_0}{k^2}(2+k^2L^2)X^2\\
&\quad + \frac{\alpha_1\beta_2}{2(-\beta_2^2+\beta_1\beta_3)}\frac{H(m+1)\gamma_1+h\gamma_2}{H(m+1)+h}X^2 - \frac{24\overline{T}_0L}{k^2}X + 12\overline{T}_0\\
&\times\left[\frac{L^2}{k^2}+\frac{\alpha_1\beta_3L^2}{k^2\alpha_2\beta_1}+\frac{2}{k^4}+\frac{2\alpha_1\beta_2^2}{k^4\alpha_2\beta_1^2}\frac{1-kL+(1+kL)\exp(-2kL)-2\exp(-kL)}{1+\exp(-2kL)}\right]\\
&\quad + \frac{\alpha_1\beta_2}{[H(m+1)+h](\beta_2^2-\beta_1\beta_3)^2}\Bigg[(\alpha_2\beta_1+\alpha_1\beta_3)[H(m+1)\gamma_1+h\gamma_2]\\
&\qquad + \alpha_2\beta_2(\gamma_1-\gamma_2)\frac{2\exp(-kL)}{1+\exp(-2kL)}\Bigg]\,.
\end{aligned}
\tag{4.38}
$$

We note that in Eq. (4.38) we have transformed the hyperbolic functions into exponential functions of appropriate argument in order to avoid numerical issues due to the high value of k, which is proportional to the sandwich heterogeneity. In the absence of electrochemistry, $\gamma_1 = \gamma_2 = 0$ and Eq. (4.38) particularizes to Eq. (27) in Bardella and Mattei (2014) for the analogous purely mechanical problem.

Uncoupling equilibrium equations[†]

To uncouple Eqs. (4.27), it is convenient to resort to Krajcinovic's treatment of the zigzag warping (Krajcinovic, 1972; Bardella and Mattei, 2014). We start by defining the displacement along the X axis of any cross-section point as

$$u(X,Y) = -Y\,\Phi(X) + \omega(Y)\Psi(X)\,, \tag{4.39}$$

in which we have introduced the average rotation of the whole sandwich cross-section Φ and the warping function Ψ in place of φ_{m} and φ_{e}. The following relations hold:

$$\varphi_{\mathrm{m}}(X) = \Phi(X) - \Psi(X)h\,, \tag{4.40a}$$

$$\varphi_{\mathrm{e}}(X) = \Phi(X) + \Psi(Y)H(m+1)\,. \tag{4.40b}$$

The zigzag function ω is related to the cross-section shearing distortion, and it is modulated by the coefficient m as follows:

$$\omega(Y) = \begin{cases} hY \quad \text{if} \quad Y \in [-H, H]\,, \\ \\ -(m+1)HY + [H(m+1)+h]H\,\mathrm{sgn}(Y) \quad \text{if} \quad |Y| \in [H, H+h]\,. \end{cases} \tag{4.41}$$

Substitution of expressions (4.28) into equilibrium Eqs. (4.27) leads to

$$\left(M^{\varphi_{\mathrm{m}}}_{\mathrm{mec}} + M^{\varphi_{\mathrm{m}}}_{\mathrm{mix}}\right)\varphi''_{\mathrm{m}} + M^{\varphi_{\mathrm{m}}\varphi_{\mathrm{e}}}_{\mathrm{mec}}\varphi''_{\mathrm{e}} = \left(V^{\gamma_{\mathrm{m}}}_{\mathrm{mec}} + V^{\gamma_{\mathrm{m}}}_{\mathrm{pol}} + V^{\gamma_{\mathrm{m}}}_{\mathrm{mix}}\right)(v' - \varphi_{\mathrm{m}})\,, \tag{4.42a}$$

$$M^{\varphi_{\mathrm{m}}\varphi_{\mathrm{e}}}_{\mathrm{mec}}\varphi''_{\mathrm{m}} + M^{\varphi_{\mathrm{e}}}_{\mathrm{mec}}\varphi''_{\mathrm{e}} = V^{\gamma_{\mathrm{e}}}_{\mathrm{mec}}(v' - \varphi_{\mathrm{e}})\,, \tag{4.42b}$$

$$\left(V^{\gamma_{\mathrm{m}}}_{\mathrm{mec}} + V^{\gamma_{\mathrm{m}}}_{\mathrm{pol}} + V^{\gamma_{\mathrm{m}}}_{\mathrm{mix}} + V^{\gamma_{\mathrm{e}}}_{\mathrm{mec}}\right)v'' - \left(V^{\gamma_{\mathrm{m}}}_{\mathrm{mec}} + V^{\gamma_{\mathrm{m}}}_{\mathrm{pol}} + V^{\gamma_{\mathrm{m}}}_{\mathrm{mix}}\right)\varphi'_{\mathrm{m}} - V^{\gamma_{\mathrm{e}}}_{\mathrm{mec}}\varphi'_{\mathrm{e}} = -\overline{T}\,. \tag{4.42c}$$

By replacing Eqs. (4.40) into Eqs. (4.42) we obtain

$$\begin{aligned} &\left(M^{\varphi_{\mathrm{m}}}_{\mathrm{mec}} + M^{\varphi_{\mathrm{m}}\varphi_{\mathrm{e}}}_{\mathrm{mec}} + M^{\varphi_{\mathrm{m}}}_{\mathrm{mix}}\right)\Phi'' + \left[-\left(M^{\varphi_{\mathrm{m}}}_{\mathrm{mec}} + M^{\varphi_{\mathrm{m}}}_{\mathrm{mix}}\right)h + M^{\varphi_{\mathrm{m}}\varphi_{\mathrm{e}}}_{\mathrm{mec}}(m+1)H\right]\Psi'' \\ &\qquad - \left(V^{\gamma_{\mathrm{m}}}_{\mathrm{mec}} + V^{\gamma_{\mathrm{m}}}_{\mathrm{pol}} + V^{\gamma_{\mathrm{m}}}_{\mathrm{mix}}\right)(v' - \Phi) - \left(V^{\gamma_{\mathrm{m}}}_{\mathrm{mec}} + V^{\gamma_{\mathrm{m}}}_{\mathrm{pol}} + V^{\gamma_{\mathrm{m}}}_{\mathrm{mix}}\right)h\Psi = 0\,, \end{aligned} \tag{4.43a}$$

$$\begin{aligned} &\left(M^{\varphi_{\mathrm{m}}\varphi_{\mathrm{e}}}_{\mathrm{mec}} + M^{\varphi_{\mathrm{e}}}_{\mathrm{mec}}\right)\Phi'' + \left[-M^{\varphi_{\mathrm{m}}\varphi_{\mathrm{e}}}_{\mathrm{mec}}h + M^{\varphi_{\mathrm{e}}}_{\mathrm{mec}}(m+1)H\right]\Psi'' \\ &\qquad - V^{\gamma_{\mathrm{e}}}_{\mathrm{mec}}(v' - \Phi) + V^{\gamma_{\mathrm{e}}}_{\mathrm{mec}}(m+1)H\Psi = 0\,, \end{aligned} \tag{4.43b}$$

$$\begin{aligned} &\left(V^{\gamma_{\mathrm{m}}}_{\mathrm{mec}} + V^{\gamma_{\mathrm{m}}}_{\mathrm{pol}} + V^{\gamma_{\mathrm{m}}}_{\mathrm{mix}} + V^{\gamma_{\mathrm{e}}}_{\mathrm{mec}}\right)(v'' - \Phi') \\ &\qquad + \left[\left(V^{\gamma_{\mathrm{m}}}_{\mathrm{mec}} + V^{\gamma_{\mathrm{m}}}_{\mathrm{pol}} + V^{\gamma_{\mathrm{m}}}_{\mathrm{mix}}\right)h - V^{\gamma_{\mathrm{e}}}_{\mathrm{mec}}(m+1)H\right]\Psi' + \overline{T} = 0\,. \end{aligned} \tag{4.43c}$$

By introducing the coefficients (4.30), the system (4.43) can be rewritten in the following more compact form, wherein each of Φ'' and Ψ'' enters one equation only:

$$\alpha_1\Phi'' + \beta_1(v' - \Phi) + \beta_3\Psi = 0\,, \tag{4.44a}$$

$$- \alpha_2 \Psi'' - \beta_2 (v' - \Phi) + \beta_3 \Psi = 0\,, \tag{4.44b}$$

$$\beta_1 (v'' - \Phi') - \beta_2 \Psi' + \overline{T} = 0\,. \tag{4.44c}$$

Through further manipulation, the system (4.44) can be uncoupled, thus obtaining the sixth-order ODE (4.31). Specifically, the functions $\Phi(X)$, $\Psi(X)$, and $v(X)$ are related to $f(X)$ as follows:

$$\Phi = \frac{\beta_1 \alpha_2}{\alpha_1 \beta_2} (k^2 f' - f''')\,, \tag{4.45a}$$

$$\Psi = -f'''\,, \tag{4.45b}$$

$$v = \frac{\alpha_2}{\beta_2} f^{IV} - \left(\frac{\beta_3}{\beta_2} + \frac{\beta_1 \alpha_2}{\alpha_1 \beta_2} \right) f'' + \frac{\beta_1 \alpha_2 k^2}{\alpha_1 \beta_2} f\,, \tag{4.45c}$$

such that, by using Eqs. (4.40), we finally obtain Eqs. (4.29). We note that the calibration of the coefficient m in Eq. (4.30f), governing the zigzag magnitude ω of the warping function Ψ, is key to uncouple equilibrium equations.

4.4 The modified Poisson-Nernst-Planck system and its perturbative solution

4.4.1 The electric displacement and the counterion flux

We follow the PPA (Pelesko and Bernstein, 2003; Cha and Porfiri, 2014) and evaluate the electrochemical response by considering a spatially one-dimensional problem, along the membrane thickness. This implies that, in writing the MPNP system, we neglect the derivatives of ψ, C, and $\tilde{\mu}$ with respect to X. Hence, by combining the relations presented in Secs. 4.2 and 4.3, we obtain the following relevant components of the electric displacement and counterion flux:

$$D_Y = -\varepsilon \frac{1 + (\varphi'_{\mathrm{m}})^2 Y^2 - 2\varphi'_{\mathrm{m}} Y \cos(\varphi - \varphi_{\mathrm{m}})}{J} \frac{\partial \psi}{\partial Y}\,, \tag{4.46a}$$

$$J_Y = -D \frac{1 + (\varphi'_{\mathrm{m}})^2 Y^2 - 2\varphi'_{\mathrm{m}} Y \cos(\varphi - \varphi_{\mathrm{m}})}{J^2} \times \left(\frac{C}{J} \varphi'_{\mathrm{m}} + \frac{\partial C}{\partial Y} + \frac{F}{\mathcal{R}T} C \frac{\partial \psi}{\partial Y} \right)\,, \tag{4.46b}$$

with J the volume ratio given by Eq. (4.19).

Here, consistently with the finite deformation finite element (FE) analyses reported in Sec. 4.7.3, we assume that the distributed load p acts along the Y direction all along the loading history, such that $v = y_0$ (see Eq. (4.16)). Hence, in Eqs. (4.46) and in the following, we use the relation $\varphi = \arcsin v'$.

The expression (4.46b) for the counterion flux can be recasted in the general theory presented in Gurtin et al. (2010) for the diffusion of species in elastic solids, with the addition of the electrophoretic term. In particular, the flux consists of three main contributions proportional to φ'_{m}, $\partial C/\partial Y$, and $\partial\psi/\partial Y$. We note that the curvature, $-\varphi'_{\mathrm{m}}$, is the through-the-thickness component of the volume ratio gradient (see Eq. (4.19)) and, in the flux (4.46b), is also modulated by the shear deformation $\varphi - \varphi_{\mathrm{m}}$.

At $t = 0^+$, that is, just after the application of the mechanical load, the IPMC state is well approximated by:

$$C \approx C_0\,, \quad \partial C/\partial Y \approx 0\,, \quad \partial\psi/\partial Y \approx 0\,, \tag{4.47}$$

which corresponds to negligible counterion migration (associated with the electrophoretic effect), whereas diffusion (associated with Fick's law) triggers the electrochemical response. By substituting conditions (4.47) in Eq. (4.46b) we obtain

$$J_Y \approx -D\left(1 + \frac{\sin^2(\varphi - \varphi_{\mathrm{m}})}{J^2}\right)\frac{C_0}{J}\varphi'_{\mathrm{m}}\,, \tag{4.48}$$

showing that the electrochemical response vanishes in the absence of curvature. However, the shear deformation amplifies the electrochemical response, because both $\sin^2(\varphi - \varphi_{\mathrm{m}}) \geq 0$ and J decreases with increasing $\varphi - \varphi_{\mathrm{m}}$ (see Eq. 4.19).

By neglecting the membrane shear deformation, Eq. (4.46b) particularizes to the analogous relation obtained in Porfiri et al. (2017). Also, even though $\varphi - \varphi_{\mathrm{m}}$ does not appear in the linearized version of Eq. (4.46b), the shear deformation indirectly affects φ'_{m} in the ZW structural model, as occurs in fully clamped regions (see Sec. 4.7).

4.4.2 The modified Poisson-Nernst-Planck system

Substitution of Eqs. (4.46) into the balance equations (4.2b) and (4.2c) leads to the MPNP system:

$$-\,\varepsilon\frac{\partial}{\partial Y}\left[\frac{1 + (\varphi'_{\mathrm{m}})^2 Y^2 - 2\varphi'_{\mathrm{m}} Y\cos(\varphi - \varphi_{\mathrm{m}})}{J}\frac{\partial\psi}{\partial Y}\right] = F(C - C_0)\,, \tag{4.49a}$$

$$\frac{\partial C}{\partial t} = D\frac{\partial}{\partial Y}\left[\frac{1 + (\varphi'_{\mathrm{m}})^2 Y^2 - 2\varphi'_{\mathrm{m}} Y\cos(\varphi - \varphi_{\mathrm{m}})}{J^2} \times\left(\frac{C}{J}\varphi'_{\mathrm{m}} + \frac{\partial C}{\partial Y} + \frac{F}{\mathcal{R}T}C\frac{\partial\psi}{\partial Y}\right)\right], \tag{4.49b}$$

on which we impose the following boundary and initial conditions:

$$\psi(\pm H, t) = 0\,, \quad t \geq 0 \quad \text{(short circuit)}\,, \tag{4.50a}$$

$$J_Y(\pm H, t) = 0\,, \quad t \geq 0 \quad \text{(ion-blocking)}\,, \tag{4.50b}$$

$$\psi(Y, 0) = 0 \quad \text{and} \quad C(Y, 0) = C_0\,, \quad Y \in [-H, H] \quad \text{(electroneutrality)}\,. \tag{4.50c}$$

Moreover, the integration of Poisson and Nernst-Planck Eqs. (4.49), in conjunction with the ion-blocking and electroneutrality conditions (4.50b) and (4.50c), reveals that (Porfiri, 2008)

$$D_Y(H, t) = D_Y(-H, t) = -Q\,, \tag{4.51}$$

with Q denoting the stored charge per unit nominal area, whose time derivative is the electric current (per unit nominal area):

$$I = \frac{\mathrm{d}Q}{\mathrm{d}t} = -\frac{\mathrm{d}D_Y(\pm H, t)}{\mathrm{d}t}\,. \tag{4.52}$$

4.4.3 Solution through matched asymptotic expansions

Nondimensional modified Poisson-Nernst-Planck system

In order to semi-analytically solve the MPNP system, we conveniently rewrite it by defining the following nondimensional variables:

$$\bar{\psi} = \psi/V_{\mathrm{th}}\,, \quad \bar{C} = C/C_0\,, \quad \bar{\varphi}'_{\mathrm{m}} = \varphi'_{\mathrm{m}} H\,, \quad \bar{Y} = Y/H\,, \quad \bar{t} = t/\tau_0\,, \tag{4.53}$$

where $V_{\mathrm{th}} = \mathcal{R}T/F$ is the thermal voltage and $\tau_0 = H/(FD)\sqrt{\varepsilon \mathcal{R}T/C_0}$ is the characteristic time (Porfiri, 2008). Hence, the MPNP system (4.49) can be rewritten as

$$-\,\delta^2 \frac{\partial}{\partial Y}\left[\frac{1 + (\varphi'_{\mathrm{m}})^2 Y^2 - 2\varphi'_{\mathrm{m}} Y \cos(\varphi - \varphi_{\mathrm{m}})}{J}\frac{\partial \psi}{\partial Y}\right] = C - 1\,, \tag{4.54a}$$

$$\frac{\partial C}{\partial t} = \delta \frac{\partial}{\partial Y}\left[\frac{1 + (\varphi'_{\mathrm{m}})^2 Y^2 - 2\varphi'_{\mathrm{m}} Y \cos(\varphi - \varphi_{\mathrm{m}})}{J^2} \right.$$
$$\left. \times \left(\frac{C}{J}\varphi'_{\mathrm{m}} + \frac{\partial C}{\partial Y} + C\frac{\partial \psi}{\partial Y}\right)\right], \tag{4.54b}$$

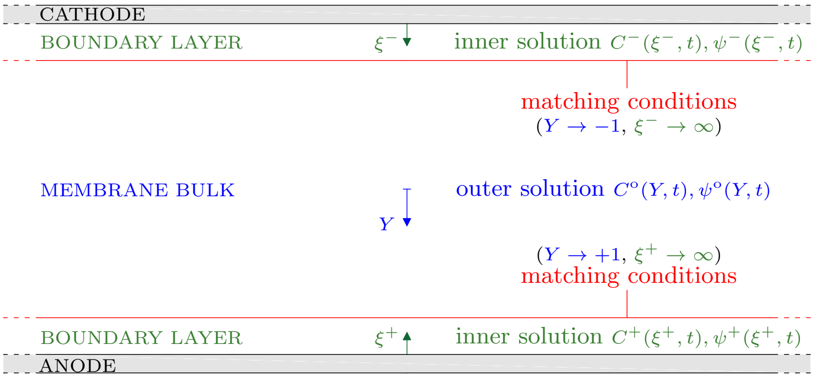

Figure 4.2: Matched asymptotic expansions: the outer solution in the membrane bulk and the inner solutions in the boundary layers are matched through proper conditions in order to obtain a composite solution valid in the whole membrane domain.

where we have dropped the overline for the nondimensional variables and

$$\delta = \frac{1}{FH}\sqrt{\frac{\varepsilon \mathcal{R} T}{C_0}} = \frac{\lambda}{H} \tag{4.55}$$

is a parameter proportional to the Debye screening length λ, whose smallness reveals that the MPNP system is a singularly perturbed differential problem, thus adequate to be solved with the method of matched asymptotic expansions (MAE) (Verhulst, 2005). Finally, the nondimensional conditions read:

$$\psi(\pm 1,t) = 0\,, \quad J_Y(\pm 1,t) = 0\,, \quad \psi(Y,0) = 0\,, \quad C(Y,0) = 1\,,$$
$$\text{along with} \quad D_Y(1,t) = D_Y(-1,t)\,. \tag{4.56}$$

Matched asymptotic expansions

The MAE method can capture the main feature of the electrochemical response, consisting of large gradients of counterion concentration and electric potential in boundary layers, at the membrane-electrode interface regions, of size on the order of δ (Porfiri, 2008).

Hence, in the following, we separately solve Eqs. (4.54) in the membrane bulk, thus obtaining the so-called *outer solution*, and in the boundary layers, thus obtaining the so-called *inner solutions*. Then, these solutions are combined, through matching conditions, in the *composite solution*, which is valid in the whole membrane domain. This approached is sketched in Fig. 4.2.

Outer solution By considering regular asymptotic expansions of C and ψ with respect to δ, the outer solution at the leading order reads

$$C^{\mathrm{o}} = 1\,, \tag{4.57a}$$

$$\psi^{\mathrm{o}} = \ln J + A_1 \left(Y + \frac{\eta}{\varphi'_{\mathrm{m}}} \arctan \frac{J}{\eta} \right) + A_2\,, \tag{4.57b}$$

where

$$\eta = \sqrt{1 - \cos^2(\varphi - \varphi_{\mathrm{m}})} \tag{4.58}$$

and A_1 and A_2 are unknown functions of time.

Inner solutions To obtain the solution in the boundary layers, we introduce the local spatial variables ξ^+ and ξ^-, defined as

$$\xi^{\pm} = \frac{1 \mp Y}{\delta}\,, \tag{4.59}$$

where the superscripts $+$ and $-$ refer to the anode ($Y \to 1$) and to the cathode ($Y \to -1$), respectively. We then rewrite the MPNP system (4.54) in terms of $\xi^{\pm}$ and, by considering the leading order of the regular asymptotic expansions of C and ψ with respect to δ, we obtain

$$-\frac{1 + (\varphi'_{\mathrm{m}})^2 \mp 2\varphi'_{\mathrm{m}} \cos(\varphi - \varphi_{\mathrm{m}})}{J^{\pm}} \frac{\partial^2 \psi^{\pm}}{\partial (\xi^{\pm})^2} = C^{\pm} - 1\,, \tag{4.60a}$$

$$\frac{\partial C^{\pm}}{\partial \xi^{\pm}} + C^{\pm} \frac{\partial \psi^{\pm}}{\partial \xi^{\pm}} = 0\,, \tag{4.60b}$$

where

$$J^{\pm} = \cos(\varphi - \varphi_{\mathrm{m}}) \mp \varphi'_{\mathrm{m}}\,. \tag{4.61}$$

We note that Eq. (4.60b) makes use of the ion-blocking condition in Eq. (4.56).

To solve system (4.60), we introduce the auxiliary functions $y^{\pm}$, such that

$$C^{\pm} = \exp\left(y^{\pm}\right)\,. \tag{4.62}$$

By substituting Eq. (4.62) in Eq. (4.60b), we obtain

$$\psi^{\pm} = -y^{\pm} + A_3^{\pm}\,, \tag{4.63}$$

where $A_3^{\pm}$ are unknown functions of time. Combination of Eqs. (4.62) and (4.63) with Eq. (4.60a) leads to the following second-order nonlinear ODEs in the unknown functions $y^{\pm}$:

$$\frac{\partial^2 y^{\pm}}{\partial(\xi^{\pm})^2} = \frac{J^{\pm}}{1+(\varphi_{\mathrm{m}}')^2 \mp 2\varphi_{\mathrm{m}}' \cos(\varphi-\varphi_{\mathrm{m}})} \left[\exp\left(y^{\pm}\right)-1\right] , \tag{4.64}$$

whose solution is provided, for the interested reader, at the end of this section.

Composite solution The matching conditions at the bulk-boundary layer interfaces for C and ψ require that (Porfiri, 2008)

$$\lim_{\xi^{\pm}\to\infty} C^{\pm} = \lim_{Y\to\pm1} C^{\mathrm{o}} = 1 , \tag{4.65a}$$

$$\lim_{\xi^{\pm}\to\infty} \psi^{\pm} = \lim_{Y\to\pm1} \psi^{\mathrm{o}} = \ln J^{\pm} + A_1 \left(\pm 1 + \frac{\eta}{\varphi_{\mathrm{m}}'} \arctan\frac{J^{\pm}}{\eta}\right) + A_2 , \tag{4.65b}$$

whereas the continuity of the flux along the membrane thickness implies

$$\underbrace{\frac{\mathrm{d}}{\mathrm{d}t}\left[\mp \frac{1+(\varphi_{\mathrm{m}}')^2 \mp 2\varphi_{\mathrm{m}}'\cos(\varphi-\varphi_{\mathrm{m}})}{J^{\pm}} \frac{\partial\psi^{\pm}}{\partial\xi^{\pm}}\bigg|_{\xi^{\pm}=0}\right]}_{Q} = A_1 , \tag{4.66}$$

where, on the basis of Eq. (4.51), we have identified the nondimensional stored charge Q, such that A_1 should be interpreted as the nondimensional electric current I flowing through the IPMC (see Eq. (4.52)).

We obtain the composite solution, valid over the whole membrane domain, by summing up the solutions in the bulk (Eqs. (4.57a) and (4.57b)) with those in the boundary layers (Eqs. (4.62) and (4.63)) and subtracting the "overlapping values" (given by Eqs. (4.65a) and (4.65b)):

$$C = -1 + \exp\left(y^{+}\right) + \exp\left(y^{-}\right) , \tag{4.67a}$$

$$\begin{aligned}\psi = {} & \ln J + A_1\left(Y + \frac{\eta}{\varphi_{\mathrm{m}}'}\arctan\frac{J}{\eta}\right) - A_2 - \ln\left(J^{+}J^{-}\right) \\ & - A_1\frac{\eta}{\varphi_{\mathrm{m}}'}\left(\arctan\frac{J^{+}}{\eta} + \arctan\frac{J^{-}}{\eta}\right) - y^{+} + A_3^{+} - y^{-} + A_3^{-} .\end{aligned} \tag{4.67b}$$

In the following, we provide details on the determination of the functions $A_1(t)$, $A_2(t)$, $A_3^{\pm}(t)$, and $y^{\pm}(\xi^{\pm}, t)$. We note that, in the composite solution, $y^{\pm}$ have to be written as functions of Y through Eq. (4.59). Finally, we remark that in the absence of shear deformation ($\eta = 0$) the composite solution reduces to that obtained by Porfiri et al. (2017).

Determination of the composite solution† In order to determine the composite solution (4.67), we start by rewriting the first and fifth conditions in Eq. (4.56) in terms of $\psi^{\pm}$:

$$\psi^{\pm}(0,t) = 0\,, \tag{4.68a}$$

$$-\frac{1+(\varphi_{\mathrm{m}}')^2 - 2\varphi_{\mathrm{m}}'\cos(\varphi-\varphi_{\mathrm{m}})}{J^+}\left.\frac{\partial\psi^+}{\partial\xi^+}\right|_{\xi^+=0} = \frac{1+(\varphi_{\mathrm{m}}')^2 + 2\varphi_{\mathrm{m}}'\cos(\varphi-\varphi_{\mathrm{m}})}{J^-}\left.\frac{\partial\psi^-}{\partial\xi^-}\right|_{\xi^-=0}. \tag{4.68b}$$

Then, by substituting the inner solutions (4.62) and (4.63) in Eqs. (4.68a) and (4.68b) and in the matching conditions (4.65a), (4.65b), and (4.66), we obtain, respectively:

$$\left.y^{\pm}\right|_{\xi^{\pm}=0} = A_3^{\pm}\,, \tag{4.69a}$$

$$-\frac{1+(\varphi_{\mathrm{m}}')^2 - 2\varphi_{\mathrm{m}}'\cos(\varphi-\varphi_{\mathrm{m}})}{J^+}\left.\frac{\partial y^+}{\partial\xi^+}\right|_{\xi^+=0} = \frac{1+(\varphi_{\mathrm{m}}')^2 + 2\varphi_{\mathrm{m}}'\cos(\varphi-\varphi_{\mathrm{m}})}{J^-}\left.\frac{\partial y^-}{\partial\xi^-}\right|_{\xi^-=0}, \tag{4.69b}$$

$$\lim_{\xi^{\pm}\to\infty} y^{\pm} = 0\,, \tag{4.69c}$$

$$A_3^{\pm} = \ln J^{\pm} + A_1\left(\pm 1 + \frac{\eta}{\varphi_{\mathrm{m}}'}\arctan\frac{J^{\pm}}{\eta}\right) + A_2\,, \tag{4.69d}$$

$$\frac{\mathrm{d}}{\mathrm{d}t}\left[\frac{1+(\varphi_{\mathrm{m}}')^2 \mp 2\varphi_{\mathrm{m}}'\cos(\varphi-\varphi_{\mathrm{m}})}{J^{\pm}}\left.\frac{\partial y^{\pm}}{\partial\xi^{\pm}}\right|_{\xi^{\pm}=0}\right] = \pm A_1\,. \tag{4.69e}$$

Combination of Eqs. (4.63), (4.69a), and (4.69c) reveals that $A_3^{\pm}$ should be interpreted as the electric potential differences across the boundary layers.

From Eqs. (4.69a) and (4.69d) we derive

$$\left.y^+\right|_{\xi^+=0} - \left.y^-\right|_{\xi^-=0} + \ln\frac{J^-}{J^+} - A_1\left[2 + \frac{\eta}{\varphi_{\mathrm{m}}'}\left(\arctan\frac{J^+}{\eta} - \arctan\frac{J^-}{\eta}\right)\right] = 0\,. \tag{4.70}$$

Moreover, by following the phase-plane analysis of Porfiri (2008, 2009) in the plane $(y^{\pm}, \partial y^{\pm}/\partial\xi^{\pm})$, we can replace conditions (4.69c), which hold for $\xi^{\pm}\to\infty$, with the following ones at $\xi^{\pm}=0$:

$$\frac{1}{2}\left(\left.\frac{\partial y^{\pm}}{\partial\xi^{\pm}}\right|_{\xi^{\pm}=0}\right)^2 + \frac{J^{\pm}}{1+(\varphi_{\mathrm{m}}')^2 \mp 2\varphi_{\mathrm{m}}'\cos(\varphi-\varphi_{\mathrm{m}})}\left[\left.y^{\pm}\right|_{\xi^{\pm}=0} - \exp\left(\left.y^{\pm}\right|_{\xi^{\pm}=0}\right) + 1\right] = 0\,, \tag{4.71}$$

as long as the following inequalities are satisfied:

$$y^+\left.\frac{\partial y^+}{\partial\xi^+}\right|_{\xi^+=0} \le 0\,,\quad y^-\left.\frac{\partial y^-}{\partial\xi^-}\right|_{\xi^-=0} \le 0\,. \tag{4.72}$$

Now, we have to solve a Cauchy problem, defined by Eqs. (4.64) along with the "initial" conditions (4.69b), (4.70), and (4.71). Since Eq. (4.70) is characterized by the presence of the unknown function of time A_1, this Cauchy problem must be combined with at least one of the two ODEs in t in Eq. (4.69e). The resulting coupled system is solved numerically, by approximating the time derivatives in Eq. (4.69e) with the following backward finite differences:

$$\frac{\mathrm{d}}{\mathrm{d}t}\left[\left.\frac{\partial y^{\pm}(\xi^{\pm},t)}{\partial \xi^{\pm}}\right|_{\xi^{\pm}=0}\right] \approx \left[\left.\frac{\partial y^{\pm}(\xi^{\pm},t)}{\partial \xi^{\pm}}\right|_{\xi^{\pm}=0} - \left.\frac{\partial y^{\pm}(\xi^{\pm},t-\Delta t)}{\partial \xi^{\pm}}\right|_{\xi^{\pm}=0}\right]\frac{1}{\Delta t}\,, \tag{4.73}$$

where Δt is a suitably small time step and we have accounted for the fact that deformation is independent of diffusion time in our sensing analysis.

At each time t, Eqs. (4.69b), (4.70), (4.71), and the time-discretized (4.69e) constitute a nonlinear algebraic system, which can be numerically solved for $y^{\pm}(\xi^{\pm},t)|_{\xi^{\pm}=0}$, $\partial y^{\pm}(\xi^{\pm},t)/\partial\xi^{\pm}|_{\xi^{\pm}=0}$, and $A_1(t)$. From these values, Eqs. (4.64) are numerically integrated to determine the functions $y^{\pm}(\xi^{\pm})$ at the selected time t. Through Eq. (4.62), we obtain $C^{\pm}$. Next, we use Eq. (4.69a) to compute $A_3^{\pm}$, to be substituted in Eq. (4.63) to find $\psi^{\pm}$. Then, we use Eq. (4.69d) to determine A_2 and, consequently, ψ^{o} through Eq. (4.57b). This completes the determination of the composite solution (4.67).

4.5 Model extension to account for counterion size[†]

If one needs to account for counterion size, the free energy density due to mixing can be reformulated as follows (Cha and Porfiri, 2014):

$$W_{\mathrm{mix}}(\mathbf{F},C) = \mathcal{R}T\frac{C_0(1-2\chi)J}{\chi(1-\chi)}\left[\frac{\chi C}{C_0 J}\ln\frac{\chi C}{C_0 J} - \frac{\chi}{J}\ln\frac{\chi}{J}\right.$$
$$\left. + \left(1-\frac{\chi C}{C_0 J}-\frac{\chi}{J}\right)\ln\left(1-\frac{\chi C}{C_0 J}-\frac{\chi}{J}\right) - \left(1-\frac{2\chi}{J}\right)\ln\left(1-\frac{2\chi}{J}\right)\right], \tag{4.74}$$

where $\chi \in (0,1)$ is the steric coefficient, defined as the initial counterion volume fraction, mainly needed to control the counterion packing at the membrane-cathode interface (Kilic et al., 2007a,b; Porfiri, 2009; Porfiri et al., 2018). Specifically, for the definiteness of Eq. (4.74), it must be

$$C < \frac{C_0}{\chi}(J-\chi)\,. \tag{4.75}$$

Accordingly, in the following, we rewrite the main equations of our theory.

The internal actions in Eqs. (4.28c) and (4.28g) become

$$M_{\mathrm{mix}} = M_{\mathrm{mix}}^{\varphi_{\mathrm{m}}} \varphi'_{\mathrm{m}} + M_{\mathrm{mix}}^{0} \quad \text{with} \quad M_{\mathrm{mix}}^{\varphi_{\mathrm{m}}} = \int_{-H}^{H} - \frac{C_0 (C - C_0) \mathcal{R} T}{(-1+\chi)(-C_0 + \chi C + \chi C_0)} Y^2 \, \mathrm{d}Y \,,$$

$$M_{\mathrm{mix}}^{0} = \int_{-H}^{H} \frac{C_0 \mathcal{R} T (-1 + 2\chi)}{\chi(-1+\chi)} \left[\ln \left(\frac{C_0 - \chi C_0 - \chi C}{C_0} \right) - \ln(1 - 2\chi) \right] Y \, \mathrm{d}Y \,, \tag{4.76a}$$

$$V_{\mathrm{mix}} = V_{\mathrm{mix}}^{\gamma_{\mathrm{m}}} (v' - \varphi_{\mathrm{m}})$$

$$\text{with} \quad V_{\mathrm{mix}}^{\gamma_{\mathrm{m}}} = \int_{-H}^{H} \frac{C_0 \mathcal{R} T (-1 + 2\chi)}{\chi(-1+\chi)} \left[\ln(1 - 2\chi) - \ln \left(\frac{C_0 - \chi C - \chi C_0}{C_0} \right) \right] \mathrm{d}Y \,. \tag{4.76b}$$

The modified Nernst-Planck Eq. (4.49b) is rewritten as

$$\frac{\partial C}{\partial t} = D \frac{\partial}{\partial Y} \left\{ \frac{1 + (\varphi'_{\mathrm{m}})^2 Y^2 - 2 \varphi'_{\mathrm{m}} Y \cos(\varphi - \varphi_{\mathrm{m}})}{J^2} \right.$$
$$\left. \times \left[\frac{1 - 2\chi}{1 - \chi} C_0 \frac{C \varphi'_{\mathrm{m}} + (J - \chi)(\partial C / \partial Y)}{-\chi C + C_0 (J - \chi)} + \frac{F}{\mathcal{R} T} C \frac{\partial \psi}{\partial Y} \right] \right\} , \tag{4.77}$$

corresponding to the following composite solution for C and ψ, replacing Eqs. (4.67):

$$C = -1 + \frac{\exp\left(\frac{1-\chi}{1-2\chi} y^+ \right)}{1 - \frac{\chi}{J^+ - \chi} + \frac{\chi}{J^+ - \chi} \exp\left(\frac{1-\chi}{1-2\chi} y^+ \right)}$$
$$+ \frac{\exp\left(\frac{1-\chi}{1-2\chi} y^- \right)}{1 - \frac{\chi}{J^- - \chi} + \frac{\chi}{J^- - \chi} \exp\left(\frac{1-\chi}{1-2\chi} y^- \right)} , \tag{4.78a}$$

$$\psi = \frac{1 - 2\chi}{1 - \chi} \ln(J - 2\chi) + A_1 \left(Y + \frac{\eta}{\varphi'_{\mathrm{m}}} \arctan \frac{J}{\eta} \right) - A_2 - y^+ + A_3^+ - y^- + A_3^-$$
$$- \frac{1 - 2\chi}{1 - \chi} \ln \left[(J^+ - 2\chi)(J^- - 2\chi) \right] - A_1 \frac{\eta}{\varphi'_{\mathrm{m}}} \left(\arctan \frac{J^+}{\eta} + \arctan \frac{J^-}{\eta} \right) . \tag{4.78b}$$

We finally obtain the functions $y^{\pm}$, A_1, A_2, and $A_3^{\pm}$ by analogy with the case neglecting steric effects, as illustrated before.

4.6 Two-dimensional finite element modeling

Here, we describe how to implement in *COMSOL Multiphysics*® a two-dimensional FE continuum model for the benchmark here of concern, depicted in Fig. 4.1. In particular, the `General Form PDE` interface allows the direct implementation of the governing equations; the software then automatically builds their discretized weak form by accounting for the chosen FE interpolation for the unknown fields.

We model the IPMC as a plane strain continuum. Moreover, we amplify the elastic modulus along the through-the-thickness direction with a parameter κ, suitably larger than one,[1] so as to abate the corresponding direct strain component. This allows us to obtain a strain field comparable to that predicted by the structural model. While for moderate strains this has no effect on the overall displacement field, it is important for electro-diffusion, which is strongly dependent on the volume ratio.

Equilibrium (4.2a) holds in the whole IPMC domain, in which we apply a spatially uniform body force of magnitude $\overline{T}/[2(H+h)]$, acting along Y, to model the transverse load. We impose $\mathbf{u} = \mathbf{0}$ at the fully clamped end, while its complementary boundary is traction-free.

The Gauss law (4.2b) and the counterion mass balance (4.2c) are relevant in the membrane domain only. At the membrane-electrode interfaces we impose both the short circuit condition $\psi = 0$ and the ion-blocking condition $\mathbf{J} \cdot \hat{\mathbf{B}} = 0$. Moreover, at the membrane sides $X = 0$ and $X = L$ (with $|Y| \leq H$) we enforce $\mathbf{D} \cdot \hat{\mathbf{A}} = 0$ and $\mathbf{J} \cdot \hat{\mathbf{A}} = 0$, to avoid pile-up of free charge in the absence of electrodes and prevent counterions from leaving the membrane, respectively.

We discretize the geometry through a mesh of 9-noded biquadratic isoparametric FEs having square shape and side equal to $h/2$, except at the membrane regions close to the electrodes, where, by referring to the *COMSOL Multiphysics®* terminology, we introduce ten `Boundary Layers`, which consist of ten rows of FEs becoming smaller toward the interfaces. Such a decrease in size is governed by a stretching factor between two consecutive FEs equal to 1.2, with the smallest FEs having thickness equal to $H/10^4$, corresponding to an acceptable aspect ratio. The time-discretization relies on Backward Differentiation Formula.

We perform two distinct FE analyses. First, to validate the structural model, we linearize the nominal stress with respect to the kinematics and adopt the PPA; the results are documented in Sec. 4.7.2. Second, we remove the PPA within a fully nonlinear kinematics; the results are presented in Sec. 4.7.3.

In the geometrically nonlinear analysis, in order to reach convergence, instead of the `General Form PDE` interface, we resort to the `Solid Mechanics` interface to solve the purely mechanical problem and we also enable the option `Nearly incompressible material`, given the closeness of the membrane Poisson ratio to 0.5 (see Sec. 4.7.1). Then, we employ the obtained deformation field to inform the electrochemical problem, still implemented within the `General Form PDE` interface. We remark that this solution procedure causes the loss of the

---

[1] More specifically, we use a linear elastic orthotropic material, with $E_Y = \kappa E_X$ and $\nu_{XY} = \nu_{YX}/\kappa$.

bidirectional coupling in the model, that is, the mechanics is assumed to be unaffected by the electrochemistry, as in the derivation of the semi-analytical solution. This notwithstanding, once ψ and C are computed, in order to be sure that the obtained solution satisfies the fully coupled original problem, we have checked that the deformation field does not significantly vary if we solve the mechanical problem by also accounting for the Maxwell and osmotic stresses, which are included through the option `External stress`.

4.7 Results and discussion

We present and discuss the results for two values of the membrane Young modulus, corresponding to either dry or saturated membrane. This difference influences the relevance of the shear deformation.

Moreover, for what concerns the validation of the semi-analytical solution presented in Secs. 4.3 and 4.4, we not only compare it with the numerical solution obtained through the FE model introduced in Sec. 4.6, but we also consider simpler semi-analytical solutions based on the Euler-Bernoulli (EB) and first order shear deformation (FOSD) theories. In the latter, the shearing rigidity is set as in Bardella (2008), that is, by evaluating it on the basis of the energy due to the shear stresses estimated by the classical Jourawski (1856) approach.

4.7.1 Benchmark data

We set the following geometrical parameters:

$$h = 20\,\mu\text{m}\,, \quad H = 100\,\mu\text{m}\,, \quad L = 10\,\text{mm}\,, \tag{4.79}$$

corresponding to a slenderness $L/[2(H+h)] \approx 40$. The load magnitude is

$$\overline{T} = 0.20\,\text{N/mm}^2\,. \tag{4.80}$$

We adopt the mechanical properties of pure platinum for the electrodes (Wei and Su, 2012):

$$E_\text{e} = 168\,\text{GPa}\,, \quad \nu_\text{e} = 0.38\,, \tag{4.81}$$

whereas, by referring to a Nafion membrane, we use (Satterfield et al., 2006; Wei and Su, 2012)

$$E_\text{m}^\text{dry} = 275\,\text{MPa}\,, \quad E_\text{m}^\text{sat} = 50\,\text{MPa}\,, \quad \nu_\text{m} = 0.487\,, \tag{4.82}$$

in which we account for the fact that the membrane Young modulus E_m may be substantially different depending on the hydration level (Satterfield et al., 2006;

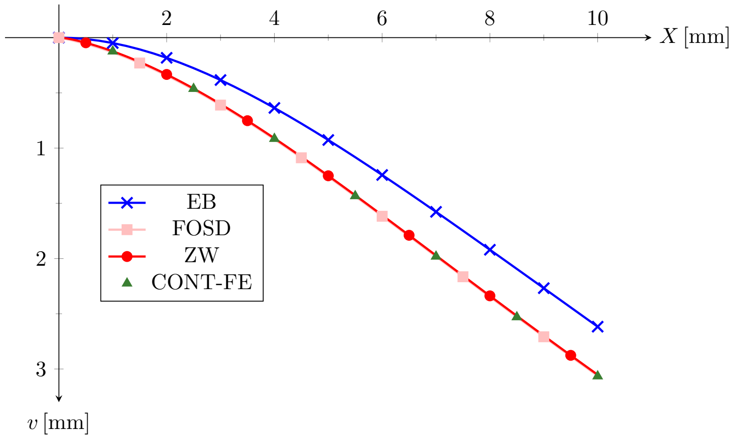

Figure 4.3: Transverse displacement $v(X)$ for a dry membrane.

Silberstein and Boyce, 2010; Page et al., 2015). Hence, we consider two extreme cases: $E_{\mathrm{m}}^{\mathrm{dry}}$ under dry condition and $E_{\mathrm{m}}^{\mathrm{sat}}$ under saturated condition. Although more slender IPMC samples are often used, and lower elastic moduli should be probably considered for the electrodes because of the manufacturing process (Kim and Shahinpoor, 2003; Akle et al., 2007), the choices above highlight the role of shear deformation. The electrochemical parameters are as those adopted by Porfiri et al. (2017):

$$T = 300\,\mathrm{K}\,,\; C_0 = 1200\,\mathrm{mol/m^3}\,,\; D = 10^{-11}\,\mathrm{m^2/s}\,,\; \varepsilon = 4.48\times10^{-5}\,\mathrm{F/m}\,. \quad (4.83)$$

4.7.2 Validation of the semi-analytical solution

In the following discussion, with reference to the two-dimensional continuum FE analysis (CONT-FE), by denoting with u_X and u_Y the displacement components along the X and Y directions, the transverse displacement is evaluated as $v(X) = u_Y(X, 0)$, the membrane curvature as $\varphi'_{\mathrm{m}}(X) = \partial^2 u_X/(\partial X \partial Y)|_{Y=0}$, and the membrane shear strain as $\gamma_{\mathrm{m}}(X) = (\partial u_X/\partial Y + \partial u_Y/\partial X)|_{Y=0}$.

As representative electrochemical parameter to evaluate the IPMC short-circuit sensing capabilities, we use the total charge, defined as the charge (per unit depth) stored along the whole electrodes, thus reading $Q_{\mathrm{tot}} = \int_0^L Q(X)\,\mathrm{d}X$, with $Q(X)$ given by Eq. (4.51).

The case of dry membrane

Figs. 4.3, 4.4, and 4.5 display the transverse displacement, membrane curvature, and membrane shear strain along the IPMC axis. About the transverse displacement, both the ZW and FOSD models are in perfect agreement with

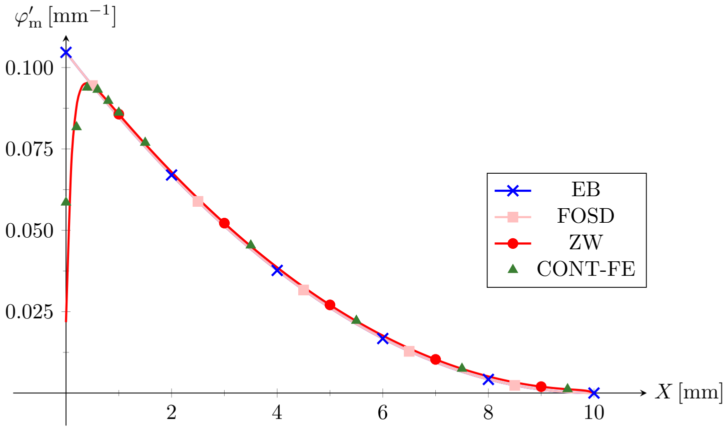

Figure 4.4: Curvature $\varphi'_{\mathrm{m}}(X)$ for a dry membrane.

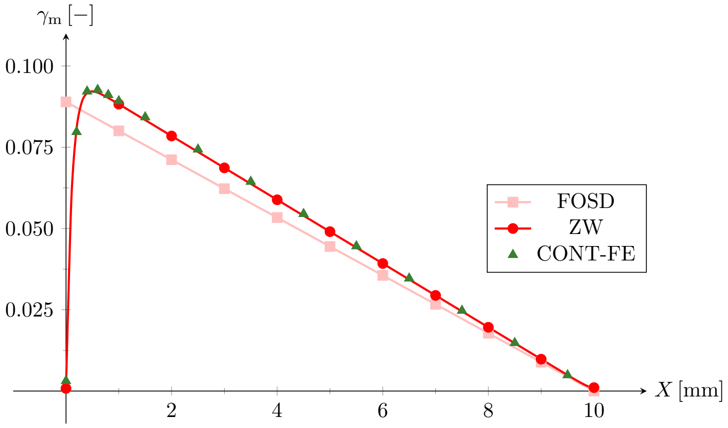

Figure 4.5: Shear strain $\gamma_{\mathrm{m}}(X) = v'(X) - \varphi_{\mathrm{m}}(X)$ for a dry membrane.

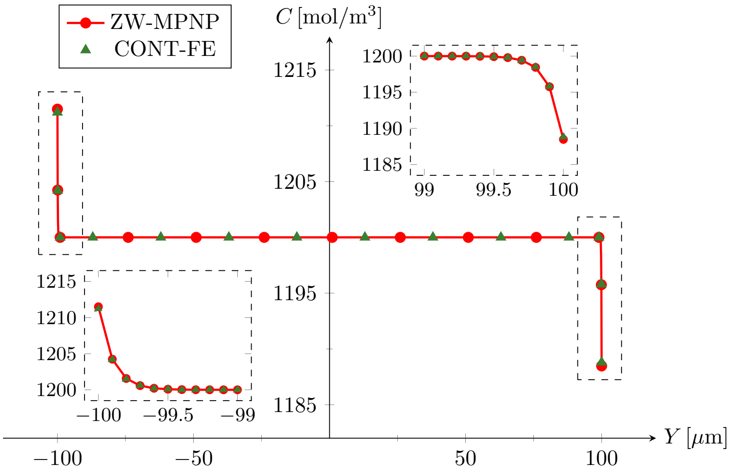

Figure 4.6: Counterion concentration $C(Y)$ at $X = 0.05\,L$ for a dry membrane.

the CONT-FE analysis, while the EB model is sensibly stiffer. Hence, shear deformation should not be neglected.

The need to employ the ZW model becomes apparent when looking at the deformation. In comparison with the CONT-FE results, this model is the only one accurately predicting the curvature at the clamped end region and the shear strain throughout the IPMC length. We underline that the dramatic decrease of curvature and shear strain at the clamped end region is typical of sandwich structures (Bardella and Mattei, 2014).

We remark that the CONT-FE solution is here obtained by considering the fully coupled electrochemo-mechanical problem, whereas the semi-analytical solution for the ZW-MPNP model is found by setting to zero the Maxwell and osmotic stresses. Hence, the agreement between the obtained results confirms the findings of Volpini et al. (2017), establishing the irrelevance of Maxwell and osmotic stresses in IPMC sensing.

We now focus on the electrochemical steady state behavior. We first consider the cross-section at $X = 0.05\,L$, in which $\varphi'_{\rm m}$ and $\gamma_{\rm m}$ approximately assume their maximum values. With reference to the ZW-MPNP model, the composite solution (4.67) for C and ψ is shown in Figs. 4.6 and 4.7, and compared with the CONT-FE results. These figures, beside the excellent agreement of the considered models, document the well-known relevance of boundary layers in IPMC electrochemistry (Porfiri, 2008).

Figs. 4.8 and 4.9 display $C(X,Y)$ and $\psi(X,Y)$ as predicted by the ZW-MPNP model in the boundary layer regions, thus highlighting their peaks. These contours suggest that the PPA is reasonable as the gradients of C and ψ along Y are larger of about two orders of magnitude than those along X.

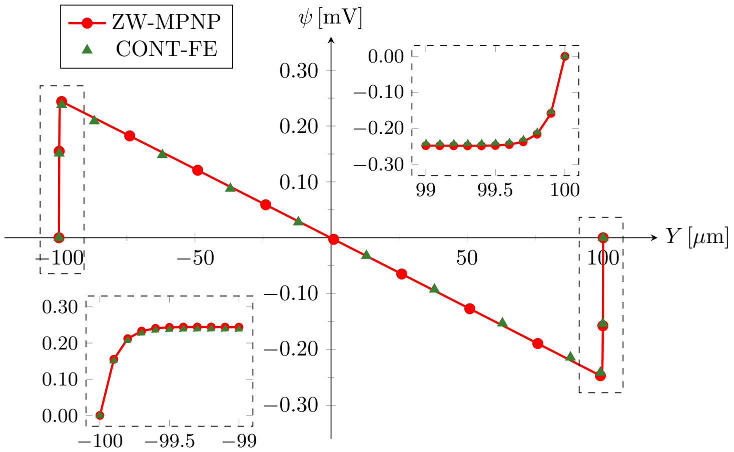

Figure 4.7: Electric potential $\psi(Y)$ at $X = 0.05\,L$ for a dry membrane.

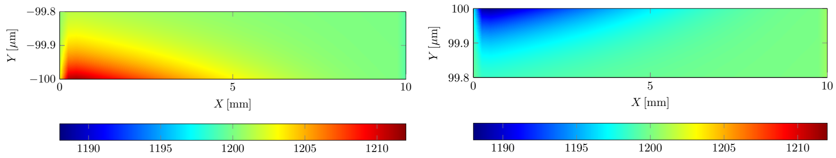

Figure 4.8: Counterion concentration $C(X, Y)$ at the membrane-cathode interface (left) and at the membrane-anode interface (right) for a dry membrane.

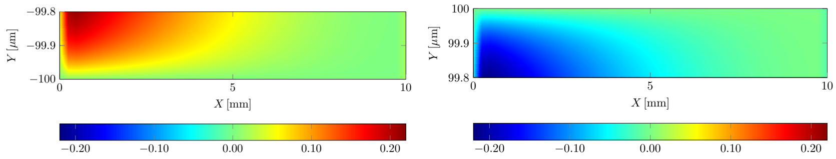

Figure 4.9: Electric potential $\psi(X, Y)$ at the membrane-cathode interface (left) and at the membrane-anode interface (right) for a dry membrane.

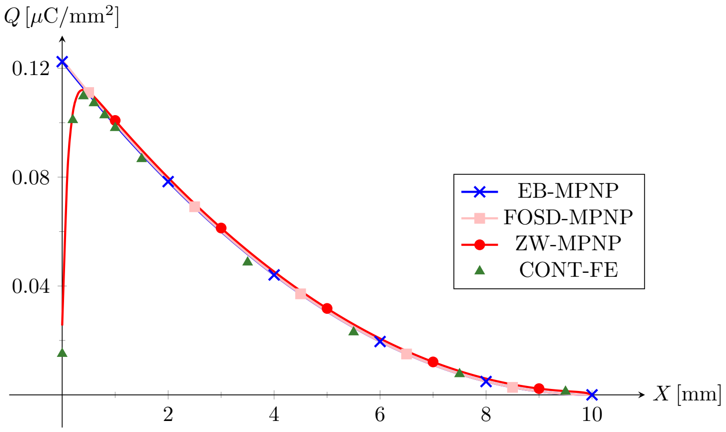

Figure 4.10: Stored charge $Q(X)$ for a dry membrane.

The internal actions due to electrochemistry are computed according to Eqs. (4.28b), (4.28c), (4.28f), and (4.28g). The results, here omitted for brevity, indicate that they are smaller than the mechanical ones of several orders of magnitude, such that they are totally negligible, as already inferred from the foregoing perfect agreement between the ZW-MPNP and CONT-FE solutions. We note that this is not the case in actuation, where instead the interplay between Maxwell and osmotic stresses has a crucial role on the resulting deformation (Porfiri et al., 2017, 2018).

Fig. 4.10 shows the stored charge (per unit nominal surface), computed from Eq. (4.51). The charge profiles follow those of the curvature, which is the main driving factor of IPMC sensing under flexure. Hence, both the ZW-MPNP and CONT-FE solutions establish a strong decrease of the charge in the clamped end region, differently from the models relying on the Bernoulli-Navier kinematics.

The total charge is $Q_{\text{tot}} \approx 0.41\,\mu\text{C/mm}$ for the ZW-MPNP solution, negligibly larger than the FE prediction $Q_{\text{tot}} \approx 0.39\,\mu\text{C/mm}$. Nevertheless, in the present case of dry membrane, where shear is not so relevant, the total charge is accurately evaluated also by the EB-MPNP and FOSD-MPNP models. Hence, in this case, even the use of the simplest structural model is adequate to estimate the global IPMC sensing capability.

The case of saturated membrane

In Figs. 4.11, 4.12, and 4.13 we present the results for the relevant kinematic quantities in the case of saturated membrane. Also in this case, the ZW and CONT-FE models predict almost exactly the same response.

The transverse displacement $v(X)$ predicted by the EB model does not appreciably differ from that for the dry membrane, given the small difference

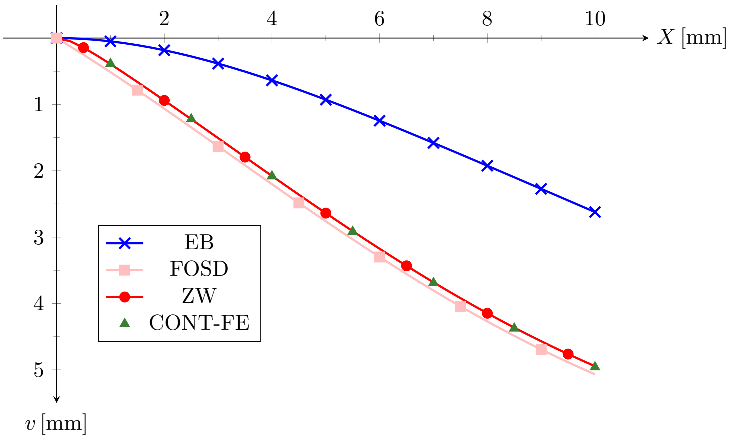

Figure 4.11: Transverse displacement $v(X)$ for a saturated membrane.

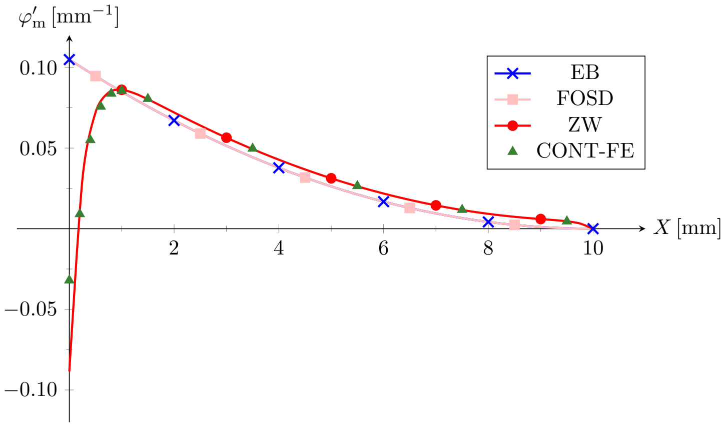

Figure 4.12: Curvature $\varphi'_{\mathrm{m}}(X)$ for a saturated membrane.

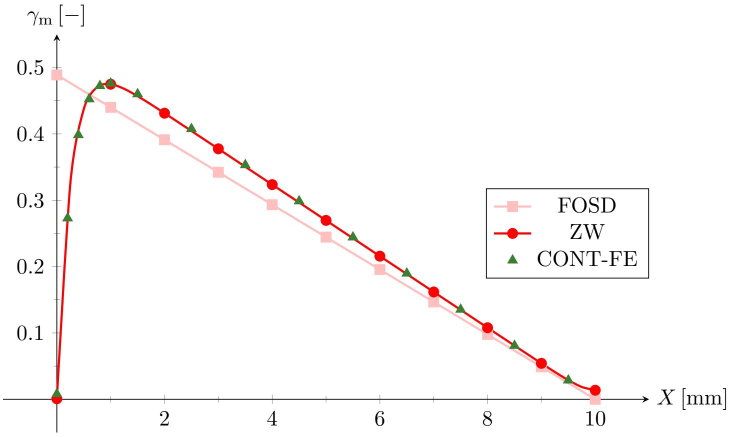

Figure 4.13: Shear strain $\gamma_{\mathrm{m}}(X) = v'(X) - \varphi_{\mathrm{m}}(X)$ for a saturated membrane.

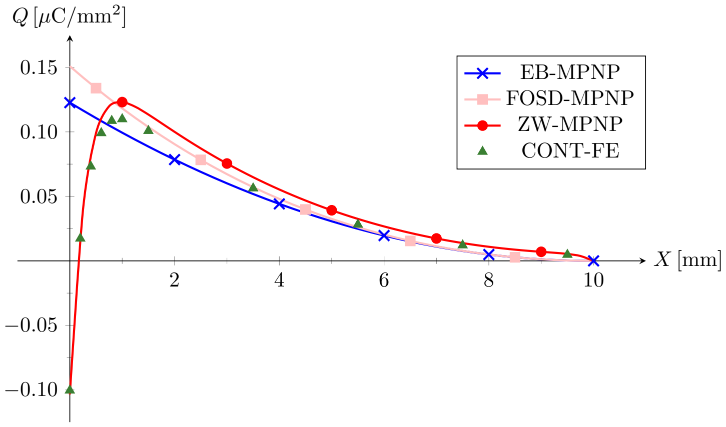

Figure 4.14: Stored charge $Q(X)$ for a saturated membrane.

in bending stiffness following the corresponding change in E_{m}. Instead, such a change significantly influences the shearing rigidity entering the FOSD model, that now predicts a much larger $v(X)$. This displacement, however, is not anymore superposed to the ZW and CONT-FE predictions.

In $X \in [\approx 0.1L, L]$, the ZW solution exhibits a slightly larger curvature compared to the other structural models, whereas at the clamped end region there is a remarkable difference even involving the curvature sign. Of course, the most relevant difference between dry and saturated conditions concerns the shear strain, which, in the latter case, increases of about five times in its peak value.

The charge profiles predicted by the different structural models are now clearly distinct, as illustrated in Fig. 4.14. Despite very relevant local differences, the total charge Q_{tot} is approximately the same according to the FOSD-MPNP and ZW-MPNP models, while the EB-MPNP model underestimates it by about 15%.

Noticeably, the ZW-MPNP and CONT-FE responses are in qualitative agreement, both predicting the increase of the electrochemical response due to shear and its dramatic decrease at the clamped end. However, the ZW-MPNP model seems to overestimate the nonlinear amplification of the counterion flux due to shear.

4.7.3 Results within nonlinear kinematics and two-dimensional electrochemistry

In the following, we consider two types of geometrically nonlinear FE analyses: in the first one, referred to as 1D-NONLIN, we maintain the PPA, whereas in the second one, referred to as 2D-NONLIN, we remove the PPA. Hence, in this subsection, the labels 1D and 2D refer to the electrochemistry. We compare these analyses with the foregoing CONT-FE analysis, assuming linear geometry and including the PPA, which, consistently with the terminology employed in this subsection, is henceforth referred to as 1D-LIN.

The results about kinematics, undisplayed for brevity, show that the transverse displacement predicted in the nonlinear case is smaller than that in the linear case, according to the smaller bending moment at the clamped end region. Moreover, the Green-Lagrange strain field within the finite deformation framework results to be totally similar to the small strain field evaluated with linearized kinematics. This suggests that the displacements an IPMC undergoes are large, whereas the deformations are relatively small.

In presenting the results, we focus on the volume ratio and its gradient components, entering the following expressions for the counterion flux components, obtained by combining relations (4.9) and (4.13c) and by neglecting the normal through-the-thickness strain $\mathcal{E}_{YY}$:

$$J_X = -\frac{D}{J^2}\left[\left(-\frac{C}{J}\frac{\partial J}{\partial X} + \frac{\partial C}{\partial X} + \frac{F}{\mathcal{R}T}C\frac{\partial \psi}{\partial X}\right) - 2\mathcal{E}_{XY}\left(-\frac{C}{J}\frac{\partial J}{\partial Y} + \frac{\partial C}{\partial Y} + \frac{F}{\mathcal{R}T}C\frac{\partial \psi}{\partial Y}\right)\right], \quad (4.84a)$$

$$J_Y = -\frac{D}{J^2}\left[-2\mathcal{E}_{XY}\left(-\frac{C}{J}\frac{\partial J}{\partial X} + \frac{\partial C}{\partial X} + \frac{F}{\mathcal{R}T}C\frac{\partial \psi}{\partial X}\right) + (2\mathcal{E}_{XX}+1)\left(-\frac{C}{J}\frac{\partial J}{\partial Y} + \frac{\partial C}{\partial Y} + \frac{F}{\mathcal{R}T}C\frac{\partial \psi}{\partial Y}\right)\right]. \quad (4.84b)$$

We notice that the shear strain $\mathcal{E}_{XY}$ modulates two main contributions to the flux, besides entering the volume ratio J. Next, we discuss the results by considering, again, the cases of dry and saturated membrane.

The case of dry membrane

In Figs. 4.15, 4.16, and 4.17 we display the volume ratio and its gradient components for a dry membrane, in the geometrically linear and nonlinear cases.

Let us focus, first, on the nonlinear case. Because of the local volume reduction due to shear deformation, already evident in Eq. (4.19) for the ZW model, J is asymmetric with respect to the mid-axis. Since the counterion flux is toward the cathode, $\partial J/\partial Y < 0$ everywhere. Noticeably, $\partial J/\partial X$ is almost everywhere negligible, with the exception of a narrow region in proximity of the

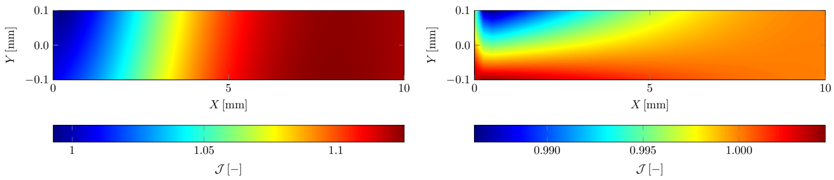

Figure 4.15: Volume ratio $J(X, Y)$ for a dry membrane, in the linear (left) and nonlinear (right) cases. It should be noted that, for the sake of clarity, here we use different contour scales for the two cases.

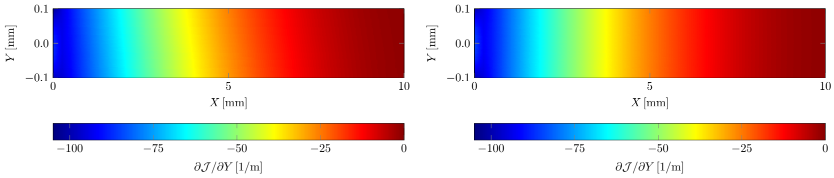

Figure 4.16: Y-component of the gradient of the volume ratio, $\partial J(X, Y)/\partial Y$, for a dry membrane, in the linear (left) and nonlinear (right) cases.

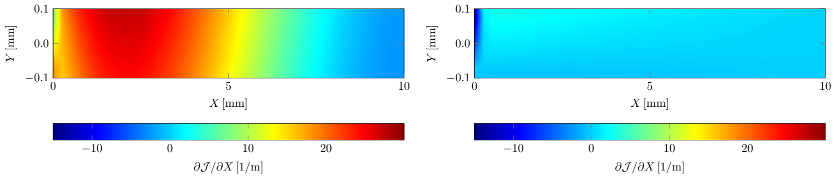

Figure 4.17: X-component of the gradient of the volume ratio, $\partial J(X, Y)/\partial X$, for a dry membrane, in the linear (left) and nonlinear (right) cases.

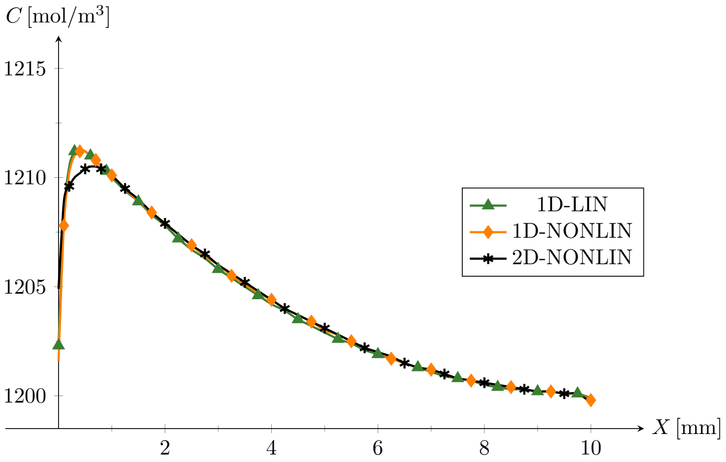

Figure 4.18: Counterion concentration $C(X)$ at the cathode $(Y = -H)$ for a dry membrane.

clamped end. This suggests the validity of the PPA, as further discussed in the following.

We remark that in the linear framework, an analysis accounting for $\partial J/\partial X$ and based on the nonlinear expression for J would lead to partly incorrect expectations on the electro-diffusion. This is demonstrated in the left contour of Fig. 4.17, clearly indicating a counterion flux along the X direction, which actually does not occur. On the contrary, in such an analysis, $\partial J/\partial Y$ turns out to be numerically very close to its counterpart computed within finite deformations, as displayed in Fig. 4.16. This is explained by the fact that the shear deformation does not affect significantly $\partial J/\partial Y$, as is clear in Eq. (4.19) for the ZW model.

Although the above inconsistency on $\partial J/\partial X$ in the case of linear kinematics would be overcome by the use of the linear expression for J, we do not consider this possibility in our investigation, as it would hide the role played by the shear deformation.

In Figs. 4.18, 4.19, and 4.20 we compare the results of the 1D-LIN, 1D-NONLIN, and 2D-NONLIN models, at the steady state, in terms of counterion concentration at the cathode, counterion concentration at the anode, and stored charge.

The 1D models, incorporating the PPA, predict approximately the same response. This is consistent with the fact that the geometric linearization does not lead to severe inaccuracies in the evaluation of $\partial J/\partial Y$, as previously discussed with reference to Fig. 4.16.

Although the 2D-NONLIN response exhibits some differences, it is overall very much similar to the responses predicted by the 1D models, thus confirming

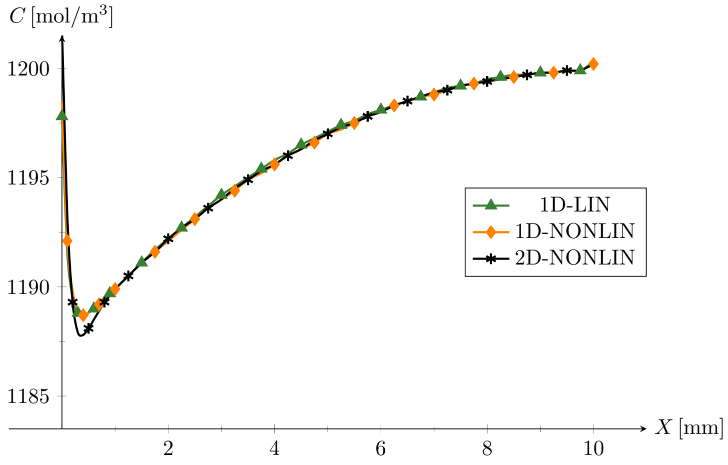

Figure 4.19: Counterion concentration $C(X)$ at the anode $(Y = H)$ for a dry membrane.

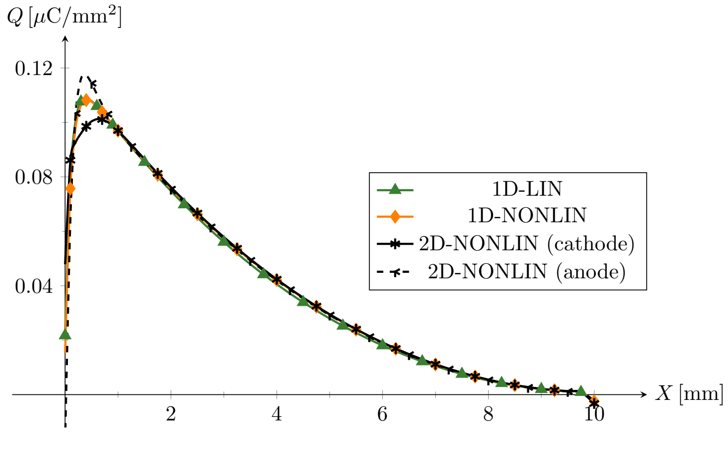

Figure 4.20: Stored charge $Q(X)$ for a dry membrane.

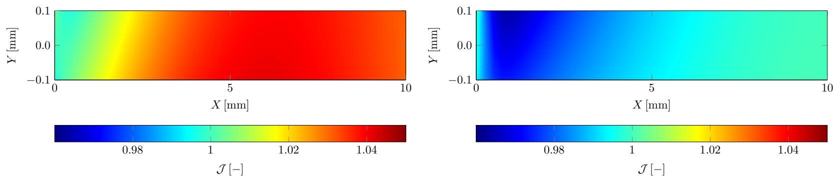

Figure 4.21: Volume ratio $J(X,Y)$ for a saturated membrane, in the linear (left) and nonlinear (right) cases.

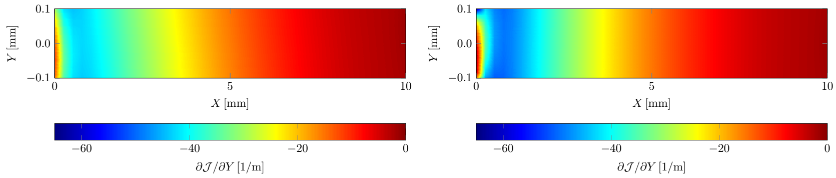

Figure 4.22: Y-component of the gradient of the volume ratio, $\partial J(X,Y)/\partial Y$, for a saturated membrane, in the linear (left) and nonlinear (right) cases.

the appropriateness of the PPA. Delving into the details, the 2D-NONLIN analysis estimates a slightly reduced positive peak of counterion concentration at the cathode, whereas, correspondingly, the counterion depletion at the anode is slightly increased.

Since in the 2D-NONLIN case Eq. (4.51) no longer holds, in Fig. 4.20 we plot $Q(X)$ at both the cathode and the anode. However, we note that, given the adopted boundary conditions, it can be easily proved that the total charge Q_{tot} must be the same at the two electrodes.

We can conclude that, if the shear deformation is not too large, the geometric nonlinearity and the two-dimensional electrochemical effects do not appreciably influence the sensing behavior, such that the proposed semi-analytical solution constitutes an effective predictive tool.

The case of saturated membrane

The results herein discussed are referred to a mechanical load $\overline{T} = 0.10\,\text{N/mm}^2$, the half of that utilized in the rest of this investigation. Such a limitation is due to convergence issues in *COMSOL Multiphysics*®.

In Figs. 4.21, 4.22, and 4.23 we compare J, $\partial J/\partial Y$, and $\partial J/\partial X$ for linear and nonlinear kinematics. Considerations similar to those for the case of dry membrane hold; however, in this case, the shear deformation is so large as to overcome the effect of curvature, such that the membrane undergoes shrinkage almost everywhere.

Figs. 4.24, 4.25, and 4.26 summarize the relevant electrochemical results. The comparison of the 1D responses demonstrates that the nonlinear model

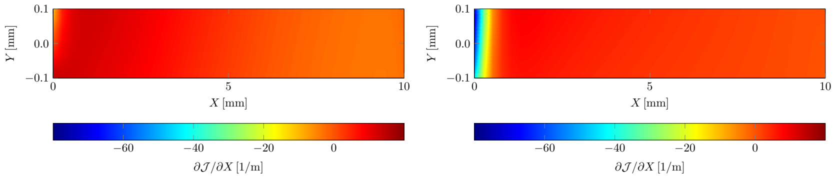

Figure 4.23: X-component of the gradient of the volume ratio, $\partial J(X,Y)/\partial X$, for a saturated membrane, in the linear (left) and nonlinear (right) cases.

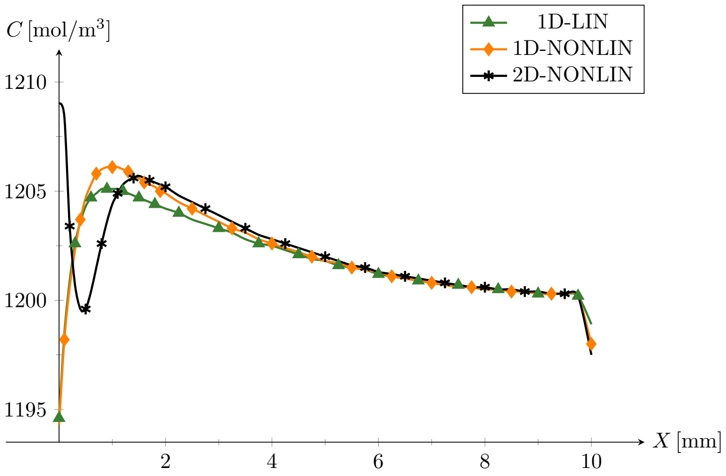

Figure 4.24: Counterion concentration $C(X)$ at the cathode ($Y = -H$) for a saturated membrane.

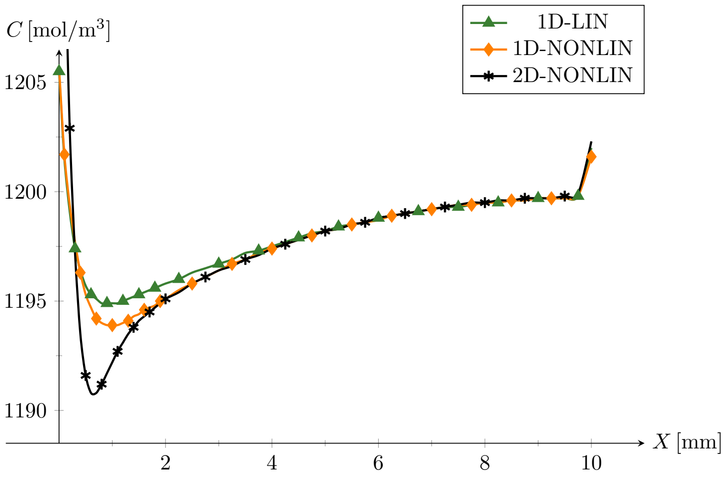

Figure 4.25: Counterion concentration $C(X)$ at the anode ($Y = H$) for a saturated membrane.

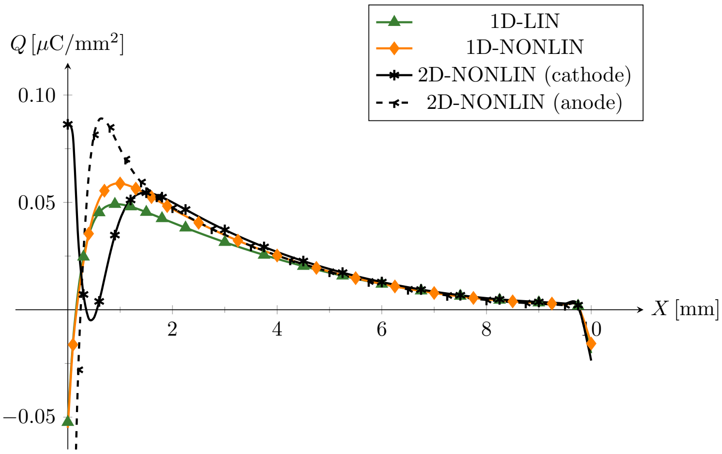

Figure 4.26: Stored charge $Q(X)$ for a saturated membrane.

predicts a larger counterion transport toward the cathode, which determines a larger charge accumulation. To explain this behavior, we simplify Eq. (4.84b) by including the PPA, thus obtaining

$$J_Y = -\frac{D}{J^2}\left(2\mathcal{E}_{XX}+1\right)\left[-\frac{C}{J}\frac{\partial J}{\partial Y}+\frac{\partial C}{\partial Y}+\frac{F}{RT}C\frac{\partial \psi}{\partial Y}\right]. \tag{4.85}$$

We further consider the instant $t = 0^+$ just after the load application, when electroneutrality approximately holds, such that

$$J_Y \approx \frac{DC_0}{J^3}\left(2\mathcal{E}_{XX}+1\right)\frac{\partial J}{\partial Y}. \tag{4.86}$$

From this relation we deduce that allowing for nonlinear kinematics leads to an amplified flux because, as shown in Figs. 4.21 and 4.22, J and $|\partial J/\partial Y|$ are, respectively, smaller and larger than the corresponding fields predicted in the linear case. It is worth noting that this enhanced electrochemical response, with respect to the 1D-LIN model, is also predicted by the ZW-MPNP model, although this structural theory employs linear kinematics (as shown in Fig. 4.14, where the results for the 1D-LIN model are labelled CONT-FE).

As for the 2D-NONLIN framework, we focus on the results unaffected by the peculiar fields observed at the clamped region. These results document a longitudinal flux toward the free end, as demonstrated by the shift of the peaks of $C(X, \pm H)$ in Figs. 4.24 and 4.25. This can be explained by considering Eq. (4.84a) at $t = 0^+$ and neglecting $\partial J/\partial X$ in comparison to $\partial J/\partial Y$ (as legitimated by the right contours of Figs. 4.22 and 4.23), which leads to

$$J_X \approx -2\frac{DC_0}{J^3}\mathcal{E}_{XY}\frac{\partial J}{\partial Y}. \tag{4.87}$$

Since $\partial J/\partial Y < 0$, the J_X is toward the free end. We note that in the case of saturated membrane the shear strain $\mathcal{E}_{XY}$ modulating Eq. (4.87) is large enough to provide a non-negligible contribution, contrary to the case of dry membrane.

Finally, while the charge Q close to the clamped end strongly depends on whether the PPA is adopted or not, the total charge Q_{tot} turns out to be basically independent of the employed model.

4.8 Concluding remarks

In this chapter, we have studied the short-circuit sensing of a cantilever IPMC subject to a uniform time-independent transverse load, with particular focus on the IPMC laminate structure, constituted by a soft ionic electroactive membrane sandwiched between two stiffer metal electrodes.

To this purpose, we have plugged the Krajcinovic (1972) structural theory for sandwiches, relying on a zigzag warping to describe the cross-section kinematics, into the electrochemo-mechanical framework of Cha and Porfiri (2014) for IPMCs. This has allowed us to develop a structural model able to accurately account for shear deformation in IPMCs under flexure.

We have obtained three coupled equilibrium equations for the laminate IPMC in terms of structural variables, and analytically solved them in the case of linearized kinematics. We remark that, in our theory, the osmotic and Maxwell stresses in the membrane contribute to both the bending moment and the shear force. Because of these contributions, it turns out that the proposed structural model predicts warping even in actuation, for a sufficiently large applied voltage across the electrodes.

Then, we have established a modified Poisson-Nernst-Planck (MPNP) system of equations, modulated by the membrane curvature and shear strain, to describe the time evolution of the electrochemical field variables, that is, the electric potential ψ and the concentration of mobile counterions C. Under the parallel plate assumption (PPA), we have obtained a semi-analytical solution of this MPNP system by applying the method of matched asymptotic expansions (Verhulst, 2005), which is particularly suited to describe the large gradients experienced by ψ and C in the thin membrane regions close to the electrodes, referred to as *boundary layers* and characterizing the IPMC electrochemistry (Porfiri, 2008; Cha and Porfiri, 2014).

By numerical inspection of the obtained system of governing equations, we have confirmed previous findings on IPMC compression sensing (Volpini et al., 2017), establishing that, in sensing, Maxwell and osmotic stresses may be neglected in solving the equilibrium equations. This allows us to first focus on the mechanical balance and, then, to solve the MPNP system for ψ and C as functions of the membrane curvature and shear strain.

We have validated the semi-analytical solution by systematically comparing its results with those of two-dimensional continuum finite element (FE) analyses of the fully coupled electrochemo-mechanical problem, implemented in *COMSOL Multiphysics*®. The adopted structural theory allows one to capture the drop of the curvature and shear strain at the IPMC clamped end, which cannot be predicted by simpler structural models relying on the Bernoulli-Navier assumption of planar cross-sections. About electrochemistry, the match between semi-analytical and FE results is very good if we set the membrane elastic moduli in such a way as to hamper the through-the-thickness direct deformation component, unaccounted for in the structural theory.

Finally, we have removed the PPA from the FE implementation, with the purpose of shedding light on the influence of the counterion flux component along the IPMC axis, typically neglected in literature. Although in these FE analyses we do not solve the fully coupled electrochemo-mechanical problem, we resort to nonlinear kinematics to evaluate the deformation field to be plugged in the MPNP system. Our results show that the global sensing response is almost coincident to that relying on the PPA, although a conspicuous shear deformation may partially alter the counterion redistribution within the membrane.

In general, we have proved that the shear deformation enhances the IPMC electrochemical response. Indeed, it nonlinearly affects the counterion flux so that more counterions diffuse toward the cathode, with respect to the case neglecting shear deformation. Correspondingly, the electric field and the stored electric charge are larger. Though this favorable effect may be negligible in ordinary IPMC samples, given their slenderness, it may become important in applications involving shorter IPMCs with stiffer electrodes (Lee et al., 2006; Akle et al., 2011; Abdulsadda and Tan, 2012).

We note that the foregoing conclusion on the sensing enhancement does not apply if the mechanical action externally applied to the IPMC consists of a displacement instead of a force. In fact, in this case, accounting for shear deformation results in a smaller curvature, overall leading to a weaker electrochemical response.

Future investigation should focus on further developing the structural model by also taking into account the through-the-thickness direct deformation of the membrane $\mathcal{E}_{YY}$, which is typically disregarded in structural theories. Except for sandwich panels with very soft core and specific boundary conditions (Frostig et al., 1992; Mattei and Bardella, 2016; Panteghini and Bardella, 2017), this assumption is adequate in purely mechanical problems. However, this is questionable in IPMCs, in which, even if considering $\mathcal{E}_{YY}$ leaves the displacement field substantially unaltered, it actually may have a relevant effect on the gradient of the volumetric deformation, which triggers IPMC sensing. In this regard, we observe that recent endeavors on IPMC actuation, also employing the Cha and Porfiri (2014) theory, have addressed the importance of accounting for the asymmetric $\mathcal{E}_{YY}$ localization in the boundary layers established by the Maxwell and osmotic stresses, whose quantification requires a reliable estimate of the membrane Poisson ratio (Boldini and Porfiri, 2020; Boldini et al., 2020).

Chapter 5

A comprehensive electrochemo-poromechanical theory for actuation and sensing of ionic polymer metal composites

This chapter is adapted from "Leronni and Bardella (2021), Modeling actuation and sensing in ionic polymer metal composites by electrochemo-poromechanics, *Journal of the Mechanics and Physics of Solids*, 148:104292".

5.1 Introduction

Like most theories in IPMC literature, the Cha and Porfiri (2014) theory disregards the solvent transport within the polymeric membrane, assuming that its electroactive response may be established by accounting for the counterion motion only (Farinholt and Leo, 2004; Branco and Dente, 2006; Chen et al., 2007; Pugal et al., 2011; Nardinocchi et al., 2011). However, a few works highlight the importance of modeling the transport of both solvent and counterions. These include (i) the contributions of Zhu and coworkers on actuation (Zhu et al., 2013) and sensing (Zhu et al., 2016), which are based on a coupled transport model of water and ions previously proposed by the same group (Zhu et al., 2011) and on the micromechanics cluster model of Nemat-Nasser and Li (2000) and Nemat-Nasser (2002), and (ii) the contribution of Schicker and Wallmersperger (2013), which relies on the electrochemo-mechanical model of Wallmersperger et al. (2007) and, again, on the cluster model of Nemat-Nasser and coworkers.

Here, in Sec. 5.2, we develop a continuum theory for IPMCs that combines relevant features of the Cha and Porfiri (2014) theory, the mixture theory (Bowen, 1980; Ateshian, 2007; Bluhm et al., 2016), and the recently developed theories for polyelectrolyte gels (Hong et al., 2010; Zhang et al., 2020). Specifically, we describe the membrane as a mixture of a charged polymer and a saturating fluid phase consisting of solvent and counterions, all coexisting within each *macroscopic* point in our continuum formulation. Moreover, each constituent is assumed to be intrinsically (that is, at the *microscopic* scale) incompressible, such that the volumetric deformation of the membrane only depends on the flow of the fluid phase. As in Leronni and Bardella (2019), we also account for the purely mechanical behavior of the electrode layers, modeled as perfect electric conductors impermeable to the fluid phase.

The model relies on four balance equations, written with respect to the reference configuration, which is undeformed and electroneutral: the *overall* momentum balance, two individual mass balances for solvent and counterions, and the Gauss law. The free energy density is assumed to consist of three contributions, namely accounting for the stretching of the polymer chains (*macroscopically* resulting in compressible hyperelasticity of the membrane), the mixing of solvent and counterions, and the dielectric polarization of the membrane. The dissipation is due to the fluxes of solvent and counterions, wherein, noticeably, we also account for their *cross-diffusion*, whereby the flux of each species is governed by the (electro)chemical potential gradients of both species (Vanag and Epstein, 2009; Zhu et al., 2011; Zhang et al., 2020).

Aiming at providing the essential multiphysical framework, including solvent transport, to thoroughly explain IPMC actuation and sensing, we assume that the fluid phase is a dilute and ideal solution, and we neglect both entropic and energetic interactions between the fluid phase and the polymeric solid phase. That is, we assume that the IPMC membrane is an *ideal* mixture (Ateshian, 2007).

Our effort results in is a theory coupling electrochemistry and poromechanics of IPMCs. Specifically, the electrochemistry describes the distribution of counterions within the membrane and the related electric potential field; it is governed by a Poisson-Nernst-Planck system of equations, which ensues from the counterion mass balance and the Gauss law, and results to be modified, with respect to its classical version (Porfiri, 2008), by both the presence of the convective counterion flux with the underlying solvent and the finite deformation framework. The poromechanics describes the deformation field of the membrane by accounting for the solvent flow in the porous network; with respect to classical poromechanics (Coussy, 2004; MacMinn et al., 2016), both the electro-osmotic solvent flux and the Maxwell stress enter the governing equations, which rely on the overall momentum balance and the solvent mass balance.

We note that previous efforts on IPMCs have already resorted to the theories of mixtures and porous media, although by either limiting the theoretical development or disregarding relevant phenomena to more easily focus on specific aspects of the IPMC behavior. For instance, Del Bufalo et al. (2008) and Tixier and Pouget (2020) have applied their mixture theory-based models to analyze the steady state actuation of IPMCs regarded as Euler-Bernoulli beams, under small and large strains, respectively. By taking advantage of the theory of porous media, Leichsenring et al. (2017) have derived a model neglecting both solvent flux and membrane deformation to study the influence of the solvent volume fraction on the IPMC electrochemistry.

Here, in Sec. 5.3, we apply our proposal to a continuum IPMC cantilever strip subject either to a fixed voltage across the electrodes (actuation problem) or to a uniformly distributed load under short-circuit condition (sensing problem). We solve these problems by resorting to the commercial finite element code *COMSOL Multiphysics*®. In actuation, as an original contribution of this work, we predict and explain the back-relaxation phenomenon (Asaka et al., 1995) in terms of the interplay between the *solvent counter-diffusion* (Shahinpoor and Kim, 2004) and the asymmetric growth of the Maxwell stress near the electrodes (Porfiri et al., 2017). Dually, in sensing, our theory can anticipate the discharge under a sustained mechanical stimulus (Farinholt and Leo, 2004) and explain it in terms of the *counterion counter-diffusion*. We demonstrate how these behaviors are influenced by the membrane elastic moduli entering the selected hyperelastic strain energy density, where volumetric and deviatoric deformations are coupled.

5.2 Modeling framework

We assume that the IPMC membrane consists of a solid phase identifying with a charged polymer and of a fluid phase represented by an uncharged solvent in which counterions are immersed. Analogously to mixture theory, all the phases coexist within each single material point (Ateshian, 2007). By definition, the deformation gradient, written in terms of the displacement vector $\mathbf{u}$, reads

$$\mathbf{F} = \mathbf{I} + \nabla \mathbf{u} \tag{5.1}$$

and describes the motion of a material point from the reference (initial) configuration, which is undeformed and electroneutral (Cha and Porfiri, 2014), to the current configuration.[1]

Importantly, the solvent always saturates the membrane. This aspect distinguishes our model from most on the swelling of polymeric gels, which identify the reference configuration with the space region occupied by the dry polymer (Hong et al., 2008; Chester and Anand, 2010).

Throughout the manuscript, we refer to *nominal* molar concentrations, that is, molar concentrations per unit *reference total* volume. Alternatively, in the literature, molar concentrations are often expressed per unit volume of the fluid phase only (Ateshian, 2007). Analogously, we define nominal molar fluxes as molar fluxes per unit reference total area.

5.2.1 Balance equations

The model relies on four balance equations, written in the reference configuration: the *overall* momentum balance (that is, the momentum balance for the mixture as a *whole*), the mass balances for solvent and counterions, and the Gauss law.

We assume that mechanical equilibrium is rapidly attained in comparison to the time scale characterizing the fluid phase transport. Hence, we neglect inertial effects, such that, in the absence of body forces, the overall momentum balance reduces to

$$\operatorname{Div}\mathbf{P} = \mathbf{0}\,, \tag{5.2}$$

where Div is the material divergence operator and $\mathbf{P}$ is the nominal stress tensor, satisfying $\mathbf{P}\mathbf{F}^{\mathrm{T}} = \mathbf{F}\mathbf{P}^{\mathrm{T}}$.

The mass balance for the solvent reads

$$\dot{C}_{\mathrm{w}} + \operatorname{Div}\mathbf{J}_{\mathrm{w}} = 0\,, \tag{5.3}$$

in which C_{w} is the nominal molar concentration of the solvent, the symbol $\dot{}$ indicates partial time derivative, and $\mathbf{J}_{\mathrm{w}}$ is the nominal molar solvent flux. Since in IPMC membranes the solvent is typically constituted by water, we adopt the subscript w to refer to physical quantities associated with the solvent.

Analogously, the mass balance for the counterions is

$$\dot{C} + \operatorname{Div}\mathbf{J} = 0\,, \tag{5.4}$$

with C and $\mathbf{J}$ denoting the nominal molar concentration of counterions and the nominal molar counterion flux, respectively.

---

[1] In Eq. (5.1), $\mathbf{I}$ is the second order identity tensor and the symbol ∇ denotes the material gradient operator.

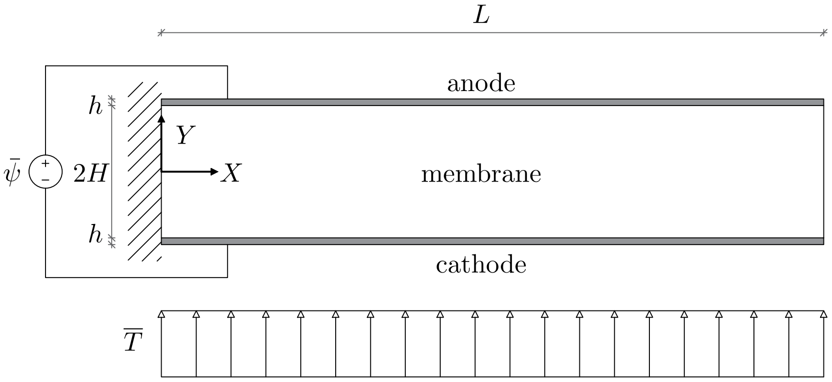

Figure 5.1: Cantilever IPMC subject to an applied voltage $\bar{\psi}$ across the electrodes (non-zero in the actuation problem) and to an imposed nominal surface load $\overline{T}$ (non-zero in the sensing problem).

Finally, the Gauss law reads

$$\operatorname{Div}\mathbf{D} = F(C - C^0)\,, \tag{5.5}$$

where $\mathbf{D}$ is the nominal electric displacement, F is the Faraday constant, and C^0 is the nominal molar concentration of the anions fixed to the polymer chains. In Eq. (5.5) we assume that both fixed anions and mobile counterions have unit valency, which is usually the case for IPMCs (Shahinpoor and Kim, 2001; Porfiri, 2008).

We treat the electrodes as perfect electric conductors impermeable to both solvent and ions. Therefore, they establish boundary conditions for the electrochemical and solvent transport problems in the membrane (see Sec. 5.2.2) and, of the foregoing balance laws, are subject to Eq. (5.2) only.

5.2.2 Boundary and initial conditions

With reference to Fig. 5.1, the IPMC has reference length L, membrane thickness $2H$, and much thinner electrodes of thickness h. We consider the usual case of a very slender IPMC, such that $L \gg 2(H + h)$.

About mechanics, in both actuation and sensing problems, we consider a cantilever configuration with clamped side at the left end, such that

$$\mathbf{u} = \mathbf{0} \quad \text{at } X = 0\,. \tag{5.6}$$

The rest of the boundary is subject to static boundary conditions. Specifically, the edges at $X = L$ and $Y = H + h$ are always stress-free, while the remaining side is either stress-free in the actuation problem or subject to

$$\mathbf{T} = \mathbf{P}\mathbf{N} = -\overline{T}\mathbf{N} \quad \text{at } Y = -H - h \tag{5.7}$$

in the sensing problem. In Eq. (5.7), $\mathbf{T}$ is the nominal traction, $\mathbf{N}$ is the outward unit normal to the reference boundary, and $\overline{T}$ is the magnitude of the uniformly distributed nominal load. In the benchmark of Sec. 5.3.4, this load will be applied in a suitably short time to unveil the effect of the counter-diffusion of mobile ions.

We assume that the electrodes are impermeable to both solvent and counterions by imposing the zero-flux boundary conditions

$$\mathbf{J}_{\mathrm{w}} \cdot \mathbf{N} = 0 \quad \text{and} \quad \mathbf{J} \cdot \mathbf{N} = 0 \quad \text{at } Y = \pm H\,, \tag{5.8}$$

where the symbol $\cdot$ denotes the inner product. Given the IPMC slenderness, we may disregard the edge effects at the IPMC ends, such that, in the simulations, we extend these boundary conditions to $X = 0$ and $X = L$ as well.

Finally, we express the boundary conditions for the electrostatics problem as

$$\psi = \frac{\bar{\psi}}{2} \quad \text{at } Y = H \quad \text{and} \quad \psi = -\frac{\bar{\psi}}{2} \quad \text{at } Y = -H\,, \tag{5.9}$$

in which ψ is the electric potential and $\bar{\psi}$ is the applied voltage drop across the electrodes. Specifically, $\bar{\psi} \neq 0$ in the actuation problem, while $\bar{\psi} = 0$ in the short-circuit sensing problem. In the actuation benchmark of Sec. 5.3.3, $\bar{\psi}$ will be suddenly applied to unveil the phenomena behind the back-relaxation. At the IPMC ends $X = 0$ and $X = L$, we prevent accumulation of surface charge by imposing $\mathbf{D} \cdot \mathbf{N} = 0$.

The mass balances also need initial conditions, which are

$$C_{\mathrm{w}} = C_{\mathrm{w}}^{0} \quad \text{at } t = 0\,, \tag{5.10a}$$

$$C = C^{0} \quad \text{at } t = 0\,, \tag{5.10b}$$

where C_{w}^{0} and C^{0} are the initial solvent and counterion concentrations, respectively. Eq. (5.10b) implies the electroneutrality of the reference configuration.

5.2.3 Thermodynamic restrictions

We follow the approach of Gurtin et al. (2010) for problems of species diffusion coupled to elasticity, suitably augmented to take into account that counterions are electrically charged. Given that we focus on isothermal conditions, we disregard the heat terms in the thermodynamic laws. Hence, the energy balance encompasses mechanical, electrical, and species transport contributions:

$$\dot{U} = \mathbf{P} \cdot \dot{\mathbf{F}} + \mathbf{E} \cdot \dot{\mathbf{D}} + \mu_{\mathrm{w}} \dot{C}_{\mathrm{w}} + \mu \dot{C} - \mathbf{J}_{\mathrm{w}} \cdot \nabla \mu_{\mathrm{w}} - \mathbf{J} \cdot \nabla \tilde{\mu} \,, \tag{5.11}$$

in which U is the nominal internal energy density,

$$\mathbf{E} = -\nabla \psi \tag{5.12}$$

is the nominal electric field, μ_{w} is the solvent chemical potential (with units of energy per mole), μ is the counterion chemical potential, and

$$\tilde{\mu} = \mu + F\psi \tag{5.13}$$

is the counterion electrochemical potential.

By introducing the nominal Helmholtz free energy density W, the second law of thermodynamics reads

$$\mathbf{P} \cdot \dot{\mathbf{F}} + \mathbf{E} \cdot \dot{\mathbf{D}} + \mu_{\mathrm{w}} \dot{C}_{\mathrm{w}} + \mu \dot{C} - \mathbf{J}_{\mathrm{w}} \cdot \nabla \mu_{\mathrm{w}} - \mathbf{J} \cdot \nabla \tilde{\mu} - \dot{W} \geq 0 \,. \tag{5.14}$$

We assume that W is a function of the primal variables $\mathbf{F}$, $\mathbf{D}$, C_{w}, and C. Hence, substituting $\dot{W}$ in Eq. (5.14) leads to

$$\begin{aligned} \left(\mathbf{P} - \frac{\partial W}{\partial \mathbf{F}}\right) \cdot \dot{\mathbf{F}} + \left(\mathbf{E} - \frac{\partial W}{\partial \mathbf{D}}\right) \cdot \dot{\mathbf{D}} + \left(\mu_{\mathrm{w}} - \frac{\partial W}{\partial C_{\mathrm{w}}}\right) \dot{C}_{\mathrm{w}} + \left(\mu - \frac{\partial W}{\partial C}\right) \dot{C} & \\ - \mathbf{J}_{\mathrm{w}} \cdot \nabla \mu_{\mathrm{w}} - \mathbf{J} \cdot \nabla \tilde{\mu} \geq 0 \,. & \end{aligned} \tag{5.15}$$

By resorting to the Coleman-Noll procedure, we obtain the general constitutive relations

$$\mathbf{P} = \frac{\partial W}{\partial \mathbf{F}} \,, \quad \mathbf{E} = \frac{\partial W}{\partial \mathbf{D}} \,, \quad \mu_{\mathrm{w}} = \frac{\partial W}{\partial C_{\mathrm{w}}} \,, \quad \mu = \frac{\partial W}{\partial C} \,, \tag{5.16}$$

such that the dissipation inequality reduces to

$$- \mathbf{J}_{\mathrm{w}} \cdot \nabla \mu_{\mathrm{w}} - \mathbf{J} \cdot \nabla \tilde{\mu} \geq 0 \,. \tag{5.17}$$

We assume that each flux is a linear combination of $\nabla \mu_{\mathrm{w}}$ and $\nabla \tilde{\mu}$:

$$\mathbf{J}_{\mathrm{w}} = -\mathbf{M}_{\mathrm{ww}} \nabla \mu_{\mathrm{w}} - \mathbf{M}_{\mathrm{w}} \nabla \tilde{\mu} \,, \tag{5.18a}$$

$$\mathbf{J} = -\mathbf{M}_{\mathrm{w}} \nabla \mu_{\mathrm{w}} - \mathbf{M} \nabla \tilde{\mu} \,, \tag{5.18b}$$

where the constitutive operators can be collected into a symmetric mobility matrix (Onsager, 1931)

$$\boldsymbol{\mathcal{M}} = \begin{bmatrix} \mathbf{M}_{\mathrm{ww}} & \mathbf{M}_{\mathrm{w}} \\ \mathbf{M}_{\mathrm{w}} & \mathbf{M} \end{bmatrix}, \tag{5.19}$$

to be defined such that Eq. (5.17) is fulfilled (see Sec. 5.2.7). The assumption that the flux of a species also depends on the (electro)chemical potential gradient of the other species (that is, $\mathbf{M}_{\mathrm{w}} \neq \mathbf{0}$) is usually referred to as *cross-diffusion* (Vanag and Epstein, 2009). The description of this phenomenon, which has been observed to be relevant for IPMCs (Zhu et al., 2013, 2016), constitutes one of the main concerns of our investigation.

5.2.4 Free energy density

We assume that W admits the additive decomposition

$$W(\mathbf{F}, C, C_{\mathrm{w}}, \mathbf{D}) = W_{\mathrm{mec}}(\mathbf{F}) + W_{\mathrm{mix}}(C, C_{\mathrm{w}}) + W_{\mathrm{pol}}(\mathbf{F}, \mathbf{D}), \tag{5.20}$$

in which W_{mec}, W_{mix}, and W_{pol} are the contributions due to the overall membrane stretching, the mixing of counterions and solvent molecules, and the membrane polarization, respectively.

To describe the mechanics of the membrane, we select the isotropic compressible Neo-Hookean material model proposed by Simo and Pister (1984):

$$W_{\mathrm{mec}}(\mathbf{F}) = \frac{G}{2}(\operatorname{tr}\mathbf{C} - 3) - G \ln J + \frac{1}{2}\lambda \ln^2 J, \tag{5.21}$$

in which $\lambda = E\nu/[(1+\nu)(1-2\nu)]$ and $G = E/[2(1+\nu)]$ are the Lamé parameters, with E and ν denoting the Young modulus and the Poisson ratio, $\mathbf{C} = \mathbf{F}^{\mathrm{T}}\mathbf{F}$ is the right Cauchy-Green deformation tensor, and

$$J = \det \mathbf{F} \tag{5.22}$$

is the volume ratio. Eq. (5.21) describes a *coupled* hyperelastic material, that is, W_{mec} cannot be decomposed into the sum of isochoric and volumetric contributions (Holzapfel, 2000). This is known to be a desirable feature if one aims at capturing the large deformation behavior of elastomers (Boyce and Arruda, 2000). With respect to the material models usually employed in electrochemo-poromechanics, such that of Hong et al. (2010) for polyelectrolyte gels, the constitutive prescription in Eq. (5.21) involves an additional volumetric term modulated by λ. The use of both Lamé parameters allows a better tuning of the overall volumetric response, strictly related with the solvent flux (see Sec. 5.2.5), as demonstrated in Section 5.3 with particular reference to the counter-diffusion phenomena occurring in IPMC actuation and sensing. Morevoer, the importance of employing both Lamé parameters for the IPMC membrane has been unveiled by the study of Boldini and Porfiri (2020) on the multiaxial deformations experienced by IPMCs.

For the metal electrodes, we adopt the Saint-Venant–Kirchhoff isotropic material model:

$$W^{\mathrm{e}}_{\mathrm{mec}}(\mathbf{F}) = \frac{\lambda_{\mathrm{e}}}{2}(\operatorname{tr}\boldsymbol{\mathcal{E}})^2 + G_{\mathrm{e}}\operatorname{tr}\left(\boldsymbol{\mathcal{E}}^2\right) , \tag{5.23}$$

in which λ_{e} and G_{e} are the Lamé parameters of the electrodes, whose Young modulus and Poisson ratio are E_{e} and ν_{e}, and $\boldsymbol{\mathcal{E}} = (\mathbf{C} - \mathbf{I})/2$ is the Green-Lagrange strain tensor.

We assume that the fluid phase behaves as an ideal solution of solvent and counterions, such that the free energy of mixing is purely entropic and reads (Ateshian, 2007)

$$W_{\mathrm{mix}}(C, C_{\mathrm{w}}) = \mathcal{R}T\left(C\ln\frac{C}{C + C_{\mathrm{w}}} + C_{\mathrm{w}}\ln\frac{C_{\mathrm{w}}}{C + C_{\mathrm{w}}}\right) , \tag{5.24}$$

in which $\mathcal{R}$ is the gas constant and T is the absolute temperature. We remark that Eq. (5.24) only describes the mixing of solvent and counterions, and this turns out to be consistent with an ideal mixture theory in which the solution of solvent and counterions identifies with the fluid phase (Ateshian, 2007), whereby we expect the solid phase, consisting of the polymer chains, to be much less relevant for mixing in IPMCs.[2]

Importantly, in this first investigation on the IPMC electrochemo-poromechanics, we assume that the solution of solvent and counterions is *dilute*, that is,

$$C \ll C_{\mathrm{w}} , \tag{5.25}$$

such that Eq. (5.24) is substituted by the approximation

$$W_{\mathrm{mix}}(C, C_{\mathrm{w}}) = \mathcal{R}TC\left(\ln\frac{C}{C_{\mathrm{w}}} - 1\right) . \tag{5.26}$$

The assumption (5.25), beside being quite reliable in comparison with actual IPMC fluid phases (Zhu et al., 2013), is convenient in the light of the challenging computational models ensuing from such multiphysical theories, even when neglecting the solvent transport (Boldini and Porfiri, 2020; Boldini et al., 2020).

By following Hong et al. (2010), Cha and Porfiri (2014), and Zhang et al. (2020), we treat the membrane as an ideal dielectric, such that the polarization

---

[2] This assumption simplifies the usual theories adopted to describe the swelling of polymeric gels (Hong et al., 2008; Chester and Anand, 2010) and polyelectrolyte gels (Hong et al., 2010; Zhang et al., 2020), in which the mixing of solvent molecules with polymer macromolecules is accounted for on the basis of the Flory-Huggins solution theory (Flory, 1942; Huggins, 1941).

contribution reads

$$W_{\text{pol}}(\mathbf{F},\mathbf{D}) = \frac{|\mathbf{FD}|^2}{2\varepsilon J}\,, \tag{5.27}$$

where ε is the absolute permittivity of the membrane.

5.2.5 Constraint on the volumetric deformation

According with the dilute solution approximation (5.25), we neglect the volume occupied by counterions (Ateshian, 2007) and hypothesize that both solvent molecules and polymer chains are intrinsically incompressible, which is a common practice for polyelectolyte gels as well (Zhang et al., 2020). Therefore, volumetric deformations are inextricably related to variations of the solvent concentration only, such that the volume ratio (5.22) is constrained as follows:

$$J = 1 + v_{\text{w}}\left(C_{\text{w}} - C_{\text{w}}^0\right)\,, \tag{5.28}$$

where v_{w} denotes the solvent molar volume. In order to impose this constraint, the free energy density (5.20) is modified as follows (Holzapfel, 2000; Hong et al., 2010; Zhang et al., 2020):

$$\begin{aligned} W = W_{\text{mec}}(\mathbf{F}) + W_{\text{mix}}(C, C_{\text{w}}) + W_{\text{pol}}(\mathbf{F},\mathbf{D}) \\ + p_{\text{w}}\left[1 + v_{\text{w}}\left(C_{\text{w}} - C_{\text{w}}^0\right) - J\right]\,, \end{aligned} \tag{5.29}$$

where p_{w} is a Lagrange multiplier field assuming the role of solvent pressure.

We remark that our $\mathbf{F}$ is purely elastic. Hence, the allowed volumetric deformation due to the solvent transport requires the selection of a *compressible* hyperelastic strain energy, as for instance proposed in Eq. (5.21). We observe that the elastic deformation could be constrained to be isochoric by adopting a richer kinematics in which $\mathbf{F}$ involves inelastic contributions, such as the swelling term in the theory of Chester and Anand (2010) for polymeric gels.

For later developments, it is convenient to rearrange Eq. (5.28) for the solvent concentration:

$$C_{\text{w}} = C_{\text{w}}^0 + \frac{1}{v_{\text{w}}}(J-1)\,, \tag{5.30}$$

whose rate is

$$\dot{C}_{\text{w}} = \frac{\dot{J}}{v_{\text{w}}}\,. \tag{5.31}$$

5.2.6 Conservative constitutive laws

Stress tensor

By combining Eqs. (5.16a), (5.21), (5.27), and (5.29), we obtain the following nominal stress:

$$\begin{aligned}\mathbf{P} = &\underbrace{G(\mathbf{F}-\mathbf{F}^{-\mathrm{T}}) + \lambda \ln J\mathbf{F}^{-\mathrm{T}}}_{\mathbf{P}_{\mathrm{mec}}} \\ &+ \underbrace{\frac{1}{2\varepsilon J}\left[2\mathbf{F}(\mathbf{D}\otimes\mathbf{D}) - \mathbf{C}\cdot(\mathbf{D}\otimes\mathbf{D})\mathbf{F}^{-\mathrm{T}}\right]}_{\mathbf{P}_{\mathrm{pol}}} \underbrace{-p_{\mathrm{w}}J\mathbf{F}^{-\mathrm{T}}}_{\mathbf{P}_{\mathrm{w}}}\,, \end{aligned} \tag{5.32}$$

where $\otimes$ denotes the tensor product. Therefore, $\mathbf{P}$ may be regarded as a *total* stress, comprising mechanical, electrostatic, and water pressure contributions. The corresponding total Cauchy stress is

$$\boldsymbol{\sigma} = \frac{1}{J}\mathbf{P}\mathbf{F}^{\mathrm{T}} = \underbrace{\frac{1}{J}[G(\mathbf{b}-\mathbf{I}) + \lambda \ln J\mathbf{I}]}_{\boldsymbol{\sigma}_{\mathrm{mec}}} + \underbrace{\frac{1}{2\varepsilon}\left[2\mathbf{d}\otimes\mathbf{d} - (\mathbf{d}\cdot\mathbf{d})\mathbf{I}\right]}_{\boldsymbol{\sigma}_{\mathrm{pol}}} \underbrace{-p_{\mathrm{w}}\mathbf{I}}_{\boldsymbol{\sigma}_{\mathrm{w}}}\,, \tag{5.33}$$

where $\mathbf{b} = \mathbf{F}\mathbf{F}^{\mathrm{T}}$ is the left Cauchy-Green deformation tensor and $\mathbf{d} = J^{-1}\mathbf{F}\mathbf{D}$ is the current electric displacement (Dorfmann and Ogden, 2005). The total pressure reads

$$p = -\frac{1}{3}\mathrm{tr}\,\boldsymbol{\sigma} = \underbrace{-\frac{1}{J}\left[G\left(\frac{1}{3}\mathrm{tr}\,\mathbf{b} - 1\right) + \lambda \ln J\right]}_{p_{\mathrm{mec}}} + \underbrace{\frac{1}{6\varepsilon}|\mathbf{d}|^2}_{p_{\mathrm{pol}}} + p_{\mathrm{w}}\,, \tag{5.34}$$

adopting the convention that each contribution to the pressure is positive if compressive.

In the jargon of poromechanics, $\boldsymbol{\sigma}_{\mathrm{mec}}$ and p_{w} are, respectively, the *effective* stress and the pore water pressure (Coussy, 2004; MacMinn et al., 2016). In electromechanics, $\boldsymbol{\sigma}_{\mathrm{pol}}$ is usually denoted as the Maxwell stress (Dorfmann and Ogden, 2005).

Electric displacement

By using Eqs. (5.12), (5.16b), and (5.27) we obtain the constitutive law for the nominal electric field, whose inversion provides the nominal electric displacement

$$\mathbf{D} = -\varepsilon J\mathbf{C}^{-1}\nabla\psi\,. \tag{5.35}$$

As is well-known, in the current configuration, this relation reads $\mathbf{d} = -\varepsilon \operatorname{grad} \psi$. In Eq. (5.35), $\varepsilon J \mathbf{C}^{-1}$ could be interpreted as a permittivity tensor, whose anisotropic nature is given by the background deformation of the dielectric material.

Solvent and counterion (electro)chemical potentials

We obtain the solvent chemical potential by combining Eqs. (5.16c), (5.26), and (5.29):

$$\mu_{\mathrm{w}} = -\mathcal{R}T \frac{C}{C_{\mathrm{w}}} + v_{\mathrm{w}} p_{\mathrm{w}} \,, \tag{5.36}$$

revealing that μ_{w} is affected both by a mechanical contribution through p_{w} and by an osmotic contribution through $\mathcal{R}TC$.

Analogously, we obtain the counterion chemical potential μ by combining Eqs. (5.16d) and (5.26), thus leading to the counterion electrochemical potential of Eq. (5.13):

$$\tilde{\mu} = \underbrace{\mathcal{R}T \ln \frac{C}{C_{\mathrm{w}}}}_{\mu} + F\psi \,. \tag{5.37}$$

We note that μ is unaffected by p_{w} because the fluid phase is assumed to be dilute, such that the counterion volume turns out to be negligible.

5.2.7 Dissipative constitutive laws

In order to obtain the expressions for $\mathbf{J}_{\mathrm{w}}$ and $\mathbf{J}$, we need to specify the mobility matrix $\boldsymbol{\mathcal{M}}$ introduced with Eq. (5.19). We adopt the form

$$\boldsymbol{\mathcal{M}} = \frac{1}{\mathcal{R}T} \mathbf{C}^{-1} \begin{bmatrix} D_{\mathrm{w}} C_{\mathrm{w}} & D_{\mathrm{w}} C \\ D_{\mathrm{w}} C & \left(D_{\mathrm{w}} \frac{C}{C_{\mathrm{w}}} + D \right) C \end{bmatrix} , \tag{5.38}$$

in which D_{w} is the solvent diffusivity in the polymer network and D is the diffusivity of the counterions in the solvent. The matrix $\boldsymbol{\mathcal{M}}$ is positive definite for non-vanishing diffusivities and concentrations, thus fulfilling the dissipation inequality (5.17). Notably, our formulation of cross-diffusion is free from additional parameters with respect to the two diffusivities required for the self-diffusion. This differs from the cross-diffusion model proposed by Zhu et al. (2013), which requires a further drag coefficient.

In light of Eq. (5.38), Eqs. (5.18) become

$$\mathbf{J}_{\mathrm{w}} = -\frac{D_{\mathrm{w}}}{\mathcal{R}T} \mathbf{C}^{-1} \left(C_{\mathrm{w}} \nabla \mu_{\mathrm{w}} + C \nabla \tilde{\mu} \right) , \tag{5.39a}$$

$$\mathbf{J} = \frac{C}{C_{\mathrm{w}}}\mathbf{J}_{\mathrm{w}} - \frac{D}{\mathcal{R}T}\mathbf{C}^{-1}C\nabla\tilde{\mu}\,. \tag{5.39b}$$

We observe that Ateshian (2007) obtains flux equations analogous to Eqs. (5.39) within the mixture theory. Indeed, equations (128) and (129) of Ateshian (2007) are the counterpart in the current configuration of Eqs. (5.39a) and (5.39b), respectively, if one assumes absence of friction between polymer chains and dilute species, as for instance in Huyghe and Janssen (1997), and considers that external body forces acting on solvent and dilute species vanish. We further note that, in order to describe the kinetics of polyelectrolyte gels, Zhang et al. (2020) follow the Maxwell-Stefan approach to mass transport in multicomponent systems (Krishna and Wesselingh, 1997), thus obtaining transport equations again corresponding to Eqs. (5.39).

Finally, combining Eqs. (5.36), (5.37), and (5.39) results in

$$\mathbf{J}_{\mathrm{w}} = -\frac{D_{\mathrm{w}}}{\mathcal{R}T}\mathbf{C}^{-1}\left(v_{\mathrm{w}}C_{\mathrm{w}}\nabla p_{\mathrm{w}} + FC\nabla\psi\right)\,, \tag{5.40a}$$

$$\mathbf{J} = \frac{C}{C_{\mathrm{w}}}\mathbf{J}_{\mathrm{w}} - D\mathbf{C}^{-1}\left(\nabla C - \frac{C}{C_{\mathrm{w}}}\nabla C_{\mathrm{w}} + \frac{FC}{\mathcal{R}T}\nabla\psi\right)\,. \tag{5.40b}$$

These equations are commented in the following.

Discussion

Let us first focus on the solvent flux given by Eq. (5.40a). About the resolution strategy, we note that the use of constraints (5.30) and (5.31) allows us to express the solvent mass balance (5.3) in terms of the solvent pressure p_{w}.

About physics, we remark that, although the solvent is assumed to be electrically neutral, its flux depends on the electric potential gradient. In particular, the last term in Eq. (5.40a) represents the solvent *electro-osmotic* flux, which is recognized by many investigators as a fundamental mechanism of solvent transport in IPMC actuation (Asaka and Oguro, 2000; Shahinpoor and Kim, 2004; Zhu et al., 2013). Indeed, as a voltage drop is applied across the electrodes, counterions migrate in the direction of the electric field, carrying along solvent molecules proportionally to the counterion concentration.

In the limit case of absence of counterions, the volumetric nominal flux of solvent $\mathbf{J}^{\mathrm{v}}_{\mathrm{w}}$, through Eq. (5.40a), reads

$$\mathbf{J}^{\mathrm{v}}_{\mathrm{w}} = v_{\mathrm{w}}\mathbf{J}_{\mathrm{w}} = -J\mathbf{C}^{-1}\frac{D_{\mathrm{w}}\varphi_{\mathrm{w}}^2}{\mathcal{R}Tc_{\mathrm{w}}}\nabla p_{\mathrm{w}}\,, \tag{5.41}$$

where we have introduced the current solvent concentration $c_{\mathrm{w}} = C_{\mathrm{w}}/J$ and the current porosity $\varphi_{\mathrm{w}} = v_{\mathrm{w}}c_{\mathrm{w}}$. Then, by defining the permeability of the polymer network to the solvent in terms of the solvent diffusivity as $k_{\mathrm{w}} = D_{\mathrm{w}}\varphi_{\mathrm{w}}^2/(\mathcal{R}Tc_{\mathrm{w}})$, one obtains the nominal version of Darcy law (MacMinn et al., 2016):

$$\mathbf{J}_{\mathrm{w}}^{\mathrm{v}} = -J\mathbf{C}^{-1}k_{\mathrm{w}}\nabla p_{\mathrm{w}}\,, \tag{5.42}$$

whose more common counterpart in the current configuration reads $\mathbf{j}_{\mathrm{w}}^{\mathrm{v}} = -k_{\mathrm{w}}\,\mathrm{grad}\,p_{\mathrm{w}}$.

By focusing now on the counterion flux in Eq. (5.40b), the first addend represents the *convective* flux of counterions with the solvent. Within our framework, it constitutes an important contribution of counterion flux in sensing, as also in Zhu et al. (2016). Indeed, upon application of a mechanical stimulus, the solvent moves down its pressure gradient, carrying along some counterions. Moreover, within this motion, the solvent establishes a volumetric deformation gradient (see Eq. (5.28)), which triggers counterion diffusion; this is considered through the third term in Eq. (5.40b), proportional to $\nabla C_{\mathrm{w}} = \nabla J/v_{\mathrm{w}}$. Counterion convection along $\mathbf{J}_{\mathrm{w}}$ and diffusion along ∇C_{w} originate an ion imbalance and, consequently, an electric signal. Our theory explains the weak response characterizing IPMC sensors (Shahinpoor and Kim, 2004) with the smallness of the foregoing flux contributions, both proportional to $C/C_{\mathrm{w}} \ll 1$.

Finally, in the limit case of immobile solvent (that is, $D_{\mathrm{w}} = 0$, also implying $\mathbf{J}_{\mathrm{w}} = \mathbf{0}$ through Eq. (5.40a)), we have $C_{\mathrm{w}} = C_{\mathrm{w}}^{0}$ (Eq. (5.3)), $J = 1$ (Eq. (5.28)), $c = C$, and $c_{\mathrm{w}} = C_{\mathrm{w}}$, such that Eq. (5.40b) reduces to

$$\mathbf{J} = -D\mathbf{C}^{-1}\left(\nabla C + \frac{FC}{\mathcal{R}T}\nabla\psi\right)\,, \tag{5.43}$$

whose counterpart in the current configuration reads $\mathbf{j} = -D\left[\mathrm{grad}\,c + Fc/(\mathcal{R}T)\,\mathrm{grad}\,\psi\right]$, which is the classical Nernst-Planck law (Porfiri, 2008), stating that both the gradient of the counterion concentration (Fick effect) and the electric field (electrophoretic effect) concur to counterion transport.

5.3 Analysis of actuation and sensing

Here, we investigate the mechanisms underlying actuation and sensing on the basis of finite element solutions of the proposed model applied to the benchmarks of Fig. 5.1.

5.3.1 Model parameters

With reference to the initial, undeformed configuration, we consider a typical IPMC of length $L = 20\,\mathrm{mm}$, membrane thickness $2H = 200\,\mu\mathrm{m}$, and electrode thickness $h = 1\,\mu$m.

We consider a saturated Nafion membrane, and adopt $G = 50\,$MPa and, unless otherwise specified, $\lambda = 300\,$MPa for the Lamé parameters (Silberstein and Boyce, 2010), such that $\nu \approx 0.4286$ and $E \approx 143\,$MPa. As for the electrodes, we select Lamé parameters two orders of magnitude larger, that is, $G_\mathrm{e} = 5\,$GPa and $\lambda_\mathrm{e} = 30\,$GPa. With respect to the usual moduli for metals, these are about one order of magnitude lower (Liu et al., 2019), as justified by their significantly larger defectiveness, due to the plating processes adopted in IPMC fabrication (Kim and Shahinpoor, 2003).

We adopt room temperature $T = 300\,$K and water as solvent, such that $v_\mathrm{w} = 18\,\mathrm{cm}^3/\mathrm{mol}$. We select $C_\mathrm{w}^0 = 20\,000\,\mathrm{mol}/\mathrm{m}^3$ (corresponding to an initial porosity $\Phi^0 \approx v_\mathrm{w} C_\mathrm{w}^0 = 0.36$), $D_\mathrm{w} = 10^{-9}\,\mathrm{m}^2/\mathrm{s}$, $D = 10^{-10}\,\mathrm{m}^2/\mathrm{s}$, $C^0 = 1\,200\,\mathrm{mol}/\mathrm{m}^3$, and $\varepsilon = 10^{-4}\,\mathrm{F}/\mathrm{m}$. These values are within the ranges propesed by Zhu et al. (2016).

5.3.2 Finite element model

The finite element solution is obtained with the commercial software *COMSOL Multiphysics*® under plane strain conditions. We adopt the `General Form PDE` interface to solve the governing equations ensuing from the mass balances (5.3) and (5.4) and the Gauss law (5.5), by employing quadratic Lagrangian shape functions to approximate the fields p_w, C, and ψ. We use the `Solid Mechanics` interface to solve the equilibrium equations (5.2), by choosing quadratic serendipity shape functions to approximate the field $\mathbf{u}$.

The mesh consists of 19 565 quadrilateral elements, whose geometry is described by quadratic serendipity shape functions. We discretize the IPMC length with 200 uniform elements of size 0.1 mm each, except for a region of width $2H = 0.2\,$mm at the clamped end, where we employ a finer mesh featuring 16 columns of elements instead of 2; this mesh region, required to obtain a sufficiently accurate deformation field therein, is displayed in Fig. 5.2. We discretize the membrane thickness with 50 elements, whose size decreases from the center to the electrodes in geometric sequence with the ratio between the largest and the smallest elements equal to 10; in the electrodes the mesh is uniform, featuring 4 elements along the thickness. We additionally introduce 16 `boundary layer` elements in each of the membrane regions next to the electrodes. These elements also have variable size along the thickness, with the smallest ones, adjacent to the electrodes, of size 10 nm, and the stretching factor between two consecutive elements equal to 1.2. These very fine mesh regions are motivated by the large gradients of C and ψ therein, which constitute the well-established essential feature of IPMC electrochemistry (Porfiri, 2008), also impacting on the solvent

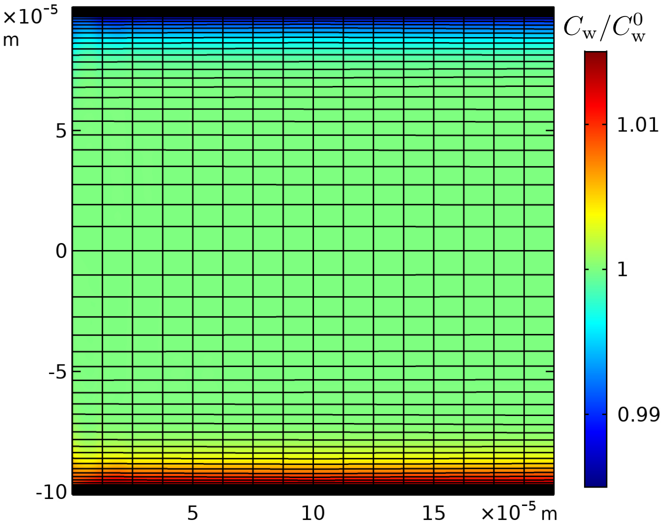

Figure 5.2: Finite element mesh at the clamped end region of the membrane, with the contour of the non-dimensional solvent concentration $C_\mathrm{w}(X,Y)/C_\mathrm{w}^0$ in the membrane bulk for the actuation problem (see Sec. 5.3.3) at time $t = 0.1\,\mathrm{s}$.

redistribution in our model. The overall number of degrees of freedom is 329 133.

We employ Backward Differentiation Formula for the time integration. At each time step, we use a `segregated` approach to solve the discretized equations. Specifically, in actuation we first solve the electrochemical problem, and then, in an iterative loop, use this solution to inform and solve the poromechanical problem. Dually, in sensing the algorithm first solves the poromechanical problem, and then uses the obtained solution as a guess for the electrochemical problem. These solution schemes are convenient as they are suggested by the underlying physics.

While the response is almost independent of X in actuation, the maximum electrochemical response in sensing is obtained in the cross-section where the bending moment attains its maximum value out of the region influenced by the fully clamped constraint, that is, at $X \approx L/100$. Our finite element model allows us to obtain accurate results within this cross-section, where, in the following, we discuss the through-the-thickness variation of the relevant fields.[3]

Finally, let us note that the accuracy of the obtained numerical solution has been assessed through proper refinement of the spatial and temporal discretizations.

---

[3] Analyzing the results so close to the fully clamped cross-section is convenient also because of its very small rotation, leading to a negligible difference between its normal in the reference and current configurations.

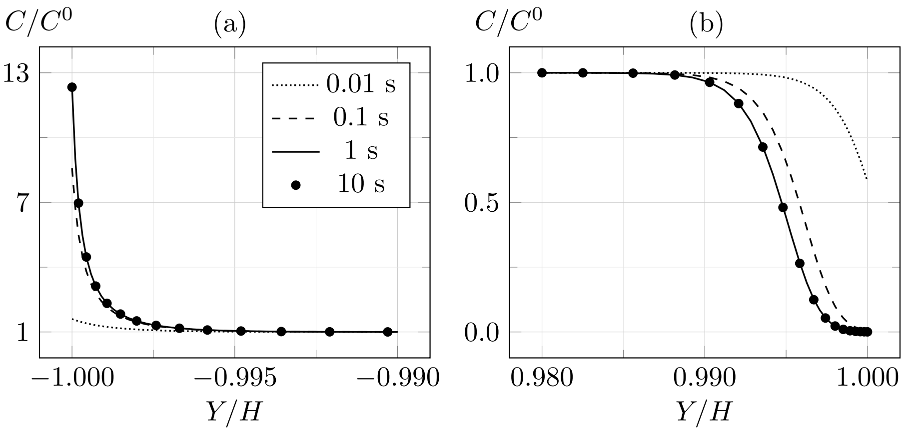

Figure 5.3: Actuation: non-dimensional counterion concentration $C(Y)/C^0$ at $X = L/100$ in the cathode (a) and anode (b) boundary layers.

5.3.3 Actuation

In actuation, the numerical model allows us to instantaneously apply a voltage drop $\bar{\psi} = 0.25\,\mathrm{V}$ across the electrodes, which is then maintained until the steady state. This elicits the counterion migration from the anode to the cathode, resulting in counterion depletion and accumulation in the boundary layers, with the membrane bulk remaining electroneutral. In Fig. 5.3 we display the counterion concentration $C(Y)$ in the boundary layers, at different time instants. At the cathode, C increases up to about $12\,C^0$ at $t \approx 1\,\mathrm{s}$, and then remains constant. At the anode, C decreases to zero at $t \approx 0.1\,\mathrm{s}$, and then the thickness of the boundary layer increases until $C(Y)$ attains its steady state profile at $t \approx 1\,\mathrm{s}$. As displayed in Fig. 5.4, the asymmetry of the boundary layers reflects on the electric potential $\psi(Y)$, which, through the Maxwell stress, is relevant for the back-relaxation (Porfiri et al., 2017). Importantly, the reason for the highlighted asymmetry is inherently electrochemical, although it is strengthened by large deformations.

As counterions migrate toward the cathode, the solvent molecules follow by electro-osmosis. In Figs. 5.5 and 5.6 we represent $C_\mathrm{w}(Y)$ in the boundary layers and in the membrane bulk, respectively. In the cathode boundary layer, the peak value of C_w increases up to about $1.36\,C_\mathrm{w}^0$ at $t \approx 1\,\mathrm{s}$, and then remains constant. Outside the cathode boundary layer, C_w increases until $t \approx 0.1\,\mathrm{s}$, and then slowly decreases, by approaching its initial value at the steady state. The anode side behaves similarly, though experiencing solvent depletion. The contour of C_w in the clamped region of the membrane at $t = 0.1\,\mathrm{s}$ is further reported in the previous Fig. 5.2, where the color bar is set in such a way as to highlight the variation of C_w in the membrane bulk only, thus obscuring its variation in the

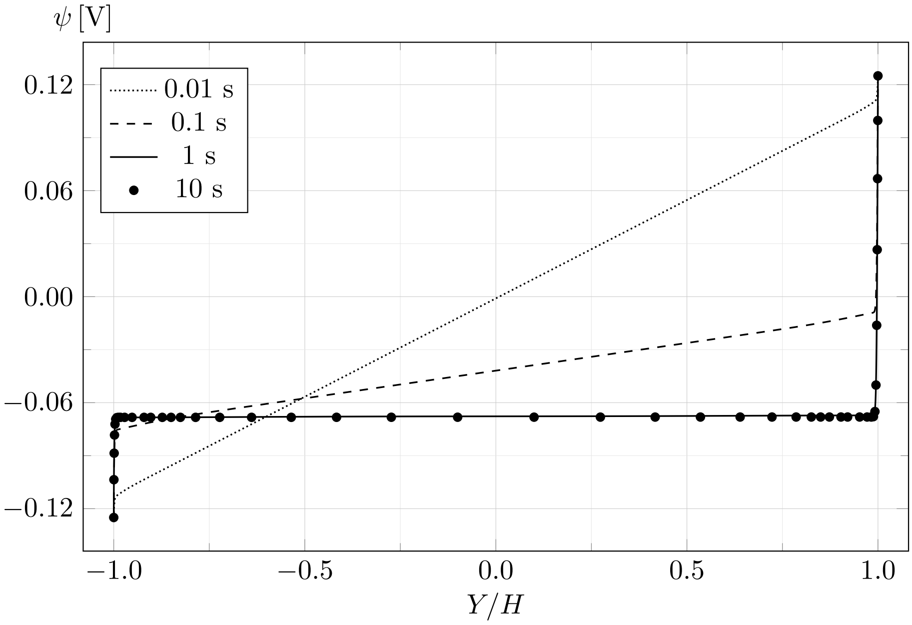

Figure 5.4: Actuation: electric potential $\psi(Y)$ at $X = L/100$ in the membrane.

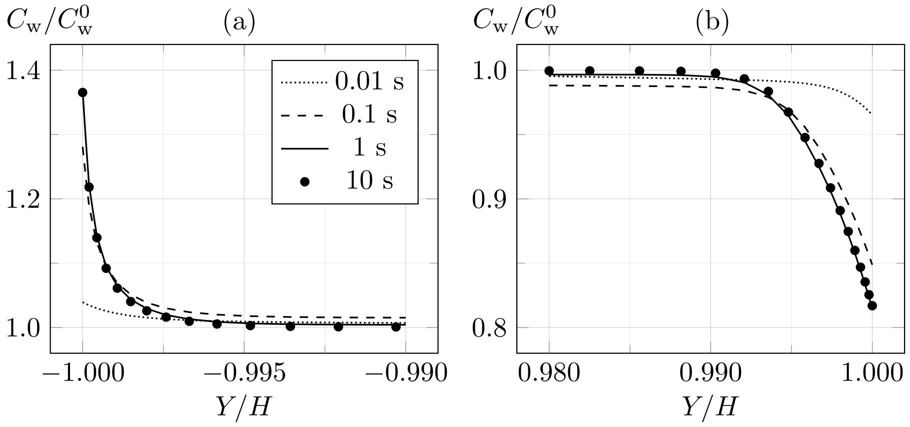

Figure 5.5: Actuation: non-dimensional solvent concentration $C_w(Y)/C_w^0$ at $X = L/100$ in the cathode (a) and anode (b) boundary layers.

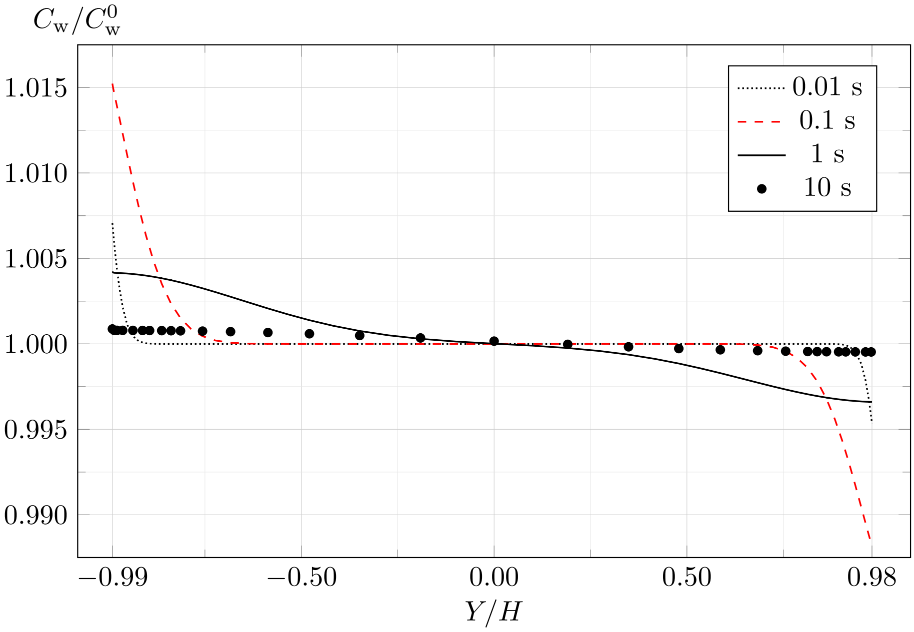

Figure 5.6: Actuation: non-dimensional solvent concentration $C_\mathrm{w}(Y)/C_\mathrm{w}^0$ at $X = L/100$ in the membrane bulk (boundary layers excluded). The curve corresponding to the time instant $t \approx 0.1\,\mathrm{s}$ at which the solvent begins counter-diffusing is highlighted in red.

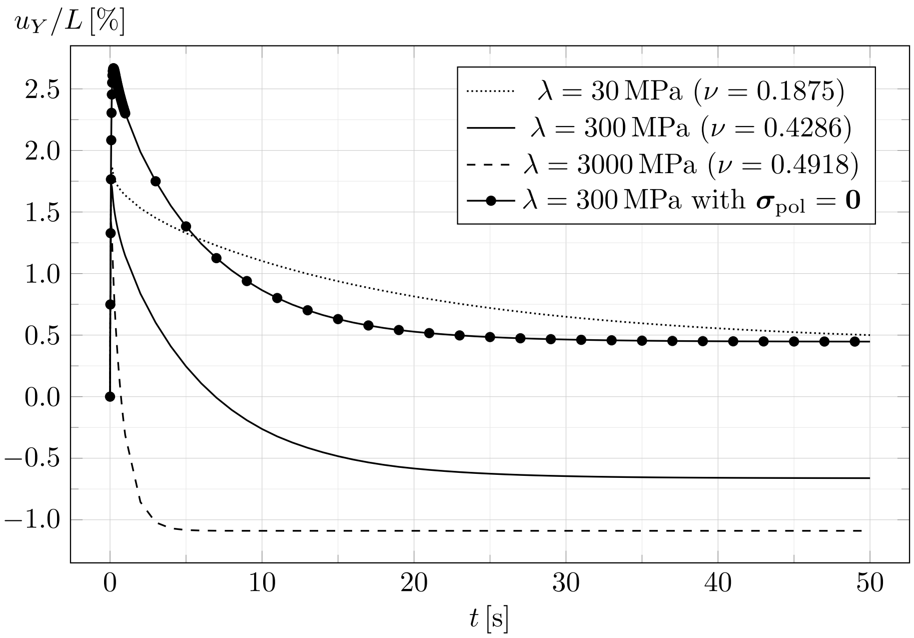

Figure 5.7: Actuation: non-dimensional transverse displacement $u_Y(t)$ evaluated at the free end $(X, Y) = (L, 0)$.

boundary layers, as in Fig. 5.6. Analogously to C, we note that the maximum solvent accumulation at the cathode, characterized by a thinner boundary layer, is larger than the maximum depletion at the anode, indicating asymmetry in the solvent redistribution. Notably, the relative change of C_{w} along the membrane thickness is much lower than that of C.

We draw the first conclusion that in the boundary layers the contribution of the solvent pressure gradient ∇p_{w} to the solvent flux never exceeds that of the electric field $\mathbf{E} = -\nabla\psi$, such that C_{w} undergoes a monotonic variation in time until the steady state. In other words, in IPMC actuation, the electrochemistry also governs the boundary layer behavior of the solvent. Instead, in the membrane bulk, the contribution of ∇p_{w} overcomes that of $\mathbf{E}$ at a certain time, after which the solvent counter-diffuses and the back-relaxation occurs.

For the flexure magnitude, in Fig. 5.7 we display the time evolution of the transverse displacement $u_Y(L, 0)$. It initially rapidly increases, reaching the peak value u_Y^{p} at t^{p}. Then the back-relaxation occurs and u_Y slowly decreases until the steady state value u_Y^{ss} at t^{ss}. With reference to the case $\lambda = 300\,\text{MPa}$: $u_Y^{\text{p}} \approx 1.7\%\,L$, $t^{\text{p}} \approx 0.1\,\text{s}$ and $u_Y^{\text{ss}} \approx -0.7\%\,L$, $t^{\text{ss}} \approx 50\,\text{s}$. Therefore, while initially the IPMC bends toward the anode, it finally undergoes opposite curvature, bending toward the cathode. This behavior and the associated timescales have been first documented in Asaka et al. (1995).

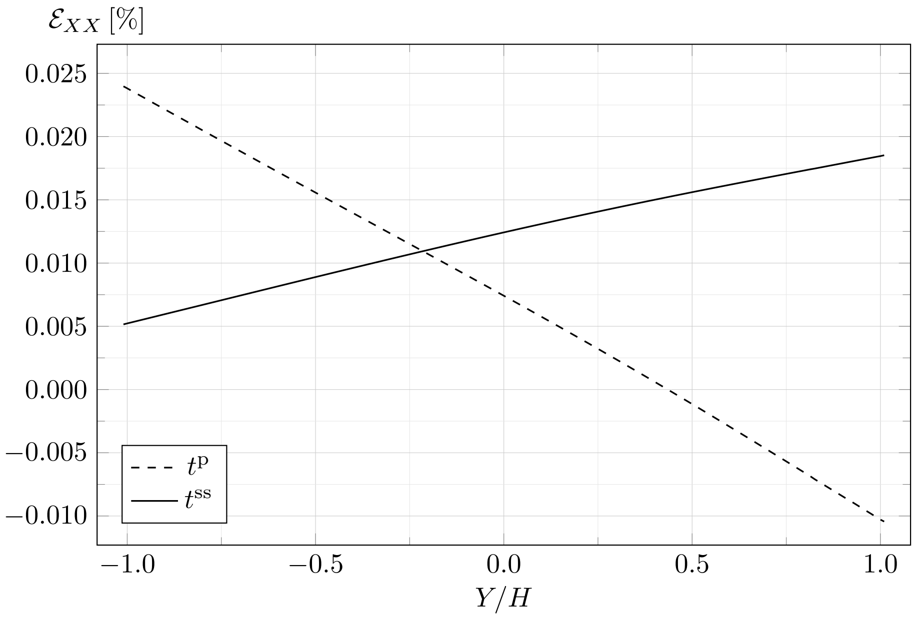

Figure 5.8: Actuation: longitudinal strain $\mathcal{E}_{XX}(Y)$ at $X = L/100$ in the membrane and electrodes.

Remarkably, as shown in Fig. 5.7 and demonstrated in the following, disregarding the Maxwell stress both leads to a significant overestimation of u_Y^{p} ($u_Y^{\mathrm{p}} \approx 2.7\%\, L$, now reached at $t^{\mathrm{p}} \approx 0.25\,\mathrm{s}$) and excludes the possibility of predicting the change in sign of the curvature, although the back-relaxation still takes place.

Fig. 5.7 also displays the dependence of the back-relaxation on the first Lamé parameter λ, whereby increasing λ anticipates the steady state and amplifies the magnitude of the back-relaxation. Moreover, it exists a sufficiently small λ such that the curvature does not change sign, although the back-relaxation still occurs. We can explain this dependence of the flexure on λ by leveraging on the two fundamental results illustrated below.

First, as illustrated in Fig. 5.8, the longitudinal (Green-Lagrange) strain $\mathcal{E}_{XX}(Y)$ remains nearly linear all along the IPMC cross-section. On this basis, let us note that Fig. 5.8 clearly reports the change of curvature sign at the steady state with respect to that at the initial peak. In more detail, at t^{p} the IPMC bends toward the anode and the neutral axis is shifted, with respect to the mid-axis, toward the anode. At t^{ss} the curvature has opposite sign, with the IPMC bending now toward the cathode; notably, the whole cross-section presents positive $\mathcal{E}_{XX}$, denoting a longitudinal elongation of the strip. The IPMC extension in actuation has also been reported in Boldini et al. (2020) on

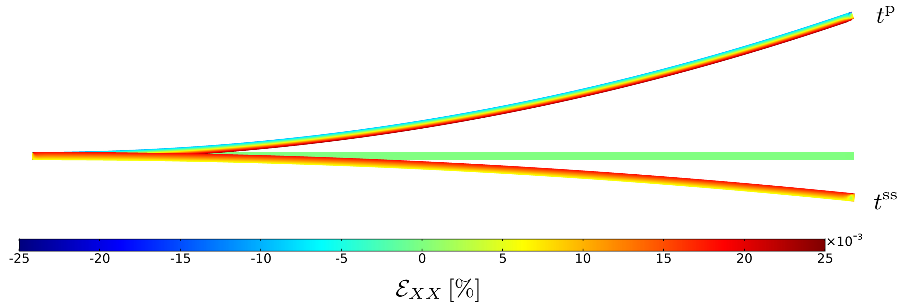

Figure 5.9: Actuation: undeformed configuration and deformed configurations (10 times amplified) at t^{p} and t^{ss}, also displaying the longitudinal strain field $\mathcal{E}_{XX}$.

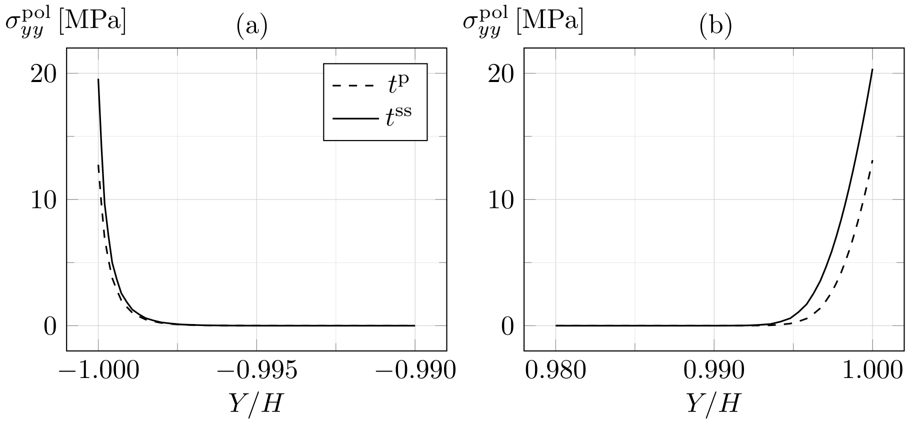

Figure 5.10: Actuation: transverse Maxwell stress $\sigma_{yy}^{\mathrm{pol}}(Y)$ at $X = L/100$ in the cathode (a) and anode (b) boundary layers.

the basis of the Cha and Porfiri (2014) theory. Generally, $\mathcal{E}_{XX}$ is small, although the bending deformation is relevant, given the strip slenderness. In Fig. 5.9 we report the undeformed configuration and the deformed configurations at t^{p} and t^{ss}, with the associated contour plots of $\mathcal{E}_{XX}$.

Second, it is crucial to notice, as documented by Fig. 5.10, how the Maxwell stress $\sigma_{yy}^{\mathrm{pol}}(Y) = -\sigma_{xx}^{\mathrm{pol}}(Y)$ grows asymmetrically in the boundary layers. Since $\partial\psi/\partial x$ is negligible, $\sigma_{yy}^{\mathrm{pol}} \approx (\varepsilon/2)(\partial\psi/\partial y)^2$ has the same sign on both sides of the membrane, where it increases in magnitude with time. Importantly, near the anode $\sigma_{yy}^{\mathrm{pol}}$ assumes slightly greater values and, most of all, it attains a relevant magnitude in a larger region, because of the thicker boundary layer therein. This asymmetry grows in time, and is expected to increase with the applied voltage (Porfiri et al., 2017).

Hence, we can explain the mechanics behind the back-relaxation documented in Fig. 5.7 by temporarily resorting to small strains and decoupling poromechanics and electrochemistry, solving the latter first. This provides, by suitably approximating the behavior observed in Fig. 5.8, a longitudinal strain $\varepsilon_{xx}(y) \approx \kappa y + \varepsilon_0$, with κ denoting the curvature and ε_0 the mid-axis strain, and a known Maxwell stress $\sigma_{yy}^{\mathrm{pol}}(y) \approx (\varepsilon/2)(\partial\psi/\partial y)^2$. Then, by resorting to the equilibrium along y, we can estimate the transverse mechanical stress $\sigma_{yy}^{\mathrm{mec}}(y) \approx -\sigma_{yy}^{\mathrm{pol}}(y) + p_{\mathrm{w}}(y)$, as confirmed by the finite element analyses. Under plane strain, the longitudinal mechanical stress reads $\sigma_{xx}^{\mathrm{mec}}(y) = [E/(1-\nu^2)]\varepsilon_{xx}(y) + [\nu/(1-\nu)]\sigma_{yy}^{\mathrm{mec}}(y)$, such that the *total* longitudinal stress in the membrane turns out to be

$$\sigma_{xx}(y) \approx \frac{E}{1-\nu^2}(\kappa y + \varepsilon_0) + \frac{\nu}{1-\nu}\left[-\sigma_{yy}^{\mathrm{pol}}(y) + p_{\mathrm{w}}(y)\right] - \sigma_{yy}^{\mathrm{pol}}(y) - p_{\mathrm{w}}(y)\,. \quad (5.44)$$

In the electrodes, we simply have

$$\sigma_{xx}(y) = \sigma_{xx}^{\mathrm{mec}}(y) \approx \frac{E_{\mathrm{e}}}{1-\nu_{\mathrm{e}}^2}(ky + \varepsilon_0)\,. \quad (5.45)$$

As no mechanical loads are applied to the IPMC in actuation, we can estimate κ and ε_0 by imposing vanishing total bending moment and total axial force. In particular, by using Eqs. (5.44) and (5.45), the first condition provides

$$\kappa \approx \frac{1}{\beta(1-\nu)}\int_{-H}^{H}[\sigma_{yy}^{\mathrm{pol}}(y) + (1-2\nu)p_{\mathrm{w}}(y)]y\,\mathrm{d}y$$
$$= -\frac{1}{\beta(1-\nu)}\left[M_{\mathrm{pol}} + (1-2\nu)M_{\mathrm{w}}\right]\,, \quad (5.46)$$

where

$$\beta = \frac{E}{1-\nu^2}\frac{2}{3}H^3 + \frac{E_{\mathrm{e}}}{1-\nu_{\mathrm{e}}^2}2H^2h \quad (5.47)$$

is the plane strain bending stiffness per unit depth relying on the Bernoulli-Navier kinematics and on the assumption of *thin skins*, and M_{pol} and M_{w} are the bending moments per unit depth due to the Maxwell stress and to the solvent pressure. It is important to notice that, in Eq. (5.46), the difference from unity of the coefficients $(1-\nu)$ and $(1-2\nu)$ ensues from the second contribution to the *mechanical* stress in Eq. (5.44), which has been overlooked so far in IPMC literature, to the best of our knowledge.

Given that the solvent moves from the anode to the cathode, Eq. (5.46) establishes that the solvent pressure always gives a negative contribution to κ, corresponding to bending toward the anode. In fact, as shown in Fig. 5.11, at the anode side $p_{\mathrm{w}} < 0$ and at the cathode side $p_{\mathrm{w}} > 0$.

Instead, the Maxwell stress $\sigma_{yy}^{\mathrm{pol}} > 0$ gives a positive contribution to κ at the anode side, while it provides a negative contribution to κ at the cathode side.

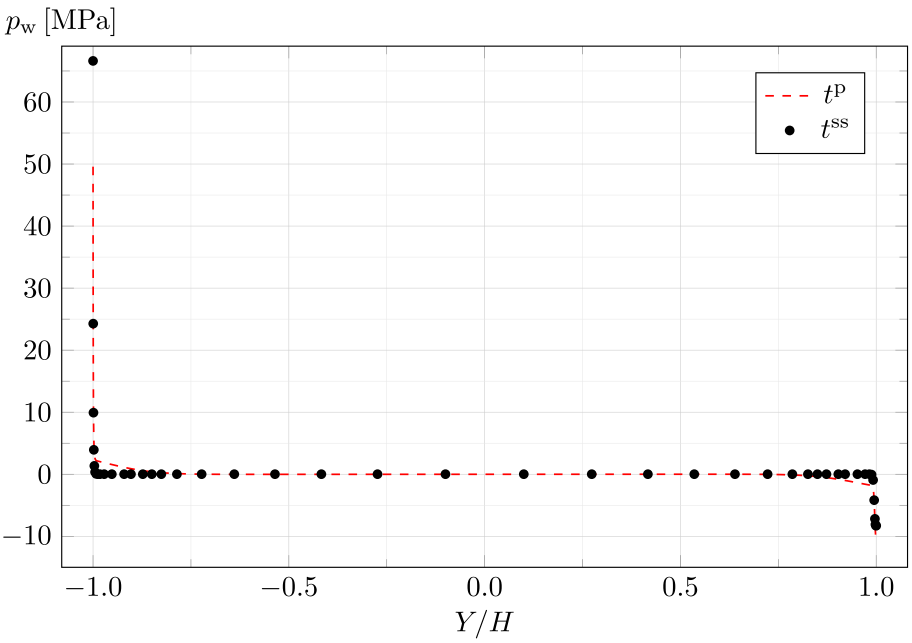

Figure 5.11: Actuation: solvent pressure $p_w(Y)$ at $X = L/100$ in the membrane.

Therefore, the back-relaxation may lead to bending toward the cathode ($\kappa > 0$) only due to the Maxwell stress, whereby this occurs when the contribution of the Maxwell stress at the anode overcomes those of the solvent pressure and of the Maxwell stress at the cathode. This turns out to be possible because of the boundary layers asymmetry described above (see, in particular, Fig. 5.10).

Moreover, Eq. (5.46) allows us to explain the back-relaxation dependence on λ, as illustrated in Fig. 5.7: increasing λ for a given G implies a larger ν, the latter approaching 0.5 as $\lambda \to \infty$; this diminishes the negative contribution to κ due to p_w, thus anticipating and emphasizing the back-relaxation.

Let us now delve into further details on the back-relaxation contribution due to the solvent counter-diffusion, on the basis of $p_w(Y)$ in Fig. 5.11. By passing from t^p to t^{ss}, $|p_w|$ diminishes everywhere, except in the cathode boundary layer, resulting in a decrease of M_w with time, as confirmed by the case disregarding the Maxwell stress in Fig. 5.7.

As recently established by Boldini and Porfiri (2020) and Boldini et al. (2020), the IPMC actuation is characterized by large gradients of all the relevant stress and strain components in the boundary layers, except for the longitudinal strain (see Fig. 5.8). This is detailed in the following within the context of the present theory. Fig. 5.12 displays the transverse Green-Lagrange strain $\mathcal{E}_{YY}(Y)$ in the membrane. The profile of $\mathcal{E}_{YY}$ is asymmetric, with the peak magnitude of $\mathcal{E}_{YY}$

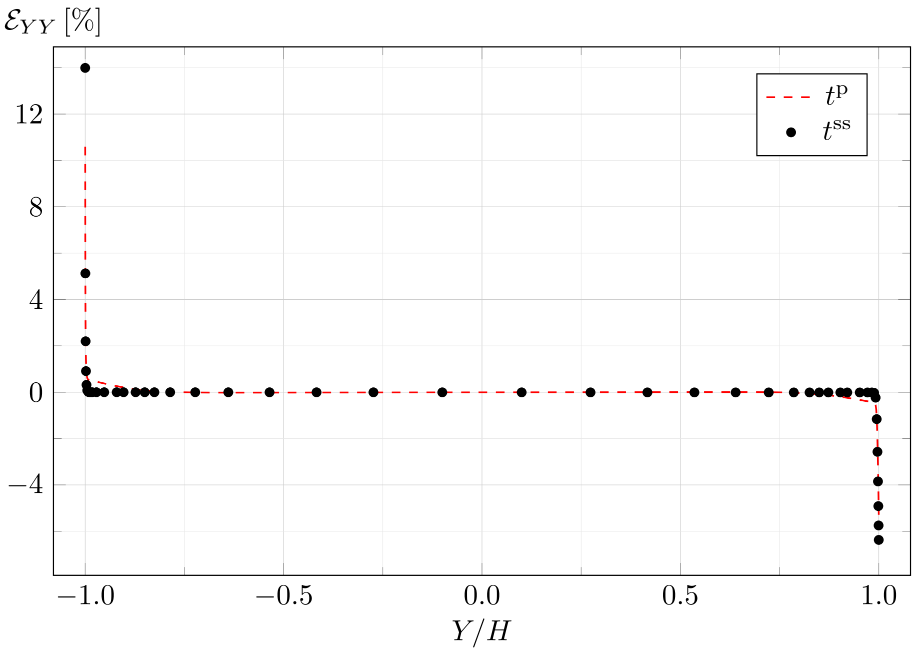

Figure 5.12: Actuation: transverse strain $\mathcal{E}_{YY}(Y)$ at $X = L/100$ in the membrane.

at the cathode being nearly double than that at the anode. Our poromechanical framework allows the model to further predict non-negligible $\mathcal{E}_{YY}$ outside the boundary layers, which vanishes at the steady state, according to the solvent redistribution (see Fig. 5.6).

Finally, in Fig. 5.13 we represent the longitudinal mechanical stress $\sigma_{xx}^{\mathrm{mec}}(Y)$ at the cathode and anode sides. It is worth noting that the steady state bending toward the cathode, due to the back-relaxation, is accompanied with a change in sign of the axial stress in the anode, which becomes larger than that at the cathode. Remarkably, $\sigma_{xx}^{\mathrm{mec}}$ and $\sigma_{yy}^{\mathrm{mec}}$ combine as to provide a longitudinal strain $\mathcal{E}_{XX}$ that is well approximated by an affine function of Y, see Fig. 5.8.

In Porfiri et al. (2017), the importance of the Maxwell stress in IPMC back-relaxation was first advanced, on the basis of the Cha and Porfiri (2014) theory, which neglects the solvent flow, and assumes that actuation is triggered by an osmotic pressure term proportional to the difference in concentration between counterions and fixed ions. Given that counterions are unlikely to counter-diffuse in actuation, in the Cha and Porfiri (2014) framework the back-relaxation can be explained exclusively through electrostatic arguments. Conversely, Zhu et al. (2013) account for the cross-diffusion of solvent and counterions, but neglect the Maxwell stress; indeed, Zhu et al. (2013) predict a back-relaxation without reversal of the curvature.

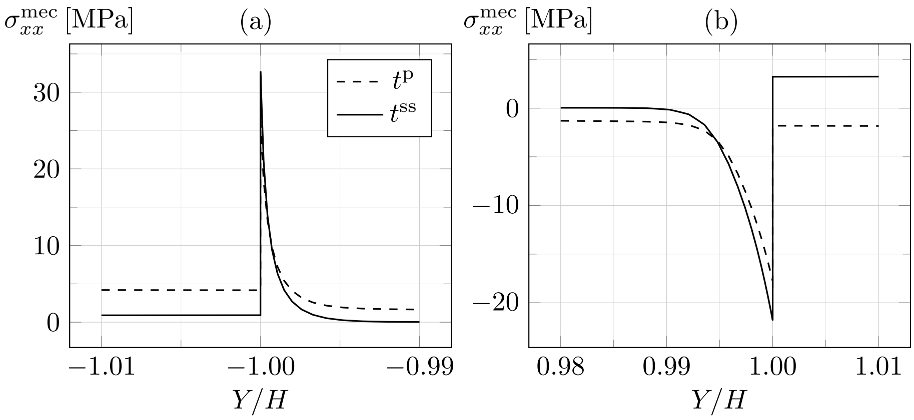

Figure 5.13: Actuation: longitudinal mechanical stress $\sigma_{xx}^{\mathrm{mec}}(Y)$ at $X = L/100$ in the cathode (a) and in the anode (b), including the boundary layers in the membrane.

The present theory is, to the best of our knowledge, the first one to effectively combine the classical model of the back-relaxation, based on the solvent counter-diffusion, with the more recent (so far, alternative) description relying on the relevance of the Maxwell stress. Furthermore, our theory allows one to establish a precise link between the steady state bending response and the Lamé constants, thus suggesting a possible strategy for the identification of the model parameters.

5.3.4 Sensing

In short-circuit sensing, we impose a uniformly distributed nominal load of magnitude $\overline{T} = 50\,\mathrm{N/m^2}$. The numerical model does not allow us to instantaneously apply this load; hence, we linearly enforce it in a suitably short time interval $t^{\mathrm{i}} = 0.1\,\mathrm{s}$, and then maintain it until the steady state. The load application leads to a sensing response triggered by poromechanics, as described in the following.

In Fig. 5.14 we represent the longitudinal mechanical stress $\sigma_{xx}^{\mathrm{mec}}$ and the solvent pressure p_{w} along the membrane thickness, at $t^{\mathrm{i}} = 0.1\,\mathrm{s}$ and $t^{\mathrm{ss}} \approx 50\,\mathrm{s}$. While $|\sigma_{xx}^{\mathrm{mec}}|$ increases in time, $|p_{\mathrm{w}}|$ decreases and nearly vanishes everywhere at the steady state. At each time instant, we observe that $\sigma_{xx}^{\mathrm{mec}}(t) - p_{\mathrm{w}}(t) \approx \sigma_{xx}^{\mathrm{mec}}(t^{\mathrm{ss}})$, showing, incidentally, that the time evolution of the Maxwell stress is irrelevant. In Fig. 5.15 we display the longitudinal, $\mathcal{E}_{XX}$, and transverse, $\mathcal{E}_{YY}$, Green-Lagrange strains. The cathode side extends longitudinally and shortens transversely, while the anode side exhibits opposite behavior. Progressively, $|\mathcal{E}_{XX}|$ slightly increases, while $|\mathcal{E}_{YY}|$ decreases. In Fig. 5.16 we represent the solvent concentration C_{w}, which is directly related with the volumetric deformation by Eq. (5.28). It increases with time at the cathode side while

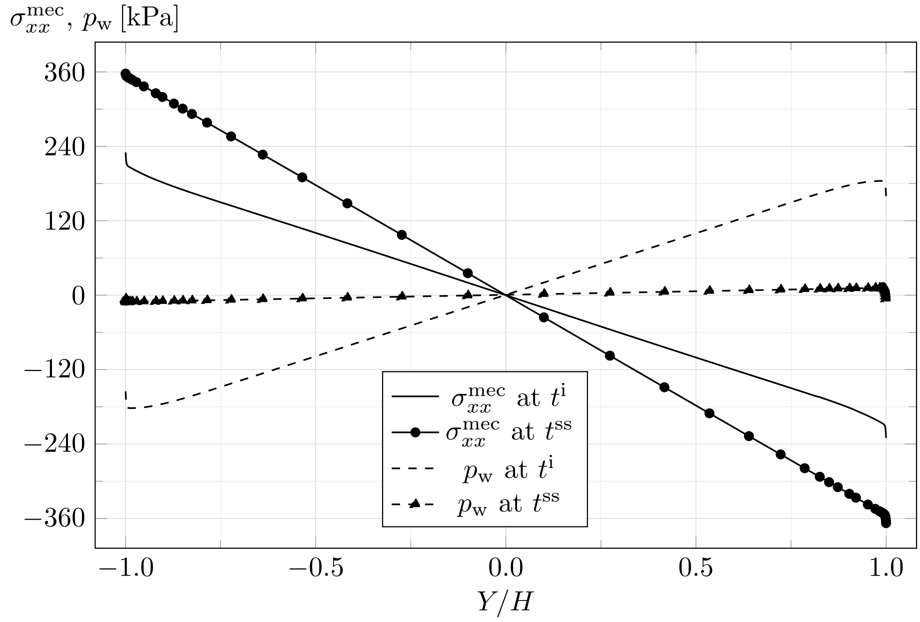

Figure 5.14: Sensing: longitudinal mechanical stress $\sigma_{xx}^{\mathrm{mec}}(Y)$ and solvent pressure $p_{\mathrm{w}}(Y)$ at $X = L/100$ in the membrane.

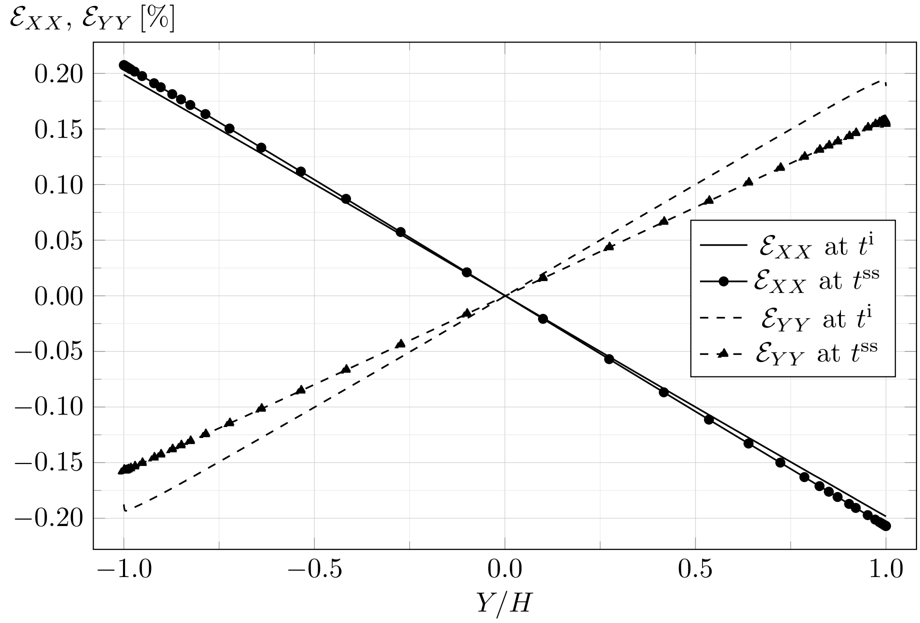

Figure 5.15: Sensing: longitudinal, $\mathcal{E}_{XX}(Y)$, and transverse, $\mathcal{E}_{YY}(Y)$, strains at $X = L/100$ in the membrane.

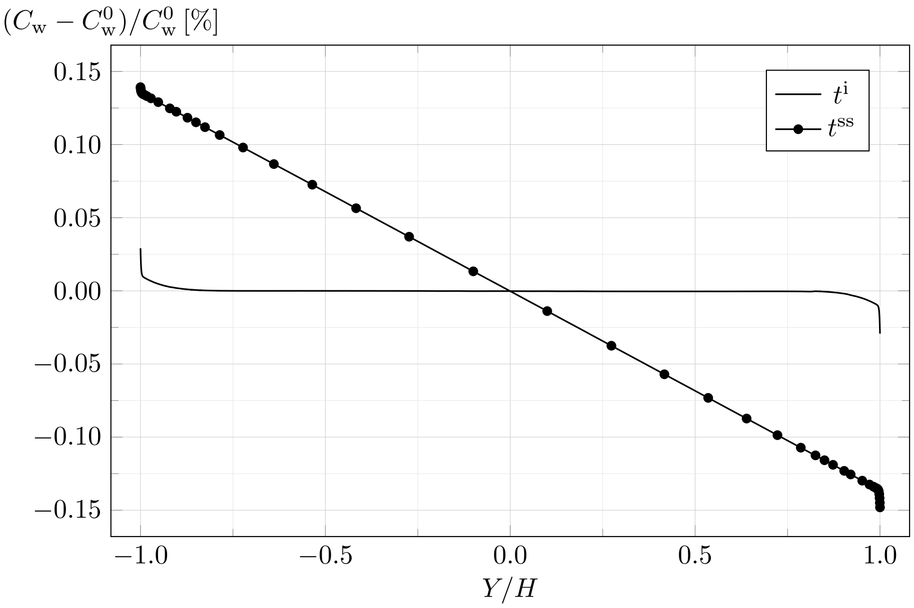

Figure 5.16: Sensing: relative solvent concentration $\left[C_\mathrm{w}(Y) - C_\mathrm{w}^0\right]/C_\mathrm{w}^0$ at $X = L/100$ in the membrane.

decreasing at the anode side. All the poromechanical fields are nearly symmetric with respect to the mid-axis, except for some asymmetry arising in the boundary layers as the steady state is approached.

In Fig. 5.17 we represent the time evolution of the transverse displacement at the free end, $u_Y(L, 0)$, which is non-dimensionalized through its value estimated with the linear elastic Euler-Bernoulli beam theory $u_Y^\mathrm{EB} = \overline{T}L^4/(8\beta) \approx 2.14\,\mathrm{mm}$, where β is given by Eq. (5.47). As the load is progressively applied, the IPMC bends toward the anode, with a tip displacement $u_Y^\mathrm{i} \approx 0.945\,u_Y^\mathrm{EB}$ at t^i. As long as the load is maintained, the tip displacement increases with time, reaching the steady state value $u_Y^\mathrm{ss} \approx 0.985\,u_Y^\mathrm{EB}$. Therefore, the time-delayed displacement is $u_Y^\mathrm{ss} - u_Y^\mathrm{i} \approx 4\%\,u_Y^\mathrm{ss}$.

The observed poromechanics can be explained by temporarily resorting to small strains within the Euler-Bernoulli kinematics for the whole IPMC cross-section and disregarding the effect of the electric field. Under plane strain, the volume ratio reads $J(x, y) = 1 + \nu[\sigma_{xx}^\mathrm{mec}(x, y) + \sigma_{yy}^\mathrm{mec}(x, y)]/\lambda$. The applied load $\overline{T}$ is associated with a bending moment $M(x) = \overline{T}(x^2 - 2Lx + L^2)/2$, which is partly equilibrated by the total longitudinal stress in the membrane, such that $\sigma_{xx}^\mathrm{mec}(x, y) = p_\mathrm{w}(x, y) - [E/(1 - \nu^2)]M(x)y/\beta$. Given the smallness of the applied load and the thinness of the IPMC, the equilibrium in the y direction requires that $\sigma_{yy}^\mathrm{mec}(x, y) \approx p_\mathrm{w}(x, y)$, as also confirmed by the finite element

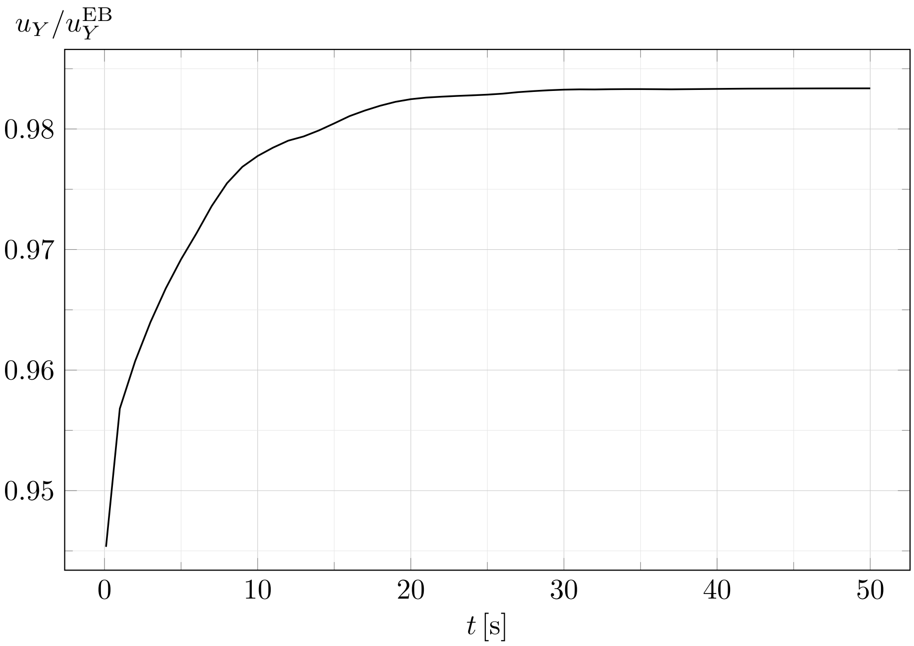

Figure 5.17: Sensing: non-dimensional transverse displacement $u_Y(t)$ at $(X,Y) = (L,0)$ relative to the value u_Y^{EB} predicted by the linear elastic Euler-Bernoulli beam model.

results. Consequently, the volume ratio can be rewritten as

$$\begin{aligned} J(x,y) &\approx 1 + \frac{\nu}{\lambda}\left[2p_{\text{w}}(x,y) - \frac{E}{1-\nu^2}\frac{M(x)}{\beta}y\right] \\ &= 1 + \frac{1}{2(\lambda+G)}\left[2p_{\text{w}}(x,y) - \frac{4G(\lambda+G)}{\lambda+2G}\frac{M(x)}{\beta}y\right], \end{aligned} \tag{5.48}$$

in which the last form is convenient to discuss the influence of λ. By neglecting $\partial p_{\text{w}}/\partial x$, which is small compared to $\partial p_{\text{w}}/\partial y$, the solvent mass balance (5.3) reduces to

$$\dot{p}_{\text{w}}(x,y) - (\lambda+G)k_{\text{w}}\frac{\partial^2 p_{\text{w}}(x,y)}{\partial y^2} \approx \frac{4G(\lambda+G)}{\lambda+2G}\frac{\dot{M}(x)}{2\beta}y\,, \tag{5.49}$$

in which $k_{\text{w}} = D_{\text{w}}v_{\text{w}}^2 C_{\text{w}}^0/(\mathcal{R}T)$. Eq. (5.49) is a diffusion-type equation to be solved, at each x, for the solvent pressure field $p_{\text{w}}(y,t)$, given the initial condition $p_{\text{w}}(y) = 0$ at $t = 0$ and the boundary conditions $\partial p_{\text{w}}/\partial y\big|_{y=\pm H} = 0$, corresponding to imposing zero-flux at the electrodes. All the other relevant poromechanical fields can be readily reconstructed once Eq. (5.49) is solved.

While the load is linearly increased during the ramp of time length t^{i}, the constant $\dot{M} = \overline{T}(x^2 - 2Lx + L^2)/(2t^{\text{i}})$ generates a progressively increasing solvent pressure gradient along the membrane thickness. The solvent pressure p_{w} enters the equilibrium, such that $|\sigma_{xx}^{\mathrm{mec}}|$ is less than it would be for a non-porous material. Then, while the load is kept constant after the loading ramp, $\dot{M} = 0$ and the solvent progressively moves down its pressure gradient, $|p_{\mathrm{w}}|$ reduces, and a larger fraction of the applied load is equilibrated by $|\sigma_{xx}^{\mathrm{mec}}|$, which increases in time, while $|\sigma_{yy}^{\mathrm{mec}}| \approx |p_{\mathrm{w}}|$ decreases. Therefore, $|\mathcal{E}_{XX}|$ progressively increases, along with the IPMC deflection. At the steady state, the excess solvent pressure is dissipated, such that the solvent becomes irrelevant for the equilibrium. Correspondingly, in the membrane the total longitudinal stress σ_{xx} tends to coincide with its mechanical contribution $\sigma_{xx}^{\mathrm{mec}}$, and the deflection to the Euler-Bernoulli beam value u_Y^{EB}.[4]

Within our framework, the smallness of the time-dependent deflection $u_Y^{\mathrm{ss}} - u_Y^{\mathrm{i}}$ is explained by the fact that a considerable part of the applied load is instantaneously equilibrated by the longitudinal stress in the electrodes, $\sigma_{xx} = \sigma_{xx}^{\mathrm{mec}} = -[E_{\mathrm{e}}/(1-\nu_{\mathrm{e}}^2)]My/\beta$.

So far, we have neglected the electric field contribution to the solvent flux. Actually, at the steady state, the solvent pressure is not exactly zero (see Fig. 5.14), as the component of the solvent flux proportional to ∇p_{w} must balance the electro-osmotic contribution, proportional to $\mathbf{E}$. The mechanical stress state is in turn partly altered by the electro-osmotic flux of the solvent, but not by the Maxwell stress, which turns out to be negligible. Consequently, the final deflection is slightly less than that predicted by the Euler-Bernoulli beam theory.

We can now comment on the electrochemical response elicited by the solvent flux, with reference to Fig. 5.18, in which we represent the counterion concentration $C(Y)$ in the boundary layers, and Fig. 5.19, where we display the electric potential $\psi(Y)$ in the membrane. At the cathode, C increases with time until $t \approx 0.5\,\mathrm{s}$, which is five times longer than the loading ramp duration t^{i}, and then decreases. The analogous opposite behavior is observed at the anode. We conclude that counterions initially flow toward the cathode by convection with the solvent and by diffusion toward regions of larger volume ratio, until they counter-diffuse as their concentration gradient becomes sufficiently large (see Eq. (5.40b)). At the steady state, the convective and electro-diffusive fluxes are individually null. The electric potential field of Fig. 5.19 results from the counterion redistribution, on the basis of Gauss law (5.5).

In Fig. 5.20(a) we represent the time evolution of the total stored charge per

---

[4] This picture is reminiscent of the consolidation problem of soil mechanics. However, in the classical problem of consolidation (Biot, 1941), the process is allowed by the drainage of water from the soil surface, whereby the total "vertical" stress is uniform along the soil depth. Here, differently, the solvent is prevented from draining, but the process is allowed by the presence of a total longitudinal stress gradient along the membrane thickness.

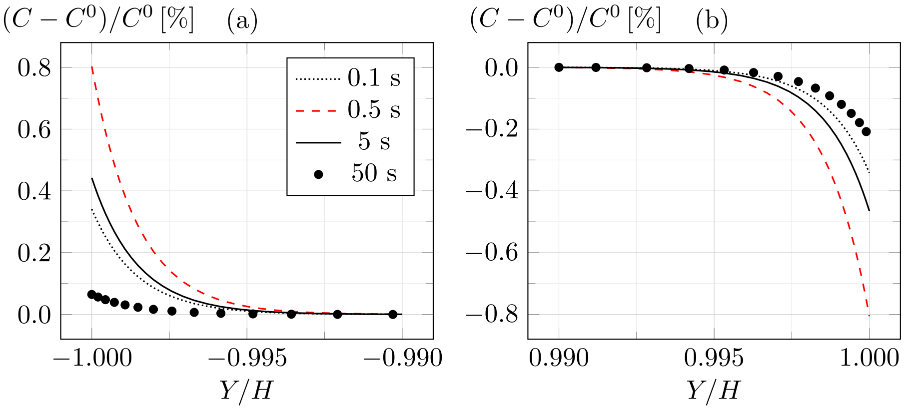

Figure 5.18: Sensing: relative counterion concentration $[C(Y) - C^0]/C^0$ at $X = L/100$ in the cathode (a) and anode (b) boundary layers. The curves corresponding to the time instant at which counterions begin counter-diffusing are highlighted in red.

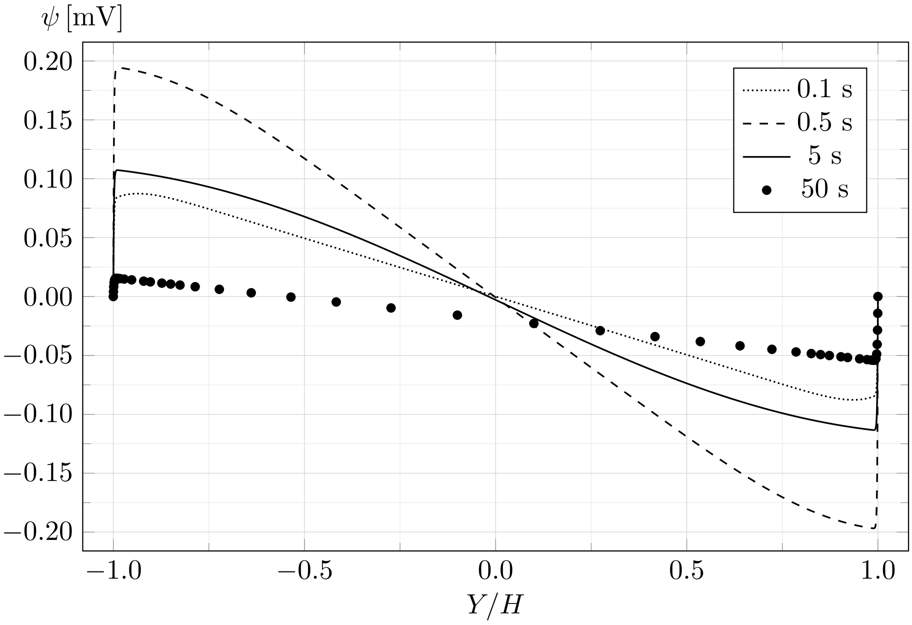

Figure 5.19: Sensing: electric potential $\psi(Y)$ at $X = L/100$ in the membrane.

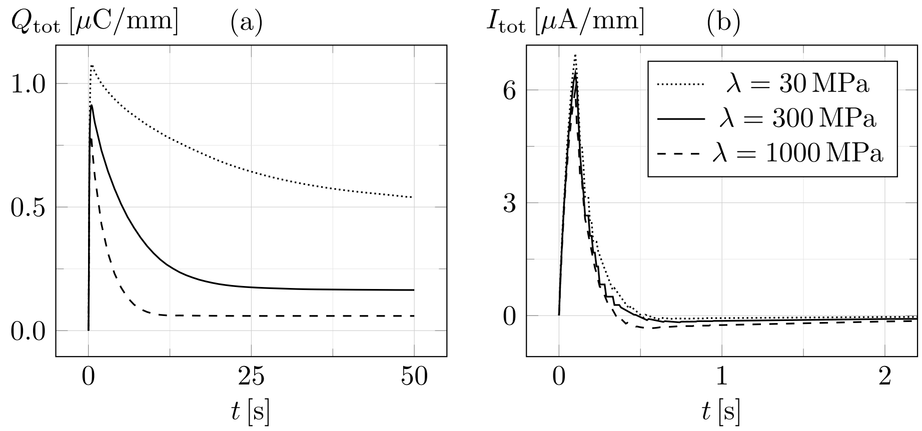

Figure 5.20: Sensing: total stored charge $Q_{\mathrm{tot}}(t)$ (a) and electric current $I_{\mathrm{tot}}(t)$ (b) per unit depth.

unit depth, defined as

$$Q_{\mathrm{tot}} = \int_0^L \Big| D_Y(Y = \pm H) \Big| \,\mathrm{d}X\,. \tag{5.50}$$

It increases until $t \approx 0.5\,$s, when, with reference to the case $\lambda = 300\,$MPa, it reaches the peak value $Q^{\mathrm{p}}_{\mathrm{tot}} \approx 0.91\,\mu$C/mm. Then it starts decreasing slowly to the steady state value $Q^{\mathrm{ss}}_{\mathrm{tot}} \approx 0.16\,\mu\mathrm{C/mm} \approx 18\%\,Q^{\mathrm{p}}_{\mathrm{tot}}$. This decrease of Q_{tot}, which can be deleterious for IPMCs employed in energy harvesting, is clearly due to the counterion counter-diffusion. The reversal of the counterion flux is also confirmed by the change in sign of the total electric current per unit depth, defined as $I_{\mathrm{tot}} = \dot{Q}_{\mathrm{tot}}$, whose time evolution is shown in Fig. 5.20(b). The current increases with the load application; then, it decreases rapidly and becomes negative at $t \approx 0.5\,$s, when counterions begin counter-diffusing; finally, it slowly goes to zero at the steady state. Qualitatively, the same results in terms of stored charge and electric current have been experimentally observed by Farinholt and Leo (2004) in response to an imposed tip displacement.

Fig. 5.20 also displays the time evolution of the total stored charge and electric current obtained by varying the Lamé parameter λ, with G held equal to 50 MPa.[5] By decreasing λ, the peak stored charge $Q^{\mathrm{p}}_{\mathrm{tot}}$ increases and, most of all, the counterion counter-diffusion is milder, such that, for $\lambda = 30\,$MPa, $Q^{\mathrm{ss}}_{\mathrm{tot}} \approx 0.5\,Q^{\mathrm{p}}_{\mathrm{tot}}$. This behavior is explained by the fact that, by diminishing λ, the solvent flux toward the cathode increases, along with the counterion flux. Indeed, Eq. (5.48) reveals that $|J(y)|$, and correspondingly $|C_{\mathrm{w}}(y)|$ through the

---

[5] Differently from the actuation problem, our numerical model exhibits convergence issues if we set $\lambda = 3000\,$MPa in this sensing problem, such that we limit λ to 1000 MPa.

constraint (5.30), increase by decreasing λ. Moreover, Fig. 5.20 shows that the discharge process requires a significantly larger time for smaller λ. This is explained by the diffusion equation (5.49), which shows that the "solvent pressure flux", defined as $-(\lambda + G)k_{\mathrm{w}}\partial p_{\mathrm{w}}/\partial y$, decreases with λ, thus requiring more time for the solvent pressure to be dissipated. This analysis might offer a criterion for selecting the most efficient ionomer for an IPMC employed as a sensor on the basis of the resulting elastic moduli.

Finally, we remark that, in sensing, the time-increasing asymmetry in $C(Y)$ and, especially, $\psi(Y)$ (see Figs. 5.18 and 5.19), can be captured only by considering a finite deformation framework. Indeed, although the deformations are relatively small (see Fig. 5.15), the time-varying deformation field non-negligibly modulates the electrochemistry, characterized in sensing by small deviations from the initial electroneutral state. This effect is expected to be amplified by the application of larger loads than that considered here.

5.4 Concluding remarks

We have herein proposed a model for IPMCs by suitably modifying the electrochemo-mechanical theory of Cha and Porfiri (2014). As a main novelty, we have accounted for the transport of the solvent, which establishes the volumetric deformation of the membrane and cross-diffuses with counterions.

Specifically, by referring to the mixture theory (Ateshian, 2007), we have regarded the IPMC membrane as the superposition of a solid phase, identifying with a negatively charged polymer, and a fluid phase, consisting of counterions immersed in a solvent. Toward the simplest possible model thoroughly describing the complex IPMC multiphysics, we have assumed that each constituent is incompressible and that the fluid phase is dilute, such that the volumetric deformation of the membrane only depends on the solvent redistribution. The model is governed by four coupled equations consisting of an overall momentum balance, the mass balances for solvent and counterions, and the Gauss law, to be solved for the displacement field, the solvent pressure, the counterion concentration, and the electric potential. We have proposed a free energy density encompassing the contributions due to the overall stretching of the membrane, the mixing of solvent and counterions, and the dielectric polarization of the membrane. As for the dissipation, we have accounted for cross-diffusion (Vanag and Epstein, 2009), that is, we have assumed that the (electro)chemical potential gradient of each species influences the flux of every species. Finally, we have modeled the electrodes as perfect electric conductors impermeable to the fluid phase, contributing to the overall bending stiffness of the IPMC.

Our model results in two mutually coupled building blocks, addressing the electrochemistry and the poromechanics of IPMCs. The electrochemistry is described by a Poisson-Nernst-Planck system of equations (Porfiri, 2008), augmented to consider the convective transport of counterions with the solvent, and modified, with respect to its conventional form, by being modulated through finite deformations. The poromechanics relies on Biot theory for saturated media (Biot, 1941), extended to include both the electro-osmotic transport of the solvent and the Maxwell stress. The electrochemistry drives the poromechanical response in actuation; dually, the poromechanics triggers the electrochemical response in sensing. This clearly emerges from the results of the finite element analyses of the proposed theory implemented in the commercial code *COMSOL Multiphysics*®.

More specifically, in actuation the applied voltage drop across the electrodes elicits the migration of counterions toward the cathode; simultaneously, the electro-osmosis of the solvent in the same direction occurs, such that the cathode side swells, while the anode side shrinks. As soon as the solvent pressure gradient increases sufficiently, the solvent starts counter-diffusing, with a consequent relaxation of the bending deformation. Moreover, as the imbalance of ions near the electrodes grows asymmetrically in time (Porfiri et al., 2017), the Maxwell stress is responsible for a time-increasing bending deformation toward the cathode, which can overcome the effect of the solvent pressure and determine a reversal of the curvature (Asaka et al., 1995).

In sensing, the applied mechanical load establishes a solvent pressure gradient along the membrane thickness, which is then progressively dissipated as the solvent diffuses toward the cathode. Correspondingly, counterions move in the same direction by convection with the solvent and diffusion toward regions of larger volume ratio, and electrical charge is stored at the electrodes. When the counterion concentration gradient becomes large enough, counterions start counter-diffusing, with a consequent reduction of the harvested electrical energy, as experimentally observed in Farinholt and Leo (2004).

As a further novelty with respect to IPMC literature, we have described the membrane deformation through a compressible coupled hyperlastic model dependent on both Lamé parameters (Simo and Pister, 1984). We have demonstrated that, for a given shear modulus, the calibration of the first Lamé parameter λ allows one to modulate the entity of the back-relaxation in actuation and of the electric discharge in sensing, whereby larger values of λ emphasize both phenomena. On the one hand, this sheds light on the electrochemo-poromechanics of IPMCs. On the other hand, given the recent advancements in IPMC manufacturing (Carrico et al., 2015), it might provide a criterion for designing and selecting the optimal material for the membrane.

Future work should, first of all, focus on *efficiently* solving meaningful benchmarks governed by the here developed theory in order to quantitatively compare its predictions against *ad hoc* experimental results. In fact, our present finite element implementation in *COMSOL Multiphysics*® is computationally cumbersome and suffers convergence issues if we apply too large loads or set quite extreme values of some parameters, such as the first Lamé constant. Two strategies could be followed to address this issue: developing either an *ad hoc* finite element code or manageable and reliable semi-analytical solutions. Similar tasks have been recently accomplished for the Cha and Porfiri (2014) theory, encompassing a two-dimensional user defined finite element for continuum analysis in *Abaqus*® (Boldini and Porfiri, 2020; Boldini et al., 2020) and enriched structural theories accounting for the through-the-thickness deformation of the membrane and for the IPMC laminate structure, combined with asymptotic methods for the electrochemistry (Leronni and Bardella, 2019; Boldini and Porfiri, 2020; Boldini et al., 2020).

Moreover, in order to accurately predict experimental data, the model should be extended to account for the large variation of material properties due to both the electrode roughness (Porfiri, 2009) and the presence of metal particles in thin membrane regions adjacent to the electrodes, in the literature variously referred to as “intermediate layers” (Tiwari and Kim, 2010), “composite layers” (Cha et al., 2012), and “polymer-metal composite electrodes” (Liu et al., 2019). Accounting for these composite layers, possibly along with the volume occupied by counterions, would mitigate the large gradients of counterion concentration in the boundary layers and the associated high stress concentrations, at the price of additional computational difficulties (Porfiri et al., 2018; Volpini and Bardella, 2021). One would achieve an even more pronounced mitigation if such regions of variable properties were more appropriately modeled as functionally graded materials (Suresh and Mortensen, 1998). Finally, the same goal could be reached also by adopting a constitutive law limiting the maximum mechanical stress, for instance involving viscoplastic deformation (Silberstein and Boyce, 2010); in fact such limitation, by equilibrium, would hamper a too large increase of the Maxwell stress and the solvent pressure, which are proportional to the fluid phase concentration gradient.

Establishing the range of applicability of the present theory would pave the way to elaborate on the main hypotheses the theory relies on. For instance, as a major point, removing the assumption of dilute fluid phase of solvent and counterions might quantitatively impact the predicted response, as IPMC electrochemistry is characterized by a large accumulation of counterions at the cathode. Let us recall that in Cha and Porfiri (2014) theory this effect is prevented by introducing a so-called steric coefficient in the Borukhov-like (Borukhov et al., 2000) mixing free energy density of counterions and polymer chains. Within our framework, removing the dilute solution approximation would require (i) adopting a proper mixing free energy density for a non-ideal solution, (ii) modifying the solvent and counterion fluxes to account for the friction between counterions and polymer network, and (iii) relating the volume ratio to both solvent and counterion concentrations. Finally, let us observe that, to the best of our knowledge, the mixing of solvent molecules and polymer chains has so far been overlooked in IPMC theories. Again, experiments should demonstrate the need for such an addition to the modeling, which is instead a common feature in the literature of polyelectrolyte gels (Hong et al., 2010; Zhang et al., 2020).

Chapter 6

Discussion

In this final chapter on IPMCs, we analyze and compare the electrochemo-mechanical (ECM) and electrochemo-poromechanical (ECPM) theories presented in Secs. 4.2 and 5.2, respectively.

First, we note that the ECM and ECPM theories adopt different strain energy densities. Indeed, the former employs the Saint-Venant–Kirchhoff law (4.8), which, although representing a simple extension of the linear elastic law to large deformations, is convenient to obtain analytical solutions through asymptotic expansions, requiring appropriate linearizations. The latter assumes instead the compressible coupled Neo-Hookean law (5.21), which is expected to be more suitable to study the large deformations experienced by elastomeric materials. However, despite the utilization of different material models, the mechanical free energies enter the ECM and ECPM theories in the same way, as well as the polarization free energies (4.10) and (5.27), the latter resulting in identical expressions for the electric displacement and Maxwell stress in the two theories. The main difference between the ECM and ECPM theories lies instead in the adopted mixing free energies, as discussed in the following.

In the ECM theory, not accounting for the solvent transport, the mixing free energy is expressed as a function of the volume ratio (see Eq. (4.12)). As a result, through Eq. (4.4b), an osmotic stress $\mathbf{P}_{\mathrm{mix}} = -\mathcal{R}T(C - C_0)\mathbf{F}^{-\mathrm{T}}$, dependent on the counterion concentration difference with respect to the initial state $C - C_0$, enters the mechanical equilibrium (4.13a). Therefore, the counterion redistribution is directly responsible of deformation, as the osmotic stress in general needs to be equilibrated by a suitable mechanical stress $\mathbf{P}_{\mathrm{mec}}$.

In the ECPM theory, accounting for the solvent transport, the mixing free energy is instead expressed in terms of the solvent concentration (see Eq. (5.26)). Therefore, the differentiation of the free energy with respect to the deformation gradient does not give rise to an osmotic stress $\mathbf{P}_{\mathrm{mix}}$ entering the mechanical equilibrium (5.2). Instead, the chemical potential of the solvent (5.36), obtained by differentiating the free energy with respect to the solvent concentration, depends on the osmotic pressure $\mathcal{R}TC$, which should therefore be interpreted as a potential for the solvent to move, rather than a pressure in the jargon of solid mechanics.

If then, in the ECPM theory, one assumes that the constituents of the porous material are incompressible and that the fluid phase is dilute, the solvent concentration may be expressed as a function of the volume ratio (see Eq. (5.30)). However, such a constraint introduces another independent variable, namely, a Lagrange multiplier playing the role of solvent pressure (see Eq. (5.29)), for which the solvent mass balance (5.3) should be solved. Notably, the solvent pressure p_w enters both the chemical potential of the solvent (5.36) and the mechanical equilibrium (5.32) through $\mathbf{P}_\mathrm{w}$, the latter replacing the osmotic stress $\mathbf{P}_\mathrm{mix}$ of the ECM theory.

We note that, for a non-dilute solution, the counterion concentration would enter the constraint (5.28). In such a case, the solvent concentration should be expressed as a function of both the volume ratio and the counterion concentration, while the Lagrange multiplier should be interpreted as the solution pressure, where the term *solution* denotes the overall fluid phase.

One could argue that, despite the osmotic pressure enters the solvent chemical potential, it eventually lacks in the solvent flux (5.40a). This is specifically due to accounting for cross-diffusing effects. Indeed, when one assumes that the counterion electrochemical potential affects the solvent flux (Eq. (5.18a)), the osmotic pressure gradient contribution to the solvent flux is automatically replaced by the electro-osmotic contribution, proportional to the product of the counterion concentration and the electric field (Eq. (5.40a)). Specifically, we note that the electro-osmotic flux has exactly the same form of the electrophoretic counterion flux in Eq. (5.40b). Although osmosis and electro-osmosis would provide qualitatively the same effect, they are characterized by different timescales: indeed, osmosis follows ion migration, while electro-osmosis occurs simultaneously with ion migration.

In both the ECM and ECPM theories, the purely diffusive counterion flux, given by Fick's law, actually consists of two contributions: one proportional to the nominal counterion concentration gradient and one to the volume ratio gradient, the latter analogous to the solvent concentration gradient in the ECPM theory (Eqs. (4.13c) and (5.40b)). This represents Fick's law in deformable bodies, whereby both changes in concentration at fixed volume and changes in volume drive the counterion flux. The usage of a Lagrangian finite deformation theory allows one to single out the two contributions, which would instead collapse into a unique term by using the current counterion concentration, as this is expressed per unit deformed volume.

Finally, to summarize, the ECPM theory introduces, with respect to the ECM theory, the explicit modeling of the solvent transport. In both the processes of actuation and sensing, the solvent transport could be regarded as a mediator of the electrochemical and mechanical responses. Indeed, in actuation, the applied electric field triggers, through counterion migration, the transport of the solvent, in turn responsible of the deformation field; conversely, in sensing, the applied mechanical load elicits the solvent transport, the latter determining the counterion redistribution and, therefore, the output of an electric signal. Then, accounting for cross-diffusion allows one to consider further coupling effects, namely, the solvent electro-osmosis and the counterion convection. The ECM theory simply skips the intermediate water transport modeling, by relying, in actuation, on an osmotic stress dependent on the counterion concentration, and, in sensing, on a counterion flux component proportional to the volume ratio gradient.

We remark that in our ECPM model only the mixing of solvent and counterions is considered, while the polymeric solid phase is not considered in the mixing process. In Hong et al. (2010) and Zhang et al. (2020), dealing with the swelling of polyelectrolyte gels, the free energy additionally accounts for the mixing of solvent molecules and polymer macromolecules, by resorting to the Flory-Huggins solution theory (Flory, 1942; Huggins, 1941). Correspondingly, in the same works they identify the reference configuration with the space region occupied by the dry polymer, being mainly interested in the swelling process, while, in our theory, the IPMC membrane is already swollen in the reference configuration.

While the ECM theory could be expanded to account for the counterion finite size by operating directly on the mixing free energy, as for example proposed in Sec. 4.5, the same goal could be reached in the ECPM theory by modifying the constraint (5.28), in order to account for the volume occupied by counterions. In such a case, the solution pressure would also drive the counterion motion, as it would enter the counterion electrochemical potential. As anticipated in Sec. 5.4, considering the counterion volume would also require, first, using a mixing free energy suitable for a non-dilute and non-ideal solution, and, second, accounting for the friction between counterions and polymer network. Notably, this would lead to a quite severe complication of the governing equations, including the introduction of further parameters, namely, the counterion molar volume, the counterion and solvent activity coefficients, and the counterion diffusivity in the porous material, which would become distinct from that in free solution (see equation (126) of Ateshian, 2007).

Ultimately, we point out that the structural model employed in Sec. 4.3 to study the effect of shear on sensing could in principle be employed to study actuation as well. However, its direct usage in actuation may be questionable, as the assumptions of zero mid-axis stretching (underlying Eqs. (4.16)) and, mostly, zero through-the-thickness direct strain are clearly violated by the results of continuum models for IPMCs, as established by both the ECM theory in Boldini and Porfiri (2020) and our ECPM theory (see in particular Figs. 5.8 and 5.12). Recently, an enriched Euler-Bernoulli beam model, accounting for the localized through-the-thickness deformation in the membrane boundary layers, has been successfully applied to study IPMC actuation, though being limited to slender IPMCs with thin electrodes (Boldini et al., 2020). Notably, for such IPMCs, employed in Sec. 5.3, the effect of shear is totally negligible in sensing as well, justifying the interpretation of the results in terms of simple Euler-Bernoulli kinematics.

Part II

Cell clusters

Chapter 7

Introduction

Traditionally, developmental biology has been studied from a genetic and biochemical perspective. Indeed, the pivotal contribution of Turing (1952) proposes that chemical patterns generated through reaction and diffusion of chemical substances instruct embryo development. The work of Wolpert (1969) suggests instead that the concentration gradient of morphogens provides positional information toward cell pattern formation.

However, recent endeavors have documented that, alongside genetic and biochemical cues, bioelectrical and mechanical signaling are important for development (McCaig et al., 2005; Mammoto and Ingber, 2010).

7.1 Developmental endogenous bioelectricity

In this work, consistently with the literature (Levin et al., 2017), we use the term *bioelectricity* to refer to the redistribution of ions, and related membrane potential variations, within a cell cluster. Specifically, ion fluxes lead to membrane *depolarization* or *hyperpolarization*, that is, to *increment* or *decrement* of the membrane potential.

More specifically, we treat *endogenous* bioelectricity, whereby the exchange of ions is triggered by internal factors, such as the spatio-temporal activity of ion channels, and not by external ones, which for instance include the imposition of an electric field. In particular, we remark that we do not deal with neurons or muscle cells, historically associated with ion channels. Rather, we refer to the role of ion channels in the developmental processes undergone by non-excitable cell clusters (Bates, 2015). This justifies the locution *developmental* bioelectricity.

Indeed, it has been shown that, through ion channels and pumps, bioelectricity regulates important developmental processes at the single cell level, such as the progression of the cell cycle and, in particular, the tendency of the cell to proliferate or to differentiate. Moreover, by also taking advantage of the activity of gap junctions, which couple neighboring cells electrically, bioelectricity controls processes at the tissue level, such as embryonic development, symmetry breaking, cancer progression, wound healing, and regeneration. In the following, we provide an overview of relevant discoveries in the field of developmental endogenous bioelectricity. The interested reader may find exhaustive reviews about this topic in McCaig et al. (2005) and Levin et al. (2017).

First of all, bioelectricity is fundamental for the advancement of the cell cycle. Blackiston et al. (2009) argue that *hyperpolarization*, that is, a *decrease* of the membrane potential with respect to the resting value, is required for the initiation of the S phase, in which the DNA is replicated. This hyperpolarization seems to be mainly due to the activation of several families of potassium channels. Conversely, *depolarization*, that is, an *increase* of the membrane potential with respect to the resting value, is necessary for entering the M phase, in which the mother cell undergoes mitosis, that is, it divides into two daughter cells. This depolarization is associated with a reduction in the activity of potassium channels, and a concomitant chloride efflux resulting from the activation of chloride channels.

Consistently with the foregoing considerations, Sundelacruz et al. (2009) advance that hyperpolarized somatic cells tend to be quiescent and to not undergo mitosis. Instead, developing and cancer cells are typically characterized by a depolarized state, thus being highly proliferative.

While proliferation is associated with depolarization, differentiation is paired with hyperpolarization. Indeed, differentiating cells are typically more hyperpolarized than stem cells. The degree of hyperpolarization generally increases with the differentiation time and is specific of the cell lineage into which stem cells are differentiating. For instance, Sundelacruz et al. (2008) show that human mesenchymal stem cells differentiating into either fat or bone are hyperpolarized, and that the hyperpolarization is larger for adipogenic differentiation. Importantly, inducing depolarization by either increasing the EC potassium concentration or blocking the Na^+, K^+-ATPase prevents both adipogenic and osteogenic differentiation.

The bioelectric behavior of the single cell then reflects on the tissue-scale behavior. Regarding tumorigenesis, Chernet and Levin (2013b) show that tumor-like structures induced by human oncogenes in embryos of *Xenopus laevis* may be detected by their characteristic depolarized state, even before these tumors become morphologically apparent. Moreover, they prove that manipulating ion channels in order to hyperpolarize these cells leads to an influx of butyrate through sodium-butyrate exchangers, which in turn suppresses the formation of tumors.

Endogenous bioelectricity seems to be involved in wound healing as well (Nuccitelli, 2003). When a wound occurs, the transepithelial potential is locally disrupted. This results in a local electric field in the epithelium plane, which is directed toward the wound. Notably, many epithelial cells, such as the human keratinocytes of the epidermis, can detect this electric field and migrate along its direction in a process called galvanotaxis, such as to close the wound. It also seems that applying electric fields externally may accelerate the process of wound healing.

Bioelectricity has even implications in tissue regeneration. For instance, manipulating the bioelectric pattern may alter the anterior-posterior polarity of a regenerating planarian (Beane et al., 2011). Typically, the head blastema of a regenerating planarian is characterized by a depolarized state, while the tail blastema is associated with a hyperpolarized state. Suppressing the activity of the H^+, K^+-ATPase in the head blastema through the SCH inhibitor determines a hyperpolarization and hampers the formation of the head, while the opening of the glutamate-gated chloride channel in the tail blastema through the ivermectin activator determines a depolarization and leads to the formation of a head instead of a tail.

The establishment of left-right asymmetry may also be initiated by bioelectricity. Levin et al. (2002) argue that, in early *Xenopus laevis* and chick embryos, the left-right asymmetric activity of the H^+, K^+-ATPase determines a leftward membrane potential gradient, which is responsible of a rightward flux of small positively charged molecules through gap junctions. This flux, in turn, could be the reason for the asymmetric gene expression that leads to left-right asymmetries in the positioning and anatomy of organs.

Importantly, bioelectric signals may also coordinate morphogenetic events at long-range, not only at short-range. In Pai et al. (2015), experimentally disrupting the bioelectric signaling within the developing neural tube region of a *Xenopus laevis* locally alters the apoptosis and proliferation of cells, which results in brain mispatterning. Notably, the normal brain pattern can be restored by fine-tuning the membrane potential field in the ventral non-neural region, that is, at long-range.

The foregoing evidences leave no doubt that bioelectricity is heavily involved in developmental processes. First, the membrane potential qualifies as a useful readout of the biological state of a cell cluster, with depolarization and hyperpolarization generally indicating a propensity to proliferate and to be quiescent, respectively. Second, more importantly, the membrane potential acts as an instructive factor, for example by initiating a biochemical or genetic signaling cascade toward a specific biological goal. Therefore, manipulating ion channels through genetic or pharmacological techniques may be useful for directing pattern formation, reducing cancer progression, accelerating wound closure, and controlling regeneration. Beyond these important implications in biomedicine, the fine-tuning of the bioelectric field is expected to have even stronger impact on the fields of synthetic biology and bioengineering, and especially on the design of soft robots (Mustard and Levin, 2014).

In order to understand the dynamics of bioelectric networks and manipulate them toward the specific desired outcomes, it is necessary to develop quantitative and bio-realistic simulators. Pietak and Levin (2016) have proposed a finite-volume multiphysics simulator written in *Python*™, referred to as the *BioElectric Tissue Simulation Engine* (BETSE), which can be used to compute the bioelectrical fluxes of ions, and related membrane potential changes, in a two-dimensional cell cluster.

In Pietak and Levin (2017), BETSE has been augmented to consider the interplay between genetic, biochemical, and bioelectrical dynamics. This approach has begun to identify interventions controlling complex morphogenesis of whole organs, such as repairing defects in a developing frog brain that would otherwise result from exposure to teratogens (Pai et al., 2018).

7.1.1 Developmental endogenous mechanobioelectricity

Alongside chemical, genetic, and electrical cues, mechanical signals also play a key role in developmental processes. This is confirmed by the emergence of *mechanobiology* as a discipline at the interface between cell biology and cell mechanics (Huang et al., 2012).

The understanding of *mechanotransduction*, which is the conversion of mechanical signals into biochemical responses, is at the core of mechanobiology (Ingber, 2006). Mediators of this process are cellular components such as the cytoskeletal filaments and the cell membrane, membrane components such as ion channels and surface receptors, extracellular matrix components, cell-cell junctions such as cadherins and gap junctions, and cell-extracellular matrix junctions such as integrins and focal adhesions. Importantly, all these components work concertedly within the structural hierarchy of tissues and organs.

Mechanotransduction is crucial during all stages of embryogenesis (Mammoto and Ingber, 2010): in early development, by influencing egg activation, early asymmetric cell divisions, and the establishment of the initial embryonic polarity; in mid-development, by regulating the sorting of progenitor cells, anterior-posterior axis formation, tissue folding, dorsal closure, and the establishment of planar cell polarity; and in later development, orchestrating organogenesis. Mechanotransduction is also important for maintaining tissue homeostasis after the development is completed (Shishvan et al., 2018). Moreover, a wide range of seemingly unrelated diseases are the result of the modification of either cell mechanics, tissue structure, or the activity of mechanotransduction molecules (Ingber, 2003). Cancer itself could be seen as a disease of tissue development often characterized by abnormal mechanotransduction.

Integrating the knowledge of chemical, genetic, electrical, and mechanical signaling pathways might be of great importance for the design of multicellular engineered living systems (Kamm et al., 2018). Although the approaches to developmental biology based on biochemistry and molecular genetics have pervaded the literature in the last century, the important roles of electricity and mechanics have been recognized in the recent years. However, despite the presence of works addressing the interplay between the more established fields of biochemistry and genetics and the avant-gardes of bioelectricity and mechanobiology, the mutual relationship between these last two disciplines has almost never been addressed in a developmental context.

Notably, as argued by Silver and Nelson (2018), bioelectrical and mechanical cues are expected to affect each other. Indeed, on the one hand, the membrane potential and the osmotic pressure are strictly related. Specifically, depolarization is often associated with an influx of sodium, and consequently with an in increase of osmotic pressure; conversely, hyperpolarization typically occurs because of the efflux of potassium, leading to a decrease of osmotic pressure. On the other hand, several ion channels are mechanosensitive, that is, they respond electrically to changes in the membrane mechanics (Martinac, 2004).

Later, Silver et al. (2020) have proved that mechanotransduction may effectively direct the establishment of membrane potential gradients within a tissue. In particular, they show that connexin hemichannels, which are mechanosensitive, preferentially open in the peripheral regions of mammary epithelial tissues, characterized by a higher endogenous mechanical stress, thus leading to local depolarization. This, in turn, is responsible of transcriptional changes that promote cell proliferation.

By following this exciting line of research, to which we refer to by using the term *mechanobioelectricity*, we next explore the interplay between endogenous mechanical and electrical signaling in cell clusters. This task is first accomplished in Ch. 8 by extending the BETSE code, documented in Pietak and Levin (2016), to the realm of mechanics. In Ch. 9, we build a more general theory that further accounts for the modeling of the water flow within the cluster. Chs. 8 and 9 are adapted from Leronni et al. (2020) and Leronni (2020), respectively.

Before starting, in the next Sec. 7.2, we describe in more detail the object of our modeling, that is, the cell cluster and its internal constituents. Then, in Sec. 7.3, we present the classical equations used in cell membrane electrophysiology, which we often refer to throughout our treatment.

7.2 Constituents of cell clusters

With reference to Fig. 7.1, we start by describing the constituents of animal cell clusters relevant for their electrochemo-poromechanical response. These can be subdivided into three broad categories, namely, constituents involved in the mechanics of the cluster (Sec. 7.2.1), constituents acting as a barrier either between the intracellular (IC) and extracellular (EC) spaces of the cluster or between the cluster and the surrounding bath (Sec. 7.2.2), and constituents involved in the bioelectricity of the cluster (Sec. 7.2.3). The interested reader can find additional information on classical books of cell biology, such as Alberts (1983). A good overview of the mechanics of the cytoskeleton and of the cell membrane is given by Huang et al. (2012). Ion channels, at the core of bioelectricity, are thoroughly addressed in Hille (1984).

7.2.1 Cytoskeletal filaments and anchoring junctions

The mechanical behavior of the cluster is essentially established by a polymer network constituted by cytoskeletal filaments and anchoring junctions, similarly to epithelial tissues of animals.

The **cytoskeleton** governs the mechanics of the single cell. It results from the assembly of three interconnected families of protein filaments, namely, actin filaments, microtubules, and intermediate filaments. *Actin filaments* are double-stranded helical polymers with a diameter of $5-9\,\mathrm{nm}$, composed of repeated units of the protein actin. They are highly concentrated in the so-called "cortex" underneath the cell membrane. *Microtubules* are long and hollow cylindrical polymers with a diameter of $25\,\mathrm{nm}$, composed of laterally associated protofilaments of dimers of α- and β-tubulin. They typically depart from a centrosome located in the proximity of the nucleus. *Intermediate filaments* are rope-like polymers with a diameter of $10\,\mathrm{nm}$, composed of a very diversified array of intermediate filament proteins, mainly keratin in epithelial tissues, where they play a key role.

Anchoring junctions mechanically connect the cytoskeletons of different cells one another, thereby allowing the transmission of mechanical stress within the cluster. They are constituted by transmembrane proteins of the cadherin superfamily. They can be subdivided in *adherens junctions*, which connect actin filament bundles, and *desmosomes*, which connect intermediate filaments.

Epithelial sheets are attached to an underneath thin layer of extracellular matrix, referred to as "basal lamina", in turn sitting on the connective tissue. This connection occurs through other types of anchoring junctions, typically constituted by transmembrane proteins of the integrin superfamily, including actin-linked cell-matrix adhesions and hemidesmosomes. However, we remark

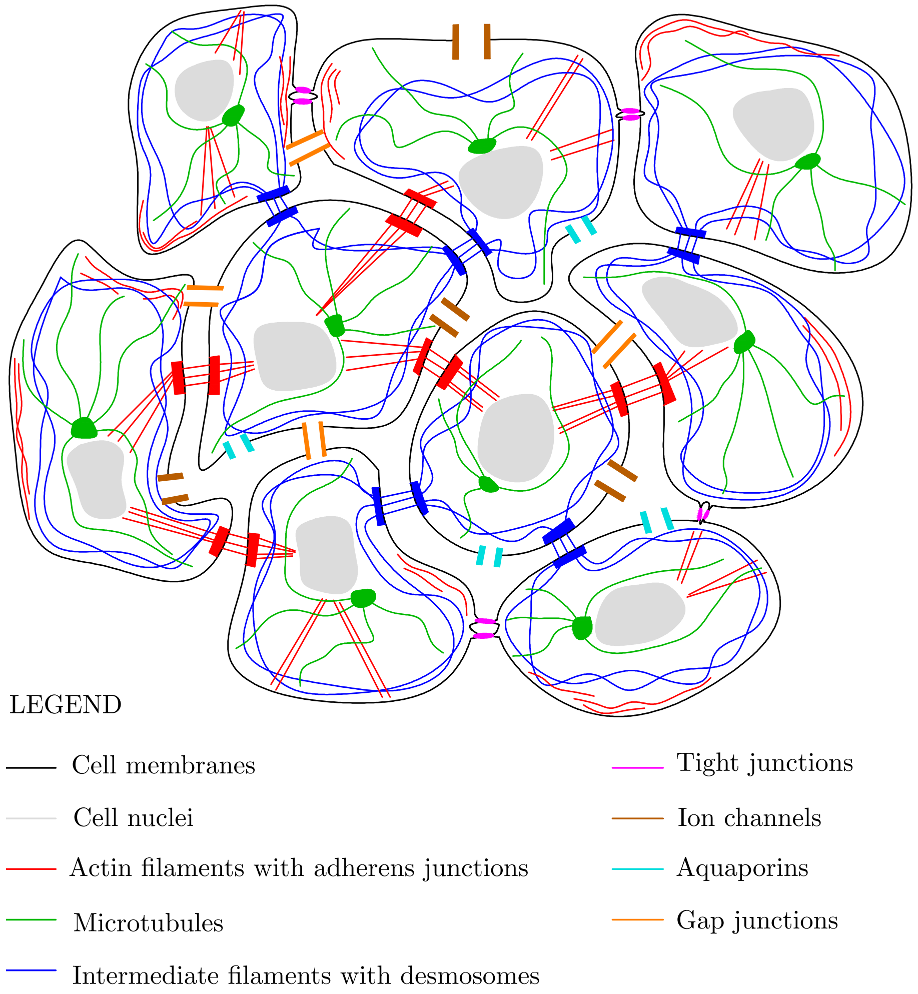

Figure 7.1: Animal cell cluster with the main constituents involved in its electrochemo-poromechanical response.

that, in the present work, we specifically refer to clusters of closely packed cells joined through anchoring junctions, thereby excluding the presence of the underneath extracellular matrix and connective tissue.

In plants, anchoring junctions are replaced by the *cell wall*, surrounding each cell and cementing plant cells one another. The cell wall is typically thick and much stiffer than other cell components. It is composed of a polymer network of cellulose microfibrils and cross-linking glycans, embedded within a matrix of pectin polysaccharides. The polymer lignin is abundant in the secondary cell wall, which stiffens and waterproofs the whole wall.

Since the cytoskeleton, the anchoring junctions of animal cells, and the cell walls of plant cells are all constituted by networks of cross-linked polymer filaments, it is convenient to resort to the well established literature on the constitutive modeling of rubber elasticity (Boyce and Arruda, 2000) to study their macroscopic mechanical behavior.

7.2.2 Cell membranes and tight junctions

We assume that within the cluster, despite the close-packing of the cells, a thin network of EC spaces exists, separating cells one another. The IC and EC spaces are delimited by **cell membranes**. These are essentially constituted by 5 nm-thick lipid bilayers. The most abundant lipid molecules in bilayers are phospholipids, consisting of an hydrophilic head and two hydrophobic tails. Given their structure and composition, they spontaneously arrange into bilayers in aqueous environments, which tend to fold over themselves in order to form sealed compartments. Lipid molecules can freely flow within individual monolayers, thus giving the membrane a fluid-like behavior.

Tissues are characterized by very different IC and EC concentrations of ions. While sodium and chloride are abundant in the EC space, potassium concentration is higher in the IC space, also containing many other fixed anions. This imbalance of ions across the cell membrane sets the *membrane potential*, defined as the difference between the IC and EC electric potentials, whose resting value ranges from $-40\,\mathrm{mV}$ to $-70\,\mathrm{mV}$.

The presence of ions at different concentrations in the IC and EC spaces will require us to treat the IC and EC ion concentrations as independent variables.

Lipid bilayers host a large number of transmembrane proteins, including the cadherins and integrins described before, and those mediating the transport of ions and water molecules between the IC and EC spaces or directly between cells, which are described in the next section. The cell membranes are not significant for the overall mechanical behavior of the cluster. However, the mechanics of the membrane is important for the opening of mechanosensitive ion channels, as illustrated in the next section.

While cell membranes act as selectively permeable barriers between the IC and EC spaces, epithelial sheets behave similarly in separating the fluid bathing their apical side and the connective tissue underlying their basal side. This barrier function is allowed by **tight junctions**, mainly constituted by claudin transmembrane proteins, which seal together neighboring cells, thus preventing the leakage of small molecules in the intercellular spaces (Tsukita et al., 2001). Tight junctions may be differently permeable to distinct ion species and water molecules, and even alter dynamically their permeability.

In our two-dimensional cell clusters, which, differently from epithelia, are not polarized, tight junctions may be present at the cluster boundary, sealing cells one another. We assume that, if present, tight junctions are completely impermeable to the passage of both ions and water.

As the separation of charge across the cell membrane establishes the membrane potential, the separation of charge across tight junctions, that is, in our context, between the interior and the exterior of the cluster, originates the so-called *transepithelial potential*.

7.2.3 Ion channels, aquaporins, and gap junctions

Lipid bilayers are substantially impermeable to ions. Therefore, ion transport across cell membranes is mostly mediated by two classes of transmembrane proteins, namely, channels and pumps.

Ion channels are pore-forming structures for the passive transport of ions, that is, the transport down their electrochemical potential gradient. Ion channels can be non-selective or selective to specific ions, depending on their size and charge. Importantly, ion channels are not always open, but alternate open and closed states. They can be classified according to their gating mechanism: we can distinguish *voltage-gated* channels, which are affected by changes in the membrane potential value, *ligand-gated* channels, which open when a certain molecule binds them intracellularly or extracellularly, and *mechanosensitive* channels, which respond to the mechanics of the cell membrane. Other gating mechanisms have been acknowledged.

Sometimes ion channels can undergo an inactivated state, that is, they remain inactive despite the presence of the opening stimulus. However, in the investigation of Ch. 8, we will restrict our treatment to ion channels modeled as two-state systems, being either open or closed.

In the same Ch. 8, we will particularly focus on **mechanosensitive channels** (MCs), since they are at the core of electrochemo-mechanics, as they convert mechanical stimuli into electrochemical signals (Martinac, 2004). In particular, it seems that most MCs respond directly to the membrane tension, which can be produced, for instance, by little differences in the transmembrane osmolarity, or by shear stresses due to fluid flow. Other MCs are supposed to be tethered to cytoskeletal or extracellular matrix proteins, whose deflection causes the opening of the channel. The first MC that has been studied at a molecular level is the large-conductance MC in bacteria, which mainly works as a safety valve to prevent bacterial cells from bursting when facing hypotonic environments. MCs are also abundant in eukaryotic cells. Important families of eukaryotic MCs are the potassium-selective TREK and TRAAK channels, and the more recently discovered cation non-selective PIEZO channels (Coste et al., 2010). The functions performed by eukaryotic MCs are much more diversified than those of prokaryotic MCs, and their understanding is at its dawn.

Ions are also actively transported across the cell membrane through ion pumps, though at slower rates. Active transport occurs up the electrochemical potential gradient of ions, thus requiring energy to be carried out. The energy source can be provided by the passive transport of another ion, by the ATP hydrolysis, or by light. A remarkable example of an ATP-driven ion pump is the well-known sodium-potassium pump, also known as Na^+, K^+-ATPase, which mainly works to reestablish the resting concentrations of sodium and potassium in the IC and EC spaces, and consequently the resting membrane potential.

We note that, in this investigation, we limit our attention to passive species transport, thereby not accounting for ion pumps.

Although the cell membrane is more permeable to water than to ions, the transmembrane transport of water is facilitated by the presence of specific channel proteins called **aquaporins** (Verkman and Mitra, 2000; Agre, 2006). These allow the rapid passage of water molecules in a single row by osmosis, and are completely impermeable to ions. Typically, their density on the cell membrane is much larger than that of ion channels. Moreover, different from ion channels, aquaporins are usually always open, though mechanisms of regulation have also been acknowledged.

Finally, **gap junctions** are channels directly connecting two adjacent cells, allowing the direct passage of ions from cell to cell (Goodenough and Paul, 2009). They are constituted by two connexons joined across the intercellular space. Differently from ion channels, gap junctions are not selective to specific ions. More precisely, any water-soluble molecule up to a certain size or mass can permeate through gap junctions. Water molecules themselves are allowed to pass through gap junctions (Gao et al., 2011). Importantly, like ion channels, gap junctions can also alternate between open and closed states, depending on different stimuli. The presence of gap junctions is fundamental in cell clusters, as it allows the electrochemical coupling among cells.

In plants, *plasmodesmata* directly connect the cytoplasms of two adjacent cells, forming pore-like structures that cross the thick cell walls separating cells. Although they are structurally different from the gap junctions of animal cells, they perform the same functions and possess similar properties.

7.3 The Goldman-Hodgkin-Katz equations

In electrophysiology, the transmembrane ion fluxes and the membrane potential are classically described by the Goldman-Hodgkin-Katz flux and voltage equations (Hille, 1984).

The Goldman-Hodgkin-Katz flux equation gives the transmembrane flux $J_{\mathrm{i}}^{\mathrm{m}}$ of an ion i as a function of the membrane potential ψ^{m} and of the intracellular and extracellular ion concentrations c_{i} and $c_{\mathrm{i}}^{\mathrm{e}}$. It reads

$$J_{\mathrm{i}}^{\mathrm{m}} = \frac{z_{\mathrm{i}} F}{\mathcal{R} T} \frac{D_{\mathrm{i}}^{\mathrm{m}}}{t^{\mathrm{m}}} \psi^{\mathrm{m}} \frac{c_{\mathrm{i}} - c_{\mathrm{i}}^{\mathrm{e}} \exp\left(-\dfrac{z_{\mathrm{i}} F}{\mathcal{R} T}\psi^{\mathrm{m}}\right)}{1 - \exp\left(-\dfrac{z_{\mathrm{i}} F}{\mathcal{R} T}\psi^{\mathrm{m}}\right)}, \tag{7.1}$$

where z_{i} is the ion valency, F is the Faraday constant, $\mathcal{R}$ is the gas constant, T is the absolute temperature, $D_{\mathrm{i}}^{\mathrm{m}}$ is the ion transmembrane diffusivity, and t^{m} is the membrane thickness. The Goldman-Hodgkin-Katz flux equation is obtained from the one-dimensional Nernst-Planck equation (Rubinstein, 1990) written along the membrane thickness, by assuming steady state conditions and uniform electric field.

In general, different ion species contribute to the membrane potential, such that a flux of the type (7.1) can be written for each ion species. By imposing that the *net* electric current density across the cell membrane is zero, that is, $F \sum_{\mathrm{i}} z_{\mathrm{i}} J_{\mathrm{i}}^{\mathrm{m}} = 0$, and solving for ψ_{m}, one obtains the Goldman-Hodgkin-Katz voltage equation (also simply known as Goldman equation). By only considering monovalent ions, it reads

$$\psi^{\mathrm{m}} = \frac{RT}{F} \ln \frac{\sum_{\mathrm{i}+} D_{\mathrm{i}+}^{\mathrm{m}} c_{\mathrm{i}+}^{\mathrm{e}} + \sum_{\mathrm{i}-} D_{\mathrm{i}-}^{\mathrm{m}} c_{\mathrm{i}-}}{\sum_{\mathrm{i}+} D_{\mathrm{i}+}^{\mathrm{m}} c_{\mathrm{i}+} + \sum_{\mathrm{i}-} D_{\mathrm{i}-}^{\mathrm{m}} c_{\mathrm{i}-}^{\mathrm{e}}}, \tag{7.2}$$

where $c_{\mathrm{i}+}$ and $c_{\mathrm{i}+}^{\mathrm{e}}$ are the intracellular and extracellular concentrations of cations, $c_{\mathrm{i}-}$ and $c_{\mathrm{i}-}^{\mathrm{e}}$ are the intracellular and extracellular concentrations of anions, and $D_{\mathrm{i}+}^{\mathrm{m}}$ and $D_{\mathrm{i}-}^{\mathrm{m}}$ are the transmembrane diffusivities of cations and anions.

We note that, for Eq. (7.2) to hold, it is not necessary that each individual ion flux is zero, but only the net current. However, at equilibrium, each individual ion flux is balanced by an active contribution due to ion pumps, such that the individual ion concentrations are approximately constant. Finally, if a single ion species is transported across the membrane, the Goldman equation reduces to the standard Nernst equation of electrochemistry (Bard and Faulkner, 2001):

$$\psi^{\mathrm{m}} = \frac{RT}{z_{\mathrm{i}}F} \ln \frac{c_{\mathrm{i}}^{\mathrm{e}}}{c_{\mathrm{i}}} \, . \tag{7.3}$$

We remark that, according to the Goldman-Hodgkin-Katz formalism, the driving forces for the transmembrane ion transport are the ion concentration gradients and the electric field only, thus neglecting, for example, the potential role of intracellular and extracellular water concentrations and membrane mechanics.

Chapter 8

On the coupling of mechanics with bioelectricity and its role in morphogenesis

This chapter is adapted from “Leronni et al. (2020), On the coupling of mechanics with bioelectricity and its role in morphogenesis, *Journal of the Royal Society Interface*, 17(167):20200177”.

8.1 Introduction

In order to numerically address the coupling between mechanical and bioelectrical signaling, here we endow the *BioElectric Tissue Simulation Engine* (BETSE), introduced in Pietak and Levin (2016), with a solid mechanics module.

Our effort is motivated by the arguments advanced in Silver and Nelson (2018), and inspired by recent theories coupling electro-diffusion and elasticity (Hong et al., 2010; Cha and Porfiri, 2014). These theories have been fostered by the emergence of soft smart materials for actuation and sensing in robotics and biomedicine (Trivedi et al., 2008; Kim et al., 2013; Rus and Tolley, 2015).

Specifically, first, the imbalance of charge and ion concentrations within the cluster is expected to generate electrostatic and osmotic forces, impacting its mechanical behavior. By resorting to the soft robotics terminology, cells are *actuated* by endogenous bioelectricity.

Moreover, cells *sense* mechanical stimuli through several molecular structures

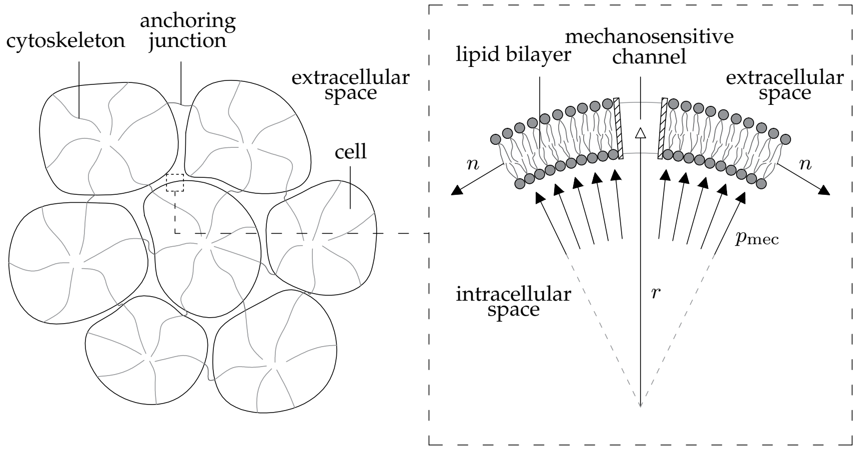

Figure 8.1: Cell cluster (left) and equilibrium of a membrane patch (right).

(Ingber, 2006). Here, we account for mechanosensitive ion channels (MCs), whose activation depends on the membrane mechanics (Martinac, 2004), where larger tension increases the opening probability (Wiggins and Phillips, 2004). This, in turn, alters transmembrane ion fluxes, and consequently the membrane potential. Ultimately, the latter qualifies both as an instructor and as a readout of the mechanical state of the cluster.

We detail the modeling and implementation in BETSE of the foregoing mechanisms of actuation and sensing in cell clusters in Secs. 8.2 and 8.3, respectively. Then, in Sec. 8.4, we employ the augmented BETSE code, referred to as "mecBETSE",[1] to explore possible feedback loops triggered by osmotic pressure and MCs in morphogenesis.

This investigation represents a first step toward a rigorous integration of bioelectricity with mechanobiology. Such integration has the potential to help understanding embryogenesis, control of regeneration, and the transformation toward, or normalization of, cancer (Chernet and Levin, 2013a; Mathews and Levin, 2018). In the long term, unveiling the multiscale interconnections of electrostatic, osmotic, and mechanical signals may be of great importance for the design of engineered living systems (Kamm et al., 2018).

8.2 *Bio-actuation*: how bioelectrical forces shape the multicellular mechanical response

We consider a cluster of closely packed cells, as depicted in Fig. 8.1. Ion channels allow for ion transport between the intracellular space and the thin extracellular

---

[1] The mecBETSE code is freely available at `https://gitlab.com/betse/mecbetse`.

space separating neighboring cells. Ion fluxes also occur freely in the extracellular space, which is connected to a bath surrounding the cluster. Here, we focus on the *physical* role of ions as carriers of charge and mass (thus disregarding any chemical processes they could be involved in) through the Nernst-Planck description of ion electro-diffusion (Pietak and Levin, 2016).

We assume for the cluster mechanics a Cauchy continuum description, and neglect the thin extracellular space in evaluating the electrostatic and osmotic forces exchanged by cells. Since the timescale associated with ion transport is much longer than that to achieve mechanical equilibrium (Gurtin et al., 2010), we neglect inertial effects in the linear momentum balance, which, in the absence of body forces, reads

$$\operatorname{div}\boldsymbol{\sigma} = \mathbf{0}\,, \tag{8.1}$$

where div and $\boldsymbol{\sigma}$ denote the divergence operator and the stress tensor, respectively. In the framework for synthetic materials that inspired us (Cha and Porfiri, 2014) $\boldsymbol{\sigma}$ could be regarded as a *total* stress, consisting of several contributions:

$$\boldsymbol{\sigma} = \boldsymbol{\sigma}_{\mathrm{mec}} + \boldsymbol{\sigma}_{\mathrm{pol}} + \boldsymbol{\sigma}_{\mathrm{mix}}\,, \tag{8.2}$$

with $\boldsymbol{\sigma}_{\mathrm{mec}}$, $\boldsymbol{\sigma}_{\mathrm{pol}}$, and $\boldsymbol{\sigma}_{\mathrm{mix}}$ respectively denoting mechanical, electrostatic, and osmotic stresses, ensuing from contributions to the free energy density due to mechanical deformation, dielectric polarization, and ion mixing.

In this first contribution on the interaction between bioelectricity and mechanobiology, we assume isotropic linear elasticity within a small deformation framework, such that the mechanical stress reads

$$\boldsymbol{\sigma}_{\mathrm{mec}} = 2G\boldsymbol{\varepsilon} + \lambda(\operatorname{tr}\boldsymbol{\varepsilon})\mathbf{I}\,, \tag{8.3}$$

where $G = E/[2(1+\nu)]$ and $\lambda = E\nu/[(1+\nu)(1-2\nu)]$ are the Lamé parameters (with E the Young modulus and ν the Poisson ratio), tr denotes the trace operator, $\mathbf{I}$ is the second-order identity tensor, and $\boldsymbol{\varepsilon}$ is the small strain tensor, which in turn is given by

$$\boldsymbol{\varepsilon} = \frac{1}{2}\left[(\operatorname{grad}\mathbf{u}) + (\operatorname{grad}\mathbf{u})^{\mathrm{T}}\right]\,, \tag{8.4}$$

with grad and $\mathbf{u}$ denoting the gradient operator and the displacement vector, respectively. Henceforth, we consider spatially uniform elastic moduli, referring to the *effective* behavior of closely packed cells of given cytoskeleton and anchoring junctions.

For an isotropic linear dielectric, the electrostatic (or Maxwell) stress reads

(Dorfmann and Ogden, 2017)

$$\boldsymbol{\sigma}_{\text{pol}} = \varepsilon_0 \left[\varepsilon_{\text{r}} \mathbf{e} \otimes \mathbf{e} - \frac{1}{2} (\mathbf{e} \cdot \mathbf{e}) \mathbf{I} \right] , \tag{8.5}$$

in which $\otimes$ and $\cdot$ indicate the tensor and inner products respectively, ε_0 and ε_{r} are the vacuum and relative permittivities, and $\mathbf{e} = -\text{grad}\,\psi$ is the electric field, with ψ denoting the electric potential. We consider the electrostatic stress across neighboring membranes only, because elsewhere the electric field is irrelevant (Pietak and Levin, 2016).

For suitably small ion concentrations the osmotic stress is linear (Gurtin et al., 2010):

$$\boldsymbol{\sigma}_{\text{mix}} = -\mathcal{R}T \sum_{\text{i}} (c_{\text{i}} - c_{\text{i}}^0) \mathbf{I} = -\mathcal{R}T (c - c^0) \mathbf{I} = -p_{\text{mix}} \mathbf{I} , \tag{8.6}$$

in which $\mathcal{R}$ is the gas constant, T is the absolute temperature, c_{i} is the intracellular concentration of the ion species i, and c is the sum of the intracellular ion concentrations (that is, the osmotic concentration), with c_{i}^0 and c^0 their spatially uniform initial values; finally, p_{mix} represents the osmotic pressure.

We disregard the explicit modeling of the water flow allowed by aquaporins (Agre, 2006), whereby this is *phenomenologically* described by $\boldsymbol{\sigma}_{\text{mix}}$, which is, as $\boldsymbol{\sigma}_{\text{pol}}$, an *active* stress to be equilibrated by $\boldsymbol{\sigma}_{\text{mec}}$ through Eq. (8.1), thus coupling bioelectricity and mechanics.

Under small strains, we are able to compute the electrostatic and osmotic stresses in terms of membrane potential and ion concentrations. Then, we introduce the electrostatic and osmotic body forces $\mathbf{f}_{\text{pol}} = \text{div}\,\boldsymbol{\sigma}_{\text{pol}}$ (Dorfmann and Ogden, 2017) and $\mathbf{f}_{\text{mix}} = \text{div}\,\boldsymbol{\sigma}_{\text{mix}}$, such that

$$\mathbf{f} = \mathbf{f}_{\text{pol}} + \mathbf{f}_{\text{mix}} = \text{div}(\boldsymbol{\sigma}_{\text{pol}} + \boldsymbol{\sigma}_{\text{mix}}) \tag{8.7}$$

and equilibrium (8.1) becomes

$$\text{div}\,\boldsymbol{\sigma}_{\text{mec}} + \mathbf{f} = \mathbf{0} . \tag{8.8}$$

By combining Eqs. (8.3), (8.4), and (8.8) we obtain the following Cauchy-Navier equations, accounting for bioelectrical phenomena:

$$\text{div} \left[G\,\text{grad}\,\mathbf{u} + G(\text{grad}\,\mathbf{u})^{\text{T}} + \lambda(\text{div}\,\mathbf{u})\mathbf{I} \right] + \mathbf{f}(\mathbf{e}, c) = \mathbf{0} . \tag{8.9}$$

We refer to the in-plane behavior of a monolayer of cells, and assume that its mechanics is adequately described by either *plane stress* or *plane strain* states, whereby the real scenario lies in between. Hence, Eq. (8.9) consists of two coupled equations, to be solved in terms of $\mathbf{f}$ for the in-plane displacement components u_x and u_y.

Since electro-diffusion is time-dependent, $\mathbf{f}$ varies in time, leading to a time-varying mechanical response. We adopt a partly explicit time-integration scheme in which, at each step, we compute the displacement increment from Eq. (8.9) by evaluating $\mathbf{f}$ as a function of $\mathbf{e}$ and c at the beginning of the step; then, we employ the mechanical fields to update the bioelectrical fields at the following step, as illustrated in Sec. 8.3.

Eq. (8.9) needs boundary conditions, which could be either kinematic:

$$\mathbf{u} = \bar{\mathbf{u}} \quad \text{on } S_{\mathrm{u}} \,, \tag{8.10}$$

with $\bar{\mathbf{u}}$ denoting the imposed displacement, or static:

$$\mathbf{t}_{\mathrm{mec}} = \boldsymbol{\sigma}_{\mathrm{mec}} \mathbf{n} = \bar{\mathbf{t}}_{\mathrm{mec}} \quad \text{on } S_{\mathrm{t}} \,, \tag{8.11}$$

with $\bar{\mathbf{t}}_{\mathrm{mec}}$ denoting the imposed mechanical traction. In Eqs. (8.10) and (8.11) S_{u} and S_{t} are complementary parts of the total boundary S. In this investigation we restrict attention to homogeneous mechanical boundary conditions, implying either $\bar{\mathbf{u}} = \mathbf{0}$ or $\bar{\mathbf{t}}_{\mathrm{mec}} = \mathbf{0}$, which are suitable for a cluster surrounded by a relatively stiff or compliant environment, respectively.

The finite volume discretization of Eq. (8.9) in BETSE is detailed in the next Sec. 8.2.1 for the interested reader.

8.2.1 The finite volume discretization of the Cauchy-Navier equations†

We discretize Eq. (8.9) through the finite volume method (Schäfer, 2006; Quarteroni, 2009), by assuming that each biological cell occupies a finite domain of polygonal shape, and undergoes uniform displacements, strains, and stresses. Although in the simulations in the main article we consider a regular hexagonal grid, here we present a more generic discretization also suitable for an irregular grid. We remark that cells are actually separated by thin extracellular spaces allowing transmembrane ion transport; however, we assume that a reliable *overall* mechanical response can be obtained by neglecting these extracellular spaces in solving Eq. (8.9).

For a plane mechanical problem, Eq. (8.9) is equivalent to the following system of equations:

$$\operatorname{div}\left[G \operatorname{grad} u_x + G\,\mathbf{u}_{,x} + \tilde{\lambda}(\operatorname{div}\mathbf{u})\mathbf{i}\right] + f_x = 0 \,, \tag{8.12a}$$

$$\operatorname{div}\left[G \operatorname{grad} u_y + G\,\mathbf{u}_{,y} + \tilde{\lambda}(\operatorname{div}\mathbf{u})\mathbf{j}\right] + f_y = 0 \,, \tag{8.12b}$$

in which $\mathbf{u}_{,x} = \partial\mathbf{u}/\partial x$, $\mathbf{u}_{,y} = \partial\mathbf{u}/\partial y$, $\mathbf{i}$ is the unit vector in the x-direction, and $\mathbf{j}$ is the unit vector in the y-direction. Under plane strain conditions

$$\tilde{\lambda} = \lambda = \frac{E\nu}{(1+\nu)(1-2\nu)}\,, \tag{8.13}$$

whereas under plane stress conditions

$$\tilde{\lambda} = \frac{E\nu}{1-\nu^2}\,. \tag{8.14}$$

Integral form of the Cauchy-Navier equations

We write Eqs. (8.12) in integral form for each cell of the cluster. We refer to the generic cell m, with $m = 1, ..., M$ and M the number of cells in the cluster. Upon applying the divergence theorem, we obtain

$$\int_{\partial V_m} \Big[G\, \mathrm{grad}\, u_x + G\, \mathbf{u}_{,x} + \tilde{\lambda}(\mathrm{div}\, \mathbf{u})\mathbf{i}\Big] \cdot \mathbf{n}\, \mathrm{d}A + \int_{V_m} f_x\, \mathrm{d}V = 0\,, \tag{8.15a}$$

$$\int_{\partial V_m} \Big[G\, \mathrm{grad}\, u_y + G\, \mathbf{u}_{,y} + \tilde{\lambda}(\mathrm{div}\, \mathbf{u})\mathbf{j}\Big] \cdot \mathbf{n}\, \mathrm{d}A + \int_{V_m} f_y\, \mathrm{d}V = 0\,, \tag{8.15b}$$

where V_m is the space region occupied by the cell m, ∂V_m is its boundary, and $\mathbf{n}$ is the outward unit normal to ∂V_m.

Since we model cells as polygons (in particular, as hexagons), the surface integrals in Eqs. (8.15) can be split in the sum of the integrals over the cell faces:

$$\sum_{n=1}^{N_m} \int_{\partial V_{mn}} \Big[G(\mathrm{grad}\, u_x \cdot \mathbf{n}^{mn}) + G(\mathbf{u}_{,x} \cdot \mathbf{n}^{mn}) + \tilde{\lambda}(\mathrm{div}\, \mathbf{u})(\mathbf{i} \cdot \mathbf{n}^{mn})\Big]\, \mathrm{d}A + \int_{V_m} f_x\, \mathrm{d}V = 0\,, \tag{8.16a}$$

$$\sum_{n=1}^{N_m} \int_{\partial V_{mn}} \Big[G(\mathrm{grad}\, u_y \cdot \mathbf{n}^{mn}) + G(\mathbf{u}_{,y} \cdot \mathbf{n}^{mn}) + \tilde{\lambda}(\mathrm{div}\, \mathbf{u})(\mathbf{j} \cdot \mathbf{n}^{mn})\Big]\, \mathrm{d}A + \int_{V_m} f_y\, \mathrm{d}V = 0\,, \tag{8.16b}$$

with N_m being the number of faces of the cell m, $\partial V_m = \bigcup_{n=1}^{N_m} \partial V_{mn}$, and ∂V_{mn} denoting the region occupied by the face n of the cell m, of area A_{mn} and outward unit normal $\mathbf{n}^{mn}$ (spatially uniform along each cell face). We note that, in this two-dimensional problem, volume integrals become surface integrals, and surface integrals become line integrals, linearly weighed by the thickness along the z-direction.

Discretization

We now introduce appropriate numerical schemes to evaluate the integrals and the derivatives. By adopting the mid-point rule for the integrals, we obtain

$$\sum_{n=1}^{N_m} \Big[G(\mathrm{grad}\, u_x)^{mn} \cdot \mathbf{n}^{mn} + G(\mathbf{u}_{,x})^{mn} \cdot \mathbf{n}^{mn} + \tilde{\lambda}(\mathrm{div}\,\mathbf{u})^{mn}(\mathbf{i} \cdot \mathbf{n}^{mn}) \Big]\, A_{mn} \\ + f_x^m\, V_m = 0\,, \tag{8.17a}$$

$$\sum_{n=1}^{N_m} \Big[G(\mathrm{grad}\, u_y)^{mn} \cdot \mathbf{n}^{mn} + G(\mathbf{u}_{,y})^{mn} \cdot \mathbf{n}^{mn} + \tilde{\lambda}(\mathrm{div}\,\mathbf{u})^{mn}(\mathbf{j} \cdot \mathbf{n}^{mn}) \Big]\, A_{mn} \\ + f_y^m\, V_m = 0\,, \tag{8.17b}$$

where the superscript mn means "evaluated in the mid-point of the face n of the cell m", whereas the superscript m means "evaluated in the center of the cell m". More explicitly, we have:

$$\sum_{n=1}^{N_m} \big[G(u_{x,x}^{mn} n_x^{mn} + u_{x,y}^{mn} n_y^{mn}) + G(u_{x,x}^{mn} n_x^{mn} + u_{y,x}^{mn} n_y^{mn}) \\ + \tilde{\lambda}(u_{x,x}^{mn} n_x^{mn} + u_{y,y}^{mn} n_x^{mn}) \big]\, A_{mn} + f_x^m\, V_m = 0\,, \tag{8.18a}$$

$$\sum_{n=1}^{N_m} \big[G(u_{y,x}^{mn} n_x^{mn} + u_{y,y}^{mn} n_y^{mn}) + G(u_{x,y}^{mn} n_x^{mn} + u_{y,y}^{mn} n_y^{mn}) \\ + \tilde{\lambda}(u_{x,x}^{mn} n_y^{mn} + u_{y,y}^{mn} n_y^{mn}) \big]\, A_{mn} + f_y^m\, V_m = 0\,, \tag{8.18b}$$

and, after a convenient re-arrangement, we obtain

$$\sum_{n=1}^{N_m} \Big[(\tilde{\lambda} + 2G) u_{x,x}^{mn} n_x^{mn} + G\, u_{x,y}^{mn} n_y^{mn} + G\, u_{y,x}^{mn} n_y^{mn} + \tilde{\lambda} u_{y,y}^{mn} n_x^{mn} \Big]\, A_{mn} + f_x^m\, V_m = 0\,, \tag{8.19a}$$

$$\sum_{n=1}^{N_m} \Big[(\tilde{\lambda} + 2G) u_{y,y}^{mn} n_y^{mn} + G\, u_{x,y}^{mn} n_x^{mn} + G\, u_{y,x}^{mn} n_x^{mn} + \tilde{\lambda} u_{x,x}^{mn} n_y^{mn} \Big]\, A_{mn} + f_y^m\, V_m = 0\,. \tag{8.19b}$$

To approximate the derivatives at mn, we resort to the local reference system ξ_{mn}, η_{mn}, represented for regular and non-regular grids in Fig. 8.2. This reference system is such that ξ_{mn} connects the centers of the cells m and n, whereas η_{mn} is aligned with the face mn. The axis ξ_{mn} is directed from the cell m to the cell n and, by counterclockwise numbering the cells surrounding the cell m, the axis η_{mn} is directed from the cell $n-1$ to the cell $n+1$, when there is no jump in numbering. We remark that, for a regular (hexagonal) grid, ξ_{mn} is normal to the face n, such that ξ_{mn} and η_{mn} define an orthogonal reference system. In general, this is not the case for a non-regular

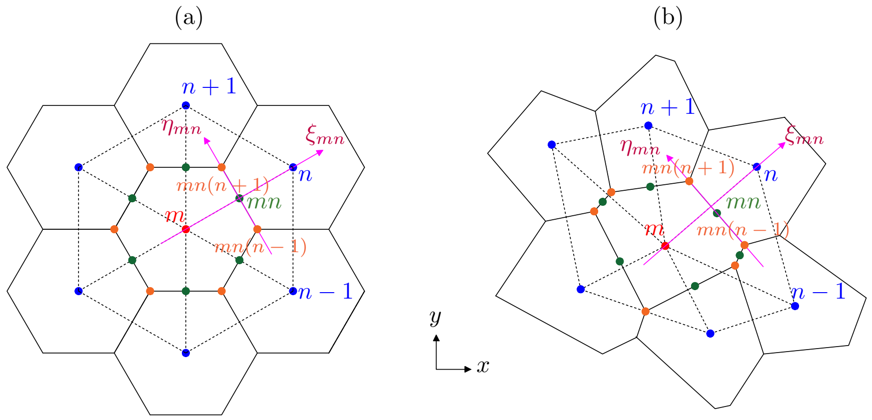

Figure 8.2: Regular (a) and non-regular (b) grids with the local reference system ξ_{mn} , η_{mn}.

grid.

The derivatives of u_i (with $i = x, y$) with respect to ξ_{mn} and η_{mn} can be expressed, through the chain rule, as follows:

$$\begin{bmatrix} u_{i,\xi}^{mn} \\ \\ u_{i,\eta}^{mn} \end{bmatrix} = \underbrace{\begin{bmatrix} x_{,\xi}^{mn} & y_{,\xi}^{mn} \\ \\ x_{,\eta}^{mn} & y_{,\eta}^{mn} \end{bmatrix}}_{\underline{\underline{J}}^{mn}} \begin{bmatrix} u_{i,x}^{mn} \\ \\ u_{i,y}^{mn} \end{bmatrix} , \tag{8.20}$$

in which $\underline{\underline{J}}^{mn}$ is the Jacobian matrix of the coordinate transformation. By inverting $\underline{\underline{J}}^{mn}$, we find the desired expressions for $u_{i,x}^{mn}$ and $u_{i,y}^{mn}$:

$$\begin{bmatrix} u_{i,x}^{mn} \\ \\ u_{i,y}^{mn} \end{bmatrix} = \frac{1}{J^{mn}} \begin{bmatrix} y_{,\eta}^{mn} & -y_{,\xi}^{mn} \\ \\ -x_{,\eta}^{mn} & x_{,\xi}^{mn} \end{bmatrix} \begin{bmatrix} u_{i,\xi}^{mn} \\ \\ u_{i,\eta}^{mn} \end{bmatrix} , \tag{8.21}$$

where $J^{mn} = \det \underline{\underline{J}}^{mn} = x_{,\xi}^{mn} y_{,\eta}^{mn} - x_{,\eta}^{mn} y_{,\xi}^{mn}$. We approximate the metric quantities as

$$x_{,\xi}^{mn} \approx \frac{x^n - x^m}{\xi^n - \xi^m} , \qquad y_{,\xi}^{mn} \approx \frac{y^n - y^m}{\xi^n - \xi^m} , \tag{8.22a}$$

$$x_{,\eta}^{mn} \approx \frac{x^{mn(n+1)} - x^{mn(n-1)}}{\eta^{mn(n+1)} - \eta^{mn(n-1)}} , \qquad y_{,\eta}^{mn} \approx \frac{y^{mn(n+1)} - y^{mn(n-1)}}{\eta^{mn(n+1)} - \eta^{mn(n-1)}} , \tag{8.22b}$$

where the superscripts $mn(n+1)$ and $mn(n-1)$ indicate the vertexes in common among cells m, n, $n+1$ and m, n, $n-1$ (see Fig. 8.2). In the case of a regular (hexagonal) grid, $\underline{\underline{J}}^{mn}$ describes the usual transformation rule for vector components between orthogonal reference systems, Eqs. (8.22) are exact, and $J^{mn} = 1$. We approximate the displacement derivatives $u_{i,\xi}^{mn}$ and $u_{i,\eta}^{mn}$ through the central finite difference scheme:

$$u_{i,\xi}^{mn} \approx \frac{u_i^n - u_i^m}{\xi^n - \xi^m} , \tag{8.23a}$$

$$u_{i,\eta}^{mn} \approx \frac{u_i^{mn(n+1)} - u_i^{mn(n-1)}}{\eta^{mn(n+1)} - \eta^{mn(n-1)}} \,. \tag{8.23b}$$

However, the displacement components in the vertexes are not the unknowns of the problem; hence, we approximate them through the average of the corresponding values in the surrounding cell centers:

$$u_i^{mn(n+1)} \approx \frac{u_i^m + u_i^n + u_i^{n+1}}{3} \,, \tag{8.24a}$$

$$u_i^{mn(n-1)} \approx \frac{u_i^m + u_i^n + u_i^{n-1}}{3} \,. \tag{8.24b}$$

For a non-regular grid, the terms in Eqs. (8.24) should be weighed through the relative distances between vertexes and centers. By substituting Eqs. (8.24) into Eq. (8.23b), we obtain

$$u_{i,\eta}^{mn} \approx \frac{(u_i^{n+1} - u_i^{n-1})/3}{\eta^{mn(n+1)} - \eta^{mn(n-1)}} \,. \tag{8.25}$$

Finally, by replacing Eqs. (8.22), (8.23a), and (8.25) into Eq. (8.21), we get

$$u_{i,x}^{mn} = \frac{(y^{mn(n+1)} - y^{mn(n-1)})(u_i^n - u_i^m) - (y^n - y^m)(u_i^{n+1} - u_i^{n-1})/3}{(x^n - x^m)(y^{mn(n+1)} - y^{mn(n-1)}) - (y^n - y^m)(x^{mn(n+1)} - x^{mn(n-1)})} \,, \tag{8.26a}$$

$$u_{i,y}^{mn} = \frac{-(x^{mn(n+1)} - x^{mn(n-1)})(u_i^n - u_i^m) + (x^n - x^m)(u_i^{n+1} - u_i^{n-1})/3}{(x^n - x^m)(y^{mn(n+1)} - y^{mn(n-1)}) - (y^n - y^m)(x^{mn(n+1)} - x^{mn(n-1)})} \,, \tag{8.26b}$$

where it is clear that in the approximation of the derivatives of the displacement components at mn also the cells $n+1$ and $n-1$ are involved, even in the case of a regular grid. Substitution in Eqs. (8.19) leads to

$$\begin{aligned}
&\sum_{n=1}^{N_m} \Big[(x^n - x^m)(y^{mn(n+1)} - y^{mn(n-1)}) - (y^n - y^m)(x^{mn(n+1)} - x^{mn(n-1)})\Big]^{-1} \\
&\Big\{(\tilde{\lambda} + 2G)\big[(y^{mn(n+1)} - y^{mn(n-1)})(u_x^n - u_x^m) - (y^n - y^m)(u_x^{n+1} - u_x^{n-1})/3\big] n_x^{mn} \\
&\quad + G\big[-(x^{mn(n+1)} - x^{mn(n-1)})(u_x^n - u_x^m) + (x^n - x^m)(u_x^{n+1} - u_x^{n-1})/3\big] n_y^{mn} \\
&\quad + G\big[(y^{mn(n+1)} - y^{mn(n-1)})(u_y^n - u_y^m) - (y^n - y^m)(u_y^{n+1} - u_y^{n-1})/3\big] n_y^{mn} \\
&+ \tilde{\lambda}\big[-(x^{mn(n+1)} - x^{mn(n-1)})(u_y^n - u_y^m) + (x^n - x^m)(u_y^{n+1} - u_y^{n-1})/3\big] n_x^{mn}\Big\} A_{mn} \\
&\qquad + f_x^m V_m = \sum_{n=1}^{N_m} H_x^{mn} A_{mn} + f_x^m V_m = 0 \,,
\end{aligned} \tag{8.27a}$$

$$
\begin{aligned}
&\sum_{n=1}^{N_m}\Big[(x^n-x^m)(y^{mn(n+1)}-y^{mn(n-1)})-(y^n-y^m)(x^{mn(n+1)}-x^{mn(n-1)})\Big]^{-1}\\
&\Big\{(\tilde{\lambda}+2G)\big[-(x^{mn(n+1)}-x^{mn(n-1)})(u_y^n-u_y^m)+(x^n-x^m)(u_y^{n+1}-u_y^{n-1})/3\big]n_y^{mn}\\
&\quad+G\big[-(x^{mn(n+1)}-x^{mn(n-1)})(u_x^n-u_x^m)+(x^n-x^m)(u_x^{n+1}-u_x^{n-1})/3\big]n_x^{mn}\\
&\quad+G\big[(y^{mn(n+1)}-y^{mn(n-1)})(u_y^n-u_y^m)-(y^n-y^m)(u_y^{n+1}-u_y^{n-1})/3\big]n_x^{mn}\\
&\quad+\tilde{\lambda}\big[(y^{mn(n+1)}-y^{mn(n-1)})(u_x^n-u_x^m)-(y^n-y^m)(u_x^{n+1}-u_x^{n-1})/3\big]n_y^{mn}\Big\}A_{mn}\\
&\qquad+f_y^m V_m=\sum_{n=1}^{N_m}H_y^{mn}A_{mn}+f_y^m V_m=0\,,
\end{aligned}
\tag{8.27b}
$$

where we remind that n_x^{mn} and n_y^{mn} are the components of the normal unit vector directed from the cell m to the cell n, whereas H_x^{mn} and H_y^{mn} are the components of the *numerical flux* $\mathbf{H}^{mn}$ exchanged between the cells m and n (Quarteroni, 2009), here physically corresponding to a mechanical traction vector, and also depending on the unknowns in the cells $n+1$ and $n-1$. Eqs. (8.27) can be readjusted in a more convenient form, as follows:

$$
\sum_{n=1}^{N_m}\big(a_{mn}^{xx}u_x^n+a_{mn}^{xy}u_y^n\big)+a_{mm}^{xx}u_x^m+a_{mm}^{xy}u_y^m+f_x^m V_m=0\,,
\tag{8.28a}
$$

$$
\sum_{n=1}^{N_m}\big(a_{mn}^{yx}u_x^n+a_{mn}^{yy}u_y^n\big)+a_{mm}^{yx}u_x^m+a_{mm}^{yy}u_y^m+f_y^m V_m=0\,,
\tag{8.28b}
$$

where

$$
\begin{aligned}
a_{mn}^{xx}&=\frac{(\tilde{\lambda}+2G)(y^{mn(n+1)}-y^{mn(n-1)})n_x^{mn}-G(x^{mn(n+1)}-x^{mn(n-1)})n_y^{mn}}{(x^n-x^m)(y^{mn(n+1)}-y^{mn(n-1)})-(y^n-y^m)(x^{mn(n+1)}-x^{mn(n-1)})}A_{mn}\\
&+\frac{1}{3}\frac{-(\tilde{\lambda}+2G)(y^{n-1}-y^m)n_x^{m(n-1)}+G(x^{n-1}-x^m)n_y^{m(n-1)}}{(x^{n-1}-x^m)(y^{mn(n-1)}-y^{mn(n-2)})-(y^{n-1}-y^m)(x^{mn(n-1)}-x^{mn(n-2)})}A_{m(n-1)}\\
&+\frac{1}{3}\frac{(\tilde{\lambda}+2G)(y^{n+1}-y^m)n_x^{m(n+1)}-G(x^{n+1}-x^m)n_y^{m(n+1)}}{(x^{n+1}-x^m)(y^{mn(n+2)}-y^{mn(n+1)})-(y^{n+1}-y^m)(x^{mn(n+2)}-x^{mn(n+1)})}A_{m(n+1)}\,,
\end{aligned}
\tag{8.29a}
$$

$$
\begin{aligned}
a_{mn}^{xy}&=\frac{G(y^{mn(n+1)}-y^{mn(n-1)})n_y^{mn}-\tilde{\lambda}(x^{mn(n+1)}-x^{mn(n-1)})n_x^{mn}}{(x^n-x^m)(y^{mn(n+1)}-y^{mn(n-1)})-(y^n-y^m)(x^{mn(n+1)}-x^{mn(n-1)})}A_{mn}\\
&+\frac{1}{3}\frac{-G(y^{n-1}-y^m)n_y^{m(n-1)}+\tilde{\lambda}(x^{n-1}-x^m)n_x^{m(n-1)}}{(x^{n-1}-x^m)(y^{mn(n-1)}-y^{mn(n-2)})-(y^{n-1}-y^m)(x^{mn(n-1)}-x^{mn(n-2)})}A_{m(n-1)}\\
&+\frac{1}{3}\frac{G(y^{n+1}-y^m)n_y^{m(n+1)}-\tilde{\lambda}(x^{n+1}-x^m)n_x^{m(n+1)}}{(x^{n+1}-x^m)(y^{mn(n+2)}-y^{mn(n+1)})-(y^{n+1}-y^m)(x^{mn(n+2)}-x^{mn(n+1)})}A_{m(n+1)}\,,
\end{aligned}
\tag{8.29b}
$$

$$
a_{mm}^{xx}=\sum_{n=1}^{N_m}\frac{-(\tilde{\lambda}+2G)(y^{mn(n+1)}-y^{mn(n-1)})n_x^{mn}+G(x^{mn(n+1)}-x^{mn(n-1)})n_y^{mn}}{(x^n-x^m)(y^{mn(n+1)}-y^{mn(n-1)})-(y^n-y^m)(x^{mn(n+1)}-x^{mn(n-1)})}A_{mn}\,,
\tag{8.29c}
$$

$$a^{xy}_{mm} = \sum_{n=1}^{N_m} \frac{-G(y^{mn(n+1)} - y^{mn(n-1)})n_y^{mn} + \tilde{\lambda}(x^{mn(n+1)} - x^{mn(n-1)})n_x^{mn}}{(x^n - x^m)(y^{mn(n+1)} - y^{mn(n-1)}) - (y^n - y^m)(x^{mn(n+1)} - x^{mn(n-1)})} A_{mn} \,, \tag{8.29d}$$

$$\begin{aligned} a^{yx}_{mn} = {} & \frac{-G(x^{mn(n+1)} - x^{mn(n-1)})n_x^{mn} + \tilde{\lambda}(y^{mn(n+1)} - y^{mn(n-1)})n_y^{mn}}{(x^n - x^m)(y^{mn(n+1)} - y^{mn(n-1)}) - (y^n - y^m)(x^{mn(n+1)} - x^{mn(n-1)})} A_{mn} \\ & + \frac{1}{3} \frac{G(x^{n-1} - x^m)n_x^{m(n-1)} - \tilde{\lambda}(y^{n-1} - y^m)n_y^{m(n-1)}}{(x^{n-1} - x^m)(y^{mn(n-1)} - y^{mn(n-2)}) - (y^{n-1} - y^m)(x^{mn(n-1)} - x^{mn(n-2)})} A_{m(n-1)} \\ & + \frac{1}{3} \frac{-G(x^{n+1} - x^m)n_x^{m(n+1)} + \tilde{\lambda}(y^{n+1} - y^m)n_y^{m(n+1)}}{(x^{n+1} - x^m)(y^{mn(n+2)} - y^{mn(n+1)}) - (y^{n+1} - y^m)(x^{mn(n+2)} - x^{mn(n+1)})} A_{m(n+1)} \,, \end{aligned} \tag{8.29e}$$

$$\begin{aligned} a^{yy}_{mn} = {} & \frac{-(\tilde{\lambda} + 2G)(x^{mn(n+1)} - x^{mn(n-1)})n_y^{mn} + G(y^{mn(n+1)} - y^{mn(n-1)})n_x^{mn}}{(x^n - x^m)(y^{mn(n+1)} - y^{mn(n-1)}) - (y^n - y^m)(x^{mn(n+1)} - x^{mn(n-1)})} A_{mn} \\ & + \frac{1}{3} \frac{(\tilde{\lambda} + 2G)(x^{n-1} - x^m)n_y^{m(n-1)} - G(y^{n-1} - y^m)n_x^{m(n-1)}}{(x^{n-1} - x^m)(y^{mn(n-1)} - y^{mn(n-2)}) - (y^{n-1} - y^m)(x^{mn(n-1)} - x^{mn(n-2)})} A_{m(n-1)} \\ & + \frac{1}{3} \frac{-(\tilde{\lambda} + 2G)(x^{n+1} - x^m)n_y^{m(n+1)} + G(y^{n+1} - y^m)n_x^{m(n+1)}}{(x^{n+1} - x^m)(y^{mn(n+2)} - y^{mn(n+1)}) - (y^{n+1} - y^m)(x^{mn(n+2)} - x^{mn(n+1)})} A_{m(n+1)} \,, \end{aligned} \tag{8.29f}$$

$$a^{yx}_{mm} = \sum_{n=1}^{N_m} \frac{G(x^{mn(n+1)} - x^{mn(n-1)})n_x^{mn} - \tilde{\lambda}(y^{mn(n+1)} - y^{mn(n-1)})n_y^{mn}}{(x^n - x^m)(y^{mn(n+1)} - y^{mn(n-1)}) - (y^n - y^m)(x^{mn(n+1)} - x^{mn(n-1)})} A_{mn} \,, \tag{8.29g}$$

$$a^{yy}_{mm} = \sum_{n=1}^{N_m} \frac{(\tilde{\lambda} + 2G)(x^{mn(n+1)} - x^{mn(n-1)})n_y^{mn} - G(y^{mn(n+1)} - y^{mn(n-1)})n_x^{mn}}{(x^n - x^m)(y^{mn(n+1)} - y^{mn(n-1)}) - (y^n - y^m)(x^{mn(n+1)} - x^{mn(n-1)})} A_{mn} \,. \tag{8.29h}$$

We note that each coefficient a^{xx}_{mn}, a^{xy}_{mn}, a^{yx}_{mn}, and a^{yy}_{mn} is given by the sum of three contributions, whereby the first is associated with $\mathbf{H}^{mn}$, the second with $\mathbf{H}^{m(n-1)}$, and the third with $\mathbf{H}^{m(n+1)}$. Moreover, for the conservation of linear momentum for the cell m, it can be shown that

$$\sum_{n=1}^{N_m} \left(a^{xx}_{mn} + a^{xy}_{mn}\right) + a^{xx}_{mm} + a^{xy}_{mm} = 0 \,, \tag{8.30a}$$

$$\sum_{n=1}^{N_m} \left(a^{yx}_{mn} + a^{yy}_{mn}\right) + a^{yx}_{mm} + a^{yy}_{mm} = 0 \,. \tag{8.30b}$$

After writing Eqs. (8.28) for each cell, we obtain a linear algebraic system of $2M$ equations of the type $\underline{\underline{A}}\,\underline{u} = \underline{b}$, where $\underline{u}$ is the unknown vector, containing the displacement components in the cell centers, $\underline{b}$ is the known vector, containing the body force components (due to electrostatic and osmotic stresses) in the cell centers, and $\underline{\underline{A}}$ is the coefficient matrix, depending on geometry and mechanical properties.

The coefficient matrix

We order the components of $\underline{u}$ and $\underline{b}$ as follows:

$$\underline{u}^{\mathrm{T}} = \left[u_x^1, u_y^1, ..., u_x^M, u_y^M\right] \,, \tag{8.31}$$

$$\underline{b}^{\mathrm{T}} = -\left[f_x^1 V_1, f_y^1 V_1, ..., f_x^M V_M, f_y^M V_M\right] \,, \tag{8.32}$$

such that $\underline{\underline{A}}$ is a block symmetric matrix:

$$\underline{\underline{A}} = \begin{bmatrix} \underline{\underline{A}}^{11} & \underline{\underline{A}}^{12} & \cdots & \underline{\underline{A}}^{1M} \\ \underline{\underline{A}}^{12} & \underline{\underline{A}}^{22} & \cdots & \underline{\underline{A}}^{2M} \\ \vdots & \vdots & \ddots & \vdots \\ \underline{\underline{A}}^{1M} & \underline{\underline{A}}^{2M} & \cdots & \underline{\underline{A}}^{MM} \end{bmatrix} \,, \tag{8.33}$$

where, for $m = 1, ..., M$ and $n > m$,

$$\underline{\underline{A}}^{mn} = \begin{bmatrix} a_{mn}^{xx} & a_{mn}^{xy} \\ \\ a_{mn}^{yx} & a_{mn}^{yy} \end{bmatrix} \tag{8.34}$$

if the cell n adjoins the cell m, otherwise $\underline{\underline{A}}^{mn} = \underline{\underline{0}}$, and, for $m = 1, ..., M$,

$$\underline{\underline{A}}^{mm} = \begin{bmatrix} a_{mm}^{xx} & a_{mm}^{xy} \\ \\ a_{mm}^{yx} & a_{mm}^{yy} \end{bmatrix} = -\sum_{n \neq m} \underline{\underline{A}}^{mn} \,. \tag{8.35}$$

We observe that the block symmetry of $\underline{\underline{A}}$ originates because $\xi_{mn} = -\xi_{nm}$, $\eta_{mn} = -\eta_{nm}$, and $\mathbf{n}^{mn} = -\mathbf{n}^{nm}$, that is, because adjoining cells exchange equal and opposite fluxes: $H_x^{mn} = -H_x^{nm}$, $H_y^{mn} = -H_y^{nm}$; the matrices $\underline{\underline{A}}^{mn}$ and $\underline{\underline{A}}^{mm}$ are not symmetric; most of the $\underline{\underline{A}}^{mn}$ matrices are zero matrices, and consequently $\underline{\underline{A}}$ is sparse; because of Eq. (8.35), deriving from the conservation of linear momentum for each cell, $\underline{\underline{A}}$ is block diagonally dominant. The linear system can be solved by inverting the coefficient matrix: $\underline{u} = \underline{\underline{A}}^{-1}\underline{b}$, once the boundary conditions are implemented.

The body force

Under small deformations, the body force can be computed once the coupled problems of electrostatics and ion transport are solved, that is, when the electric potential and ion concentrations are known in the cell cluster (Pietak and Levin, 2016). We write the discretized form of the body force by starting from Eq. (8.7). After integration, application of the divergence theorem, and split of the surface integral, we have

$$\begin{aligned} \int_{V_m} \mathbf{f}\, \mathrm{d}V = \int_{V_m} \mathrm{div}(\boldsymbol{\sigma}_{\mathrm{pol}} + \boldsymbol{\sigma}_{\mathrm{mix}})\, \mathrm{d}V &= \int_{\partial V_m} (\boldsymbol{\sigma}_{\mathrm{pol}} + \boldsymbol{\sigma}_{\mathrm{mix}})\mathbf{n}\, \mathrm{d}A \\ &= \sum_{n=1}^{N_m} \int_{\partial V_{mn}} (\boldsymbol{\sigma}_{\mathrm{pol}} + \boldsymbol{\sigma}_{\mathrm{mix}})\mathbf{n}^{mn}\, \mathrm{d}A \,. \end{aligned} \tag{8.36}$$

By using the mid-point integration rule, we obtain

$$\int_{V_m} \mathbf{f}\, \mathrm{d}V \approx \sum_{n=1}^{N_m} (\boldsymbol{\sigma}_{\mathrm{pol}}^{mn} + \boldsymbol{\sigma}_{\mathrm{mix}}^{mn})\mathbf{n}^{mn} A_{mn} \,. \tag{8.37}$$

Upon substitution of Eqs. (8.5) and (8.6), Eq. (8.37) becomes

$$\int_{V_m} \mathbf{f}\,\mathrm{d}V \approx \varepsilon_0 \sum_{n=1}^{N_m} A_{mn} \begin{bmatrix} \left[(\varepsilon_r - 1/2)(e_x^{mn})^2 - 1/2(e_y^{mn})^2\right] n_x^{mn} + \varepsilon_r e_x^{mn} e_y^{mn} n_y^{mn} \\ \\ \varepsilon_r e_x^{mn} e_y^{mn} n_x^{mn} + \left[(\varepsilon_r - 1/2)(e_y^{mn})^2 - 1/2(e_x^{mn})^2\right] n_y^{mn} \end{bmatrix}$$

$$- \mathcal{R}T \sum_{n=1}^{N_m} A_{mn}(c^{mn} - c^0) \begin{bmatrix} n_x^{mn} \\ \\ n_y^{mn} \end{bmatrix} . \tag{8.38}$$

We assume the electric field across two cells to be normal to their interface, such that

$$e_x^{mn} = e^{mn} n_x^{mn} , \tag{8.39a}$$

$$e_y^{mn} = e^{mn} n_y^{mn} , \tag{8.39b}$$

where e^{mn} is computed through the central finite difference scheme, as the difference between the membrane potentials of the neighboring cells divided by the double of the membrane thickness:

$$e^{mn} \approx -\frac{\psi_{\mathrm{m}}^n - \psi_{\mathrm{m}}^m}{2t_{\mathrm{m}}} , \tag{8.40}$$

in which ψ_{m} is the membrane potential and t_{m} is the membrane thickness. We approximate the osmotic concentration by averaging the values of the adjoining cells:

$$c^{mn} \approx \frac{c^n + c^m}{2} . \tag{8.41}$$

Eqs. (8.39), (8.40) and (8.41) must be replaced in Eq. (8.38), and the latter substituted in Eqs. (8.27) and in the following equations for $f_x^m V_m$ and $f_y^m V_m$.

The contribution of a boundary cell face $\partial V_{mn} \in S$ (with S cluster boundary) to the body force in the corresponding boundary cell is computed as $(\Delta\boldsymbol{\sigma}_{\mathrm{pol}}^{mn} + \Delta\boldsymbol{\sigma}_{\mathrm{mix}}^{mn})\mathbf{n}^{mn} A_{mn}$, where $\Delta\boldsymbol{\sigma}_{\mathrm{pol}}^{mn} = \bar{\boldsymbol{\sigma}}_{\mathrm{pol}}^{mn} - \boldsymbol{\sigma}_{\mathrm{pol}}^{m}$ and $\Delta\boldsymbol{\sigma}_{\mathrm{mix}}^{mn} = \bar{\boldsymbol{\sigma}}_{\mathrm{mix}}^{mn} - \boldsymbol{\sigma}_{\mathrm{mix}}^{m}$ are the jumps in the electrostatic and osmotic stresses across the boundary, with $\bar{\boldsymbol{\sigma}}_{\mathrm{pol}}^{mn}$ and $\bar{\boldsymbol{\sigma}}_{\mathrm{mix}}^{mn}$ electrostatic and osmotic stresses in the bath surrounding the cluster. Since the boundary is physically represented by the concatenation of portions of cell membranes, which are comparable to capacitors (Pietak and Levin, 2016), we assume the electric field at both sides of the boundary to be zero, such that $\Delta\boldsymbol{\sigma}_{\mathrm{pol}}^{mn} = \mathbf{0}$. Upon using Eq. (8.6) for $\Delta\boldsymbol{\sigma}_{\mathrm{mix}}^{mn}$, we obtain $\Delta\boldsymbol{\sigma}_{\mathrm{mix}}^{mn} = -\mathcal{R}T(\bar{c}^{mn} - c^m)$, in which $\bar{c}^{mn}$ is the osmotic concentration in the bath.

The boundary conditions

Boundary conditions must be incorporated in the linear system $\underline{\underline{A}}\,\underline{u} = \underline{b}$. We first consider the kinematic boundary condition (8.10). If $\partial V_{mn} \in S_{\mathrm{u}}$, when the corresponding numerical flux has to be evaluated, we use the backward (instead of the central) finite difference scheme to approximate the derivatives with respect to ξ_{mn}, such that, in place of Eqs. (8.22a) and (8.23a), we have

$$x_{,\xi}^{mn} \approx \frac{x^{mn} - x^m}{\xi^{mn} - \xi^m} , \quad y_{,\xi}^{mn} \approx \frac{y^{mn} - y^m}{\xi^{mn} - \xi^m} , \tag{8.42a}$$

$$u_{i,\xi}^{mn} \approx \frac{u_i^{mn} - u_i^m}{\xi^{mn} - \xi^m} = \frac{\bar{u}_i^{mn} - u_i^m}{\xi^{mn} - \xi^m}\,, \tag{8.42b}$$

where Eq. (8.10) has been introduced in Eq. (8.42b). Regarding the derivatives with respect to η_{mn}, Eq. (8.22b) remains valid, and, upon usage of Eq. (8.10), Eq. (8.23b) becomes

$$u_{i,\eta}^{mn} \approx \frac{\bar{u}_i^{mn(n+1)} - \bar{u}_i^{mn(n-1)}}{\eta^{mn(n+1)} - \eta^{mn(n-1)}}\,. \tag{8.43}$$

The linear system modifies according to Eqs. (8.42a), (8.42b), and (8.43), with the flux terms proportional to $\bar{u}_i^{mn}$, $\bar{u}_i^{mn(n+1)}$, and $\bar{u}_i^{mn(n-1)}$ embedded in b_{2m-1} and b_{2m}, and those proportional to u_i^m embedded in $\underline{\underline{A}}^{mm}$. If $\bar{\mathbf{u}}$ is uniform along the face, vertexes included, one has $u_{i,\eta}^{mn} = 0$. Moreover, if $\bar{\mathbf{u}} = \mathbf{0}$, there are no additional terms in b_{2m-1} and b_{2m}.

Regarding the static boundary condition (8.11), if $\partial V_{mn} \in S_{\mathrm{t}}$, we set

$$\mathbf{H}^{mn} = \mathbf{t}_{\mathrm{mec}}^{mn} = \bar{\mathbf{t}}_{\mathrm{mec}}^{mn} \tag{8.44}$$

and we add the components of this numerical flux to b_{2m-1} and b_{2m}, respectively. Again, if $\bar{\mathbf{t}}_m = \mathbf{0}$, there are no additional terms in b_{2m-1} and b_{2m}.

Deformation and stress fields

Once obtained the displacement vector $\mathbf{u}$, we evaluate the in-plane deformation field in the cell centers by resorting to the compatibility equations (8.4). This requires the computation of the discrete displacement gradient in the cell centers, which is obtained by averaging the discrete displacement gradients at the cell faces mid-points:

$$(\operatorname{grad}\mathbf{u})^m \approx \frac{1}{N_m}\sum_{n=1}^{N_m}(\operatorname{grad}\mathbf{u})^{mn} \approx \frac{1}{N_m}\sum_{n=1}^{N_m}\begin{bmatrix} u_{x,x}^{mn} & u_{x,y}^{mn} \\ u_{y,x}^{mn} & u_{y,y}^{mn}\end{bmatrix} \tag{8.45}$$

for $m = 1, ..., M$, where in turn $u_{i,x}^{mn}$ and $u_{i,y}^{mn}$ (with $i = x, y$) are given by Eqs. (8.26). More accurate approximations, also accounting for the relative distances between cell faces and cell center, should be employed for a non-regular grid. Under plane stress conditions, $\varepsilon_{zz} = -\nu(\varepsilon_{xx} + \varepsilon_{yy})/(1-\nu)$.

After obtaining $\boldsymbol{\varepsilon}$, we compute the in-plane mechanical stress field through the constitutive law

$$\boldsymbol{\sigma}_{\mathrm{mec}} = 2G\boldsymbol{\varepsilon} + \tilde{\lambda}(\varepsilon_{xx} + \varepsilon_{yy})\mathbf{I}\,. \tag{8.46}$$

Under plane strain conditions, $\sigma_{zz} = \lambda(\varepsilon_{xx} + \varepsilon_{yy})$.

8.3 *Bio-sensing*: how mechanosensitive ion channels sense the cell membrane mechanics

Mechanosensitive ion channels (MCs) respond to the mechanics of the cell membrane (Martinac, 2004). Here, we assume that, for a given membrane

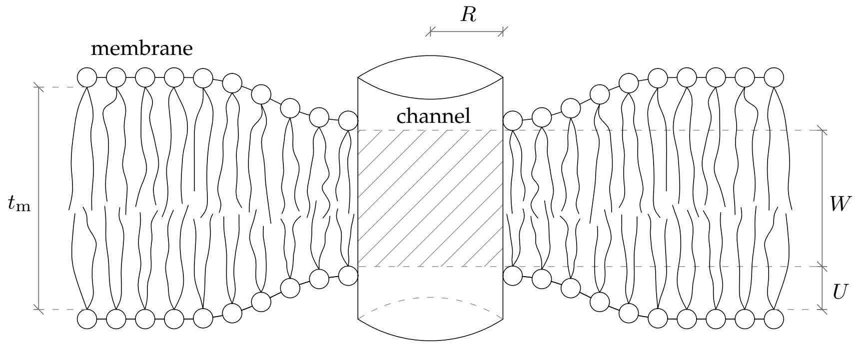

Figure 8.3: Geometry of the channel-membrane system (adapted from Wiggins and Phillips (2004)).

mechanical state, MCs instantaneously reach their steady state open probability. Moreover, as proposed by Wiggins and Phillips (2004), we adopt the following energy form governing the MCs behavior:

$$\mathcal{G} = \frac{1}{2} C K U^2 - n A \,, \tag{8.47}$$

which depends on the *hydrophobic mismatch* $2U$ between channel and membrane (Fig. 8.3) and on the membrane tension n; moreover, $C = 2\pi R$ and $A = \pi R^2$ are the circumference and area of the channel, whose radius is R, and K is the *effective elastic modulus* of the membrane, resulting from the hydrophobic mismatch linear elastic problem. As in Fig. 8.3, $2U = t_\mathrm{m} - W$, in which t_m is the membrane thickness and W is the channel hydrophobic length.

Wiggins and Phillips (2004) consider the channel as a two-state system, which may be either closed, with radius R_C, or open, with radius R_O. Hence, by expressing Eq. (8.47) in terms of R and imposing $\mathcal{G}(R_O) = \mathcal{G}(R_C)$, the opening membrane tension results

$$n_\mathrm{open} = \frac{K U^2}{R_O + R_C} \,. \tag{8.48}$$

The open state is energetically favored when $n > n_\mathrm{open}$. Then, one resorts to the Boltzmann distribution for the channel open probability p_open, increasing with n and being half if $n = n_\mathrm{open}$:

$$p_\mathrm{open} = \frac{1}{1 + \exp\left[\pi \left(R_O^2 - R_C^2\right)\left(n_\mathrm{open} - n\right)/(k_\mathrm{B} T)\right]} \,, \tag{8.49}$$

with k_B the Boltzmann constant.

In this work, we neglect interactions of neighbor MCs, thus assuming the following relation for the membrane diffusivity of the ion species i:

$$D_{\mathrm{m}}^{\mathrm{i}} = D_{\mathrm{m},0}^{\mathrm{i}} + D_{\mathrm{MC}}^{\mathrm{i}}\, p_{\mathrm{open}}(n)\,, \tag{8.50}$$

where $D_{\mathrm{m},0}^{\mathrm{i}}$ is the diffusivity in the absence of open MCs and $D_{\mathrm{MC}}^{\mathrm{i}}$ is the additional diffusivity for all available channels open. The diffusivity $D_{\mathrm{m}}^{\mathrm{i}}$ governs the transmembrane electro-diffusion by entering the Goldman-Hodgkin-Katz flux equation (7.1), as implemented in BETSE (Pietak and Levin, 2016).

We remark that MCs may exhibit an inactivated state (Coste et al., 2010; Peyronnet et al., 2014), whose effect would impact our model by reducing the membrane diffusivity. Albeit relevant to quantitatively solve specific problems, accounting for this would not change the qualitative outcome of our investigation.

As bioelectricity influences biomechanics through the active stresses entering $\mathbf{f}$ in Eq. (8.9), biomechanics influences bioelectricity through MCs gating. As already mentioned, in our resolution strategy we assume a simple partly explicit algorithm in which, at time t, we employ $\mathbf{e}$ and c to evaluate $\mathbf{f}$. By choosing a suitably small time step Δt, solving Eq. (8.9) provides $\boldsymbol{\sigma}_{\mathrm{mec}}(t + \Delta t)$, which determines n as follows, and finally $D_{\mathrm{m}}^{\mathrm{i}}$ through Eqs. (8.49) and (8.50).

We treat the cell membrane as a *structural* membrane subject to a mechanical pressure difference Δp_{mec}, having principal curvature radii r_1 and r_2. Equilibrium establishes that (Huang et al., 2012)

$$n = \Delta p_{\mathrm{mec}} \frac{r_1 r_2}{r_1 + r_2}\,. \tag{8.51}$$

In our framework, each cell experiences a uniform intracellular mechanical pressure $p_{\mathrm{mec}} = (\mathrm{tr}\, \boldsymbol{\sigma}_{\mathrm{mec}})/3$, while the extracellular mechanical pressure vanishes, since the extracellular space is continuous and connected with the bath surrounding the cluster, and hence relatively free to accommodate deformation. In the adopted small strains setting, balance equations are written on the undeformed configuration, such that r_1 and r_2 are the initial curvature radii. Moreover, as illustrated in Fig. 8.1, to obtain an *average* membrane tension, we consider a cell of in-plane circular shape with radius $r_1 = r$, such that, the out-of-plane radius being $r_2 \to \infty$, Eq. (8.51) particularizes to

$$n = p_{\mathrm{mec}} r\,. \tag{8.52}$$

The membrane equibiaxial tension state underlying Eq. (8.51) relies on the relatively small bending and shear stiffnesses of the membrane (Huang et al., 2012), the former conferred by the inner cytoskeleton and the surrounding glycocalyx, the latter resulting from the liquid-like behavior of lipid molecules, freely flowing within the membrane surface. We remark that in patch clamp

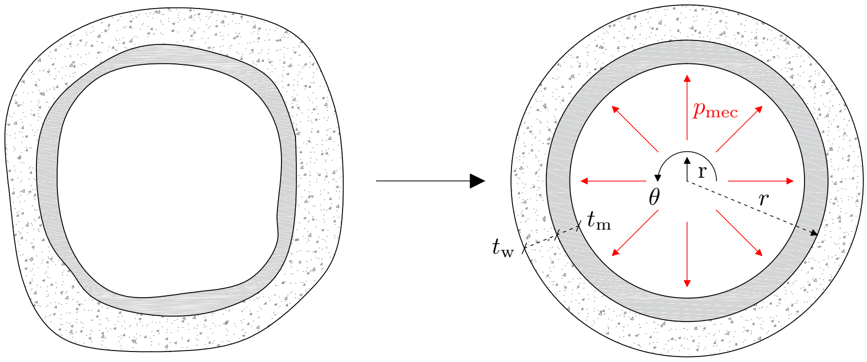

Figure 8.4: Membrane surrounded by a cell wall; real (left) and model (right).

electrophysiology, used to investigate MCs gating, Eq. (8.51) is also adopted to estimate n resulting from an applied pressure and a measured geometry (Haswell et al., 2011). This experimental technique circumvents known issues in singling out the tension felt by membranes in intact animal cells (Hoffmann et al., 2009).

In the next Sec. 8.3.1, for the interested reader, we determine n on the basis of two richer models. First, we consider the case of plant cells, where the plasma membrane, in which MCs are embedded (Peyronnet et al., 2014; Hamilton et al., 2015), is surrounded by a stiff cell wall, contributing to the mechanics of the cluster in place of the anchoring junctions. Second, back to the case of animal cells, we account for the through-the-thickness membrane stretch and for the transmembrane electric field; this analysis establishes the validity of Eq. (8.52).

8.3.1 Estimation of the cell membrane tension†

Membrane surrounded by a cell wall under small strains

Here, we propose how to estimate the membrane tension when the membrane curvature radius and the internal pressure acting on the membrane are known. We first propose a relation valid for cells with wall, such as plant cells, and then we particularize it to the case of cells without wall, such as animal cells.

A reliable estimate can be obtained, under plane strain conditions, by considering a circular membrane of outer radius r and thickness t_{m}, surrounded by a wall of thickness t_{w}. Isotropic linear elasticity provides the following radial displacement field (Love, 1927):

$$u_{\mathrm{r}}^{\mathrm{m}} = A_{\mathrm{m}}\mathrm{r} + B_{\mathrm{m}}/\mathrm{r} \quad \mathrm{r} \in [r - t_{\mathrm{m}}, r]\,, \tag{8.53a}$$

$$u_{\mathrm{r}}^{\mathrm{w}} = A_{\mathrm{w}}\mathrm{r} + B_{\mathrm{w}}/\mathrm{r} \quad \mathrm{r} \in [r, r + t_{\mathrm{w}}]\,, \tag{8.53b}$$

where the integration constants A_{m}, B_{m}, A_{w}, and B_{w} must be determined by imposing the boundary and interfacial conditions. The relevant strain components are

$$\varepsilon_{\mathrm{rr}} = \frac{\mathrm{d}u_{\mathrm{r}}}{\mathrm{dr}} \,, \tag{8.54a}$$

$$\varepsilon_{\theta\theta} = \frac{u_{\mathrm{r}}}{\mathrm{r}} \,, \tag{8.54b}$$

where $\varepsilon_{\mathrm{rr}}$ is the radial strain and $\varepsilon_{\theta\theta}$ is the circumferential strain. The corresponding stress components read

$$\sigma^{\mathrm{i}}_{\mathrm{rr}} = \frac{2G_{\mathrm{i}}}{1-2\nu_{\mathrm{i}}}\left[(1-\nu_{\mathrm{i}})\varepsilon_{\mathrm{rr}} + \nu_{\mathrm{i}}\varepsilon_{\theta\theta}\right] \,, \tag{8.55a}$$

$$\sigma^{\mathrm{i}}_{\theta\theta} = \frac{2G_{\mathrm{i}}}{1-2\nu_{\mathrm{i}}}\left[\nu_{\mathrm{i}}\varepsilon_{\mathrm{rr}} + (1-\nu_{\mathrm{i}})\varepsilon_{\theta\theta}\right] \,, \tag{8.55b}$$

in which G_{i} and ν_{i} are the shear modulus and Poisson ratio of the layer i, with $\mathrm{i} = \mathrm{m}, \mathrm{w}$.

In the case in which the internal pressure is p_{mec} and the external pressure vanishes, the boundary conditions read

$$\sigma^{\mathrm{m}}_{\mathrm{rr}}(r - t_{\mathrm{m}}) = -p_{\mathrm{mec}} \,, \tag{8.56a}$$

$$\sigma^{\mathrm{w}}_{\mathrm{rr}}(r + t_{\mathrm{w}}) = 0 \,. \tag{8.56b}$$

At the interface between membrane and wall the radial displacement and stress must be continuous:

$$u^{\mathrm{m}}_{\mathrm{r}}(r) = u^{\mathrm{w}}_{\mathrm{r}}(r) \,, \tag{8.57a}$$

$$\sigma^{\mathrm{m}}_{\mathrm{rr}}(r) = \sigma^{\mathrm{w}}_{\mathrm{rr}}(r) \,. \tag{8.57b}$$

Eqs. (8.56) and (8.57) can be solved for A_{m}, B_{m}, A_{w}, and B_{w}.

The membrane tension n is defined as the integral of $\sigma^{\mathrm{m}}_{\theta\theta}$ over t_{m}:

$$n = \int_{r-t_{\mathrm{m}}}^{r} \sigma^{\mathrm{m}}_{\theta\theta} \, \mathrm{d}r \,. \tag{8.58}$$

In the limit of $t_{\mathrm{m}}, t_{\mathrm{w}} \ll r$ we finally obtain

$$n = \left[1 + \frac{t_{\mathrm{w}}G_{\mathrm{w}}/(1-\nu_{\mathrm{w}})}{t_{\mathrm{m}}G_{\mathrm{m}}/(1-\nu_{\mathrm{m}})}\right]^{-1} p_{\mathrm{mec}} r \,. \tag{8.59}$$

We note that the geometrical and mechanical properties of both plasma membrane and cell wall contribute to determine the membrane tension. Since $t_{\mathrm{w}}G_{\mathrm{w}}$ is larger than $t_{\mathrm{m}}G_{\mathrm{m}}$, Eq. (8.59) establishes that a relatively large p_{mec} is required to obtain a membrane tension n able to open a mechanosensitive channel; indeed, compatibility and material properties dictate that a much larger circumferential stress $\sigma_{\theta\theta}$ must develop in the wall, whereby the integral of $\sigma_{\theta\theta}$ over the whole thickness must equilibrate $p_{\mathrm{mec}}r$.

Finally, we note that, by setting $t_{\mathrm{w}} = 0$, that is, in the absence of wall, Eq. (8.59) particularizes to the relation relevant for our investigation on wall-free cells, that is, Eq. (8.52). We note that this relation can also be established by equilibrium considerations only (Huang et al., 2012), without involving compatibility and constitutive equations.

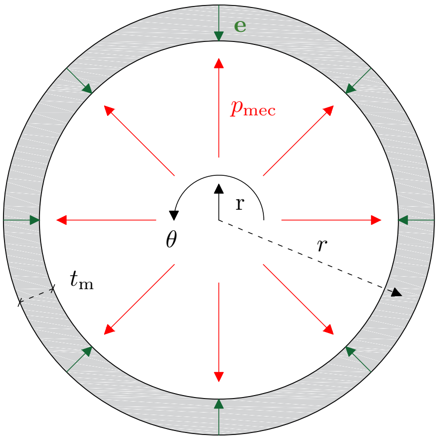

Figure 8.5: Membrane without cell wall (model).

Membrane without cell wall under large strains

Animal cells, being wall-free, are softer than plant cells. Therefore, in the case here of interest of animal cells, it is worth to evaluate to which extent variations of r can affect the membrane tension n. Beside considering the effect of the intracellular mechanical pressure p_{mec}, we also consider that of the electric field $\mathbf{e}$ acting across the membrane thickness. Indeed, it has been shown that applying a voltage across a cell membrane may result in a change in the membrane tension and, consequently, in the cell radius (Nguyen et al., 2012).

We refer to the nonlinear electroelastic problem of a circular cylindrical tube presented in Melnikov and Ogden (2016). By considering the membrane as an incompressible isotropic Neo-Hookean solid and by introducing the thin-walled tube approximation, we obtain for the radial stretch λ_{r}:

$$\lambda_{\mathrm{r}} = \lambda_z^{-1/2} \left[1 - \frac{1}{G_{\mathrm{m}}} \left(\frac{p_{\mathrm{mec}} \lambda_z r}{t_{\mathrm{m}}} + \varepsilon_0 \varepsilon_{\mathrm{r}} \lambda_z^2 |\mathbf{e}|^2 \right) \right]^{1/4} , \tag{8.60}$$

where λ_z is the out-of-plane stretch. By further assuming vanishing total radial stress σ_{rr}, the membrane tension n reads

$$n = \sigma_{\theta\theta} t_{\mathrm{m}} = p_{\mathrm{mec}} r \lambda_z^{-1} \lambda_{\mathrm{r}}^{-2} = p_{\mathrm{mec}} r \left[1 - \frac{1}{G_{\mathrm{m}}} \left(\frac{p_{\mathrm{mec}} \lambda_z r}{t_{\mathrm{m}}} + \varepsilon_0 \varepsilon_{\mathrm{r}} \lambda_z^2 |\mathbf{e}|^2 \right) \right]^{-1/2} , \tag{8.61}$$

where $\sigma_{\theta\theta}$ is the total circumferential stress. Since both p_{mec} and $\mathbf{e}$ induce a membrane thinning ($\lambda_{\mathrm{r}} < 1$ in Eq. (8.60)), considering λ_{r} in Eq. (8.61) increases the membrane tension.

We estimate the parameter G_{m} through the experimental value for the membrane elastic stiffness to equibiaxial tension K_{a} (Phillips et al., 2012), under the assumption of incompressible elasticity:

$$G_{\mathrm{m}} = \frac{K_{\mathrm{a}}}{3t_{\mathrm{m}}} \approx 10^7\,\mathrm{N/m^2}\,, \tag{8.62}$$

whereas $\varepsilon_{\mathrm{r}} = 3$ (Gramse et al., 2013). The electric field strength depends on the membrane potential ψ_{m}:

$$|\mathbf{e}| = \frac{|\psi_{\mathrm{m}}|}{t_{\mathrm{m}}}\,. \tag{8.63}$$

We now refer to plane strain conditions ($\lambda_z = 1$). By considering a quite large mechanical pressure $p_{\mathrm{mec}} = 1\,\mathrm{kPa}$, a typical resting membrane potential $\psi_{\mathrm{m}} = -50\,\mathrm{mV}$, and ordinary geometrical parameters $r = 5\,\mu\mathrm{m}$ and $t_{\mathrm{m}} = 7.5\,\mathrm{nm}$, we obtain $\lambda_{\mathrm{r}} = 0.98$ and $n = 1.04\,p_{\mathrm{mec}}r$, in which the contribution of $\mathbf{e}$ to λ_{r} is negligible with respect to that of p_{mec}. The small increase in n allows us to neglect the effect of λ_{r}, such that Eq. (8.61) reduces to Eq. (8.52), employed in our simulations. Under plane stress conditions we expect no significant variations of the results.

We remark that, in the case in which λ_{r} was accounted for, the MC open probability in Eq. (8.49) would increase not only because of an increase of n, but also because of a lowering of n_{open} associated with the reduction of U.

8.4 Simulations

We consider four initial boundary-value problems relevant to morphogenesis. We limit our simulations to relatively short time intervals, such that the cluster evolution involves suitably small strains.

To simplify the interpretation of the results, we focus on a minimum number of ion species, that is, sodium ions Na^+ and potassium ions K^+, whose electrochemical potential gradients are directed outside and inside the cell, respectively. Depolarization of specific regions is triggered by increasing the membrane diffusivity to Na^+, while hyperpolarization is obtained through K^+-selective or cation non-selective MCs. Generic charge-balancing anions M^- and fixed negatively charged proteins P^- contribute as well to the membrane potential. Chloride ions could be considered for specific applications: accounting for their inflow would provide an osmotic effect qualitatively similar to Na^+, along with a polarization effect similar to that due to the outflow of K^+. Calcium is present at very small concentrations in cells and signals by virtue of its chemical nature: hence, it would not play a relevant role in our model.

As shown in Pietak and Levin (2016), voltage-gated ion channels and gap junctions are involved in bioelectrical signaling. In the following we provide only some comments about their possible qualitative effect in our simulations, where we restrict attention to MCs, which are the most relevant when investigating on the interplay between mechanics and bioelectricity.

8.4.1 Model parameters

The simulations are conducted at body temperature $T = 310\,\mathrm{K}$. Unless otherwise specified, we adopt the following model parameters.

We select a Young modulus $E = 1.6\,\mathrm{kPa}$, as obtained through indentation tests on healthy human cervical epithelial cells (Guz et al., 2014). By assuming nearly incompressible material behavior, we set Poisson ratio $\nu = 0.49$. As relative permittivity of the cell membrane we adopt $\varepsilon_{\mathrm{r}} = 3$, as measured in Gramse et al. (2013).

The initial intracellular concentrations are: $c^0_{\mathrm{Na}^+} = 10\,\mathrm{mol/m^3}$, $c^0_{\mathrm{K}^+} = 140\,\mathrm{mol/m^3}$, $c^0_{\mathrm{P}^-} = 135\,\mathrm{mol/m^3}$, and $c^0_{\mathrm{M}^-} = 15\,\mathrm{mol/m^3}$. The initial extracellular concentrations are: $c^{\mathrm{e},0}_{\mathrm{Na}^+} = 145\,\mathrm{mol/m^3}$, $c^{\mathrm{e},0}_{\mathrm{K}^+} = 5\,\mathrm{mol/m^3}$, $c^{\mathrm{e},0}_{\mathrm{P}^-} = 10\,\mathrm{mol/m^3}$, and $c^{\mathrm{e},0}_{\mathrm{M}^-} = 140\,\mathrm{mol/m^3}$. The adopted Na^+ and K^+ concentrations are in the ranges of those found in physiological conditions in mammalian cells. Both inside and outside cells, the initial osmotic concentration is uniform and equal to $c^0 = 300\,\mathrm{mol/m^3}$, whereas the free charge $\rho = F \sum_{\mathrm{i}} z_{\mathrm{i}} c_{\mathrm{i}}$ (with z_{i} denoting the valency of the ion i) is zero, corresponding to null active stresses. Hence, the initial configuration is undeformed. We note that this, although being convenient on the modeling side, does not correspond to physiological conditions, characterized by a resting membrane potential, which can be estimated through the Goldman-Hodgkin-Katz voltage equation (7.2) (Pietak and Levin, 2016), and residual mechanical stresses (Lanir, 2009).

The diffusivity $D^{\mathrm{i}}_{\mathrm{m},0}$ of all mobile ions is $10^{-18}\,\mathrm{m^2/s}$ (Pietak and Levin, 2016), except for specific regions where we increase $D^{\mathrm{Na}^+}_{\mathrm{m},0}$ as a convenient way to trigger depolarization.

With reference to a MC of large conductance, we use $R_O = 3.5\,\mathrm{nm}$ and $R_C = 2.3\,\mathrm{nm}$ as open and closed radii (Wiggins and Phillips, 2004). By considering a *1,2-dioleoyl-sn-glycero-3-phosphocholine* lipid, abundant in lipid bilayers, the effective elastic modulus of the membrane and the hydrophobic mismatch are $K = 27 k_{\mathrm{B}} T\,\mathrm{nm}^{-3}$ and $2U = 0.4\,\mathrm{nm}$, respectively (Wiggins and Phillips, 2004). Therefore, the opening tension (8.48) results $n_{\mathrm{open}} = 0.19 k_{\mathrm{B}} T\,\mathrm{nm}^{-2} = 0.8\,\mathrm{mN/m}$, which agrees with experiments (Phillips et al., 2012). Finally, we adopt an in-plane cell radius $r = 5\,\mu\mathrm{m}$.

8.4.2 Simulation 1: cancer progression

We deal with a circular cluster of diameter $\approx 150\,\mu\mathrm{m}$, composed of ≈ 175 cells. We posit plane stress state and, with reference to Eq. (8.10), we enforce $\bar{\boldsymbol{u}} = \mathbf{0}$ on $S = S_{\mathrm{u}}$.

We assume that a region of diameter $\approx 50\,\mu\mathrm{m}$ in the center of the cluster consists of cancerous cells, which are typically characterized by a depolarized membrane potential (Chernet and Levin, 2013b). This may be due to large intracellular Na^+ level (Yang and Brackenbury, 2013) and/or high expression of Na^+ channels (Djamgoz, 2014). To reproduce this situation, we choose to increase $D_{\mathrm{m},0}^{\mathrm{Na}^+}$ in the central region, thus therein setting $D_{\mathrm{m},0}^{\mathrm{Na}^+} = 50 \times 10^{-18}\,\mathrm{m}^2/\mathrm{s}$. Owing to structural modifications of the cytoskeleton, cancerous cells often appear softer than healthy ones (Lekka, 2016); thus, we adopt $E = 1.4\,\mathrm{kPa}$ for them (Guz et al., 2014). Fig. 8.6 illustrates the results of the simulation at $t = 10\,\mathrm{s}$.

In the cancerous region, a depolarized membrane potential ψ_m and an increased osmotic concentration c originate because of the influx of Na^+. The results show that ψ_m reaches the steady state in some milliseconds, while c continuously increases in the internal region during the simulation. Indeed, at steady state membrane potential (as given by the Goldman-Hodgkin-Katz voltage equation (7.2)) the *net* transmembrane electric current is zero, while *individual* transmembrane ion fluxes (as given by the Goldman-Hodgkin-Katz flux equation (7.1)) are in general non-vanishing.

The depolarized region and the surrounding cluster attract each other by the electrostatic force $\mathbf{f}_\mathrm{pol}$. Simultaneously, the strong gradient of c between the two regions generates a large outward osmotic force $\mathbf{f}_\mathrm{mix}$. An outward $\mathbf{f}_\mathrm{mix}$ also arises at the cluster boundary, because of the difference in c between the boundary cells and the surrounding bath, the latter being progressively ion-depleted.

The $\mathbf{f}_\mathrm{pol}$ field is irrelevant for the mechanical response. Instead, due to the $\mathbf{f}_\mathrm{mix}$ field, we register a large positive mechanical pressure p_mec in the cancerous region, and a smaller negative p_mec in the healthy cells, compressed by the expansion of the tumor mass. The qualitative expansion of the inner region is independent of the mechanical boundary condition applied to the cluster, while the latter affects the qualitative deformation of the healthy cells, that would for instance expand as well if we applied $\bar{\boldsymbol{t}}_\mathrm{mec} = \mathbf{0}$ on $S = S_\mathrm{t}$.

To conclude, this simulation suggests that the depolarized state of cancerous cells may result in an osmotically-driven expansion of the tumor, which is enhanced by their large compliance. We note that osmosis has already been related to cancer progression in literature. Specifically, Stroka et al. (2014) have demonstrated that differential osmosis through the leading and trailing edges of a single tumor cell in a narrow channel promotes cell migration; Hui et al. (2019) have shown that migration of individual cancer cells in a confined environment, driven by osmotic concentration gradients, is reduced by abating the concentration of aquaporins, suggesting that cancer progression might be hampered by reducing transmembrane osmosis.

Finally, we add that if gap junctions were accounted for, they would result in some transport of Na^+ from the inner region to the surrounding, that is, to a reduction of the local depolarization accompanied with an increase of the

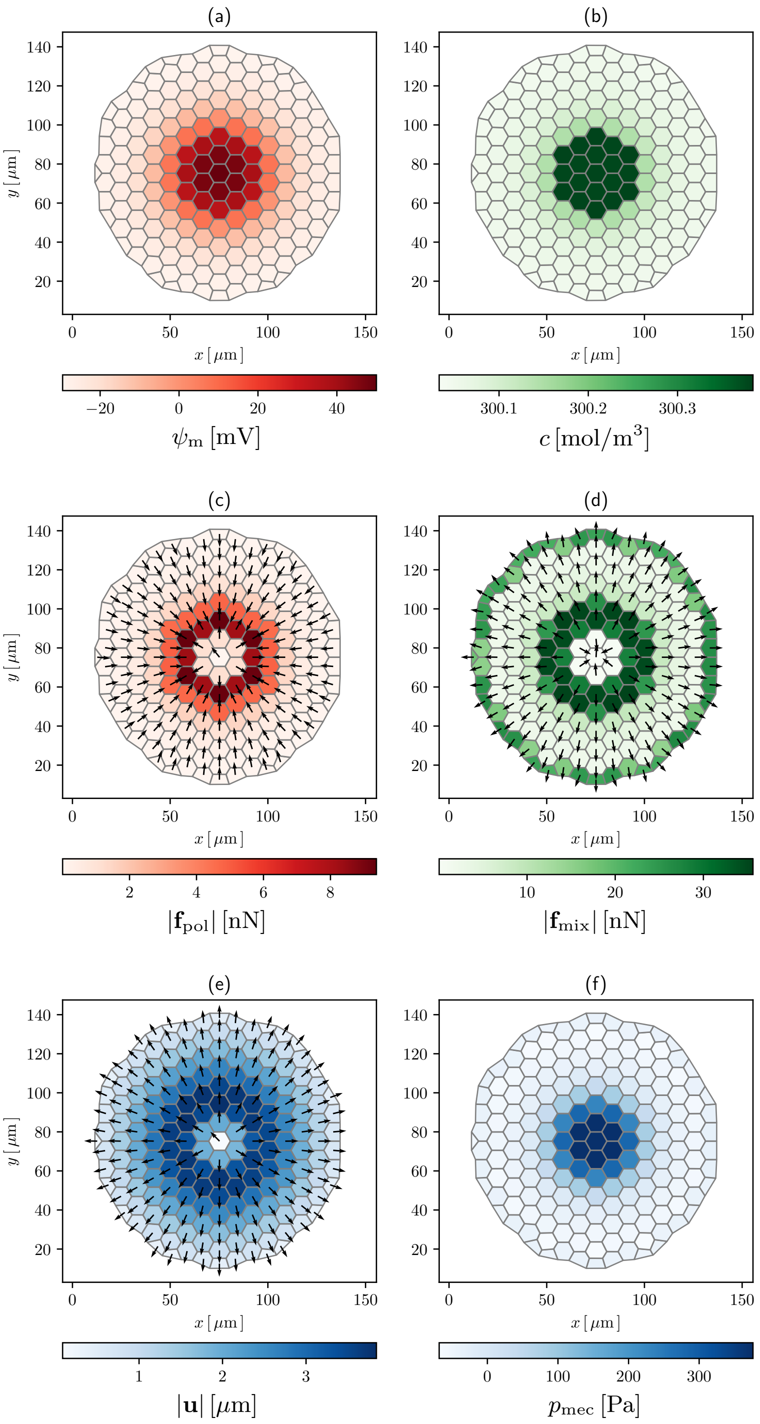

Figure 8.6: (a) Membrane potential $\psi_\mathrm{m}(\mathbf{x})$, (b) osmotic concentration $c(\mathbf{x})$, (c) electrostatic force $\mathbf{f}_\mathrm{pol}(\mathbf{x})$, (d) osmotic force $\mathbf{f}_\mathrm{mix}(\mathbf{x})$, (e) displacement vector $\mathbf{u}(\mathbf{x})$, and (f) mechanical pressure $p_\mathrm{mec}(\mathbf{x})$ at $t = 10\,\mathrm{s}$. The central depolarized region, in which ions accumulate, is expanded by osmotic forces.

depolarized area.

8.4.3 Simulation 2: osmoregulation

Here we investigate the role of MCs as osmoregulators. We consider the same benchmark of Simulation 1, and additionally account for either K^+-selective MCs,[2] with $D_{\mathrm{MC}}^{\mathrm{K}^+} = 10^{-16}\,\mathrm{m}^2/\mathrm{s}$, or cation non-selective MCs,[3] allowing transport of both K^+ and Na^+, with $D_{\mathrm{MC}}^{\mathrm{K}^+} = D_{\mathrm{MC}}^{\mathrm{Na}^+} = 10^{-16}\,\mathrm{m}^2/\mathrm{s}$. In Fig. 8.7 we represent $\psi_{\mathrm{m}}(t)$, $c(t)$, and $p_{\mathrm{mec}}(t)$ for the innermost cell of the cluster, comparing the responses obtained by accounting or not for MCs.

Without MCs, ψ_{m} is nearly constant, whereas c and p_{mec} increase about linearly. With K^+-selective MCs, when p_{mec}, and hence the membrane tension, become sufficiently large, channels open, such that ψ_{m} nonlinearly decreases and c increases less than linearly, since the inflow of Na^+ due to the high $D_{\mathrm{m}}^{\mathrm{Na}^+}$ competes with the outflow of K^+ through MCs. This effect hinders the increase of $\mathbf{f}_{\mathrm{mix}}$, such that, at the end of the simulation, the value of p_{mec} is about half of that in the absence of MCs. Given the selected diffusivities, we observe the same qualitative behavior, though milder, in the case of cation non-selective MCs.

The foregoing negative feedback loop (where *negative* refers to the pressure *reduction* due to channel opening) represents a possible mechanism for cells to regulate osmotic pressure and, hence, their volume. Notably, MCs in bacteria, despite being non-selective to cations and anions (Martinac, 2004), are hypothesized to operate as “safety valves” to prevent the membrane failure when osmotic shock occurs (Phillips et al., 2012). The role of MCs as regulators of cell volume in vertebrates is still debated, although several TRP channels exhibit osmosensitivity (Hoffmann et al., 2009).

Furthermore, this simulation suggests that genetically modifying cells to induce a high expression of K^+-selective MCs could help to restore the membrane potential of cancerous cells to its normal value, thereby hampering cancer progression. Importantly, Chernet and Levin (2013b) have shown that an artificial hyperpolarization obtained by overexpressing specific ion channels can inhibit tumor formation. Beside tumor cells, also embryonic and stem cells tend to be more depolarized than others (Levin, 2014), such that their activity could potentially be guided through the aforementioned control plans.

We finally note that accounting for voltage-gated K^+-selective or cation non-selective channels in place of the corresponding MCs would have the same qualitative effect on this benchmark, since pressurized regions are also depolar-

---

[2] K^+-selective MCs are, for example, TREK and TRAAK channels, which can be found in eukaryotes (Martinac, 2004).

[3] Cation non-selective MCs are, for example, the eukaryotic Piezo channels (Coste et al., 2010).

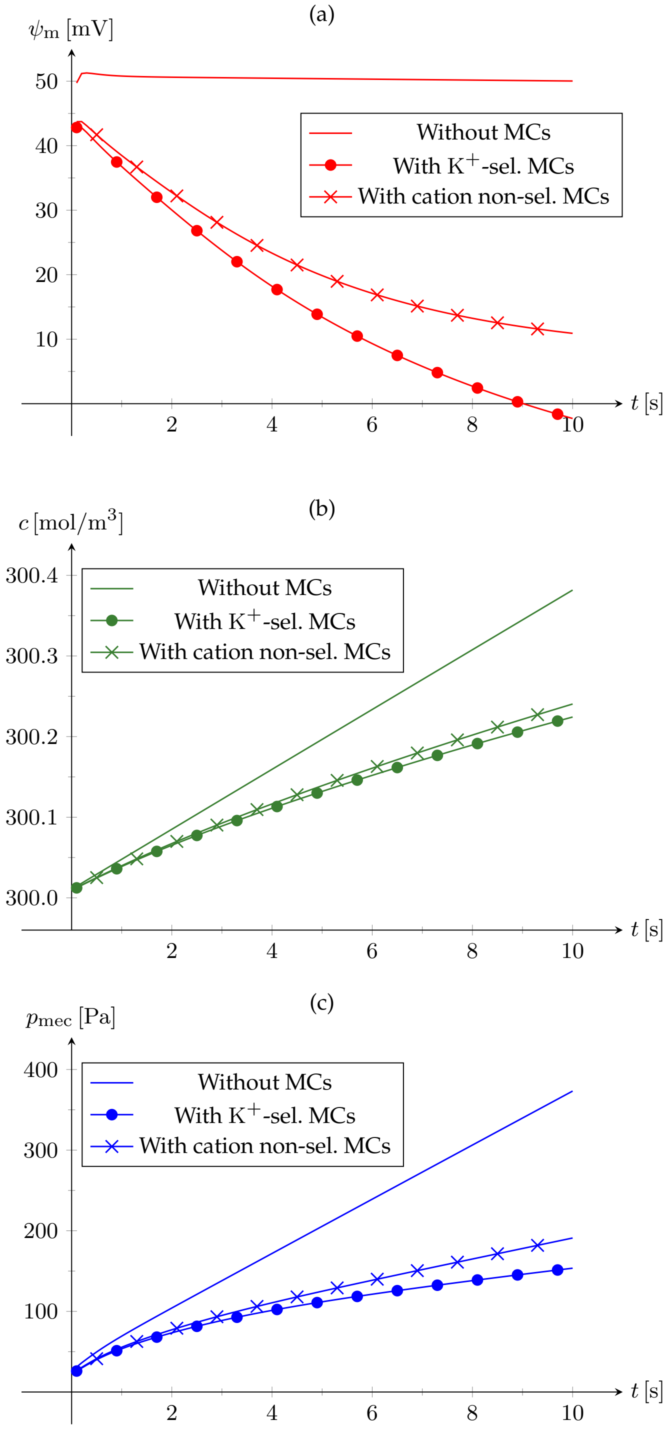

Figure 8.7: (a) Membrane potential $\psi_m(t)$, (b) osmotic concentration $c(t)$, and (c) mechanical pressure $p_{mec}(t)$ in the innermost cell of the cluster. The activation of MCs reduces ψ_m and the increase rate of c and p_{mec}.

ized.

8.4.4 Simulation 3: symmetry breaking

In the ion flux model of *left-right asymmetry* (Vandenberg and Levin, 2013), the asymmetric expression of K^+ channels and H^+ pumps leads to ψ_m differences between left and right sides of the embryo, which in turn cause an asymmetric gene expression. Here we show that an asymmetric expression of K^+-selective MCs can *mechanically* induce asymmetric patterning.

We consider the elongated cluster in Fig. 8.8, with major axis $\approx 300\,\mu$m along the x-direction and minor axis $\approx 100\,\mu$m along the y-direction, consisting of ≈ 300 cells. Under plane stress, with reference to Eqs. (8.10) and (8.11), we impose $\bar{\boldsymbol{u}} = \mathbf{0}$ on the straight top and bottom sides, along with $\bar{\boldsymbol{t}}_\mathrm{mec} = \mathbf{0}$ on the curved left and right boundaries. In the central region $\mathcal{V} = \{100 < x < 200\,\mu\mathrm{m}, \forall y\}$ we set $D_{\mathrm{m},0}^{\mathrm{Na}^+} = 10^{-17}\,\mathrm{m}^2/\mathrm{s}$.

As shown in Fig. 8.8, ψ_m and c are symmetric in the absence of MCs, with $\mathcal{V}$ strongly depolarized for the influx of Na^+. Osmotic forces at the boundary of $\mathcal{V}$ determine a horizontal symmetric elongation.

If K^+-selective MCs (with $D_\mathrm{MC}^{\mathrm{K}^+} = 10^{-16}\,\mathrm{m}^2/\mathrm{s}$) are present only in the right half part of $\mathcal{V}$, a local hyperpolarization occurs, as represented in Fig. 8.9. Eventually, the asymmetric expression of MCs is responsible of a "left-right asymmetry" in the cell migration pattern: indeed, the vertical line corresponding to nil horizontal displacement is on the left of the mid-axis, and left side cells migrate slightly more than right side cells.

Fig. 8.10 represents, as functions of t, the maxima of $|u_x|$ on the left and right sides of the cluster, u_x^l and u_x^r respectively. After MCs activate, $u_x^l(t)$ becomes progressively larger than $u_x^r(t)$, with both being reduced with respect to the case without MCs.

In conclusion, differently from previous literature (see Vandenberg and Levin, 2013 and references therein), where left-right asymmetry of organs arises from asymmetric gene expression, here asymmetric patterning is originated by physical forces. In both cases, though, ion channels are fundamental in modulating the phenomenon.

Finally, we also argue that additional osmotically-driven asymmetric morphogenesis should occur in the case of spatially non-uniform mechanical properties.

8.4.5 Simulation 4: long-range bioelectric signaling

Non-local bioelectricity (that is, the functional impact of the electrical state of cells at long distance from a morphogenetic event *in vivo*) is involved in tumorigenesis (Chernet and Levin, 2014), brain patterning (Pai et al., 2015),

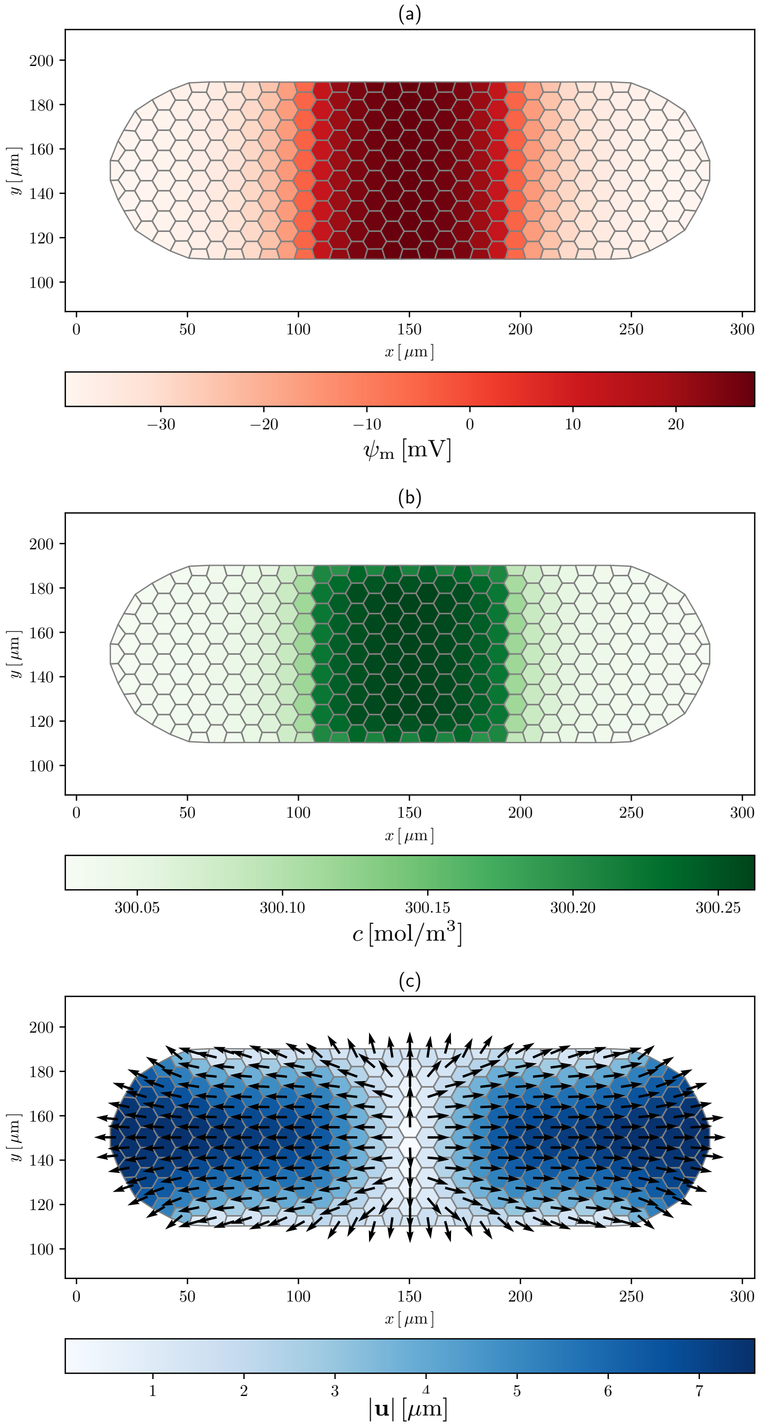

Figure 8.8: (a) Membrane potential $\psi_\mathrm{m}(\mathbf{x})$, (b) osmotic concentration $c(\mathbf{x})$, and (c) displacement vector $\mathbf{u}(\mathbf{x})$ at $t = 10\,\mathrm{s}$, without MCs. The central depolarized region, in which ions accumulate, determines a symmetric horizontal elongation of the cluster.

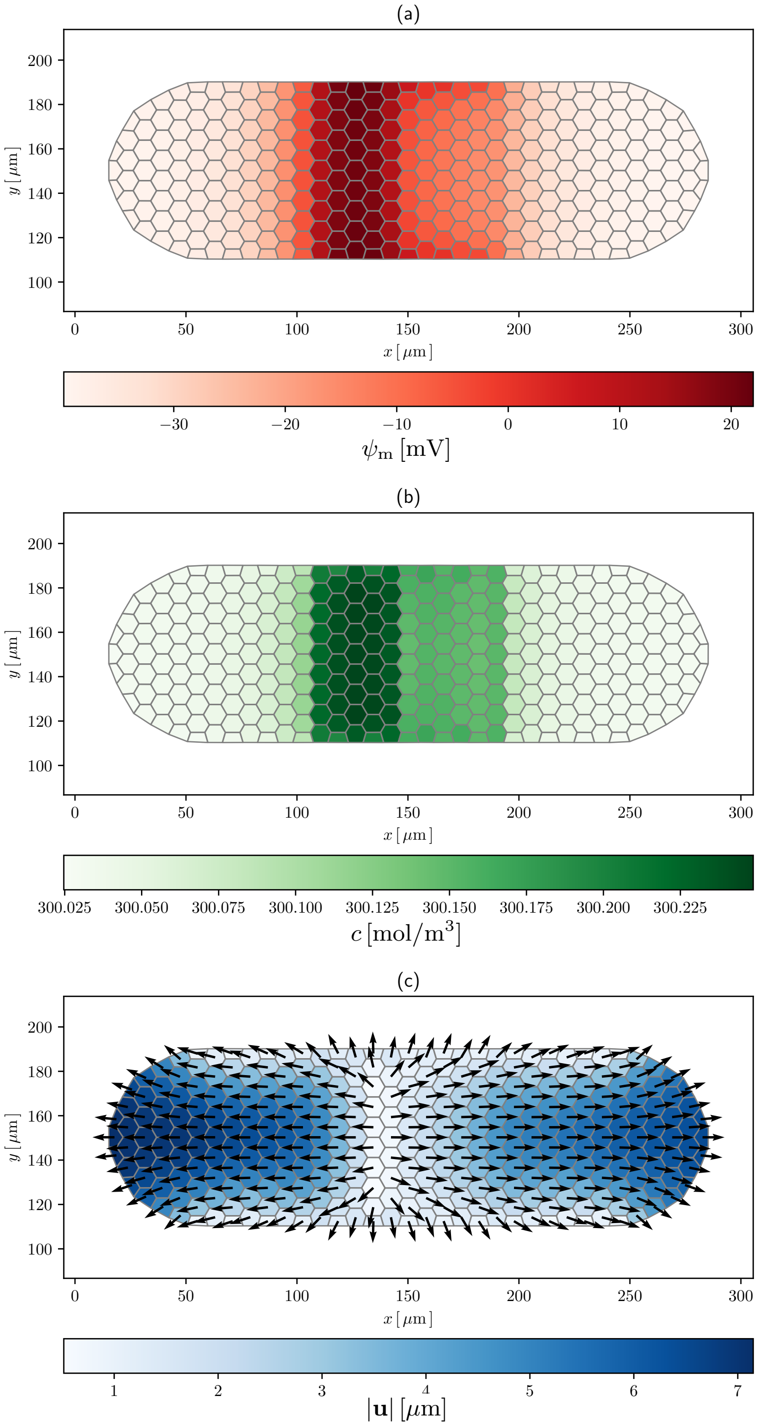

Figure 8.9: (a) Membrane potential $\psi_\mathrm{m}(\mathbf{x})$, (b) osmotic concentration $c(\mathbf{x})$, and (c) displacement vector $\mathbf{u}(\mathbf{x})$ at $t = 10\,\mathrm{s}$, with MCs. The asymmetric expression of MCs determines a symmetry breaking in the migration pattern.

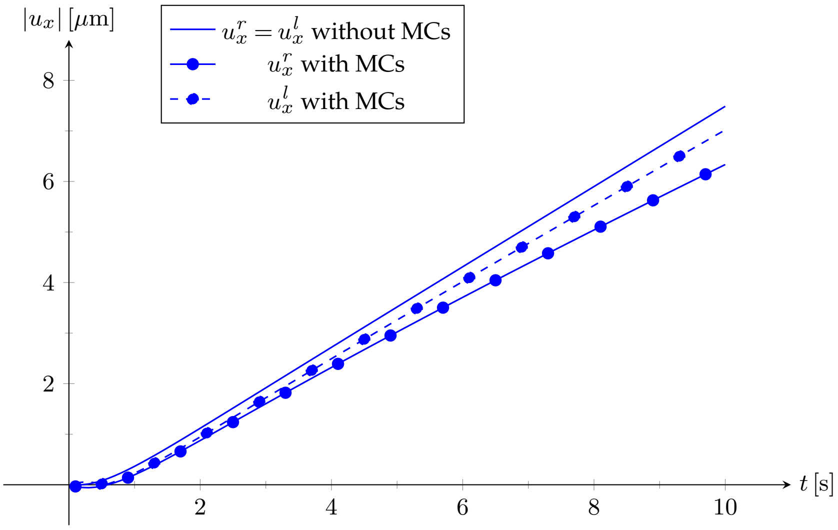

Figure 8.10: Maxima of $|u_x|$ on the right and left sides of the cluster. They progressively diverge in time because of the asymmetric distribution of MCs.

and planarian regeneration (Levin et al., 2019). Here, we explore whether and how long-range bioelectric signaling is mediated by cluster mechanics.

We deal with the same geometry of Simulation 3, but, under plane strain, we impose $\bar{\boldsymbol{u}} = \boldsymbol{0}$ on the curved left boundary, along with $\bar{\boldsymbol{t}}_{\mathrm{mec}} = \boldsymbol{0}$ on the rest of the boundary. In the rightmost region of the domain $\mathcal{V}_r = \{x > 250\,\mu\mathrm{m}, \forall y\}$ we select $D_{\mathrm{m},0}^{\mathrm{Na}^+} = 2 \times 10^{-18}\,\mathrm{m}^2/\mathrm{s}$. We perform two 5 s long analyses, one without MCs, and one with uniformly distributed K^+-selective MCs featuring $D_{\mathrm{MC}}^{\mathrm{K}^+} = 10^{-17}\,\mathrm{m}^2/\mathrm{s}$.

Without MCs, as shown in Fig. 8.11, $\mathcal{V}_r$ appears depolarized. The large gradient of c between $\mathcal{V}_r$ and the ion-depleted bath produces large osmotic forces at the right end, determining a rightward expansion. The mechanical pressure field is non-trivial, being large in the depolarized region, reducing in the inner cluster region, and then increasing again near the fixed left end.

As represented in Fig. 8.12, the MCs opening produces a hyperpolarization of cells, which is larger near the curved boundaries, where p_{mec} is larger. Notably, while in Simulations 2 and 3 the initial depolarization is reduced by the *local* opening of MCs, here MCs also open outside the depolarized region (that is, *non-locally*). This results in the hyperpolarization of the left end region, located far from the imposed bioelectrical perturbation. We note that, under plane stress, this long-range effect would be largely mitigated by the stress relaxation due to the free out-of-plane strain component.

Therefore, Simulation 4 highlights a possible case in which long-range bioelectric signaling, mediated by biomechanical properties, occurs. Specifically,

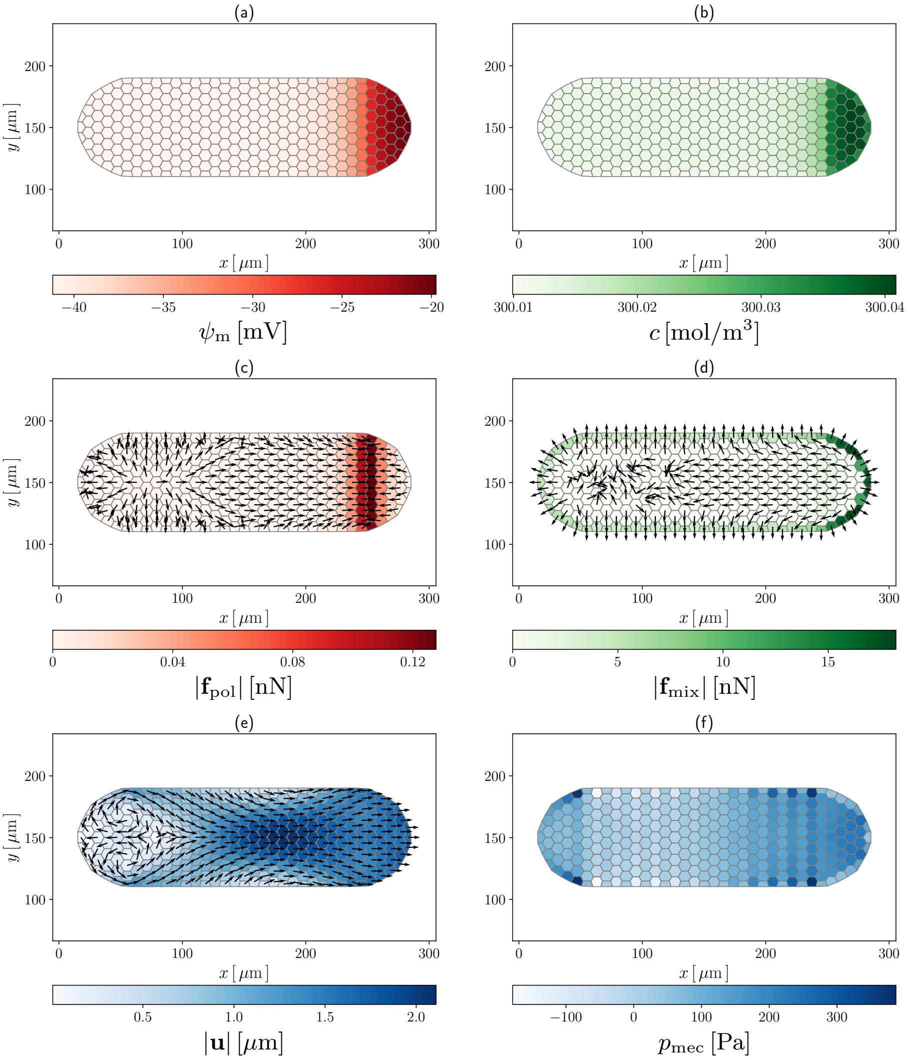

Figure 8.11: (a) Membrane potential $\psi_\mathrm{m}(\mathbf{x})$, (b) osmotic concentration $c(\mathbf{x})$, (c) electrostatic force $\mathbf{f}_\mathrm{pol}(\mathbf{x})$, (d) osmotic force $\mathbf{f}_\mathrm{mix}(\mathbf{x})$, (e) displacement vector $\mathbf{u}(\mathbf{x})$, and (f) mechanical pressure $p_\mathrm{mec}(\mathbf{x})$ at $t = 5\,\mathrm{s}$, without MCs. Osmotic forces at the right end produce a rightward elongation of the cluster and a large mechanical pressure near the fixed left end.

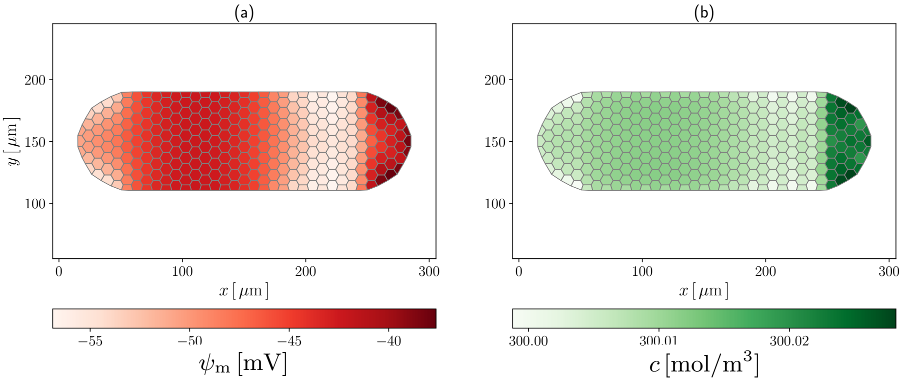

Figure 8.12: (a) Membrane potential $\psi_\mathrm{m}(\mathbf{x})$ and (b) osmotic concentration $c(\mathbf{x})$ at $t = 5\,\mathrm{s}$, with MCs. These open because of the osmotic forces at the right end, and trigger a change in ψ_m near the fixed left end.

MCs-driven long-range signaling is most likely to be induced in cluster regions attracting larger mechanical stresses, thereby promoting MCs opening. This may be due to specific mechanical boundary conditions or spatially variable mechanical properties.

Moreover, while in Simulations 2 and 3 MCs trigger a negative feedback loop by acting, respectively, as regulators of p_mec (Fig. 8.7) and u_x (Fig. 8.10), this simulation exhibits a *positive* feedback loop, where the displacement field *increases* because of the channel opening (Fig. 8.13). This is ultimately due to non-local signaling, and specifically to the emergence of a region, in the center-left part of the cluster (Fig. 8.12), where ψ_m and c are larger, thereby producing further expansion forces.

8.5 Concluding remarks

The behavior of bioelectric networks in tissues is complex; thus, the use of quantitative, bio-realistic simulators is essential to understand the dynamics of such signals and to infer interventions driving cellular systems to biomedically-desirable states. The *BioElectric Tissue Simulation Engine* is a finite volume multiphysics simulator, written in *Python*$^\mathrm{TM}$ language, developed in Pietak and Levin (2016) to model bioelectrical interactions in cell clusters, which we have here extended to mechanics. On the one hand, the existence of electric fields and ion concentration gradients originates electrostatic and osmotic forces, which in turn, by equilibrium, lead to a mechanical stress field and, hence, to deformation. On the other hand, the mechanics of the cell membrane impacts the opening of ion channels, which are responsible for the transmembrane electro-diffusion, eventually modulating bioelectrical forces.

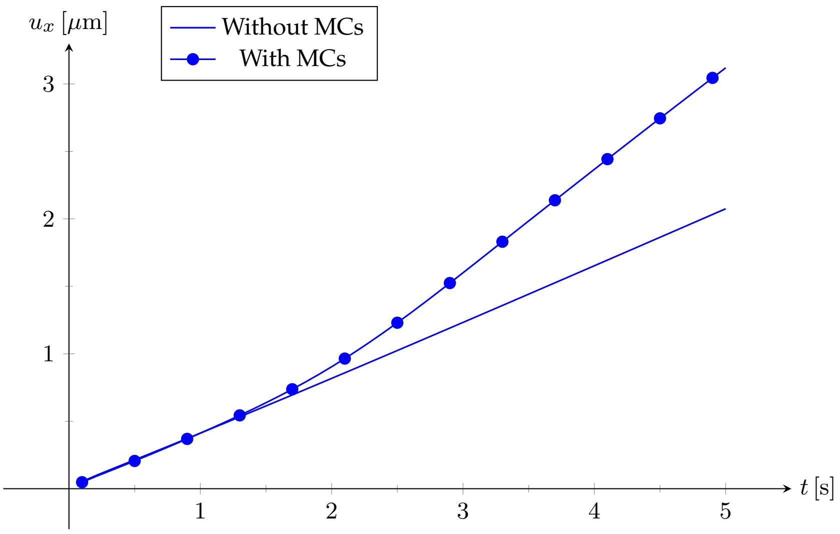

Figure 8.13: Maximum of u_x as a function of t. It increases more rapidly after MCs activate.

Our simulations show that osmotic forces induce an expansion of depolarized regions (such as tumor, embryonic, and stem cell ensembles), while electrostatic forces are negligible.[4] We suggest that overexpressing K^+-selective mechanosensitive channels (MCs) in depolarized cells could help to hinder cancer progression or to regulate the activity of embryonic and stem cells. Moreover, K^+-selective MCs may be exploited to obtain asymmetric patterning, or to induce non-local bioelectric signals in regions with larger mechanical stress, as it may occur under specific constraints. Such constraints may even allow K^+-selective MCs to trigger a positive feedback loop that amplifies the mechanical response, while MCs usually establish negative feedback loops that regularize the global mechanical behavior.

To summarize, in this work we have investigated a mechanism of mutual coupling between mechanobioelectrical actuation and sensing, which may inspire the design of biological smart soft robots with physically integrated control structures (Pfeifer and Bongard, 2006; Cheney et al., 2014). However, relevant tasks should be accomplished to achieve this goal. On the experimental side, the suggested intervention strategies should be verified, by resorting to *in vivo* manipulation of ion channels through pharmacological or optogenetic techniques, and quantification of the corresponding membrane potential variations, including long-range signaling. On the modeling side, the extension to *large deformations* is a crucial step for the following reasons.

---

[4] We expect that the Maxwell stress would instead play a major role in the case of *exogenous* bioelectricity. Indeed, cells experience relevant deformations when subject to external electric fields (see, e.g., Nodargi et al., 2017).

First, finite deformations would permit the accurate investigation of long-lasting morphogenetic events involving non-regular cell clusters. Moreover, finite deformations would allow the modeling of growth. This could provide insight on the mechanics of bioelectricity-driven regeneration, toward illustrating the ability of some biological systems to maintain a complex anatomical state despite drastic injury - a kind of homeostatic process (Pezzulo and Levin, 2016). Indeed, bioelectric patterns and long-range signaling seem to be implicated in regeneration, as in planaria (Levin et al., 2019). Furthermore, large deformations are necessary to introduce more appropriate mechanical constitutive laws, eventually accounting for the cell's internal structure. For instance, the mechanics of the cytoskeleton could be described in more detail by leveraging, for example, on a statistical treatment of cross-linked polymers (De Tommasi et al., 2015) or on a soft tensegrity structure model (Fraldi et al., 2019). Lastly, large deformations would enable a more accurate evaluation of the cell membrane tension through the availability of the membrane local curvature in the deformed configuration.

Another major advancement would be the modeling of osmotically-driven water fluxes, both across the membrane via aquaporins (Agre, 2006) and freely in the extracellular space, by resorting, as an instance, to a *poroelastic* framework in which volumetric deformations depend on the water flow (Coussy, 2004).

Finally, the inclusion of voltage-gated ion channels, gap junctions, and bio-actuation proteins, such as *prestins*, converting the membrane potential to force in the surrounding membrane (Dallos and Fakler, 2002), would allow the investigation of further nonlinear feedback loops that might be exploited by cells in morphogenesis and fine-tuned in synthetic biology applications.

Notably, the extension to large deformation poroelasticity is addressed in the next chapter.

Chapter 9

An electrochemo-poromechanical theory for the mechanobioelectricity of cell clusters

This chapter is adapted from "Leronni (2020), Modeling the mechanobioelectricity of cell clusters, *Biomechanics and Modeling in Mechanobiology*".

9.1 Introduction

The mecBETSE platform, presented in Leronni et al. (2020) and in the foregoing Ch. 8, is limited to small deformations, thus hampering developmental applications. Moreover, it does not account for the water flow triggered by osmotic pressure gradients, which, according to *poromechanics* frameworks (Coussy, 2004), largely employed for cells (Moeendarbary et al., 2013), is strictly related with deformation.

In order to overcome the previous limits, and inspired by the framework adopted for IPMCs in Sec. 5.2, we propose a continuum finite strain theory coupling the bioelectricity and the poromechanics of cell clusters. In this theory, the bioelectrical response is governed by mass balances for the intracellular (IC) and extracellular (EC) concentrations of sodium, potassium, and chloride ions, and by Gauss laws for the IC and EC electric potentials. The difference between IC and EC electric potentials provides the membrane potential. The poromechanical response is determined by mass balances for the IC and EC concentrations of water molecules, and by an overall momentum balance for the displacement field. An important feature of the model is the possibility of accounting for the transmembrane ion and water exchange through self-balancing source terms in the IC and EC mass balances.

Previous efforts in the literature have already focused on the interplay between cell mechanics and transmembrane ion and water transport, including the contributions of Sun and coworkers. In particular, Jiang and Sun (2013) have proposed a mathematical model for the study of volume and pressure regulation in eukaryotic cells, featuring water permeation, mechanosensitive ion channels, ion pumps, and a quite detailed mechanics of the cell cortex. Later, Yellin et al. (2018) have augmented the model in order to account for multiple ionic species and the membrane potential. While Jiang and Sun (2013) and Yellin et al. (2018) focus on the response of a single cell, here we rather aim at developing a minimal tool able to deal with the overall electrochemo-poromechanics of a cell cluster. However, in order to limit the complexity of our theory, in this first contribution we neglect the modeling of both active ion pumps and gating of ion channels. These aspects will be addressed in future investigations.

We systematically derive our theory in Sec. 9.2, starting from first principles. In Sec. 9.3, with reference to a 1D axisymmetric benchmark, we discuss the finite element solution of the proposed model obtained through the commercial software *COMSOL Multiphysics*®. We examine different conditions, including the effect of accounting for gap junctions (Sec. 9.3.5) and tight junctions (Sec. 9.3.6). Finally, in Sec. 9.4 we draw the conclusions of our study, and outline possible future developments.

9.2 Modeling framework

In the following, we develop a continuum Lagrangian finite strain theory addressing the mechanobioelectricity of the cell cluster described in Sec. 7.2 and sketched in Fig. 7.1. By relying on *mixture theory* (Ateshian, 2007), we assume that the solid network and the IC and EC spaces coexist within the same material point, such that transmembrane fluxes should be regarded as *local* fluxes.

9.2.1 Balance equations

The momentum balance, to be solved for the displacement field $\mathbf{u}$, describes the mechanics of the cluster, governed by a solid network of cytoskeletal filaments and anchoring junctions. Under the quasi-static approximation, and in the absence of bulk loads, it reduces to the mechanical equilibrium

$$\mathrm{Div}\,\mathbf{P} = \mathbf{0}\,, \tag{9.1}$$

where Div is the material divergence and $\mathbf{P}$ is the nominal stress tensor.

The mass balances for the IC and EC water concentrations read

$$\Phi_0 \dot{C}_{\mathrm{w}} + \mathrm{Div}\,\mathbf{J}_{\mathrm{w}} = -J_{\mathrm{w}}^{\mathrm{m}} A^{\mathrm{c}}/V^{\mathrm{c}}\,, \tag{9.2a}$$

$$\Phi_0^{\mathrm{e}} \dot{C}_{\mathrm{w}}^{\mathrm{e}} + \mathrm{Div}\,\mathbf{J}_{\mathrm{w}}^{\mathrm{e}} = J_{\mathrm{w}}^{\mathrm{m}} A^{\mathrm{c}}/V^{\mathrm{c}}\,, \tag{9.2b}$$

where Φ_0 and Φ_0^{e} are the initial IC and EC porosities, C_{w} and $C_{\mathrm{w}}^{\mathrm{e}}$ are the IC and EC molar concentrations of water per unit reference volume of the IC and EC spaces, $\mathbf{J}_{\mathrm{w}}$ and $\mathbf{J}_{\mathrm{w}}^{\mathrm{e}}$ are the IC and EC nominal molar fluxes of water, $J_{\mathrm{w}}^{\mathrm{m}}$ is the transmembrane nominal molar flux of water, positive if water moves from the IC to the EC space, A^{c} is the reference cell membrane area, and V^{c} is the reference cell volume. The symbol $\dot{}$ indicates time derivative, that is, $\dot{C}_{\mathrm{w}} = \partial C_{\mathrm{w}}/\partial t$. Since the cluster is constituted by closely packed cells, $\Phi_0^{\mathrm{e}} \ll \Phi_0$. The terms on the right-hand sides are self-balancing, that is, a source of water for the IC space is a sink for the EC space, or vice versa.

Similarly, the mass balances for the IC and EC concentrations of mobile ion i read

$$\Phi_0 \dot{C}_{\mathrm{i}} + \mathrm{Div}\,\mathbf{J}_{\mathrm{i}} = -J_{\mathrm{i}}^{\mathrm{m}} A^{\mathrm{c}}/V^{\mathrm{c}}\,, \tag{9.3a}$$

$$\Phi_0^{\mathrm{e}} \dot{C}_{\mathrm{i}}^{\mathrm{e}} + \mathrm{Div}\,\mathbf{J}_{\mathrm{i}}^{\mathrm{e}} = J_{\mathrm{i}}^{\mathrm{m}} A^{\mathrm{c}}/V^{\mathrm{c}}\,, \tag{9.3b}$$

where C_{i} and $C_{\mathrm{i}}^{\mathrm{e}}$ are the IC and EC molar concentrations of ion i per unit reference volume of the IC and EC spaces, $\mathbf{J}_{\mathrm{i}}$ and $\mathbf{J}_{\mathrm{i}}^{\mathrm{e}}$ are the IC and EC nominal molar fluxes of ion i, and $J_{\mathrm{i}}^{\mathrm{m}}$ is the transmembrane nominal molar flux of ion i.

For the sake of clarity, $\mathbf{J}_{\mathrm{w}}$ and $\mathbf{J}_{\mathrm{i}}$, $\mathbf{J}_{\mathrm{w}}^{\mathrm{e}}$ and $\mathbf{J}_{\mathrm{i}}^{\mathrm{e}}$, and $J_{\mathrm{w}}^{\mathrm{m}}$ and $J_{\mathrm{i}}^{\mathrm{m}}$ represent the water and ion fluxes between cells through gap junctions (GJs), in the interconnected intercellular spaces, and across cell membranes through aquaporins and ion channels, respectively.

Finally, the Gauss laws for the IC and EC electric potentials ψ and ψ^{e} read

$$\mathrm{Div}\,\mathbf{D} = \Phi_0 F \sum_{\mathrm{i}} z_{\mathrm{i}} C_{\mathrm{i}}\,, \tag{9.4a}$$

$$\mathrm{Div}\,\mathbf{D}^{\mathrm{e}} = \Phi_0^{\mathrm{e}} F \sum_{\mathrm{i}} z_{\mathrm{i}} C_{\mathrm{i}}^{\mathrm{e}}\,, \tag{9.4b}$$

where $\mathbf{D}$ and $\mathbf{D}^{\mathrm{e}}$ are the IC and EC nominal electric displacements, F is the Faraday constant, and z_{i} is the valency of ion i. The terms on the right-hand sides represent the IC and EC nominal free charges, and account for both mobile and fixed ions.

9.2.2 Boundary and initial conditions

In our benchmark, we consider that the cluster is traction-free, that is, we supplement Eq. (9.1) with the boundary condition

$$\mathbf{PN} = \mathbf{0}\,, \tag{9.5}$$

where $\mathbf{N}$ is the outward unit normal to the reference boundary.

The initial conditions for the mass balances (9.2) and (9.3) read

$$C_{\mathrm{w}} = C_{\mathrm{w}}^{0}\,, \quad C_{\mathrm{w}}^{\mathrm{e}} = C_{\mathrm{w}}^{\mathrm{e},0}\,, \tag{9.6a}$$

$$C_{\mathrm{i}} = C_{\mathrm{i}}^{0}\,, \quad C_{\mathrm{i}}^{\mathrm{e}} = C_{\mathrm{i}}^{\mathrm{e},0}\,. \tag{9.6b}$$

We assume that water and ions can be exchanged with the bath surrounding the cluster through the EC space only, provided that tight junctions (TJs) are absent. Therefore, we equip Eqs. (9.2a) and (9.3a) with the boundary conditions

$$\mathbf{J}_{\mathrm{w}} \cdot \mathbf{N} = 0\,, \tag{9.7a}$$

$$\mathbf{J}_{\mathrm{i}} \cdot \mathbf{N} = 0\,, \tag{9.7b}$$

where the symbol $\cdot$ denotes the inner product.

As for Eqs. (9.2b) and (9.3b), in the absence of TJs we impose chemical equilibrium at the boundary, that is

$$\mu_{\mathrm{w}}^{\mathrm{e}} = \bar{\mu}_{\mathrm{w}} = \mu_{\mathrm{w}}^{\mathrm{e},0}\,, \tag{9.8a}$$

$$\mu_{\mathrm{i}}^{\mathrm{e}} = \bar{\mu}_{\mathrm{i}} = \mu_{\mathrm{i}}^{\mathrm{e},0}\,, \tag{9.8b}$$

where $\mu_{\mathrm{w}}^{\mathrm{e}}$ and $\mu_{\mathrm{i}}^{\mathrm{e}}$ are the EC chemical potentials of water and ion i, coinciding with those of the bath $\bar{\mu}_{\mathrm{w}}$ and $\bar{\mu}_{\mathrm{i}}$, in turn supposed to be equal to the initial EC ones. Instead, in the presence of sealing TJs, we impose the boundary conditions

$$\mathbf{J}_{\mathrm{w}}^{\mathrm{e}} \cdot \mathbf{N} = 0\,, \tag{9.9a}$$

$$\mathbf{J}_{\mathrm{i}}^{\mathrm{e}} \cdot \mathbf{N} = 0\,. \tag{9.9b}$$

Therefore, we assume that TJs are completely impermeable to both water and ions.

We assign to Eq. (9.4a) the boundary condition

$$\mathbf{D}\cdot\mathbf{N} = \bar{D}^{\mathrm{m}}\,, \tag{9.10}$$

in which $\bar{D}^{\mathrm{m}}$ is the transmembrane electric displacement at the boundary, which will be defined in Sec. 9.2.6.

As for Eq. (9.4b), in the absence of TJs we impose electrical equilibrium, that is

$$\psi^{\mathrm{e}} = \bar{\psi} = 0\,, \tag{9.11}$$

where $\bar{\psi}$ is the electric potential of the bath, assumed to be zero. Instead, in the presence of TJs, we impose

$$\mathbf{D}^{\mathrm{e}}\cdot\mathbf{N} = \bar{D}^{\mathrm{tj}}\,, \tag{9.12}$$

with $\bar{D}^{\mathrm{tj}}$ denoting the electric displacement across the TJs, which will be defined in Sec. 9.2.6.

While in the present work we focus on *endogenous* mechanobioelectricity, we remark that our framework may be also adopted to investigate the effect of an externally applied mechanical load or electric field, or of the exposure to an hypotonic or hypertonic environment, by enforcing appropriate boundary conditions.

9.2.3 Thermodynamic restrictions

We follow the approach of Gurtin et al. (2010) for coupled problems of mechanics and species transport, suitably augmented to account for the electric charge of ions. Therefore, under isothermal conditions, the energy balance reads

$$\begin{aligned}\dot{U} = {}& \mathbf{P}\cdot\dot{\mathbf{F}} + \Phi_0\Big(\mu_{\mathrm{w}}\dot{C}_{\mathrm{w}} + \sum_{\mathrm{i}}\mu_{\mathrm{i}}\dot{C}_{\mathrm{i}}\Big) + \Phi_0^{\mathrm{e}}\Big(\mu_{\mathrm{w}}^{\mathrm{e}}\dot{C}_{\mathrm{w}}^{\mathrm{e}} + \sum_{\mathrm{i}}\mu_{\mathrm{i}}^{\mathrm{e}}\dot{C}_{\mathrm{i}}^{\mathrm{e}}\Big) + \mathbf{E}\cdot\dot{\mathbf{D}} + \mathbf{E}^{\mathrm{e}}\cdot\dot{\mathbf{D}}^{\mathrm{e}}\\ & - \mathbf{J}_{\mathrm{w}}\cdot\nabla\mu_{\mathrm{w}} - \sum_{\mathrm{i}}\mathbf{J}_{\mathrm{i}}\cdot\nabla\tilde{\mu}_{\mathrm{i}} - \mathbf{J}_{\mathrm{w}}^{\mathrm{e}}\cdot\nabla\mu_{\mathrm{w}}^{\mathrm{e}} - \sum_{\mathrm{i}}\mathbf{J}_{\mathrm{i}}^{\mathrm{e}}\cdot\nabla\tilde{\mu}_{\mathrm{i}}^{\mathrm{e}}\\ & - A^{\mathrm{c}}/V^{\mathrm{c}}\Big[J_{\mathrm{w}}^{\mathrm{m}}(\mu_{\mathrm{w}}^{\mathrm{e}} - \mu_{\mathrm{w}}) + \sum_{\mathrm{i}}J_{\mathrm{i}}^{\mathrm{m}}(\tilde{\mu}_{\mathrm{i}}^{\mathrm{e}} - \tilde{\mu}_{\mathrm{i}})\Big]\,,\end{aligned} \tag{9.13}$$

where U is the nominal internal energy density, $\mathbf{F} = \mathbf{I} + \nabla\mathbf{u}$ is the deformation gradient (with $\mathbf{I}$ denoting the second-order identity tensor and ∇ denoting the material gradient), μ_{w} and μ_{i} are the IC chemical potentials of water and ion i,

$$\mathbf{E} = -\nabla\psi\,, \quad \mathbf{E}^{\mathrm{e}} = -\nabla\psi^{\mathrm{e}} \tag{9.14}$$

are the IC and EC nominal electric fields, and

$$\tilde{\mu}_{\mathrm{i}} = \mu_{\mathrm{i}} + F z_{\mathrm{i}} \psi \,, \quad \tilde{\mu}^{\mathrm{e}}_{\mathrm{i}} = \mu^{\mathrm{e}}_{\mathrm{i}} + F z_{\mathrm{i}} \psi^{\mathrm{e}} \tag{9.15}$$

are the IC and EC electrochemical potentials of ion i.

Upon combining Eq. (9.13) with the second law of thermodynamics and introducing the nominal Helmholtz free energy density W, we obtain the free energy imbalance

$$\begin{aligned} -\dot{W} + \mathbf{P} \cdot \dot{\mathbf{F}} + \Phi_0 \Big(\mu_{\mathrm{w}} \dot{C}_{\mathrm{w}} + \sum_{\mathrm{i}} \mu_{\mathrm{i}} \dot{C}_{\mathrm{i}}\Big) + \Phi^{\mathrm{e}}_0 \Big(\mu^{\mathrm{e}}_{\mathrm{w}} \dot{C}^{\mathrm{e}}_{\mathrm{w}} + \sum_{\mathrm{i}} \mu^{\mathrm{e}}_{\mathrm{i}} \dot{C}^{\mathrm{e}}_{\mathrm{i}}\Big) + \mathbf{E} \cdot \dot{\mathbf{D}} + \mathbf{E}^{\mathrm{e}} \cdot \dot{\mathbf{D}}^{\mathrm{e}} \\ - \mathbf{J}_{\mathrm{w}} \cdot \nabla \mu_{\mathrm{w}} - \sum_{\mathrm{i}} \mathbf{J}_{\mathrm{i}} \cdot \nabla \tilde{\mu}_{\mathrm{i}} - \mathbf{J}^{\mathrm{e}}_{\mathrm{w}} \cdot \nabla \mu^{\mathrm{e}}_{\mathrm{w}} - \sum_{\mathrm{i}} \mathbf{J}^{\mathrm{e}}_{\mathrm{i}} \cdot \nabla \tilde{\mu}^{\mathrm{e}}_{\mathrm{i}} \\ - A^{\mathrm{c}}/V^{\mathrm{c}} \Big[J^{\mathrm{m}}_{\mathrm{w}} (\mu^{\mathrm{e}}_{\mathrm{w}} - \mu_{\mathrm{w}}) + \sum_{\mathrm{i}} J^{\mathrm{m}}_{\mathrm{i}} (\tilde{\mu}^{\mathrm{e}}_{\mathrm{i}} - \tilde{\mu}_{\mathrm{i}})\Big] \geq 0 \,. \end{aligned} \tag{9.16}$$

We assume that W is a function of the independent variables $\mathbf{F}$, C_{w}, C_{i}, $C^{\mathrm{e}}_{\mathrm{w}}$, $C^{\mathrm{e}}_{\mathrm{i}}$, $\mathbf{D}$, and $\mathbf{D}^{\mathrm{e}}$, such that Eq. (9.16) becomes

$$\begin{aligned} \left(\mathbf{P} - \frac{\partial W}{\partial \mathbf{F}}\right) \cdot \dot{\mathbf{F}} + \left(\Phi_0 \mu_{\mathrm{w}} - \frac{\partial W}{\partial C_{\mathrm{w}}}\right) \dot{C}_{\mathrm{w}} + \sum_{\mathrm{i}} \left(\Phi_0 \mu_{\mathrm{i}} - \frac{\partial W}{\partial C_{\mathrm{i}}}\right) \dot{C}_{\mathrm{i}} \\ + \left(\Phi^{\mathrm{e}}_0 \mu^{\mathrm{e}}_{\mathrm{w}} - \frac{\partial W}{\partial C^{\mathrm{e}}_{\mathrm{w}}}\right) \dot{C}^{\mathrm{e}}_{\mathrm{w}} + \sum_{\mathrm{i}} \left(\Phi^{\mathrm{e}}_0 \mu^{\mathrm{e}}_{\mathrm{i}} - \frac{\partial W}{\partial C^{\mathrm{e}}_{\mathrm{i}}}\right) \dot{C}^{\mathrm{e}}_{\mathrm{i}} + \left(\mathbf{E} - \frac{\partial W}{\partial \mathbf{D}}\right) \cdot \dot{\mathbf{D}} \\ + \left(\mathbf{E}^{\mathrm{e}} - \frac{\partial W}{\partial \mathbf{D}^{\mathrm{e}}}\right) \cdot \dot{\mathbf{D}}^{\mathrm{e}} - \mathbf{J}_{\mathrm{w}} \cdot \nabla \mu_{\mathrm{w}} - \sum_{\mathrm{i}} \mathbf{J}_{\mathrm{i}} \cdot \nabla \tilde{\mu}_{\mathrm{i}} - \mathbf{J}^{\mathrm{e}}_{\mathrm{w}} \cdot \nabla \mu^{\mathrm{e}}_{\mathrm{w}} - \sum_{\mathrm{i}} \mathbf{J}^{\mathrm{e}}_{\mathrm{i}} \cdot \nabla \tilde{\mu}^{\mathrm{e}}_{\mathrm{i}} \\ - A^{\mathrm{c}}/V^{\mathrm{c}} \Big[J^{\mathrm{m}}_{\mathrm{w}} (\mu^{\mathrm{e}}_{\mathrm{w}} - \mu_{\mathrm{w}}) + \sum_{\mathrm{i}} J^{\mathrm{m}}_{\mathrm{i}} (\tilde{\mu}^{\mathrm{e}}_{\mathrm{i}} - \tilde{\mu}_{\mathrm{i}})\Big] \geq 0 \,. \end{aligned} \tag{9.17}$$

By relying on the Coleman-Noll procedure, we obtain the following constitutive prescriptions:

$$\mathbf{P} = \frac{\partial W}{\partial \mathbf{F}} \,, \tag{9.18a}$$

$$\mu_{\mathrm{w}} = \frac{1}{\Phi_0} \frac{\partial W}{\partial C_{\mathrm{w}}} \,, \quad \mu^{\mathrm{e}}_{\mathrm{w}} = \frac{1}{\Phi^{\mathrm{e}}_0} \frac{\partial W}{\partial C^{\mathrm{e}}_{\mathrm{w}}} \,, \tag{9.18b}$$

$$\mu_{\mathrm{i}} = \frac{1}{\Phi_0} \frac{\partial W}{\partial C_{\mathrm{i}}} \,, \quad \mu^{\mathrm{e}}_{\mathrm{i}} = \frac{1}{\Phi^{\mathrm{e}}_0} \frac{\partial W}{\partial C^{\mathrm{e}}_{\mathrm{i}}} \,, \tag{9.18c}$$

$$\mathbf{E} = \frac{\partial W}{\partial \mathbf{D}} \,, \quad \mathbf{E}^{\mathrm{e}} = \frac{\partial W}{\partial \mathbf{D}^{\mathrm{e}}} \,. \tag{9.18d}$$

Consequently, Eq. (9.17) reduces to the dissipation inequality

$$
\begin{aligned}
-\mathbf{J}_{\mathrm{w}}\cdot\nabla\mu_{\mathrm{w}} - \sum_{\mathrm{i}}\mathbf{J}_{\mathrm{i}}\cdot\nabla\tilde{\mu}_{\mathrm{i}} - \mathbf{J}^{\mathrm{e}}_{\mathrm{w}}\cdot\nabla\mu^{\mathrm{e}}_{\mathrm{w}} - \sum_{\mathrm{i}}\mathbf{J}^{\mathrm{e}}_{\mathrm{i}}\cdot\nabla\tilde{\mu}^{\mathrm{e}}_{\mathrm{i}} \\
- A^{\mathrm{c}}/V^{\mathrm{c}}\Big[J^{\mathrm{m}}_{\mathrm{w}}(\mu^{\mathrm{e}}_{\mathrm{w}}-\mu_{\mathrm{w}}) + \sum_{\mathrm{i}} J^{\mathrm{m}}_{\mathrm{i}}(\tilde{\mu}^{\mathrm{e}}_{\mathrm{i}}-\tilde{\mu}_{\mathrm{i}})\Big] \geq 0\,. \qquad (9.19)
\end{aligned}
$$

We remark that the terms in the second line are local dissipation terms, arising from the exchange of water and ions across the cell membrane within the same material point.

Since water and ions share the same IC and EC spaces, we assume that each IC or EC flux is affected by the chemical potential gradient of water and by the electrochemical potential gradients of all mobile ions, that is,

$$\mathbf{J}_{\mathrm{w}} = -\mathbf{M}_{\mathrm{ww}}\nabla\mu_{\mathrm{w}} - \sum_{\mathrm{i}}\mathbf{M}_{\mathrm{wi}}\nabla\tilde{\mu}_{\mathrm{i}}\,, \qquad (9.20\mathrm{a})$$

$$\mathbf{J}_{\mathrm{i}} = -\mathbf{M}_{\mathrm{wi}}\nabla\mu_{\mathrm{w}} - \mathbf{M}_{\mathrm{ii}}\nabla\tilde{\mu}_{\mathrm{i}} - \sum_{\mathrm{j}}\mathbf{M}_{\mathrm{ij}}\nabla\tilde{\mu}_{\mathrm{j}}\,, \quad \mathrm{j}\neq\mathrm{i}\,, \qquad (9.20\mathrm{b})$$

$$\mathbf{J}^{\mathrm{e}}_{\mathrm{w}} = -\mathbf{M}^{\mathrm{e}}_{\mathrm{ww}}\nabla\mu^{\mathrm{e}}_{\mathrm{w}} - \sum_{\mathrm{i}}\mathbf{M}^{\mathrm{e}}_{\mathrm{wi}}\nabla\tilde{\mu}^{\mathrm{e}}_{\mathrm{i}}\,, \qquad (9.20\mathrm{c})$$

$$\mathbf{J}^{\mathrm{e}}_{\mathrm{i}} = -\mathbf{M}^{\mathrm{e}}_{\mathrm{wi}}\nabla\mu^{\mathrm{e}}_{\mathrm{w}} - \mathbf{M}^{\mathrm{e}}_{\mathrm{ii}}\nabla\tilde{\mu}^{\mathrm{e}}_{\mathrm{i}} - \sum_{\mathrm{j}}\mathbf{M}^{\mathrm{e}}_{\mathrm{ij}}\nabla\tilde{\mu}^{\mathrm{e}}_{\mathrm{j}}\,, \quad \mathrm{j}\neq\mathrm{i}\,, \qquad (9.20\mathrm{d})$$

where the constitutive operators can be collected into the symmetric (Onsager, 1931) mobility matrices

$$\underline{\underline{M}} = \begin{bmatrix} \mathbf{M}_{\mathrm{ww}} & \mathbf{M}_{\mathrm{w1}} & \mathbf{M}_{\mathrm{w2}} & \dots \\ \mathbf{M}_{\mathrm{w1}} & \mathbf{M}_{11} & \mathbf{M}_{12} & \dots \\ \mathbf{M}_{\mathrm{w2}} & \mathbf{M}_{12} & \mathbf{M}_{22} & \dots \\ \vdots & \vdots & \vdots & \ddots \end{bmatrix}, \qquad (9.21\mathrm{a})$$

$$\underline{\underline{M}}^{\mathrm{e}} = \begin{bmatrix} \mathbf{M}^{\mathrm{e}}_{\mathrm{ww}} & \mathbf{M}^{\mathrm{e}}_{\mathrm{w1}} & \mathbf{M}^{\mathrm{e}}_{\mathrm{w2}} & \dots \\ \mathbf{M}^{\mathrm{e}}_{\mathrm{w1}} & \mathbf{M}^{\mathrm{e}}_{11} & \mathbf{M}^{\mathrm{e}}_{12} & \dots \\ \mathbf{M}^{\mathrm{e}}_{\mathrm{w2}} & \mathbf{M}^{\mathrm{e}}_{12} & \mathbf{M}^{\mathrm{e}}_{22} & \dots \\ \vdots & \vdots & \vdots & \ddots \end{bmatrix}, \qquad (9.21\mathrm{b})$$

in which the off-diagonal entries account for the so-called *cross-diffusion* (Vanag and Epstein, 2009).

Conversely, aquaporins and ion channels are specific for water and ion transport. Therefore, the transmembrane fluxes of water and ion i only depend on the difference between the EC and IC chemical potentials of water and electrochemical potentials of ion i, respectively:

$$J_{\mathrm{w}}^{\mathrm{m}} = -M_{\mathrm{w}}^{\mathrm{m}}(\mu_{\mathrm{w}}^{\mathrm{e}} - \mu_{\mathrm{w}})\,, \tag{9.22a}$$

$$J_{\mathrm{i}}^{\mathrm{m}} = -M_{\mathrm{i}}^{\mathrm{m}}(\tilde{\mu}_{\mathrm{i}}^{\mathrm{e}} - \tilde{\mu}_{\mathrm{i}})\,. \tag{9.22b}$$

We assume the mobility matrices $\underline{\underline{M}}$ and $\underline{\underline{M}}^{\mathrm{e}}$ to be positive definite and the mobility coefficients $M_{\mathrm{w}}^{\mathrm{m}}$ and $M_{\mathrm{i}}^{\mathrm{m}}$ to be positive, in order to fulfill Eq. (9.19), as detailed in Sec. 9.2.7.

9.2.4 Free energy density

We choose the following additive decomposition for the free energy density:

$$W = W_{\mathrm{mec}}(\mathbf{F}) + W_{\mathrm{mix}}(C_{\mathrm{w}}, C_{\mathrm{i}}) + W_{\mathrm{mix}}^{\mathrm{e}}(C_{\mathrm{w}}^{\mathrm{e}}, C_{\mathrm{i}}^{\mathrm{e}}) \\ + W_{\mathrm{pol}}(\mathbf{F}, \mathbf{D}) + W_{\mathrm{pol}}^{\mathrm{e}}(\mathbf{F}, \mathbf{D}^{\mathrm{e}})\,, \tag{9.23}$$

where W_{mec} accounts for the elasticity of the cluster, W_{mix} and $W_{\mathrm{mix}}^{\mathrm{e}}$ account for the mixing of water and ions in the IC and EC spaces, and W_{pol} and $W_{\mathrm{pol}}^{\mathrm{e}}$ account for the dielectric polarization of the IC and EC spaces.

We adopt for W_{mec} the compressible Neo-Hookean model proposed by Simo and Pister (1984):

$$W_{\mathrm{mec}}(\mathbf{F}) = \frac{G}{2}(\operatorname{tr}\mathbf{C} - 3) - G\ln J + \frac{1}{2}\lambda \ln^2 J\,, \tag{9.24}$$

where λ and G are the first and second Lamé parameters, $\mathbf{C} = \mathbf{F}^{\mathrm{T}}\mathbf{F}$ is the right Cauchy-Green deformation tensor, and

$$J = \det \mathbf{F} \tag{9.25}$$

is the Jacobian, that is, the volume ratio.

We assume the IC and EC solutions of water and ions to be ideal, such that W_{mix} and $W_{\mathrm{mix}}^{\mathrm{e}}$ are purely entropic and read (Ateshian, 2007)

$$W_{\mathrm{mix}}(C_{\mathrm{w}}, C_{\mathrm{i}}) = \mathcal{R}T\Phi_0 \\ \times \left(C_{\mathrm{w}} \ln \frac{C_{\mathrm{w}}}{C_{\mathrm{w}} + \sum_{\mathrm{j}} C_{\mathrm{j}}} + \sum_{\mathrm{i}} C_{\mathrm{i}} \ln \frac{C_{\mathrm{i}}}{C_{\mathrm{w}} + \sum_{\mathrm{j}} C_{\mathrm{j}}} \right)\,, \tag{9.26a}$$

$$W^{\mathrm{e}}_{\mathrm{mix}}(C^{\mathrm{e}}_{\mathrm{w}}, C^{\mathrm{e}}_{\mathrm{i}}) = \mathcal{R}T\Phi^{\mathrm{e}}_0 \times \left(C^{\mathrm{e}}_{\mathrm{w}} \ln \frac{C^{\mathrm{e}}_{\mathrm{w}}}{C^{\mathrm{e}}_{\mathrm{w}} + \sum_{\mathrm{j}} C^{\mathrm{e}}_{\mathrm{j}}} + \sum_{\mathrm{i}} C^{\mathrm{e}}_{\mathrm{i}} \ln \frac{C^{\mathrm{e}}_{\mathrm{i}}}{C^{\mathrm{e}}_{\mathrm{w}} + \sum_{\mathrm{j}} C^{\mathrm{e}}_{\mathrm{j}}} \right) , \tag{9.26b}$$

where $\mathcal{R}$ is the gas constant and T is the absolute temperature. We underline that W_{mix} and $W^{\mathrm{e}}_{\mathrm{mix}}$ account for both mobile and fixed ions, also the latter being part of the IC and EC solutions. We further hypothesize that the IC and EC solutions are dilute, that is, $\sum_{\mathrm{i}} C_{\mathrm{i}} \ll C_{\mathrm{w}}$ and $\sum_{\mathrm{i}} C^{\mathrm{e}}_{\mathrm{i}} \ll C^{\mathrm{e}}_{\mathrm{w}}$, such that we may rewrite Eqs. (9.26) as

$$W_{\mathrm{mix}}(C_{\mathrm{w}}, C_{\mathrm{i}}) = \mathcal{R}T\Phi_0 \sum_{\mathrm{i}} C_{\mathrm{i}} \left(\ln \frac{C_{\mathrm{i}}}{C_{\mathrm{w}}} - 1 \right) , \tag{9.27a}$$

$$W^{\mathrm{e}}_{\mathrm{mix}}(C^{\mathrm{e}}_{\mathrm{w}}, C^{\mathrm{e}}_{\mathrm{i}}) = \mathcal{R}T\Phi^{\mathrm{e}}_0 \sum_{\mathrm{i}} C^{\mathrm{e}}_{\mathrm{i}} \left(\ln \frac{C^{\mathrm{e}}_{\mathrm{i}}}{C^{\mathrm{e}}_{\mathrm{w}}} - 1 \right) . \tag{9.27b}$$

Finally, we treat the IC and EC solutions as ideal dielectrics, such that W_{pol} and $W^{\mathrm{e}}_{\mathrm{pol}}$ read (Hong et al., 2010)

$$W_{\mathrm{pol}}(\mathbf{F}, \mathbf{D}) = \frac{|\mathbf{F}\mathbf{D}|^2}{2\varepsilon_0\varepsilon_{\mathrm{r}}J} , \tag{9.28a}$$

$$W^{\mathrm{e}}_{\mathrm{pol}}(\mathbf{F}, \mathbf{D}^{\mathrm{e}}) = \frac{|\mathbf{F}\mathbf{D}^{\mathrm{e}}|^2}{2\varepsilon_0\varepsilon_{\mathrm{r}}J} , \tag{9.28b}$$

in which ε_0 is the vacuum permittivity and ε_{r} is the relative permittivity of the IC and EC solutions, assumed to coincide with that of water given their diluteness.

9.2.5 Constraint on the volumetric deformation

We assume that the solid phase, water, and ions are incompressible, such that the volume ratio of Eq. (9.25) is inextricably related to the redistribution of water and ions, namely

$$J = 1 + \Phi_0 \Big(v_{\mathrm{w}} C_{\mathrm{w}} + \sum_{\mathrm{i}} v_{\mathrm{i}} C_{\mathrm{i}} - 1 \Big) + \Phi^{\mathrm{e}}_0 \Big(v_{\mathrm{w}} C^{\mathrm{e}}_{\mathrm{w}} + \sum_{\mathrm{i}} v_{\mathrm{i}} C^{\mathrm{e}}_{\mathrm{i}} - 1 \Big) , \tag{9.29}$$

where v_{w} and v_{i} are the molar volumes of water and ion i. In the limit of dilute IC and EC solutions, Eq. (9.29) reduces to

$$J = 1 + \Phi_0 \Big(v_{\mathrm{w}} C_{\mathrm{w}} - 1 \Big) + \Phi^{\mathrm{e}}_0 \Big(v_{\mathrm{w}} C^{\mathrm{e}}_{\mathrm{w}} - 1 \Big) , \tag{9.30}$$

implying that

$$C_{\mathrm{w}}^{0} = C_{\mathrm{w}}^{\mathrm{e},0} = \frac{1}{v_{\mathrm{w}}}\,, \tag{9.31}$$

to be replaced in Eq. (9.6a). Moreover:

$$c_{\mathrm{i}} = \frac{C_{\mathrm{i}}}{v_{\mathrm{w}} C_{\mathrm{w}}}\,, \qquad c_{\mathrm{i}}^{\mathrm{e}} = \frac{C_{\mathrm{i}}^{\mathrm{e}}}{v_{\mathrm{w}} C_{\mathrm{w}}^{\mathrm{e}}} \tag{9.32}$$

are the IC and EC molar concentrations of ion i per unit *current* volume of the IC and EC spaces.

In order to impose the constraint (9.30), we modify the free energy density (9.23) as (Hong et al., 2010)

$$\begin{aligned} W = {} & W_{\mathrm{mec}}(\mathbf{F}) + W_{\mathrm{mix}}(C_{\mathrm{w}}, C_{\mathrm{i}}) + W_{\mathrm{mix}}^{\mathrm{e}}(C_{\mathrm{w}}^{\mathrm{e}}, C_{\mathrm{i}}^{\mathrm{e}}) + W_{\mathrm{pol}}(\mathbf{F}, \mathbf{D}) + W_{\mathrm{pol}}^{\mathrm{e}}(\mathbf{F}, \mathbf{D}^{\mathrm{e}}) \\ & + p_{\mathrm{w}} \left[1 + \Phi_0 \Big(v_{\mathrm{w}} C_{\mathrm{w}} - 1 \Big) + \Phi_0^{\mathrm{e}} \Big(v_{\mathrm{w}} C_{\mathrm{w}}^{\mathrm{e}} - 1 \Big) - J \right]\,, \end{aligned} \tag{9.33}$$

where p_{w} is a Lagrange multiplier field assuming the role of water pressure. For later developments, we rearrange Eq. (9.30) for the IC water concentration:

$$C_{\mathrm{w}} = \frac{1}{v_{\mathrm{w}}} + \frac{1}{\Phi_0 v_{\mathrm{w}}} \left[J - 1 - \Phi_0^{\mathrm{e}} \Big(v_{\mathrm{w}} C_{\mathrm{w}}^{\mathrm{e}} - 1 \Big) \right]\,. \tag{9.34}$$

Notably, this operation removes C_{w} from the list of the independent variables, in favor of the independent variable p_{w} introduced by Eq. (9.33).

9.2.6 Conservative constitutive laws

We obtain the nominal stress $\mathbf{P}$ by combining Eqs. (9.18a), (9.24), and (9.33):

$$\begin{aligned} \mathbf{P} = {} & \underbrace{G(\mathbf{F} - \mathbf{F}^{-\mathrm{T}}) + \lambda \ln J \mathbf{F}^{-\mathrm{T}}}_{\mathbf{P}_{\mathrm{mec}}} + \underbrace{\frac{1}{2\varepsilon_0\varepsilon_{\mathrm{r}} J} \left[2\mathbf{F}(\mathbf{D} \otimes \mathbf{D}) - \mathbf{C} \cdot (\mathbf{D} \otimes \mathbf{D}) \mathbf{F}^{-\mathrm{T}} \right]}_{\mathbf{P}_{\mathrm{pol}}} \\ & + \underbrace{\frac{1}{2\varepsilon_0\varepsilon_{\mathrm{r}} J} \left[2\mathbf{F}(\mathbf{D}^{\mathrm{e}} \otimes \mathbf{D}^{\mathrm{e}}) - \mathbf{C} \cdot (\mathbf{D}^{\mathrm{e}} \otimes \mathbf{D}^{\mathrm{e}}) \mathbf{F}^{-\mathrm{T}} \right]}_{\mathbf{P}_{\mathrm{pol}}^{\mathrm{e}}} \underbrace{- p_{\mathrm{w}} J \mathbf{F}^{-\mathrm{T}}}_{\mathbf{P}_{\mathrm{w}}}\,, \end{aligned} \tag{9.35}$$

where $\otimes$ denotes the tensor product. The stresses $\mathbf{P}_{\mathrm{pol}}$ and $\mathbf{P}_{\mathrm{pol}}^{\mathrm{e}}$ are the electrostatic (or Maxwell) nominal stresses in the IC and EC spaces, while $\mathbf{P}_{\mathrm{w}}$ is the nominal stress due to water pressure. These could be regarded as *active* stresses (or *eigenstresses*), to be balanced by the mechanical nominal stress $\mathbf{P}_{\mathrm{mec}}$ through equilibrium (9.1). Therefore, $\mathbf{P}$ is the *total* nominal stress. The corresponding total Cauchy stress is

$$\boldsymbol{\sigma} = \frac{1}{J}\mathbf{P}\mathbf{F}^{\mathrm{T}} = \underbrace{\frac{1}{J}\Big[G(\mathbf{b}-\mathbf{I}) + \lambda \ln J\mathbf{I}\Big]}_{\boldsymbol{\sigma}_{\mathrm{mec}}} + \underbrace{\frac{1}{2\varepsilon_0\varepsilon_{\mathrm{r}}}\Big[2\mathbf{d}\otimes\mathbf{d} - (\mathbf{d}\cdot\mathbf{d})\mathbf{I}\Big]}_{\boldsymbol{\sigma}_{\mathrm{pol}}} + \underbrace{\frac{1}{2\varepsilon_0\varepsilon_{\mathrm{r}}}\Big[2\mathbf{d}^{\mathrm{e}}\otimes\mathbf{d}^{\mathrm{e}} - (\mathbf{d}^{\mathrm{e}}\cdot\mathbf{d}^{\mathrm{e}})\mathbf{I}\Big]}_{\boldsymbol{\sigma}^{\mathrm{e}}_{\mathrm{pol}}} \underbrace{-p_{\mathrm{w}}\mathbf{I}}_{\boldsymbol{\sigma}_{\mathrm{w}}}, \tag{9.36}$$

where $\mathbf{b} = \mathbf{F}\mathbf{F}^{\mathrm{T}}$ is the left Cauchy-Green deformation tensor and $\mathbf{d} = J^{-1}\mathbf{F}\mathbf{D}$ and $\mathbf{d}^{\mathrm{e}} = J^{-1}\mathbf{F}\mathbf{D}^{\mathrm{e}}$ are the IC and EC current electric displacements. We define the total pressure, positive if compressive, as

$$p = -\frac{1}{3}\operatorname{tr}\boldsymbol{\sigma} = \underbrace{-\frac{1}{J}\left[G\left(\frac{1}{3}\operatorname{tr}\mathbf{b} - 1\right) + \lambda \ln J\right]}_{p_{\mathrm{mec}}} + \underbrace{\frac{1}{6\varepsilon_0\varepsilon_{\mathrm{r}}}|\mathbf{d}|^2}_{p_{\mathrm{pol}}} + \underbrace{\frac{1}{6\varepsilon_0\varepsilon_{\mathrm{r}}}|\mathbf{d}^{\mathrm{e}}|^2}_{p^{\mathrm{e}}_{\mathrm{pol}}} + p_{\mathrm{w}} \,. \tag{9.37}$$

By using Eqs. (9.18b), (9.27), and (9.33) we obtain the following IC and EC chemical potentials of water:

$$\mu_{\mathrm{w}} = -\mathcal{R}T\frac{C}{C_{\mathrm{w}}} + v_{\mathrm{w}}p_{\mathrm{w}}\,, \quad \mu^{\mathrm{e}}_{\mathrm{w}} = -\mathcal{R}T\frac{C^{\mathrm{e}}}{C^{\mathrm{e}}_{\mathrm{w}}} + v_{\mathrm{w}}p_{\mathrm{w}}\,, \tag{9.38}$$

where

$$C = \sum_{\mathrm{i}} C_{\mathrm{i}}\,, \quad C^{\mathrm{e}} = \sum_{\mathrm{i}} C^{\mathrm{e}}_{\mathrm{i}} \tag{9.39}$$

are the IC and EC osmotic concentrations. We remark that μ_{w} and $\mu^{\mathrm{e}}_{\mathrm{w}}$ are affected by both the IC and EC osmotic pressures $\mathcal{R}TC$ and $\mathcal{R}TC^{\mathrm{e}}$ and the water pressure p_{w}. Boundary condition (9.8a) may now be explicited for the independent variable $C^{\mathrm{e}}_{\mathrm{w}}$, thus reading

$$C^{\mathrm{e}}_{\mathrm{w}} = \frac{\mathcal{R}TC^{\mathrm{e}}}{v_{\mathrm{w}}\left(\mathcal{R}TC^{\mathrm{e},0} + p_{\mathrm{w}}\right)}\,, \tag{9.40}$$

where we have used

$$p^0_{\mathrm{w}} = 0\,. \tag{9.41}$$

By combining Eqs. (9.15), (9.18c), (9.27), and (9.33) we obtain the following IC and EC electrochemical potentials of ion i:

$$\tilde{\mu}_{\mathrm{i}} = \mathcal{R}T\ln\frac{C_{\mathrm{i}}}{C_{\mathrm{w}}} + Fz_{\mathrm{i}}\psi\,, \quad \tilde{\mu}^{\mathrm{e}}_{\mathrm{i}} = \mathcal{R}T\ln\frac{C^{\mathrm{e}}_{\mathrm{i}}}{C^{\mathrm{e}}_{\mathrm{w}}} + Fz_{\mathrm{i}}\psi^{\mathrm{e}}\,. \tag{9.42}$$

Boundary condition (9.8b) may now be explicited for the independent variable $C_{\mathrm{i}}^{\mathrm{e}}$, thus reading

$$C_{\mathrm{i}}^{\mathrm{e}} = v_{\mathrm{w}} C_{\mathrm{i}}^{\mathrm{e},0} C_{\mathrm{w}}^{\mathrm{e}} \,. \tag{9.43}$$

Finally, the usage of Eqs. (9.14), (9.18d), (9.28), and (9.33) provides the IC and EC nominal electric fields, whose inversion results in the IC and EC nominal electric displacements

$$\mathbf{D} = -\varepsilon_0 \varepsilon_{\mathrm{r}} J \mathbf{C}^{-1} \nabla \psi \,, \quad \mathbf{D}^{\mathrm{e}} = -\varepsilon_0 \varepsilon_{\mathrm{r}} J \mathbf{C}^{-1} \nabla \psi^{\mathrm{e}} \,. \tag{9.44}$$

Similarly, the electric displacements at the boundary across the cell membranes and the TJs in Eqs. (9.10) and (9.12) are given by

$$\bar{D}^{\mathrm{m}} = \varepsilon_0 \varepsilon_{\mathrm{r}}^{\mathrm{m}} \frac{\psi - \bar{\psi}}{T^{\mathrm{m}}} = \varepsilon_0 \varepsilon_{\mathrm{r}}^{\mathrm{m}} \frac{\psi}{T^{\mathrm{m}}} \,, \tag{9.45a}$$

$$\bar{D}^{\mathrm{tj}} = \varepsilon_0 \varepsilon_{\mathrm{r}}^{\mathrm{tj}} \frac{\psi^{\mathrm{e}} - \bar{\psi}}{T^{\mathrm{tj}}} = \varepsilon_0 \varepsilon_{\mathrm{r}}^{\mathrm{tj}} \frac{\psi^{\mathrm{e}}}{T^{\mathrm{tj}}} \,, \tag{9.45b}$$

in which $\varepsilon_{\mathrm{r}}^{\mathrm{m}}$ and $\varepsilon_{\mathrm{r}}^{\mathrm{tj}}$ and T^{m} and T^{tj} are the membrane and TJ relative permittivities and thicknesses, respectively. We remark that Eqs. (9.45) neglects the local deformation of the cell membranes and TJs.

9.2.7 Dissipative constitutive laws

We choose the following form for the IC and EC mobility matrices of Eqs. (9.21):

$$\begin{aligned} \underline{\underline{M}} = {} & \frac{1}{\mathcal{R}T} \mathbf{C}^{-1} \\ & \times \begin{bmatrix} D_{\mathrm{w}} C_{\mathrm{w}} & D_{\mathrm{w}} C_1 & D_{\mathrm{w}} C_2 & \dots \\ D_{\mathrm{w}} C_1 & \left(D_{\mathrm{w}} \dfrac{C_1}{C_{\mathrm{w}}} + D_1 \right) C_1 & D_{\mathrm{w}} \dfrac{C_1 C_2}{C_{\mathrm{w}}} & \dots \\ D_{\mathrm{w}} C_2 & D_{\mathrm{w}} \dfrac{C_1 C_2}{C_{\mathrm{w}}} & \left(D_{\mathrm{w}} \dfrac{C_2}{C_{\mathrm{w}}} + D_2 \right) C_2 & \dots \\ \vdots & \vdots & \vdots & \ddots \end{bmatrix} , \end{aligned} \tag{9.46a}$$

$$\underline{\underline{M}}^{\mathrm{e}} = \frac{1}{\mathcal{R}T}\mathbf{C}^{-1} \times \begin{bmatrix} D^{\mathrm{e}}_{\mathrm{w}} C^{\mathrm{e}}_{\mathrm{w}} & D^{\mathrm{e}}_{\mathrm{w}} C^{\mathrm{e}}_{1} & D^{\mathrm{e}}_{\mathrm{w}} C^{\mathrm{e}}_{2} & \dots \\ D^{\mathrm{e}}_{\mathrm{w}} C^{\mathrm{e}}_{1} & \left(D^{\mathrm{e}}_{\mathrm{w}} \frac{C^{\mathrm{e}}_{1}}{C^{\mathrm{e}}_{\mathrm{w}}} + D^{\mathrm{e}}_{1} \right) C^{\mathrm{e}}_{1} & D^{\mathrm{e}}_{\mathrm{w}} \frac{C^{\mathrm{e}}_{1} C^{\mathrm{e}}_{2}}{C^{\mathrm{e}}_{\mathrm{w}}} & \dots \\ D^{\mathrm{e}}_{\mathrm{w}} C^{\mathrm{e}}_{2} & D^{\mathrm{e}}_{\mathrm{w}} \frac{C^{\mathrm{e}}_{1} C^{\mathrm{e}}_{2}}{C^{\mathrm{e}}_{\mathrm{w}}} & \left(D^{\mathrm{e}}_{\mathrm{w}} \frac{C^{\mathrm{e}}_{2}}{C^{\mathrm{e}}_{\mathrm{w}}} + D^{\mathrm{e}}_{2} \right) C^{\mathrm{e}}_{2} & \dots \\ \vdots & \vdots & \vdots & \ddots \end{bmatrix}, \tag{9.46b}$$

in which D_{w} and $D^{\mathrm{e}}_{\mathrm{w}}$ are the water diffusivities in the IC and EC spaces, while D_{i} and $D^{\mathrm{e}}_{\mathrm{i}}$ are the diffusivities of ion i in the IC and EC water. As for the transmembrane mobility coefficients of Eqs. (9.22), by still neglecting the local deformation of the membrane, we adopt the forms

$$M^{\mathrm{m}}_{\mathrm{w}} = \frac{D^{\mathrm{m}}_{\mathrm{w}}}{\mathcal{R}T} \frac{C_{\mathrm{w}} + C^{\mathrm{e}}_{\mathrm{w}}}{2T^{\mathrm{m}}}, \tag{9.47a}$$

$$M^{\mathrm{m}}_{\mathrm{i}} = \frac{D^{\mathrm{m}}_{\mathrm{i}}}{\mathcal{R}T} \frac{C_{\mathrm{i}} + C^{\mathrm{e}}_{\mathrm{i}}}{2T^{\mathrm{m}}}, \tag{9.47b}$$

where $D^{\mathrm{m}}_{\mathrm{w}}$ and $D^{\mathrm{m}}_{\mathrm{i}}$ are the transmembrane diffusivities of water and ion i. The mobility matrices $\underline{\underline{M}}$ and $\underline{\underline{M}}^{\mathrm{e}}$ are positive definite and the mobility coefficients $M^{\mathrm{m}}_{\mathrm{w}}$ and $M^{\mathrm{m}}_{\mathrm{i}}$ are positive for non-zero diffusivities and concentrations, thus ensuring the validity of Eq. (9.19).

Substituting Eqs. (9.46) into Eqs. (9.20) leads to

$$\mathbf{J}_{\mathrm{w}} = -\frac{D_{\mathrm{w}}}{\mathcal{R}T}\mathbf{C}^{-1} \left[C_{\mathrm{w}} \nabla \mu_{\mathrm{w}} + \sum_{\mathrm{i}} C_{\mathrm{i}} \nabla \tilde{\mu}_{\mathrm{i}} \right], \tag{9.48a}$$

$$\mathbf{J}_{\mathrm{i}} = \frac{C_{\mathrm{i}}}{C_{\mathrm{w}}} \mathbf{J}_{\mathrm{w}} - \frac{D_{\mathrm{i}}}{\mathcal{R}T} \mathbf{C}^{-1} C_{\mathrm{i}} \nabla \tilde{\mu}_{\mathrm{i}}, \tag{9.48b}$$

$$\mathbf{J}^{\mathrm{e}}_{\mathrm{w}} = -\frac{D^{\mathrm{e}}_{\mathrm{w}}}{\mathcal{R}T}\mathbf{C}^{-1} \left[C^{\mathrm{e}}_{\mathrm{w}} \nabla \mu^{\mathrm{e}}_{\mathrm{w}} + \sum_{\mathrm{i}} C^{\mathrm{e}}_{\mathrm{i}} \nabla \tilde{\mu}^{\mathrm{e}}_{\mathrm{i}} \right], \tag{9.48c}$$

$$\mathbf{J}^{\mathrm{e}}_{\mathrm{i}} = \frac{C^{\mathrm{e}}_{\mathrm{i}}}{C^{\mathrm{e}}_{\mathrm{w}}} \mathbf{J}^{\mathrm{e}}_{\mathrm{w}} - \frac{D^{\mathrm{e}}_{\mathrm{i}}}{\mathcal{R}T} \mathbf{C}^{-1} C^{\mathrm{e}}_{\mathrm{i}} \nabla \tilde{\mu}^{\mathrm{e}}_{\mathrm{i}}. \tag{9.48d}$$

In the perspective of mixture theory, one would obtain the same expressions by relying on the individual momentum balances for water and ions in the IC and EC spaces separately, and assuming that the friction between the different ion species and between the ions and the solid network in either the IC or EC space is negligible, given the diluteness of the solution (Huyghe and Janssen, 1997).

Combining Eqs. (9.38), (9.42), and (9.48) provides the following IC and EC fluxes:

$$\mathbf{J}_\mathrm{w} = -D_\mathrm{w}\mathbf{C}^{-1}\left[\frac{v_\mathrm{w}C_\mathrm{w}}{\mathcal{R}T}\nabla p_\mathrm{w} + \frac{F}{\mathcal{R}T}\sum_\mathrm{i} z_\mathrm{i}C_\mathrm{i}\nabla\psi + \frac{\sum_{\mathrm{j}\neq\mathrm{i}}C_\mathrm{j}}{C_\mathrm{w}}\nabla C_\mathrm{w}\right], \tag{9.49a}$$

$$\mathbf{J}_\mathrm{i} = \frac{C_\mathrm{i}}{C_\mathrm{w}}\mathbf{J}_\mathrm{w} - D_\mathrm{i}\mathbf{C}^{-1}\left[\nabla C_\mathrm{i} - \frac{C_\mathrm{i}}{C_\mathrm{w}}\nabla C_\mathrm{w} + \frac{F}{\mathcal{R}T}z_\mathrm{i}C_\mathrm{i}\nabla\psi\right], \tag{9.49b}$$

$$\mathbf{J}^\mathrm{e}_\mathrm{w} = -D^\mathrm{e}_\mathrm{w}\mathbf{C}^{-1}\left[\frac{v_\mathrm{w}C^\mathrm{e}_\mathrm{w}}{\mathcal{R}T}\nabla p_\mathrm{w} + \frac{F}{\mathcal{R}T}\sum_\mathrm{i} z_\mathrm{i}C^\mathrm{e}_\mathrm{i}\nabla\psi^\mathrm{e} + \frac{\sum_{\mathrm{j}\neq\mathrm{i}}C^\mathrm{e}_\mathrm{j}}{C^\mathrm{e}_\mathrm{w}}\nabla C^\mathrm{e}_\mathrm{w}\right], \tag{9.49c}$$

$$\mathbf{J}^\mathrm{e}_\mathrm{i} = \frac{C^\mathrm{e}_\mathrm{i}}{C^\mathrm{e}_\mathrm{w}}\mathbf{J}^\mathrm{e}_\mathrm{w} - D^\mathrm{e}_\mathrm{i}\mathbf{C}^{-1}\left[\nabla C^\mathrm{e}_\mathrm{i} - \frac{C^\mathrm{e}_\mathrm{i}}{C^\mathrm{e}_\mathrm{w}}\nabla C^\mathrm{e}_\mathrm{w} + \frac{F}{\mathcal{R}T}z_\mathrm{i}C^\mathrm{e}_\mathrm{i}\nabla\psi^\mathrm{e}\right], \tag{9.49d}$$

where the index i refers to mobile ions, whereas the index j refers to fixed ions.

Let us first analyze the water fluxes (9.49a) and (9.49c). The first terms account for the water flux down its pressure gradient; the second terms describe the electro-osmosis of water with mobile ions; the third terms represent the osmosis of water toward fixed ions. In the absence of ions ($C_\mathrm{i} = C_\mathrm{j} = C^\mathrm{e}_\mathrm{i} = C^\mathrm{e}_\mathrm{j} = 0$), Eqs. (9.49a) and (9.49c) reduce to Darcy-like fluxes, as in standard poromechanics (Coussy, 2004).

Let us now delve into the ion fluxes (9.49b) and (9.49d). The first terms are associated with the convection of ions with water; the second and third terms account for Fick's law, whereby both the nominal (that is, at fixed volume) ion concentration gradient and the water concentration gradient contribute to ion diffusion; the fourth terms account for migration, that is, the ion transport in an electric field. For immobile water ($D_\mathrm{w} = D^\mathrm{e}_\mathrm{w} = 0$), Eqs. (9.49b) and (9.49d) reduce to standard Nernst-Planck fluxes, describing the electro-diffusion of ions (Rubinstein, 1990).

Substituting Eqs. (9.38), (9.42), and (9.47) in Eqs. (9.22) leads to the following transmembrane fluxes:

$$J^\mathrm{m}_\mathrm{w} = -D^\mathrm{m}_\mathrm{w}\frac{C_\mathrm{w} + C^\mathrm{e}_\mathrm{w}}{2T^\mathrm{m}}\left[\frac{C^\mathrm{e}_\mathrm{w}C - C_\mathrm{w}C^\mathrm{e}}{C_\mathrm{w}C^\mathrm{e}_\mathrm{w}}\right], \tag{9.50a}$$

$$J^\mathrm{m}_\mathrm{i} = -D^\mathrm{m}_\mathrm{i}\frac{C_\mathrm{i} + C^\mathrm{e}_\mathrm{i}}{2T^\mathrm{m}}\left[\ln\left(\frac{C^\mathrm{e}_\mathrm{i}}{C_\mathrm{i}}\frac{C_\mathrm{w}}{C^\mathrm{e}_\mathrm{w}}\right) - \frac{Fz_\mathrm{i}}{\mathcal{R}T}\psi^\mathrm{m}\right], \tag{9.50b}$$

where

$$\psi^\mathrm{m} = \psi - \psi^\mathrm{e} \tag{9.51}$$

is the membrane potential. Eq. (9.50a) accounts for the transmembrane osmosis through aquaporins, whereas Eq. (9.50b) accounts for the transmembrane electro-diffusion of ions through ion channels, historically addressed through the Goldman-Hodgkin-Katz flux equation (7.1) (Hille, 1984).

Finally, we note that, in light of Eq. (9.34), substituting Eqs. (9.49a) and (9.50a) into Eq. (9.2a) provides an equation to be solved for the water pressure p_{w}.

9.3 One-dimensional axisymmetric benchmark

As a representative benchmark, we consider a circular cell cluster, of reference radius R^{cl}, whose innermost circular region, of reference radius $R^{\mathrm{cl}}/2$ and denoted as Ω_{in}, is characterized by a transmembrane diffusivity to sodium $D^{\mathrm{m}}_{\mathrm{Na}^+}$ ten times larger than the surrounding annular region, denoted as Ω_{out}, simulating an overexpression of sodium channels. Given the axial symmetry of the problem, the results only depend on the radial coordinate R. We assume plane stress conditions in Eq. (9.1), and that each cell is circular in the reference configuration, such that, in Eqs. (9.2) and (9.3), $A^{\mathrm{c}}/V^{\mathrm{c}} = 2/R^{\mathrm{c}}$, with R^{c} denoting the reference cell radius.

We derive the governing equations for this 1D axisymmetric problem in Sec. 9.3.1, and detail their finite element implementation in *COMSOL Multiphysics*® in Sec. 9.3.2. After listing the model parameters in Sec. 9.3.3, we first present the results of the simulation in the absence of both GJs and TJs, in Sec. 9.3.4. Then, we introduce and comment on the role of GJs in Sec. 9.3.5. Finally, we further account for TJs in Sec. 9.3.6.

9.3.1 Governing equations†

In a 1D axisymmetric space dimension, equilibrium (9.1) reduces to

$$P'_{rR} + \frac{1}{R}(P_{rR} - P_{\theta\Theta}) = 0\,, \tag{9.52}$$

where $P'_{rR} = \partial P_{rR}/\partial R$, and P_{rR} and $P_{\theta\Theta}$ are the radial and circumferential total nominal stresses, given by (see Eq. (9.35))

$$P_{rR} = G\left(F_{rR} - \frac{1}{F_{rR}}\right) + \lambda\frac{\ln J}{F_{rR}} - p_{\mathrm{w}}\frac{J}{F_{rR}} + \frac{F_{rR}}{2\varepsilon_0\varepsilon_{\mathrm{r}}J}\left[D^2 + (D^{\mathrm{e}})^2\right]\,, \tag{9.53a}$$

$$P_{\theta\Theta} = G\left(F_{\theta\Theta} - \frac{1}{F_{\theta\Theta}}\right) + \lambda\frac{\ln J}{F_{\theta\Theta}} - p_{\mathrm{w}}\frac{J}{F_{\theta\Theta}} - \frac{F_{rR}^2}{2\varepsilon_0\varepsilon_{\mathrm{r}}JF_{\theta\Theta}}\left[D^2 + (D^{\mathrm{e}})^2\right]\,, \tag{9.53b}$$

where

$$J = F_{rR}F_{\theta\Theta}F_{zZ}\,, \tag{9.54}$$

with

$$F_{rR} = 1 + u'\,, \tag{9.55a}$$

$$F_{\theta\Theta} = 1 + \frac{u}{R}\,, \tag{9.55b}$$

and F_{zZ} denoting the radial, circumferential, and out-of-plane deformation gradient components (or stretches), and u being the radial displacement. Under plane stress conditions, the out-of-plane total nominal stress P_{zZ} is zero:

$$P_{zZ} = G\left(F_{zZ} - \frac{1}{F_{zZ}}\right) + \lambda \frac{\ln J}{F_{zZ}} - p_{\mathrm{w}} \frac{J}{F_{zZ}} - \frac{F_{rR}^2}{2\varepsilon_0 \varepsilon_{\mathrm{r}} J F_{zZ}} \left[D^2 + (D^{\mathrm{e}})^2\right] = 0\,. \tag{9.56}$$

We equip Eq. (9.52) with the following boundary conditions (see Eq. (9.5)), with that in $R = 0$ ensuing from symmetry:

$$u(0) = 0\,, \quad P_{rR}(R^{\mathrm{cl}}) = 0\,. \tag{9.57}$$

Mass balances (9.2) and (9.3) become

$$\Phi_0 \dot{C}_{\mathrm{w}} + J_{\mathrm{w}}' + \frac{J_{\mathrm{w}}}{R} = -J_{\mathrm{w}}^{\mathrm{m}} \frac{2}{R^{\mathrm{c}}}\,, \tag{9.58a}$$

$$\Phi_0^{\mathrm{e}} \dot{C}_{\mathrm{w}}^{\mathrm{e}} + (J_{\mathrm{w}}^{\mathrm{e}})' + \frac{J_{\mathrm{w}}^{\mathrm{e}}}{R} = J_{\mathrm{w}}^{\mathrm{m}} \frac{2}{R^{\mathrm{c}}}\,, \tag{9.58b}$$

$$\Phi_0 \dot{C}_{\mathrm{i}} + J_{\mathrm{i}}' + \frac{J_{\mathrm{i}}}{R} = -J_{\mathrm{i}}^{\mathrm{m}} \frac{2}{R^{\mathrm{c}}}\,, \tag{9.58c}$$

$$\Phi_0^{\mathrm{e}} \dot{C}_{\mathrm{i}}^{\mathrm{e}} + (J_{\mathrm{i}}^{\mathrm{e}})' + \frac{J_{\mathrm{i}}^{\mathrm{e}}}{R} = J_{\mathrm{i}}^{\mathrm{m}} \frac{2}{R^{\mathrm{c}}}\,, \tag{9.58d}$$

where the radial IC and EC nominal fluxes read (see Eq. (9.49))

$$J_{\mathrm{w}} = -\frac{D_{\mathrm{w}}}{F_{rR}^2} \left(\frac{\upsilon_{\mathrm{w}} C_{\mathrm{w}}}{\mathcal{R}T} p_{\mathrm{w}}' + \frac{F}{\mathcal{R}T} \sum_{\mathrm{i}} z_{\mathrm{i}} C_{\mathrm{i}} \psi' + \frac{\sum_{\mathrm{j}\neq\mathrm{i}} C_{\mathrm{j}}}{C_{\mathrm{w}}} C_{\mathrm{w}}' \right), \tag{9.59a}$$

$$J_{\mathrm{w}}^{\mathrm{e}} = -\frac{D_{\mathrm{w}}^{\mathrm{e}}}{F_{rR}^2} \left(\frac{\upsilon_{\mathrm{w}} C_{\mathrm{w}}^{\mathrm{e}}}{\mathcal{R}T} p_{\mathrm{w}}' + \frac{F}{\mathcal{R}T} \sum_{\mathrm{i}} z_{\mathrm{i}} C_{\mathrm{i}}^{\mathrm{e}} (\psi^{\mathrm{e}})' + \frac{\sum_{\mathrm{j}\neq\mathrm{i}} C_{\mathrm{j}}^{\mathrm{e}}}{C_{\mathrm{w}}^{\mathrm{e}}} (C_{\mathrm{w}}^{\mathrm{e}})' \right), \tag{9.59b}$$

$$J_{\mathrm{i}} = \frac{C_{\mathrm{i}}}{C_{\mathrm{w}}} J_{\mathrm{w}} - \frac{D_{\mathrm{i}}}{F_{rR}^2} \left(C_{\mathrm{i}}' - \frac{C_{\mathrm{i}}}{C_{\mathrm{w}}} C_{\mathrm{w}}' + \frac{F}{\mathcal{R}T} z_{\mathrm{i}} C_{\mathrm{i}} \psi' \right), \tag{9.59c}$$

$$J_{\mathrm{i}}^{\mathrm{e}} = \frac{C_{\mathrm{i}}^{\mathrm{e}}}{C_{\mathrm{w}}^{\mathrm{e}}} J_{\mathrm{w}}^{\mathrm{e}} - \frac{D_{\mathrm{i}}^{\mathrm{e}}}{F_{rR}^2} \left((C_{\mathrm{i}}^{\mathrm{e}})' - \frac{C_{\mathrm{i}}^{\mathrm{e}}}{C_{\mathrm{w}}^{\mathrm{e}}} (C_{\mathrm{w}}^{\mathrm{e}})' + \frac{F}{\mathcal{R}T} z_{\mathrm{i}} C_{\mathrm{i}}^{\mathrm{e}} (\psi^{\mathrm{e}})' \right). \tag{9.59d}$$

The IC nominal concentration of water C_{w} and the transmembrane nominal fluxes $J_{\mathrm{w}}^{\mathrm{m}}$ and $J_{\mathrm{i}}^{\mathrm{m}}$ are still given by Eqs. (9.34) and (9.50). We supply Eqs. (9.58) with the following initial conditions (see Eqs. (9.6b), (9.31), and (9.41)):

$$p_{\mathrm{w}} = 0\,, \quad C_{\mathrm{w}}^{\mathrm{e}} = \frac{1}{\upsilon_{\mathrm{w}}}\,, \tag{9.60a}$$

$$C_{\mathrm{i}} = C_{\mathrm{i}}^{0}\,, \quad C_{\mathrm{i}}^{\mathrm{e}} = C_{\mathrm{i}}^{\mathrm{e},0}\,, \tag{9.60b}$$

and with the following boundary conditions (see Eqs. (9.7), (9.9), (9.40), and (9.43)):

$$J_{\mathrm{w}}(0) = J_{\mathrm{w}}(R^{\mathrm{cl}}) = 0\,, \tag{9.61a}$$

$$\begin{aligned} &J^{\mathrm{e}}_{\mathrm{w}}(0) = 0\,,\\ &C^{\mathrm{e}}_{\mathrm{w}}(R^{\mathrm{cl}}) = \frac{\mathcal{R}TC^{\mathrm{e}}(R^{\mathrm{cl}})}{v_{\mathrm{w}}\left[\mathcal{R}TC^{\mathrm{e},0} + p_{\mathrm{w}}(R^{\mathrm{cl}})\right]} \quad \text{without TJs}\,,\\ &J^{\mathrm{e}}_{\mathrm{w}}(R^{\mathrm{cl}}) = 0 \quad \text{with TJs}\,, \end{aligned} \tag{9.61b}$$

$$J_{\mathrm{i}}(0) = J_{\mathrm{i}}(R^{\mathrm{cl}}) = 0\,, \tag{9.61c}$$

$$\begin{aligned} &J^{\mathrm{e}}_{\mathrm{i}}(0) = 0\,,\\ &C^{\mathrm{e}}_{\mathrm{i}}(R^{\mathrm{cl}}) = v_{\mathrm{w}}C^{\mathrm{e},0}_{\mathrm{i}}C^{\mathrm{e}}_{\mathrm{w}}(R^{\mathrm{cl}}) \quad \text{without TJs}\,,\\ &J^{\mathrm{e}}_{\mathrm{i}}(R^{\mathrm{cl}}) = 0 \quad \text{with TJs}\,. \end{aligned} \tag{9.61d}$$

Finally, Gauss laws (9.4) reduce to

$$D' + \frac{D}{R} = \Phi_0 F \sum_{\mathrm{i}} z_{\mathrm{i}} C_{\mathrm{i}}\,, \tag{9.62a}$$

$$(D^{\mathrm{e}})' + \frac{D^{\mathrm{e}}}{R} = \Phi^{\mathrm{e}}_0 F \sum_{\mathrm{i}} z_{\mathrm{i}} C^{\mathrm{e}}_{\mathrm{i}}\,, \tag{9.62b}$$

where the IC and EC electric displacements are given by (see Eq. (9.44))

$$D = -\varepsilon_0\varepsilon_{\mathrm{r}}\frac{J}{F_{rR}^2}\psi'\,, \tag{9.63a}$$

$$D^{\mathrm{e}} = -\varepsilon_0\varepsilon_{\mathrm{r}}\frac{J}{F_{rR}^2}(\psi^{\mathrm{e}})'\,. \tag{9.63b}$$

We complement Eqs. (9.62) with the following boundary conditions (see Eqs. (9.10)-(9.12) and (9.45)):

$$D(0) = 0\,, \quad D(R^{\mathrm{cl}}) = \varepsilon_0\varepsilon_{\mathrm{r}}^{\mathrm{m}}\frac{\psi}{T^{\mathrm{m}}}\,, \tag{9.64a}$$

$$\begin{aligned} &D^{\mathrm{e}}(0) = 0\,,\\ &\psi^{\mathrm{e}}(R^{\mathrm{cl}}) = 0 \quad \text{without TJs}\,,\\ &D^{\mathrm{e}}(R^{\mathrm{cl}}) = \varepsilon_0\varepsilon_{\mathrm{r}}^{\mathrm{tj}}\frac{\psi^{\mathrm{e}}}{T^{\mathrm{tj}}} \quad \text{with TJs}\,. \end{aligned} \tag{9.64b}$$

9.3.2 Finite element implementation†

We solve the coupled governing equations presented in Sec. 9.3.1 by employing the finite element commercial software *COMSOL Multiphysics®*. We use the `General Form PDE` interface to implement equilibrium (9.52), mass balances (9.58), and Gauss laws (9.62), and the `Domain ODEs and DAEs` interface to impose the plane stress constraint (9.56). We employ quadratic Lagrange shape functions to approximate the independent variables u, p_{w}, $C^{\mathrm{e}}_{\mathrm{w}}$, C_{i}, $C^{\mathrm{e}}_{\mathrm{i}}$, ψ, ψ^{e}, and F_{zZ}. The mesh consists of 100 elements, whose size decreases linearly from the boundaries to the interface between Ω_{in} and Ω_{out}, where the independent variables undergo steep gradients, especially in the absence of GJs. Specifically, the ratio between the largest and smallest elements is 10. We employ the BDF method for the time integration and adopt the `Fully Coupled` approach, equipped with the MUMPS linear solver, to solve all the discretized equations simultaneously at each time step.

9.3.3 Parameters

The model parameters are listed in Tab. 9.1. We refer to an average animal cell of reference radius $R^{\mathrm{c}} = 5\,\mu\mathrm{m}$ and membrane thickness $T^{\mathrm{m}} = 5\,\mathrm{nm}$. The cluster reference radius is $R^{\mathrm{cl}} = 500\,\mu\mathrm{m}$, which is much larger than R^{c}, that is, the characteristic size of a material point, thus ensuring the validity of our continuum formulation. We assume that cells are separated by a reference intercellular space of about $30\,\mathrm{nm}$ in size (Pietak and Levin, 2016), and that approximately the 70% of the cluster is occupied by fluid. Correspondingly, we obtain an estimate of $\Phi_0 = 0.695$ and $\Phi^{\mathrm{e}}_0 = 0.005$ for the initial IC and EC porosities.

The simulations are conducted at body temperature $T = 310\,\mathrm{K}$. Accordingly, $\varepsilon_{\mathrm{r}} = 80$ and $v_{\mathrm{w}} = 18\,\mathrm{cm}^3/\mathrm{mol}$ are reliable estimates for the relative permittivity and molar volume of water. We employ $\varepsilon^{\mathrm{m}}_{\mathrm{r}} = 3$ for the relative permittivity of the cell membrane (Gramse et al., 2013). The thickness of a TJ complex is about $T^{\mathrm{tj}} = 500\,\mathrm{nm}$ (Tsukita et al., 2001), and we use $\varepsilon^{\mathrm{tj}}_{\mathrm{r}} = 30$ for its relative permittivity, which is an average value between those of bulk water and proteins inside (Li et al., 2013).

We choose a representative value $E = 0.4\,\mathrm{kPa}$ for the Young modulus and assume a Poisson ratio $\nu = 0.3$ (Moeendarbary et al., 2013). The Lamé parameters entering Eq. (9.24) thus read $\lambda = E\nu/[(1+\nu)(1-2\nu)] \approx 0.23\,\mathrm{kPa}$ and $G = E/[2(1+\nu)] \approx 0.15\,\mathrm{kPa}$. In Sec. 9.3.5 we also consider the case of a larger E, simulating a cluster of plant cells, equipped with stiff cell walls.

With reference to a typical mammalian cell, the more abundant ions involved in bioelectricity are sodium, potassium, and chloride. We adopt the following initial IC and EC concentrations (Alberts, 1983): $C^0_{\mathrm{Na}^+} = 10\,\mathrm{mol/m}^3$, $C^{\mathrm{e},0}_{\mathrm{Na}^+} = 145\,\mathrm{mol/m}^3$, $C^0_{\mathrm{K}^+} = 140\,\mathrm{mol/m}^3$, $C^{\mathrm{e},0}_{\mathrm{K}^+} = 5\,\mathrm{mol/m}^3$, $C^0_{\mathrm{Cl}^-} = 10\,\mathrm{mol/m}^3$, and $C^{\mathrm{e},0}_{\mathrm{Cl}^-} = 110\,\mathrm{mol/m}^3$. We also consider a fixed generic monovalent anion, whose IC and EC concentrations are uniform and constant and equal to $C_{\mathrm{A}^-} = 140\,\mathrm{mol/m}^3$ and $C^{\mathrm{e}}_{\mathrm{A}^-} = 40\,\mathrm{mol/m}^3$. In the IC space, A^- is intended to represent negatively charged proteins, nucleic acids, and other cellular constituents. Notably, C_{A^-} and $C^{\mathrm{e}}_{\mathrm{A}^-}$ ensure the initial electroneutrality in both the IC and EC spaces (that is, $\sum_{\mathrm{i}} z_{\mathrm{i}} C^0_{\mathrm{i}} = \sum_{\mathrm{i}} z_{\mathrm{i}} C^{\mathrm{e},0}_{\mathrm{i}} = 0$) and also the equality of the initial IC and EC osmotic concentrations (that is, $C^0 = C^{\mathrm{e},0} = 300\,\mathrm{mol/m}^3$). By using Eq. (9.31), we obtain $C^0_{\mathrm{w}} = C^{\mathrm{e},0}_{\mathrm{w}} = 1/v_{\mathrm{w}} \approx 5.6 \times 10^4\,\mathrm{mol/m}^3$. Therefore, the IC and EC solutions are effectively dilute, indeed $C^0/C^0_{\mathrm{w}} = C^{\mathrm{e},0}/C^{\mathrm{e},0}_{\mathrm{w}} \approx 0.5\%$.

We employ the following transmembrane ion diffusivities: $D^{\mathrm{m}}_{\mathrm{Na}^+} = 10^{-18}\,\mathrm{m}^2/\mathrm{s}$, $D^{\mathrm{m}}_{\mathrm{K}^+} = 5 \times 10^{-18}\,\mathrm{m}^2/\mathrm{s}$, and $D^{\mathrm{m}}_{\mathrm{Cl}^-} = 5 \times 10^{-17}\,\mathrm{m}^2/\mathrm{s}$. These are on the order of

Symbol	Descr.	Ref. value	Range expl.	Unit
Reference cell radius	R^{c}	5		μm
Membrane thickness	T^{m}	5		nm
Reference cluster radius	R^{cl}	500		μm
Initial IC porosity	Φ_0	0.695		-
Initial EC porosity	Φ_0^{e}	0.005		-
Temperature	T	310		K
Water relative perm.	ε_{r}	80		-
Water molar volume	v_{w}	18		$\mathrm{cm}^3/\mathrm{mol}$
Membrane relative perm.	$\varepsilon_{\mathrm{r}}^{\mathrm{m}}$	3		-
TJ thickness	T^{tj}	500		nm
TJ relative perm.	$\varepsilon_{\mathrm{r}}^{\mathrm{tj}}$	30		-
Young modulus	E	0.4	$0.4 \div 4000$	kPa
Poisson ratio	ν	0.3		-
Initial IC Na^+ conc.	$C_{\mathrm{Na}^+}^{0}$	10		$\mathrm{mol}/\mathrm{m}^3$
Initial EC Na^+ conc.	$C_{\mathrm{Na}^+}^{\mathrm{e},0}$	145		$\mathrm{mol}/\mathrm{m}^3$
Initial IC K^+ conc.	$C_{\mathrm{K}^+}^{0}$	140		$\mathrm{mol}/\mathrm{m}^3$
Initial EC K^+ conc.	$C_{\mathrm{K}^+}^{\mathrm{e},0}$	5		$\mathrm{mol}/\mathrm{m}^3$
Initial IC Cl^- conc.	$C_{\mathrm{Cl}^-}^{0}$	10		$\mathrm{mol}/\mathrm{m}^3$
Initial EC Cl^- conc.	$C_{\mathrm{Cl}^-}^{\mathrm{e},0}$	110		$\mathrm{mol}/\mathrm{m}^3$
IC fixed anion conc.	C_{A^-}	140		$\mathrm{mol}/\mathrm{m}^3$
EC fixed anion conc.	$C_{\mathrm{A}^-}^{\mathrm{e}}$	40		$\mathrm{mol}/\mathrm{m}^3$
Transmem. Na^+ diff.	$D_{\mathrm{Na}^+}^{\mathrm{m}}$	10^{-18} (Ω_{out}) 10^{-17} (Ω_{in})		m^2/s m^2/s
Transmem. K^+ diff.	$D_{\mathrm{K}^+}^{\mathrm{m}}$	5×10^{-18}		m^2/s
Transmem. Cl^- diff.	$D_{\mathrm{Cl}^-}^{\mathrm{m}}$	5×10^{-17}		m^2/s
Transmem. water diff.	$D_{\mathrm{w}}^{\mathrm{m}}$	10^{-8}	$10^{-14} \div 10^{-8}$	m^2/s
EC Na^+, K^+, and Cl^- diff.	$D_{\mathrm{i}}^{\mathrm{e}}$	10^{-9}		m^2/s
EC water diff.	$D_{\mathrm{w}}^{\mathrm{e}}$	10^{-7}	$10^{-8} \div 10^{-6}$	m^2/s
IC Na^+, K^+, and Cl^- diff. (with GJs)	D_{i}	10^{-12}		m^2/s
IC water diff. (with GJs)	D_{w}	10^{-9}	$10^{-10} \div 10^{-8}$	m^2/s

Table 9.1: Employed model parameters.

those reported in Pietak and Levin (2016), but account for the fact that the permeability of artificial lipid bilayers to Na^+, K^+, and Cl^- is not the same (Alberts, 1983). As anticipated, in Ω_{in} we set instead $D^{\mathrm{m}}_{\mathrm{Na}^+} = 10^{-17}\,\mathrm{m}^2/\mathrm{s}$. We consider that the transmembrane water diffusivity is $D^{\mathrm{m}}_{\mathrm{w}} = 10^{-8}\,\mathrm{m}^2/\mathrm{s}$, that is, ten order of magnitudes larger than $D^{\mathrm{m}}_{\mathrm{Na}^+}$, as documented in Alberts (1983) with reference to artificial lipid bilayers. In Sec. 9.3.4, we further analyze the case of smaller $D^{\mathrm{m}}_{\mathrm{w}}$, simulating an underexpression of aquaporins.

We follow Pietak and Levin (2016) and assume $D^{\mathrm{e}}_{\mathrm{i}} = 10^{-9}\,\mathrm{m}^2/\mathrm{s}$ for the diffusivity of all ions in EC water. We set $D^{\mathrm{e}}_{\mathrm{w}} = 10^{-7}\,\mathrm{m}^2/\mathrm{s}$ for the EC water diffusivity, as approximately obtained through the Kozeny-Carman equation (Coussy, 2004). Given the uncertainty in this parameter, in Sec. 9.3.4 we also explore how the response changes by increasing or decreasing $D^{\mathrm{e}}_{\mathrm{w}}$ of one order of magnitude.

In the presence of GJs, we adopt $D_{\mathrm{i}} = 10^{-12}\,\mathrm{m}^2/\mathrm{s}$ for the diffusivity of all ions in IC water. In particular, $D_{\mathrm{i}} \leq 10^{-14}\,\mathrm{m}^2/\mathrm{s}$ should be excluded, as it has no impact on the behavior of the cluster. Finally, we adopt $D_{\mathrm{w}} = 10^{-9}\,\mathrm{m}^2/\mathrm{s}$ for the IC water diffusivity, and, in Sec. 9.3.5, we further explore how the cluster behavior is affected by variations of D_{w} of one order of magnitude.

9.3.4 Results in the absence of gap and tight junctions

We first assume that GJs are either absent or closed, such that $D_{\mathrm{w}} = D_{\mathrm{i}} = 0$ in Eqs. (9.49a) and (9.49b). Therefore, the mass balances (9.2a) and (9.3a) reduce to ordinary differential equations. Moreover, we assume that TJs are absent, such that boundary conditions (9.8) and (9.11) hold. In Fig. 9.1 we represent the relevant bioelectrical and mechanical fields as a function of R at different times.

The large $D^{\mathrm{m}}_{\mathrm{Na}^+}$ in Ω_{in} leads to a prominent influx of Na^+ from the EC to the IC space, that is, down its concentration gradient. Correspondingly, the IC osmotic concentration C rapidly increases. We register a little increase of C in Ω_{out} as well, which is essentially due to the large C_{A^-} compared to $C^{\mathrm{e}}_{\mathrm{A}^-}$, as explained by the Gibbs-Donnan effect (Overbeek, 1956). While C presents a steep gradient at $R = R^{\mathrm{cl}/2}$, due to the lack of GJs connecting Ω_{in} and Ω_{out}, the EC osmotic concentration C^{e} is smoother, because of the interconnection of the intercellular spaces. Moreover, while C^{e} initially decreases with time, it then increases as Na^+ is transported from the outside to the inside of the cluster.

The redistribution of ions establishes a negative IC electric potential ψ, as of the beginning of the simulation. This is again explained by the Gibbs-Donnan effect. In particular, Ω_{in} is depolarized with respect to Ω_{out}, and the depolarization increases over time due to the influx of Na^+. The EC electric

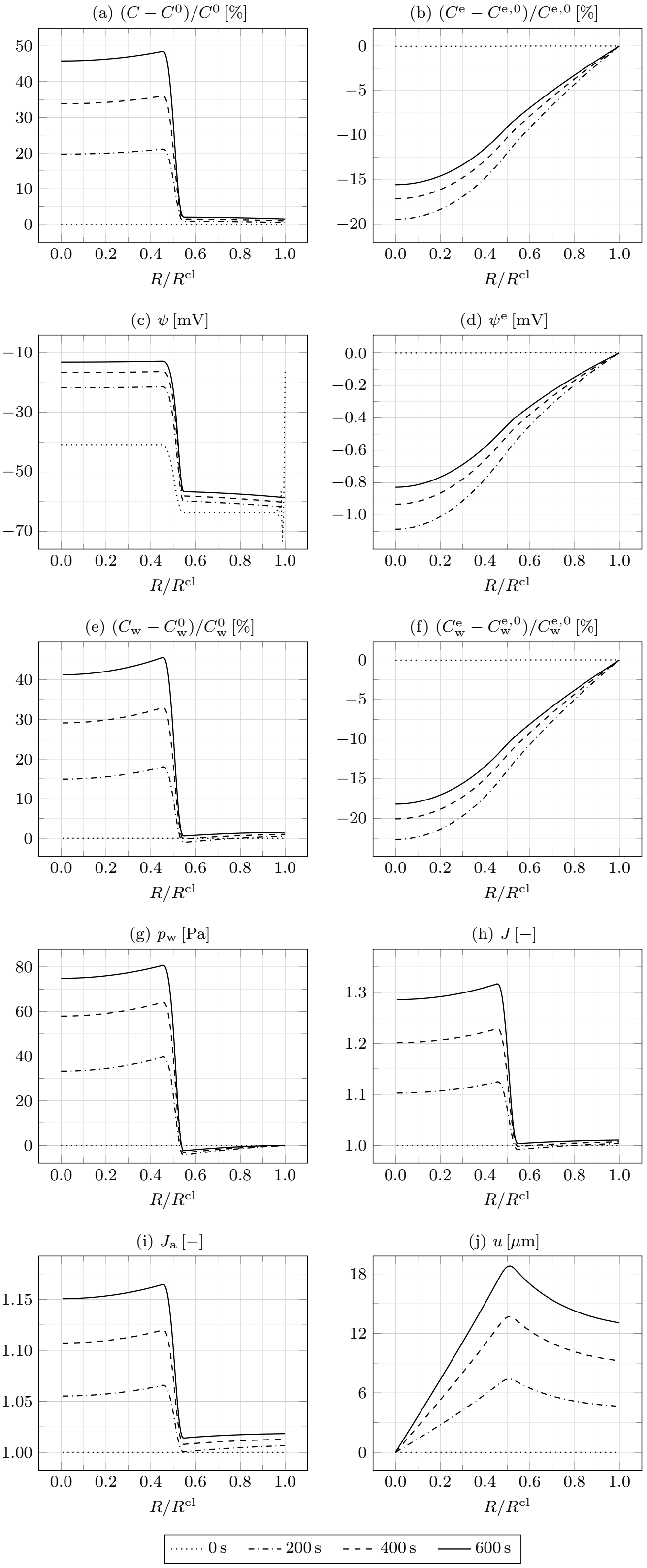

Figure 9.1: (a) Relative IC osmotic concentration, (b) relative EC osmotic concentration, (c) IC electric potential, (d) EC electric potential, (e) relative IC water concentration, (f) relative EC water concentration, (g) water pressure, (h) Jacobian, (i) areal Jacobian, and (j) radial displacement as a function of the radial coordinate at different times.

potential ψ^{e} remains rather small, such that the membrane potential ψ^{m} nearly corresponds to ψ. In particular, the value of about $-60\,\mathrm{mV}$, registered in Ω_{out}, is representative of the resting ψ^{m} associated with the adopted initial ion concentrations and transmembrane diffusivities, which can be estimated through the Goldman-Hodgkin-Katz voltage equation (7.2) (Hille, 1984).

As Na^{+} is transported from the EC to the IC space through ion channels in Ω_{in}, water follows by osmosis through aquaporins. Correspondingly, the IC water concentration C_{w} increases with time. In the EC space, as Na^{+} ions enter the cluster to cope with the request for Na^{+} in Ω_{in}, they drag water molecules by electro-osmosis. Therefore, the EC water concentration $C^{\mathrm{e}}_{\mathrm{w}}$ increases after initially decreasing, similarly to C^{e}.

As water enters Ω_{in}, the water pressure p_{w} increases therein, and is equilibrated by the mechanical stress. The IC and EC electrostatic pressures p_{pol} and $p^{\mathrm{e}}_{\mathrm{pol}}$, not represented here, are both irrelevant, being orders of magnitude lower than p_{w}. The increase of C_{w} in Ω_{in} is also accompanied by an increase of the Jacobian J. We remark that, given the smaller variation of $C^{\mathrm{e}}_{\mathrm{w}}$ compared to C_{w} except for the initial transient, and, mostly, the close cell packing, implying $\Phi_0 \gg \Phi^{\mathrm{e}}_0$, the contribution of the variation of $C^{\mathrm{e}}_{\mathrm{w}}$ to J, as described by Eq. (9.30), is negligible.

The areal Jacobian J_{a}, given by the product of the radial and circumferential deformation gradient components (or stretches) F_{rR} and $F_{\theta\Theta}$, indicates in-plane expansion everywhere, larger in Ω_{in}. By comparing J and J_{a}, we infer that there occurs an out-of-plane expansion in Ω_{in} and a little out-of-plane compression in Ω_{out}. Finally, the radial displacement u increases from $R=0$ to $R=R^{\mathrm{cl}}/2$, and then decreases.

In Fig. 9.2 we explore how the same fields are affected by variations of the EC water diffusivity $D^{\mathrm{e}}_{\mathrm{w}}$. By increasing $D^{\mathrm{e}}_{\mathrm{w}}$, water is transported more rapidly from the outside to the inside of the cluster through the EC space, and consequently from the EC to the IC space across cell membranes. Therefore, fixed the time, C_{w}, $C^{\mathrm{e}}_{\mathrm{w}}$, p_{w}, J, J_{a}, and u increase. Interestingly, C and C^{e} increase as well, since the convective contribution to ion transport grows with $D^{\mathrm{e}}_{\mathrm{w}}$ (see Eqs. (9.49c) and 9.49d). The change in the ion redistribution also impacts on ψ^{m}, though mildly. Finally, we note that, by decreasing $D^{\mathrm{e}}_{\mathrm{w}}$ to $10^{-8}\,\mathrm{m}^2/\mathrm{s}$, the demand for water in Ω_{in} can be barely sustained, such that, for a given time, C_{w} decreases from $R=R^{\mathrm{cl}}/2$ to $R=0$; furthermore, C_{w} also decreases from $R=R^{\mathrm{cl}}$ to $R=R^{\mathrm{cl}}/2$, suggesting that water is transported from the IC to the EC space in Ω_{out}, and then from Ω_{out} to Ω_{in} through the EC space, resulting in an in-plane shrinkage of Ω_{out}.

In Fig. 9.3 we consider the effect of the transmembane water diffusivity $D^{\mathrm{m}}_{\mathrm{w}}$, modulated by the density and open fraction of aquaporins. Increasing

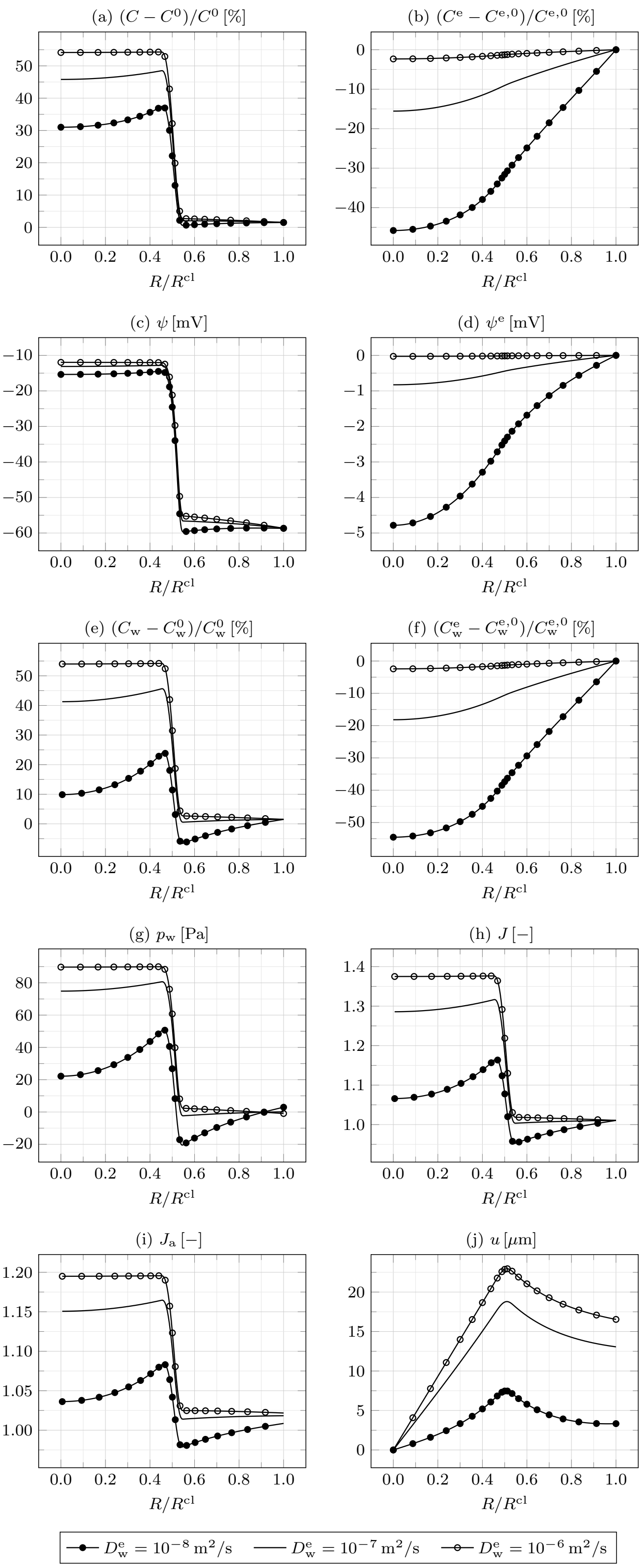

Figure 9.2: (a) Relative IC osmotic concentration, (b) relative EC osmotic concentration, (c) IC electric potential, (d) EC electric potential, (e) relative IC water concentration, (f) relative EC water concentration, (g) water pressure, (h) Jacobian, (i) areal Jacobian, and (j) radial displacement as a function of the radial coordinate at $t = 600$ s for different EC water diffusivities D_w^e.

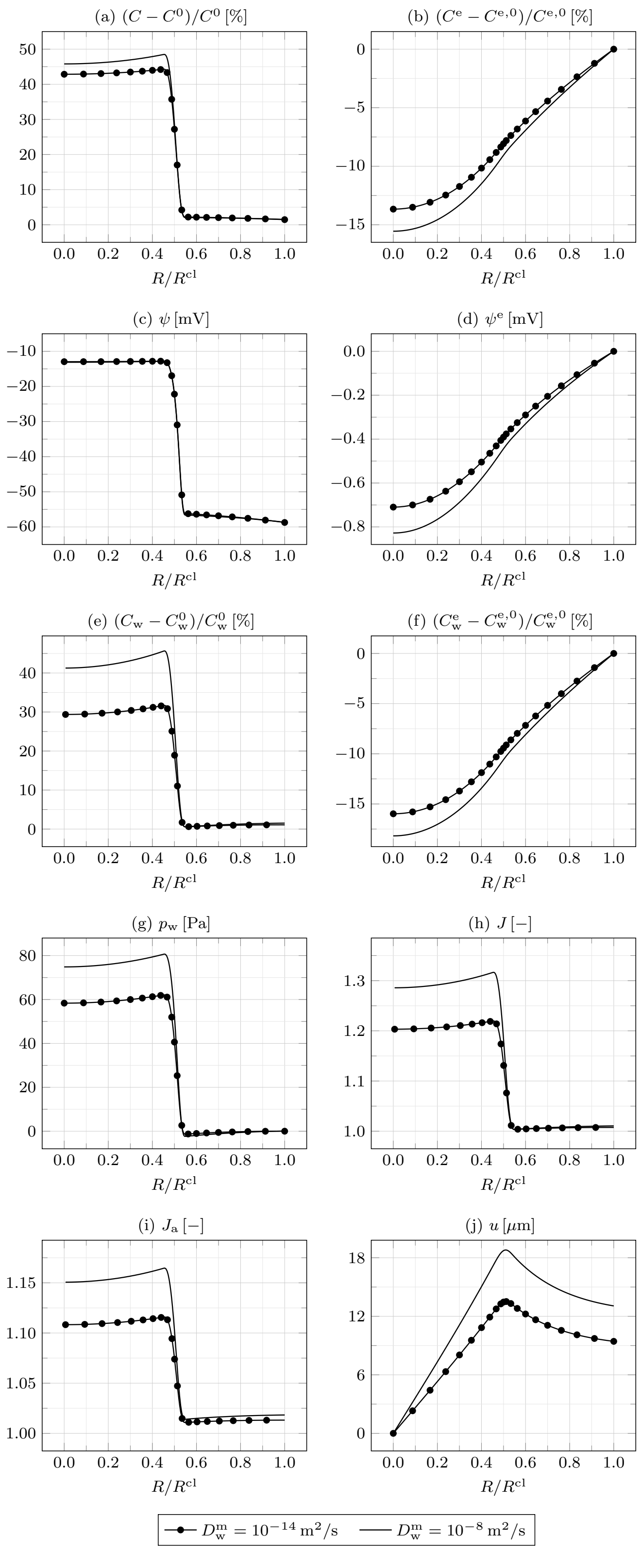

Figure 9.3: (a) Relative IC osmotic concentration, (b) relative EC osmotic concentration, (c) IC electric potential, (d) EC electric potential, (e) relative IC water concentration, (f) relative EC water concentration, (g) water pressure, (h) Jacobian, (i) areal Jacobian, and (j) radial displacement as a function of the radial coordinate at $t = 600\,\mathrm{s}$ for different transmembrane water diffusivities $D_{\mathrm{w}}^{\mathrm{m}}$.

$D_{\mathrm{w}}^{\mathrm{m}}$ above $10^{-8}\,\mathrm{m}^2/\mathrm{s}$ or decreasing it up to $10^{-12}\,\mathrm{m}^2/\mathrm{s}$ does not affect the results. By further decreasing $D_{\mathrm{w}}^{\mathrm{m}}$ to $10^{-14}\,\mathrm{m}^2/\mathrm{s}$, the transmembrane water transport is hampered, such that C_{w} strongly decreases and $C_{\mathrm{w}}^{\mathrm{e}}$ increases. In turn, this determines a decrease of p_{w}, J, J_{a}, and u. Importantly, while varying $D_{\mathrm{w}}^{\mathrm{e}}$ strongly impacted on the ion redistribution, changing $D_{\mathrm{w}}^{\mathrm{m}}$ mildly affects it. Indeed, $D_{\mathrm{w}}^{\mathrm{e}}$ enters the EC ion fluxes through the convective contribution, while $D_{\mathrm{w}}^{\mathrm{m}}$ does not govern the transmembrane ion fluxes, given that aquaporins and ion channels are specific for water and ions (see Eqs. (9.50)). The impact of $D_{\mathrm{w}}^{\mathrm{m}}$ on ψ^{m} is also negligible.

9.3.5 Introducing gap junctions

We now investigate on the role of GJs on the mechanobioelectricity of the cluster. As reported in Sec. 9.3.3, we adopt $D_{\mathrm{i}} = 10^{-12}\,\mathrm{m}^2/\mathrm{s}$ uniformly for all ions and $D_{\mathrm{w}} = 10^{-9}\,\mathrm{m}^2/\mathrm{s}$.

In Fig. 9.4 we compare the relevant fields at the end of the simulation with and without GJs. If GJs are present, the Na^+ ions entering the IC space in Ω_{in} flow down their IC electrochemical potential gradient toward Ω_{out}. Therefore, accounting for GJs smooths out the steep gradient of C at $R = R^{\mathrm{cl}}/2$, thus leading to a reduction of C in Ω_{in} and to an increase of C in Ω_{out}. The different ion redistribution in the IC space also influences ψ, with a lesser depolarization occurring in Ω_{in} and a larger one characterizing Ω_{out}. Similarly, the water entering the IC space in Ω_{in} flows toward Ω_{out} through GJs, mainly dragged by ions through electro-osmosis. Predictably, the EC fields are almost no affected by GJs. Notably, the IC water redistribution in the presence of GJs leads to a decrease of J_{a} in Ω_{in} and to an increase of J_{a} in Ω_{out}; correspondingly, $u(R^{\mathrm{cl}}/2)$ diminishes, but $u(R^{\mathrm{cl}})$ remains equal.

In Fig. 9.5 we compare the responses for different values of D_{w}. By increasing D_{w}, more water is transported from Ω_{in} to Ω_{out}, such that the difference in C_{w} between Ω_{in} and Ω_{out} reduces, along with that in J_{a}. However, again, $u(R^{\mathrm{cl}})$ remains the same. The difference in C between Ω_{in} and Ω_{out} reduces as well, which confirms the relevance of ion transport by convection as D_{w} is risen. Decreasing D_{w} below $10^{-10}\,\mathrm{m}^2/\mathrm{s}$ does not affect further the results.

In Fig. 9.6 we examine the cluster behavior by varying its Young modulus E. Increasing it up to one order of magnitude does not affect the results, except for p_{w}, which grows proportionally to E. Therefore, we conclude that, for suitably small values of E, proper of animal cells, the response of the cluster to the imposed bioelectrical perturbation is independent of E. More specifically, the ion redistribution triggers the water redistribution, which establishes the cluster deformation. However, for larger values of E, which may be proper of plant

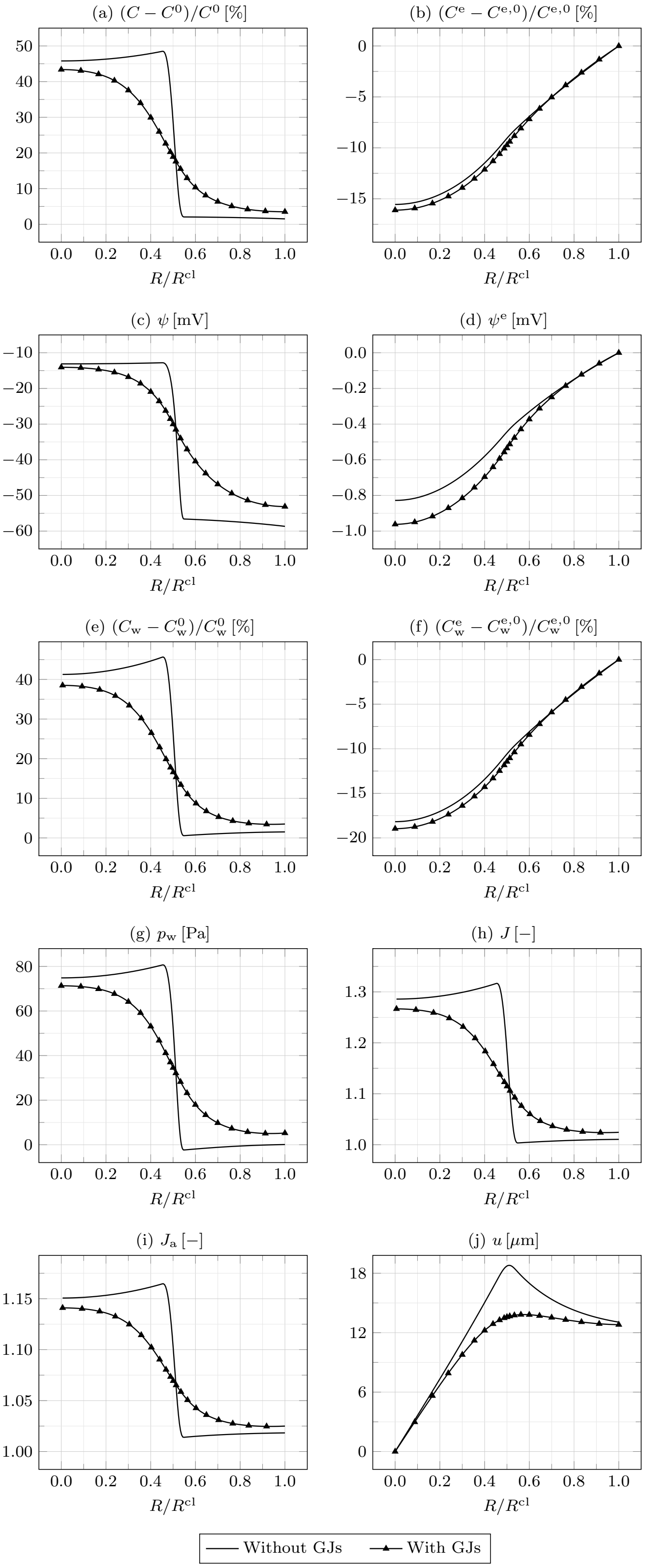

Figure 9.4: (a) Relative IC osmotic concentration, (b) relative EC osmotic concentration, (c) IC electric potential, (d) EC electric potential, (e) relative IC water concentration, (f) relative EC water concentration, (g) water pressure, (h) Jacobian, (i) areal Jacobian, and (j) radial displacement as a function of the radial coordinate at $t = 600\,\mathrm{s}$ without and with gap junctions.

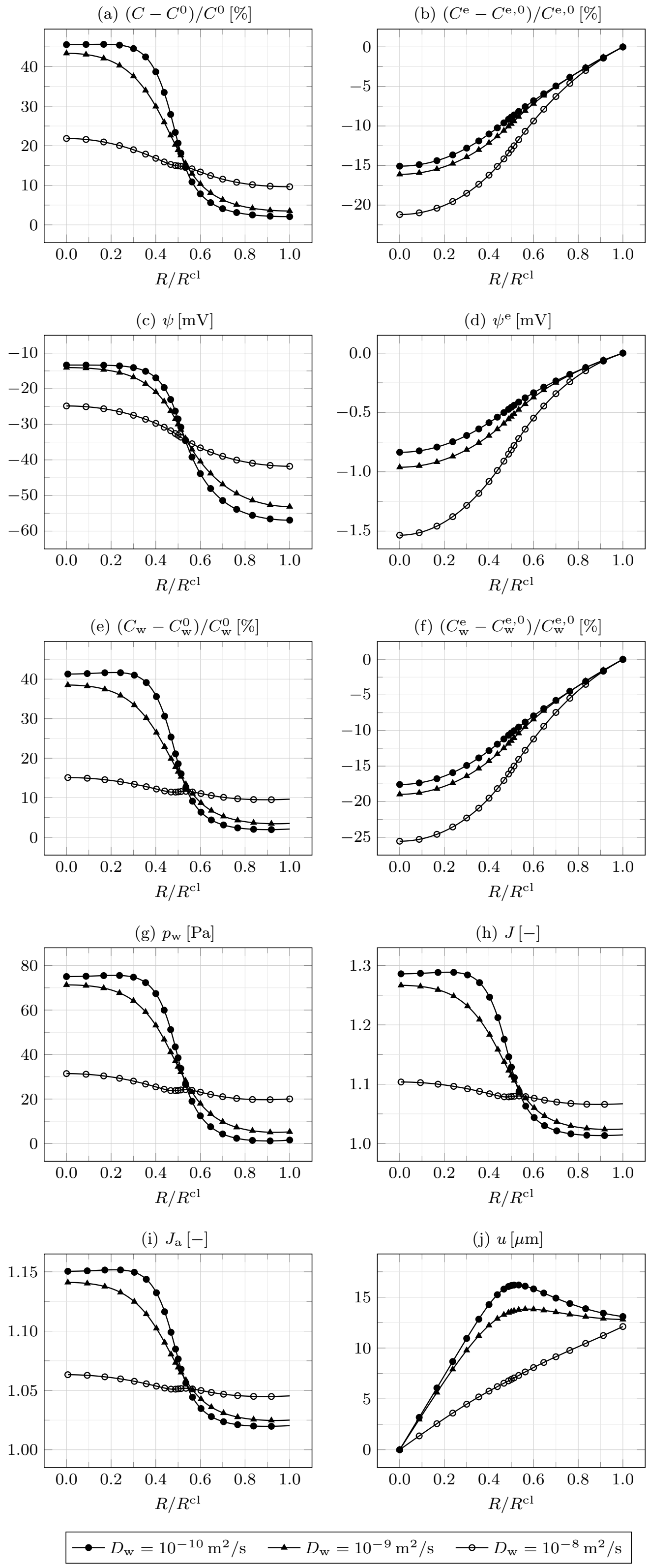

Figure 9.5: (a) Relative IC osmotic concentration, (b) relative EC osmotic concentration, (c) IC electric potential, (d) EC electric potential, (e) relative IC water concentration, (f) relative EC water concentration, (g) water pressure, (h) Jacobian, (i) areal Jacobian, and (j) radial displacement as a function of the radial coordinate at $t = 600\,\mathrm{s}$ for different IC water diffusivities D_{w}.

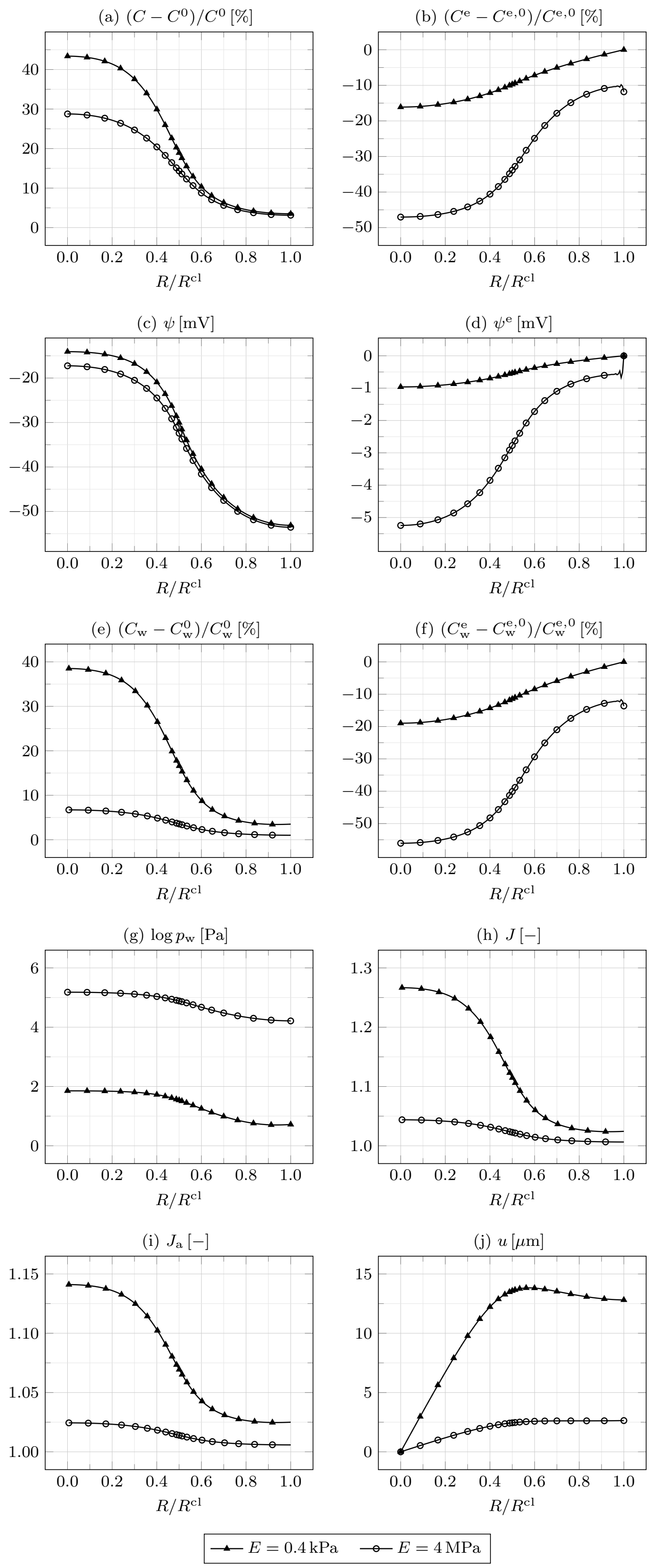

Figure 9.6: (a) Relative IC osmotic concentration, (b) relative EC osmotic concentration, (c) IC electric potential, (d) EC electric potential, (e) relative IC water concentration, (f) relative EC water concentration, (g) water pressure, (h) Jacobian, (i) areal Jacobian, and (j) radial displacement as a function of the radial coordiante at $t = 600\,$s for different Young moduli E, in the presence of gap junctions.

cells endowed with stiff walls, the mechanics affects the water redistribution as well. Indeed, in such a case, the accumulation of water in the IC space of Ω_{in} determines the build-up of a large water (turgor) pressure gradient ∇p_{w}, forcing water to flow back toward Ω_{out}, through both GJs and the EC space according to our model (see Eqs. (9.49a) and (9.49c)). Consequently, C_{w} and $C_{\mathrm{w}}^{\mathrm{e}}$ both diminish, along with J_{a} and u. Though at a lesser extent, C and C^{e} are affected as well, while ψ^{m} practically remains unaltered, given the similar reductions in both ψ and ψ^{e}.

In Fig. 9.7 we investigate the cluster behavior in the presence of GJs until the steady state, reached at about 24 h. The IC fields monotonically increase with time, both at $R = 0$ and, albeit slower, as ions and water flow outward through GJs, at $R = R^{\mathrm{cl}}$. At the steady state, the IC fields attain the uniform values $(C - C^0)/C^0 = (C_{\mathrm{w}} - C_{\mathrm{w}}^0)/C_{\mathrm{w}}^0 \approx 2.5$ and $\psi = 0$. The EC fields at $R = 0$ rapidly decrease in the first 2 min, and then slowly increase, as ions and water flow inward through the intercellular spaces. At the steady state, the EC fields $C^{\mathrm{e}} - C^{\mathrm{e},0}$, $C_{\mathrm{w}}^{\mathrm{e}} - C_{\mathrm{w}}^{\mathrm{e},0}$, and ψ^{e} attain uniform zero values. Therefore, the EC space is undeformed at the steady state. Notably, at the steady state $c = C/(v_{\mathrm{w}} C_{\mathrm{w}}) = C^0 = C^{\mathrm{e},0} = C^{\mathrm{e}}/(v_{\mathrm{w}} C_{\mathrm{w}}^{\mathrm{e}}) = c^{\mathrm{e}}$ (see Eq. (9.32)); moreover, we could show that $c_{\mathrm{i}} = c_{\mathrm{i}}^{\mathrm{e}} = C_{\mathrm{i}}^{\mathrm{e},0}\, \forall \mathrm{i}$. The volume ratio J behaves similarly to C_{w}, as $C_{\mathrm{w}}^{\mathrm{e}}$ is not significant for J in the absence of TJs. While initially $u(R^{\mathrm{cl}}/2) \approx u(R^{\mathrm{cl}})$, they progressively diverge and, at the steady state, $u(R^{\mathrm{cl}}) = 2u(R^{\mathrm{cl}}/2) \approx 0.4\, R^{\mathrm{cl}}$. To conclude, this simulation reveals that, in the absence of TJs and for a sufficiently compliant cluster (such that p_{w} is irrelevant in Eq. (9.40)) devoid of ion pumps, at the steady state the *current* IC and EC ion concentrations and the IC and EC electric potentials become equal to those of the bath surrounding the cluster, in turn coinciding with the initial EC ones. This is accompanied by large cluster deformations, exclusively attributable to the deformation of the IC space.

9.3.6 Introducing tight junctions

In this section, we comment on the cluster response in the presence of TJs, that is, by considering that the EC space cannot exchange neither water nor ions with the bath surrounding the cluster. Boundary conditions (9.9) and (9.12) now hold. As in Sec. 9.3.5, we also account for GJs. We display the results of the simulation in Fig. 9.8, by focusing on a relatively short time interval of 30 s.

As for the previous case, the large $D_{\mathrm{Na}+}^{\mathrm{m}}$ in Ω_{in} leads to a rapid inflow of Na^+ from the EC to the IC space. However, in the presence of TJs, the ions of the outside bath cannot replace those lost by the EC space. Therefore, given that $\Phi_0 \gg \Phi_0^{\mathrm{e}}$, the increase of C with time is limited, while the decrease of C^{e} is

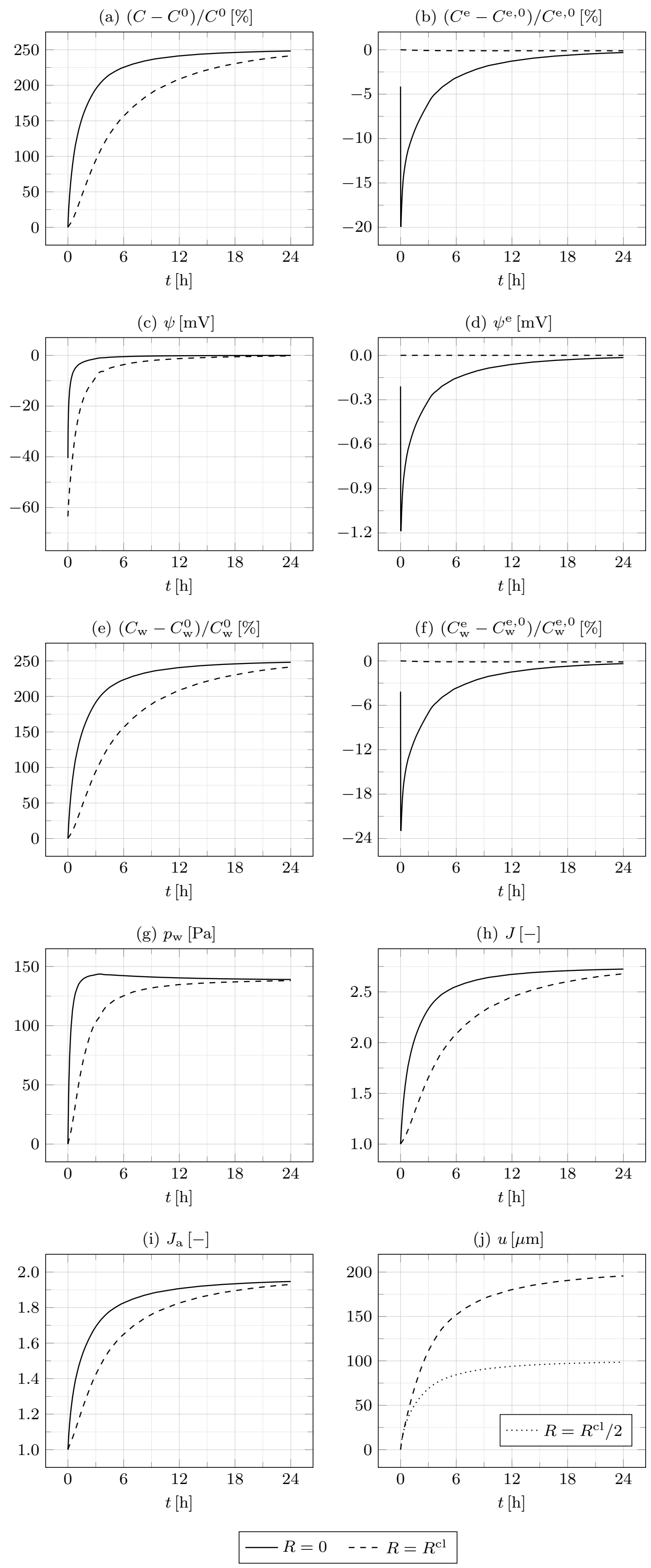

Figure 9.7: (a) Relative IC osmotic concentration, (b) relative EC osmotic concentration, (c) IC electric potential, (d) EC electric potential, (e) relative IC water concentration, (f) relative EC water concentration, (g) water pressure, (h) Jacobian, and (i) areal Jacobian at $R = 0$ and $R = R^{\mathrm{cl}}$, and (j) radial displacement at $R = R^{\mathrm{cl}}/2$ and $R = R^{\mathrm{cl}}$, as a function of time in the presence of gap junctions.

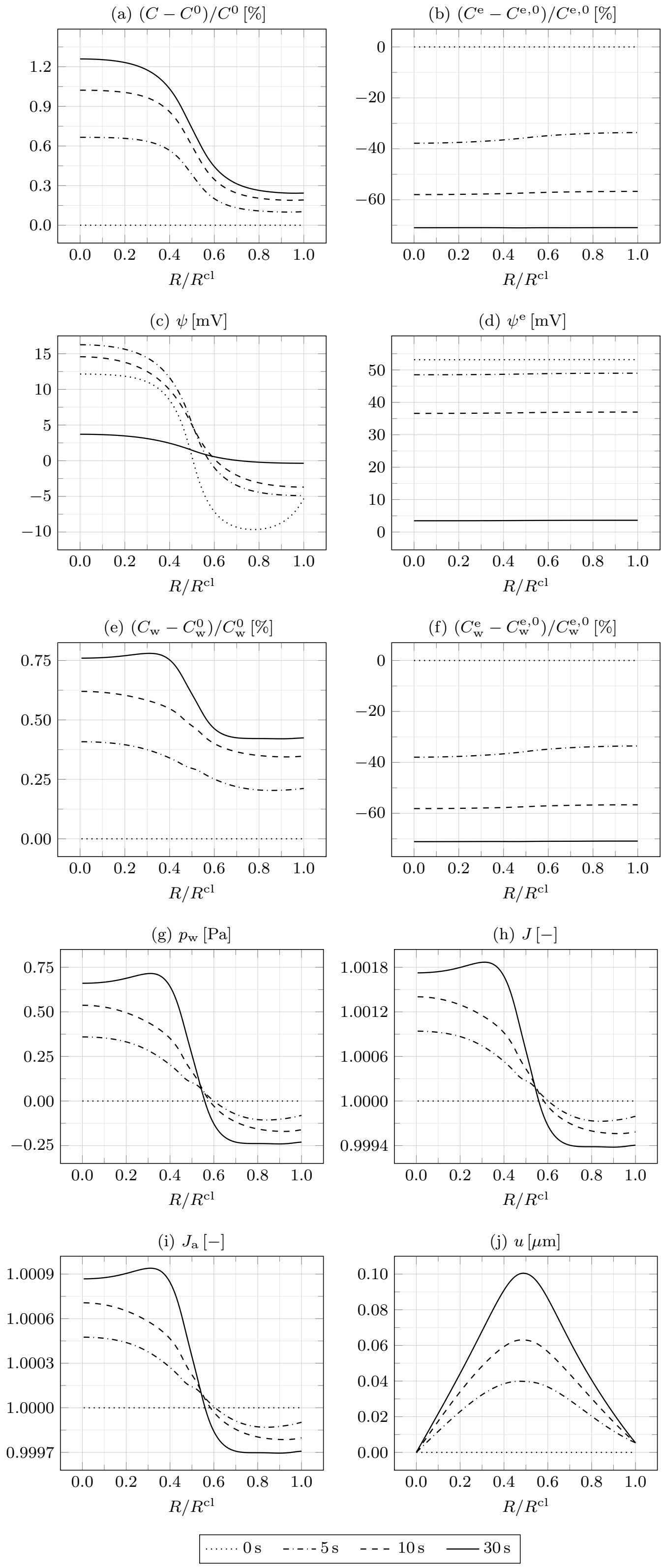

Figure 9.8: (a) Relative IC osmotic concentration, (b) relative EC osmotic concentration, (c) IC electric potential, (d) EC electric potential, (e) relative IC water concentration, (f) relative EC water concentration, (g) water pressure, (h) Jacobian, (i) areal Jacobian, and (j) radial displacement as a function of the radial coordinate at different times, in the presence of gap and tight junctions.

more pronounced and nearly uniform with R.

While ψ^{e} remained nearly null everywhere in the absence of TJs, such that ψ^{m} practically coincided with ψ, here both ψ and ψ^{e} contribute to ψ^{m}, being comparable in magnitude. We observe that, initially, ψ^{m} is very close to the value registered in the absence of TJs. We further note that the positive ψ^{e} at $R = R^{\mathrm{cl}}$ corresponds to the *transepithelial potential* established by TJs (Nuccitelli, 2003).

Following Na^{+}, water molecules pass from the EC to the IC space by osmosis through aquaporins, leading to an increase of C_{w} and to a decrease of $C_{\mathrm{w}}^{\mathrm{e}}$. As reported for C and C^{e}, given the impermeability of the boundary to water and the large difference between Φ_0 and Φ_0^{e}, C_{w} little increases, while $C_{\mathrm{w}}^{\mathrm{e}}$ strongly decreases uniformly.

Given the limited water redistribution, the mechanical fields are much smaller in magnitude than in the absence of TJs. Furthermore, we highlight that J, and consequently p_{w}, are negative in Ω_{out}, meaning that there the decrease of the EC volume is larger than the increase of the IC volume. Indeed, we remark that, in the presence of TJs, the great disparity between $|C_{\mathrm{w}} - C_{\mathrm{w}}^{0}|$ and $|C_{\mathrm{w}}^{\mathrm{e}} - C_{\mathrm{w}}^{\mathrm{e},0}|$ makes both contributions important for the estimation of J through Eq. (9.30). The radial displacement u increases from $R = 0$ to $R = R^{\mathrm{cl}}/2$, though remaining very small, and then decreases becoming nearly zero at $R = R^{\mathrm{cl}}$.

In Fig. 9.9 we display the time evolution of the relevant fields until the steady state. After quickly increasing in the first 30 s, $C(R = 0)$ slowly decreases to a steady state value $\approx 1.005\, C^{0}$, reached at about $t = 60$ min. Similarly, $C(R^{\mathrm{cl}})$ increases quite rapidly in the first 30 s, but then keeps increasing, though slower, until the same steady state value of $C(0)$. Both $C^{\mathrm{e}}(0)$ and $C^{\mathrm{e}}(R^{\mathrm{cl}})$ decrease to the same steady state value $\approx 0.3\, C^{\mathrm{e},0}$ at about $t = 30$ s. Therefore, we conclude that Na^{+} ions electro-diffuse from the EC to the IC space of Ω_{in} in the first 30 s, and then flow from Ω_{in} to Ω_{out} through GJs until the steady state, when C becomes uniform within the whole cluster.

The evolution of C_{w} and $C_{\mathrm{w}}^{\mathrm{e}}$ at $R = 0$ and $R = R^{\mathrm{cl}}$ in the first 30 s is analogous to that observed for C and C^{e}. However, between approximately $t = 30$ s and $t = 3$ min, $C_{\mathrm{w}}(0)$ increases, while $C_{\mathrm{w}}(R^{\mathrm{cl}})$ decreases. This suggests that, in this time interval, some water flows from Ω_{out} to Ω_{in}, either directly through GJs or by passing through the EC space. After 3 min, water starts flowing back from Ω_{in} to Ω_{out}, until both $C_{\mathrm{w}}(0)$ and $C_{\mathrm{w}}(R^{\mathrm{cl}})$ reach the same steady state value $\approx 1.005\, C_{\mathrm{w}}^{0}$. Notably, $c = C^{0} = C^{\mathrm{e},0} = c^{\mathrm{e}}$ at the steady state; moreover, we could show that $c_{\mathrm{i}} = c_{\mathrm{i}}^{\mathrm{e}} \approx C_{\mathrm{i}}^{0}\ \forall \mathrm{i}$.

The Jacobian J and the areal Jacobian J_{a} increase at $R = 0$ and decrease at $R = R^{\mathrm{cl}}$ until $t = 3$ min, and then asymptotically tend to one. In particular, J_{a} is equal to the out-of-plane stretch J/J_{a}. The radial displacement u at $R = R^{\mathrm{cl}}/2$ increases until $t = 3$ min and then goes to zero.

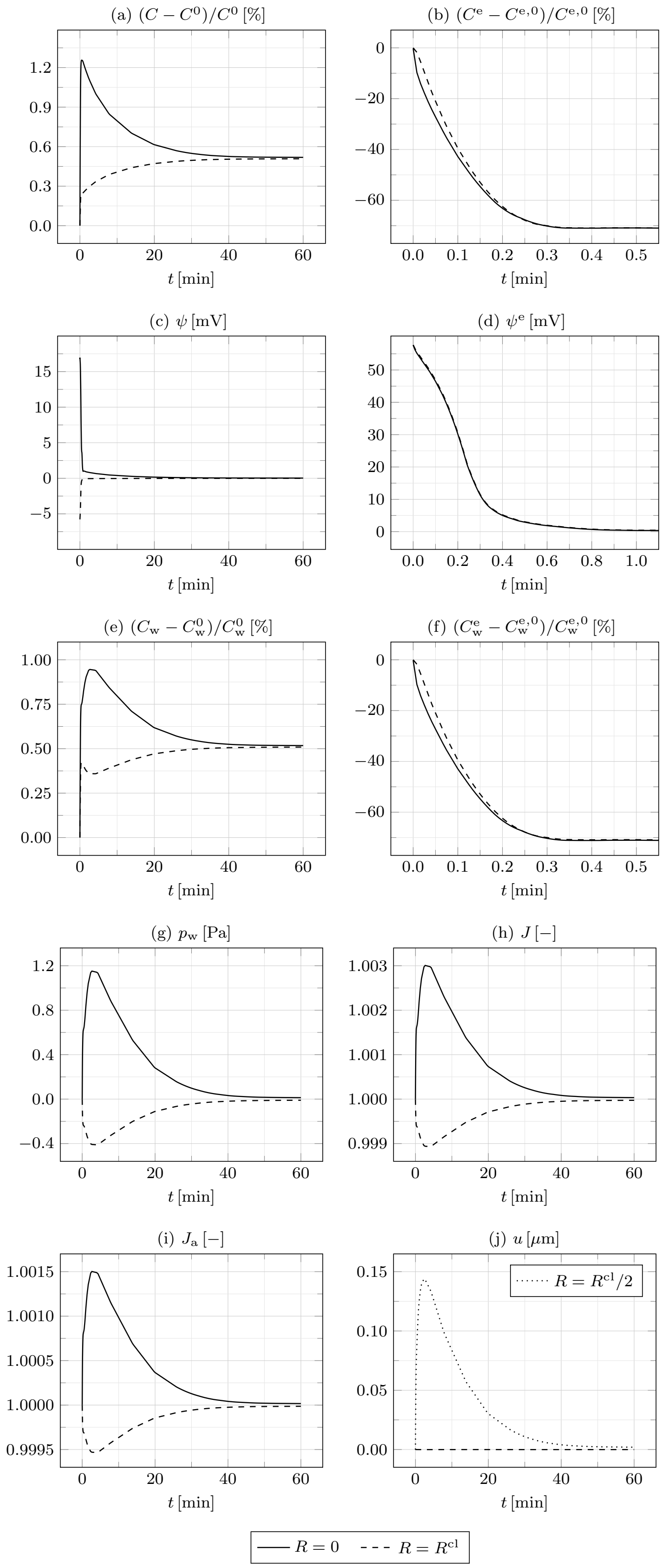

Figure 9.9: (a) Relative IC osmotic concentration, (b) relative EC osmotic concentration, (c) IC electric potential, (d) EC electric potential, (e) relative IC water concentration, (f) relative EC water concentration, (g) water pressure, (h) Jacobian, and (i) areal Jacobian at $R = 0$ and $R = R^\mathrm{cl}$, and (j) radial displacement at $R = R^\mathrm{cl}/2$ and $R = R^\mathrm{cl}$, as a function of time in the presence of gap and tight junctions.

To conclude, in the presence of TJs and in the absence of ion pumps, at the steady state the *current* IC and EC ion concentrations are equal and close to the initial IC values, and both the IC and EC spaces are electroneutral. Moreover, within the same material point, the volume increase of the IC space balances the volume decrease of the EC space, such that the cluster is globally undeformed.

9.4 Concluding remarks

We have herein proposed a continuum finite strain theory for the coupling of electrostatics, ion transport, water transport, and mechanics of a closely packed cell cluster.

Specifically, we have regarded the cluster as the superposition of a solid network of cytoskeletal filaments and anchoring junctions and intracellular (IC) and extracellular (EC) solutions of water and ions. We have described the mechanics of the cluster through compressible hyperelasticity. Given the diluteness of the IC and EC solutions and the incompressibility of all the constituents, volumetric deformations are established by water redistribution only. We have obtained the IC and EC fluxes, the first being allowed by gap junctions, by considering cross-diffusing effects. Correspondingly, the IC and EC water fluxes result from the contributions of water pressure and electro-osmosis, while the IC and EC ion fluxes are due to electro-diffusion and convection. We have further accounted for transmembrane osmosis and ion electro-diffusion through aquaporins and ion channels, respectively.

We have tested our model to an in-plane circular cluster whose central region Ω_{in} presents an overexpression of sodium channels. The model correctly predicts the accumulation of ions and, consequently, of water, in the IC space of Ω_{in}, and the resulting depolarization and in-plane expansion. The presence of gap junctions smooths out the steep gradients in all the relevant fields otherwise existing at the boundary of Ω_{in}. In the absence of applied mechanical loads, the contribution of the pressure to the water flux becomes relevant in stiff plant cell clusters only, while in deformable animal cell clusters the water flow is almost exclusively dictated by osmotic phenomena. In the absence of tight junctions, the ion and water redistribution may be severe, leading to large deformations; moreover, the membrane potential and the volumetric deformation are essentially established by the IC fields only, as the EC space remains nearly electroneutral and undeformed, except for the very initial transient. Differently, in the presence of cluster-sealing tight junctions, the ion and water redistribution is much more limited, resulting in small deformations, and both the IC and EC spaces contribute to setting the membrane potential and the volumetric deformation.

The model may be quite straightforwardly complemented with the inclusion of (i) the active transmembrane ion transport, (ii) the voltage-gating and mechanosensitivity of ion channels and gap junctions, and (iii) genetic and biochemical dynamics required for specific applications, as already addressed in the literature (Jiang and Sun, 2013; Pietak and Levin, 2016, 2017; Leronni et al., 2020).

A major and cumbersome advancement would be the inclusion of growth into the model, toward exploring the interplay between mechanical and bioelectrical dynamics in development and regeneration. This could be achieved by introducing an inelastic (growth) contribution to the deformation gradient, multiplying the elastic contribution and being modulated by the membrane potential, so as to relate growth and depolarization (Sundelacruz et al., 2009; Ambrosi et al., 2019; Silver et al., 2020). More details are provided in the next Ch. 10.

Chapter 10

Discussion

In the following, we compare the small strain electrochemo-mechanical (ECM) model developed in Secs. 8.2 and 8.3 with the large strain electrochemo-poromechanical (ECPM) model presented in Sec. 9.2. Finally, we hint at how the theory of kinematic growth (Ambrosi et al., 2019) could be plugged into the proposed large strain ECPM model.

Let us first focus on the small strain assumption underlying the ECM model. Such hypothesis, although limiting the analysis to relatively short morphogenetic events involving suitably small deformations, is convenient in bio-actuation (Sec. 8.2) for it allows a partial decoupling between electrochemistry and mechanics. Indeed, the electrostatic and osmotic stresses (8.5) and (8.6) are independent of deformation, such that one can solve first the electrochemical problem for the electric field and ion concentrations, and then the mechanical problem (8.9) for the displacement field. This is not possible under large strains, as the nominal active stresses due to electrostatics and water pressure depend on deformation (Eq. (9.35)).

Regarding bio-sensing (Sec. 8.3), conversely, once the membrane tension is known, one can compute the channel open probability (8.49) and the membrane diffusivity (8.50), modulating the electrochemical response. Again, we note that the small strain assumption, not discriminating between undeformed and deformed configurations, considerably simplifies the problem. Indeed, the Young-Laplace Eq. (8.51) may be regarded as an equilibrium equation to be solved for the membrane tension, given the membrane geometry and the pressure acting on it.

Within finite deformations, the problem becomes cumbersome, as equilibrium is established on the current configuration, in which the membrane thickness in Eq. (8.48) and the membrane radius of curvature in Eq. (8.52) are unknown, thus requiring compatibility and an appropriate constitutive law in order to solve the problem. The example of Sec. 8.3.1 partly addresses this issue, but still assumes that the cell remains circular in the deformed configuration, which does not hold true in general. Moreover, we note that in the ECPM model, although we have accounted for the cluster large strains, we have neglected the local membrane deformation (see, e.g., Eqs. (9.47)), since we were not interested in modeling the mechanosensitivity of ion channels.

Let us now focus on the issue of water flow. In the ECM model, we have not accounted for the water transport and the related volumetric deformation, but rather assumed that the osmotic stress, given by the variation of the osmotic concentration with respect to the initial state (Eq. (8.6)), is instantaneously equilibrated by the mechanical stress (8.3), thus producing deformation. This phenomenological approach considerably simplifies the problem, as it reduces the number of governing equations and their complexity. We argue that such an approach may be adequate, and recommendable given its manageability, for soft cell clusters characterized by a large density of aquaporin channels. Indeed, the simulations of Sec. 9.3 reveal that, in the case of sufficiently small Young modulus and relatively large transmembrane water diffusivity, the osmotic pressure gradient triggers fast osmotic fluxes that produce a volume change. Differently, on the one side, if the Young modulus is larger, the water flux is not only affected by the ion redistribution, but also driven by the water pressure (see Fig. 9.6); on the other side, if aquaporins are underexpressed, the transmembrane water flow following the ion redistribution and, correspondingly, the establishment of the volumetric deformation are limited (see Fig. 9.3).

Another assumption the ECM theory is grounded on is the irrelevance of the extracellular fields in establishing the mechanical response. The simulations of Secs. 9.3.4 and 9.3.5, conducted in the absence of tight junctions and accounting for both the intracellular and extracellular fields, reveal that the cluster deformation is indeed practically governed by the intracellular fields only. Correspondingly, the water pressure of the ECPM model could be regarded as an *intracellular* water pressure in the absence of tight junctions; this, again, is consistent with assuming that, in the ECM model, the jump in the mechanical pressure across the membrane coincides with the intracellular value (see Eq. (8.51) and related discussion). Differently, in the case in which tight junctions are present, both the intracellular and extracellular spaces are relevant for the overall deformation (see Sec. 9.3.6), such that the usage of the proposed ECM model would be questionable, although the small strain assumption would be valid given the limited ion and water redistribution.

To summarize, first, adopting a finite deformation framework is required when one needs to investigate developmental processes involving significant ion redistribution and/or growth, which determine large elastic and inelastic strains.

Second, resorting to the explicit water flow modeling is necessary when the cluster mechanics affects the water transport along with osmotic phenomena, and/or when water transport is for some reasons hampered because of a local low density and/or open fraction of aquaporins. Third, the thin extracellular spaces are as relevant as the intracellular spaces in deriving the mechanical response for a cluster with an impermeable boundary, but negligible otherwise.

We further note that the equilibrium Eqs. (8.9) and (9.1), pertaining to the ECM and ECPM models respectively, are structurally different. Indeed, in the former, electrostatic and osmotic stresses have been converted into body forces, such that the divergence operator is applied to the mechanical stress only, and the static boundary condition (8.11) is formulated in terms of mechanical stress. Differently, in the latter, the argument of the divergence is the total stress, and the static boundary condition (9.5) is written in terms of total stress.

About this point, another important difference distinguishes how the bath surrounding the cluster is accounted for in BETSE and in the ECPM model we have developed. Specifically, in BETSE the electrochemical boundary conditions (that is, zero electric potential and fixed ion concentrations) are applied far from the cluster boundary, that is, at the boundary of the environmental domain (see Pietak and Levin, 2016 and related Supplementary Material, Sec. 2.7). Therefore, the bath in the immediate proximity of the cluster boundary may be ion-enriched or ion-depleted during a simulation, resulting in osmotic forces at the cluster boundary. These have been included in the body force vectors pertaining to the boundary cells, as described in Sec. 8.2.1 and displayed, for instance, in Fig. 8.6(d). Differently, in the ECPM model, the sole cluster domain is modeled, such that the electrochemical boundary conditions are applied to the cluster boundary, by assuming that the external bath is a reservoir at fixed chemical and electric potentials (see, e.g., Eqs. (9.8) and (9.11)). Correspondingly, as shown in Fig. 9.1, wherein the boundary cells are characterized by a very small increment in the osmotic and water concentrations, the water pressure at the boundary is negligible.

A major open issue: the theory of bioelectric kinematic growth We conclude this discussion by proposing a way to account for growth within the proposed ECPM theoretical framework. By relying on the theory of kinematic growth (Ambrosi et al., 2019), the deformation gradient $\mathbf{F}$ is given by the following multiplicative decomposition:

$$\mathbf{F} = \mathbf{F}_{\mathrm{e}}\mathbf{F}_{\mathrm{g}} \, , \tag{10.1}$$

in which $\mathbf{F}_{\mathrm{e}}$ is the elastic deformation gradient, accounted for in the present investigation, and $\mathbf{F}_{\mathrm{g}}$ is the growth deformation gradient. Specifically, $\mathbf{F}_{\mathrm{g}}$, which has to be constitutively assigned according to biological phenomena, represents the addition of mass to a local volume element. It takes the reference configuration Ω_0 to the grown, mechanically unstressed, but generally incompatible, configuration Ω_{g}. Instead, $\mathbf{F}_{\mathrm{e}}$ generates mechanical stress, by taking the grown configuration Ω_{g} to the current compatible configuration Ω. It is convenient to adopt $\mathbf{F}$ and $\mathbf{F}_{\mathrm{g}}$ as independent kinematic variables, such that, from Eq. (10.1), we obtain $\mathbf{F}_{\mathrm{e}} = \mathbf{F}\mathbf{F}_{\mathrm{g}}^{-1}$.

By extending Eq. (9.33), we assume that the Helmholtz free energy per unit reference volume is given by the following additive decomposition:

$$
\begin{aligned}
& W(\mathbf{F}, \mathbf{F}_{\mathrm{g}}, C_{\mathrm{w}}, C_{\mathrm{i}}, C_{\mathrm{w}}^{\mathrm{e}}, C_{\mathrm{i}}^{\mathrm{e}}, \mathbf{D}, \mathbf{D}^{\mathrm{e}}) \\
& = J_{\mathrm{g}} W_{\mathrm{mec}}(\mathbf{F}\mathbf{F}_{\mathrm{g}}^{-1}) + W_{\mathrm{mix}}(C_{\mathrm{w}}, C_{\mathrm{i}}) + W_{\mathrm{mix}}^{\mathrm{e}}(C_{\mathrm{w}}^{\mathrm{e}}, C_{\mathrm{i}}^{\mathrm{e}}) + W_{\mathrm{pol}}(\mathbf{F}, \mathbf{D}) + W_{\mathrm{pol}}^{\mathrm{e}}(\mathbf{F}, \mathbf{D}^{\mathrm{e}}) \\
& \qquad + p_{\mathrm{w}} \left[1 + \Phi_0 \Big(v_{\mathrm{w}} C_{\mathrm{w}} - 1 \Big) + \Phi_0^{\mathrm{e}} \Big(v_{\mathrm{w}} C_{\mathrm{w}}^{\mathrm{e}} - 1 \Big) - J J_{\mathrm{g}}^{-1} \right], \qquad (10.2)
\end{aligned}
$$

where $J = \det \mathbf{F}$ and $J_{\mathrm{g}} = \det \mathbf{F}_{\mathrm{g}}$ are the volume ratio and the growth volume ratio. We note that W_{mec}, defined in terms of $\mathbf{F}_{\mathrm{e}}$, is an energy per unit volume of Ω_{g}; hence, it is multiplied by J_{g} in order to obtain the corresponding energy per unit reference volume. Differently, W_{mix}, $W_{\mathrm{mix}}^{\mathrm{e}}$, W_{pol}, and $W_{\mathrm{pol}}^{\mathrm{e}}$ are already defined per unit reference volume. Moreover, the water redistribution is now related to the elastic volume ratio $J_{\mathrm{e}} = J J_{\mathrm{g}}^{-1}$.

Therefore, the nominal stress tensor reads

$$
\mathbf{P} = \frac{\partial W}{\partial \mathbf{F}} = \underbrace{J_{\mathrm{g}} \frac{\partial W_{\mathrm{mec}}}{\partial \left(\mathbf{F}\mathbf{F}_{\mathrm{g}}^{-1} \right)} \mathbf{F}_{\mathrm{g}}^{-\mathrm{T}}}_{\mathbf{P}_{\mathrm{mec}}} + \underbrace{\frac{\partial W_{\mathrm{pol}}}{\partial \mathbf{F}}}_{\mathbf{P}_{\mathrm{pol}}} + \underbrace{\frac{\partial W_{\mathrm{pol}}^{\mathrm{e}}}{\partial \mathbf{F}}}_{\mathbf{P}_{\mathrm{pol}}^{\mathrm{e}}} \underbrace{- p_{\mathrm{w}} J J_{\mathrm{g}}^{-1} \mathbf{F}^{-\mathrm{T}}}_{\mathbf{P}_{\mathrm{w}}} . \qquad (10.3)
$$

Since $\mathbf{P}_{\mathrm{pol}}$, $\mathbf{P}_{\mathrm{pol}}^{\mathrm{e}}$, and $\mathbf{P}_{\mathrm{w}}$ can be regarded as active stresses, while $\mathbf{F}_{\mathrm{g}}$ as an active strain, the proposed one is a mixed active stress/strain theory (Ambrosi and Pezzuto, 2012).

In our theory, we are interested in relating growth and membrane potential. Indeed, it has been shown that depolarized cells, such as cancer and developing cells, tend to proliferate more than hyperpolarized cells, such as somatic cells (Sundelacruz et al., 2009; Yang and Brackenbury, 2013). Binggeli and Weinstein (1986) have also hypothesized that a threshold value of membrane potential may exist separating resting from proliferating cells. These evidences suggest a dependence of the rate of change of the growth deformation gradient $\dot{\mathbf{F}}_{\mathrm{g}}$ on the membrane potential ψ^{m} of the following type:

$$\dot{\mathbf{F}}_{\mathrm{g}} \begin{cases} = \mathbf{0} \quad \text{if } \psi^{\mathrm{m}} < \bar{\psi}^{\mathrm{m}} \,, \\ \\ \propto \left(\psi^{\mathrm{m}} - \bar{\psi}^{\mathrm{m}}\right) \mathbf{I} \quad \text{if } \psi^{\mathrm{m}} > \bar{\psi}^{\mathrm{m}} \,, \end{cases} \tag{10.4}$$

where $\bar{\psi}^{\mathrm{m}}$ is the aforementioned threshold value. Eq. (10.4) prescribes that isotropic growth only occurs above $\bar{\psi}^{\mathrm{m}}$, and that growth becomes faster as ψ^{m} increases. Finally, we note that assigning a meaningful evolutive constitutive law for $\mathbf{F}_{\mathrm{g}}$ is complicated by the fact that ψ^{m} is not only an overall property of cells, but changes dynamically within the cell cycle (Sundelacruz et al., 2008; Yang and Brackenbury, 2013).

Chapter 11

Concluding remarks

In this thesis, we have presented continuum electrochemo-mechanical (ECM) and electrochemo-poromechanical (ECPM) theories suitable for investigating the behavior of porous materials featuring a solid network immersed in a dilute fluid phase of solvent and ions. Specifically, the ECM theory neglects the modeling of the solvent transport, and directly couples the electro-diffusion of ions in the fluid with the elastic deformation of the solid network. The ECPM theory further accounts for the solvent transport, which mediates the electrochemical and mechanical responses. We have employed the proposed theories for describing the ionic electroactive behavior of ionic polymer metal composites (IPMCs) and the mechanobioelectricity of biological cell clusters.

In particular, in Ch. 4 we have plugged the zigzag warping structural theory proposed by Yu (1959) and Krajcinovic (1972) for sandwich beams into the ECM theory developed by Cha and Porfiri (2014) for IPMCs. The result is a model that allows one to study the influence of the shear deformation of the membrane on the counterion diffusion in IPMC sensing. Indeed, the membrane shear strain enters the counterion flux, in addition to the membrane curvature. We have proved that, for short IPMCs with stiff electrodes subject to an imposed mechanical load, the shear deformation non-negligibly enhances the counterion flux, thus improving the sensing/energy harvesting capabilities of IPMCs. More importantly, the successful application of such a structural model in predicting the IPMC electrochemo-mechanics, as confirmed by continuum finite element analyses, questions the reliability for IPMCs of the Euler-Bernoulli structural model, which has been so far pervasive in the literature. In the wake of this work, Boldini and Porfiri (2020) have further proved that through-the-thickness strain localization in the membrane regions adjacent to the electrodes occurs in actuation, which, again, cannot be captured by the Euler-Bernoulli beam theory. Later, Boldini et al. (2020) have proposed an advanced structural theory for

IPMC actuation accounting for both the layered structure of the IPMC and the through-the-thickness strain localization at the membrane-electrode interfaces.

In Ch. 5, inspired by the mixture theory (Ateshian, 2007) and by recents works on polyelectrolyte gels (Hong et al., 2010), we have modified the Cha and Porfiri (2014) theory in order to account for the solvent transport within the IPMC membrane. Additionally, we have accounted for the cross-diffusion of solvent and counterions (Vanag and Epstein, 2009), as recently accomplished by Zhang et al. (2020) for polyelectrolyte gels. Our resulting ECPM theory reveals to be suitable to qualitatively reproduce the experimentally observed IPMC curvature relaxation in actuation (Asaka et al., 1995) and electric discharge in sensing (Farinholt and Leo, 2004). Specifically, our model explains the first behavior with the solvent counter-diffusion down its pressure gradient, occurring after the solvent is initially transported toward the cathode by electro-osmosis; electrostatic phenomena may concur to strengthen the curvature relaxation, even resulting in an opposite bending (Porfiri et al., 2017). The second behavior is instead related with the ion counter-diffusion down its concentration gradient, occurring after ions are initially transported toward the cathode by convection with the solvent. Notably, the modeling of solvent transport, and especially of its cross-diffusion with counterions, is necessary in order to reproduce the foregoing counterintuitive phenomena.

In Ch. 6 we have compared the Cha and Porfiri (2014) ECM theory and the here developed ECPM theory, showing that their main difference lies in the adopted form of the mixing free energy. In particular, Cha and Porfiri (2014) propose a modified version of the Borukhov et al. (2000) mixing free energy for an electrolyte solution containing two charge carriers. Their mixing free energy depends on the deformation gradient, resulting in an osmotic *stress* increasing with the counterion concentration. Differently, our free energy accounts for the entropy increase due to the mixing of counterions and solvent molecules, resulting in an osmotic contribution, again proportional to the counterion concentration, to the solvent chemical *potential*. Moreover, in our case, the coupling between mechanics and fluid phase transport stems from the dependence of the macroscopic volumetric deformation of the membrane on the fluid phase concentration.

The proposed comprehensive ECPM model for IPMC actuation and sensing may be improved with regard to the complex behavior characterizing the membrane-electrode interfaces. First, the adopted dilute solution approximation may be questionable for IPMC actuation, as counterions largely accumulate near the cathode. Second, we have assumed a flat interface between membrane and electrodes; actually, the membrane-electrode interfaces are characterized by a rough surface, which increases the overall charge storage capacity (Porfiri, 2009).

Third, as a result of the manufacturing process, the electrodes are not perfectly uniform layers. Specifically, some authors have identified, on each IPMC side, an outer thin metal electrode layer and an inner thicker polymer-metal composite electrode layer (Kim and Shahinpoor, 2003; Tiwari and Kim, 2010; Akle et al., 2011; Liu et al., 2019). Composite electrodes have been accounted for in some IPMC modeling efforts by introducing the so-called *composite layers* between the purely polymeric membrane and the purely metallic electrodes (Cha et al., 2012).

In Ch. 8 we have combined the description of the bioelectrical ion fluxes in cell clusters, underlying the *BioElectric Tissue Simulation Engine* (Pietak and Levin, 2016), with the Cha and Porfiri (2014) description of actuation in IPMCs. Moreover, by leveraging on a model proposed by Wiggins and Phillips (2004), we have accounted for mechanosensitive ion channels and their membrane tension-dependent open probability. This has led to the *Mechanical* BioElectric Tissue Simulation Engine, allowing one to study the coupling between mechanics and bioelectricity in cell clusters. Although we have restricted our attention to the small strain setting, our analyses suggest that there may be a correlation between increase in membrane potential (that is, depolarization), and increase in mechanical stress and cell volume, due to the combined effect of osmotic pressure and mechanosensitivity of ion channels. Similar claims have been put forward in recent contributions to the literature (Yellin et al., 2018; Silver and Nelson, 2018; Silver et al., 2020). We expect that this result could motivate further investigations, given that depolarization seems to be implicated in developmental processes, such as in the proliferation of both healthy and cancer cells (Sundelacruz et al., 2009).

In Ch. 9, influenced by previous works on the poroelastic nature of cells (Moeendarbary et al., 2013) and on the coupling between cell mechanics and transmembrane osmosis (Jiang and Sun, 2013), we have proposed a thermodynamically consistent ECPM theory for cell clusters. Such a theory extends the model of Ch. 8 in three main directions. First, it additionally accounts for the water transport, which occurs directly from cell to cell, in the intercellular spaces, and across cell membranes through aquaporins. As extensively documented in Ch. 10, explicitly accounting for the water transport in addition to ion transport is especially relevant when the former does not naturally follow the latter: this occurs in stiff plant cell clusters, characterized by large turgor pressures also influencing the solvent flux, or when the closure of aquaporins hampers the transmembrane water exchange. Second, the ECPM theory additionally accounts for the effect of the extracellular fluid phase concentration on the mechanics of the cluster. This is relevant in tight junctions-sealed cell clusters, whereby, in the absence of fluid exchange with the bath surrounding the cluster, both intracellular and extracellular concentration fields concur to the deformation. Third, the proposed ECPM theory extends the contribution of Ch. 8 to a large deformation framework, thus paving the way for quantitative predictions and even developmental applications.

About this last point, in order to actually address development, regeneration, and cancer progression, our cell cluster model should be complemented with the mathematical description of growth, by relying for instance on the theory of kinematic growth (Ambrosi et al., 2019). Moreover, in order to correlate depolarization and proliferation (Sundelacruz et al., 2009), the growth part of the deformation gradient should be expressed as a function of the local bioelectrical state, as for example proposed and discussed in Ch. 10. Finally, we remark that, while in IPMCs the ion transport is purely passive, in cell clusters the transmembrane ion transport also occurs *actively*. Modeling active ion transport would require coupling the ion flow toward regions of higher electrochemical potential with a source of energy. This can be, for instance, the flow of another ion toward regions of smaller electrochemical potential in the case of coupled transporters, or the chemical reaction of ATP hydrolysis in the case of ATP-driven pumps (Alberts, 1983). About this, we note that the coupling of active transmembrane transport and cell mechanics has already been addressed in other works in the literature (Ateshian et al., 2010; Yellin et al., 2018), though limiting attention to a single cell.

In the following, the interested reader can find a further final discussion on the main differences between the electrochemo-poromechanics of IPMCs and cell clusters.

Electrochemo-poromechanics of IPMCs and cell clusters: a comparison Although we have studied IPMCs and cell clusters through similar ECM and ECPM theories, there are some notable differences in their modeling, as discussed in the following.

While in IPMCs the porosity network is unique, in cell clusters we have distinguished between intracellular (IC) and extracellular (EC) spaces, separated by cell membranes. In both the IPMC porosity network and the EC space the motion of solvent and ions is typically always allowed; differently, in the IC space the transport of species may be hampered in the case of low density or low open fraction of cell-connecting gap junctions.

Moreover, in cell clusters the IC and EC spaces can exchange mass, since water and ions are allowed to cross the cell membrane through aquaporins and ion channels, respectively. Such transmembrane fluxes have been regarded, in the context of our continuum ECPM theory, as *local* fluxes, that is, as local exchanges of mass between IC and EC spaces.

While we have regarded the IPMC and EC diffusivities as material parameters, the IC and transmembrane diffusivities are, in general, dynamically modulated by factors such as the membrane potential, the membrane tension, or the concentration of specific ligands. In particular, in our ECM theory, we have explicitly accounted for the mechanosensitivity of ion channels.

In IPMCs, a single positive mobile ion species, such as lithium, sodium, or potassium, is responsible for the electroactivity of the membrane. Differently, studying bioelectricity demands considering, at least, three different mobile ion species, namely sodium, potassium, and chloride. Each ion species requires two mass balances, one for its IC concentration and one for its EC concentration. We have neglected the friction between the different ions and between the ions and the solid network in deriving the ion and water fluxes, and adopted the same IC and EC diffusivities for all ions, given the non-selectivity of gap junctions. Differently, ion channels may be selective for certain ion species; correspondingly, we have assumed, in general, a distinct transmembrane diffusivity for each ion species. If then one wants to account for specific biochemical networks, further chemical species and related mass balances should be included in the model, as well as possible exchanges of mass due to chemical reactions.

Both IPMCs and cell clusters feature a polymer network, whose mechanics has to be described. While in IPMCs this network is represented by a synthetic ionomer such as Nafion, in cell clusters it consists of natural polymers, namely cytoskeletal filaments joined by anchoring junctions. In particular, we remark that, within our framework, cytoskeleton and anchoring junctions do not belong to the *fluid* IC and EC spaces respectively, but they are part of the same *solid* network.

Both IPMCs and cell clusters feature *fixed* anions. In the case of Nafion-based IPMCs, these are represented by monovalent sulfonate groups anchored to the polymer backbone; therefore, in our ECPM theory for IPMCs, we have assumed that the fluid phase is constituted by solvent molecules and mobile cations only. In the case of cell clusters, we have accounted for a single fixed anionic species, representing the many different anions contained in cells; specifically, this fixed anionic species has been considered as part of the IC solution, thus contributing to the IC osmotic concentration.

We have regarded IPMC ionomers and cell clusters as *homogenized* domains in which electrostatic, transport, and mechanical phenomena occur and influence each other. In IPMCs we have further accounted for the electrode domains. These have been modeled as non-porous perfect electric conductors, impermeable to both solvent and counterions, contributing to the overall IPMC stiffness. In cell clusters, the impermeability of the boundary to the external bath depends instead on the presence of cluster-sealing tight junctions.

In IPMCs, actuation and sensing are triggered by the *external* imposition of an electric field or mechanical load, respectively. In other words, the response is elicited by the applied boundary condition. Although electric fields and mechanical loads could in principle be applied to cell clusters as well, in our investigation we have focused on *endogenous* mechanobioelectricity, whereby the response depends on the spatio-temporal activity of ion channels, that is, on the variation of the transmembrane ion diffusivities in space and time.

The IPMC electrochemical response is characterized by the presence of very thin boundary layers in the membrane regions close to the electrodes, in which the counterion concentration and the electric potential experience steep gradients, especially in actuation. These boundary layers mathematically describe the electric double layers arising at the membrane-electrode interfaces. We remark that, in cell clusters, ion concentrations and electric potentials actually vary in the vicinity of cell membranes only, such that the bulk cytoplasm remains nearly electroneutral. However, our model, suitable for describing the *global* cluster response, prevents us from visualizing such *local* boundary layers.

As anticipated, in IPMC actuation the imposition of a voltage across the electrodes elicits a severe counterion redistribution and, correspondingly, a strong electric field in both boundary layers. Therefore, in IPMC actuation the Maxwell stress is as relevant as the osmotic or solvent pressure. Differently, the Maxwell stress arising at the interface between cluster regions polarized at diverse extents is totally negligible. However, we expect that the Maxwell stress would play a major role in the case of *exogenous* bioelectricity, that is, if an external electric field would be applied to the cluster.

Our simulations reveal that the contribution of the solvent pressure to the solvent flux is fundamental in IPMC sensing, whereby the application of a mechanical load triggers the solvent flow down its pressure gradient, and in actuation as well, whereby the solvent pressure gradient in the bulk is responsible for the solvent counter-diffusion, contributing to the back-relaxation. Instead, we argue that, in the absence of applied mechanical loads, the water pressure is relevant for the water flux in stiff plant cell clusters only. Differently, in compliant animal cell clusters the water flow is dictated almost exclusively by osmotic phenomena.

Cross-diffusing effects, that is, water electro-osmosis and ion convection are relevant transport mechanisms in cell clusters. In IPMCs, electro-osmosis is especially important in actuation, since solvent molecules are dragged toward the cathode with ions as the voltage drop is applied across the electrodes. Conversely, ion convection is relevant in sensing, because ions are transported toward the cathode with the underlying solvent as the mechanical load is applied.

Resorting to a large deformation framework is necessary in IPMC actuation, characterized by large through-the-thickness normal strain components localized in the boundary layers. Moreover, if one wants to explore the effect of shear deformation on ion electro-diffusion in short IPMCs with thick electrodes, then the nonlinear expression of the volume ratio should be retained in the ion flux. As for cell clusters, large deformations are registered in compliant animal cell clusters allowed to exchange water and ions with their surrounding bath. Moreover, a large deformation framework is always necessary if one needs to account for biological growth, that is, for biological mass production over time.

Bibliography

Abdulsadda, A. T. and Tan, X. (2012). An artificial lateral line system using IPMC sensor arrays. *Int. J. Smart Nano Mater.*, 3(3):226–242.

Agre, P. (2006). The aquaporin water channels. *Proc. Am. Thorac. Soc.*, 3(1):5–13.

Akle, B. J., Bennett, M. D., Leo, D. J., Wiles, K. B., and McGrath, J. E. (2007). Direct assembly process: a novel fabrication technique for large strain ionic polymer transducers. *J. Mater. Sci.*, 42(16):7031–7041.

Akle, B. J., Habchi, W., Wallmersperger, T., Akle, E. J., and Leo, D. J. (2011). High surface area electrodes in ionic polymer transducers: Numerical and experimental investigations of the electro-chemical behavior. *J. Appl. Phys.*, 109:074509.

Alberts, B. (1983). *Molecular Biology of the Cell.* Garland Science, New York, NY.

Allen, H. G. (1969). *Analysis and Design of Structural Sandwich Panels.* Pergamon Press Ltd., Oxford, UK.

Ambrosi, D., Ben Amar, M., Cyron, C. J., DeSimone, A., Goriely, A., Humphrey, J. D., and Kuhl, E. (2019). Growth and remodelling of living tissues: perspectives, challenges and opportunities. *J. R. Soc. Interface*, 16(157):20190233.

Ambrosi, D. and Pezzuto, S. (2012). Active stress vs. active strain in mechanobiology: constitutive issues. *J. Elast.*, 107(2):199–212.

Asaka, K. and Oguro, K. (2000). Bending of polyelectrolyte membrane platinum composites by electric stimuli: Part II. Response kinetics. *J. Electroanal. Chem.*, 480(1-2):186–198.

Asaka, K., Oguro, K., Nishimura, Y., Mizuhata, M., and Takenaka, H. (1995). Bending of polyelectrolyte membrane-platinum composites by electric stimuli I. Response characteristics to various waveforms. *Polym. J.*, 27(4):436–440.

Ateshian, G. A. (2007). On the theory of reactive mixtures for modeling biological growth. *Biomech. Model. Mechanobiol.*, 6(6):423–445.

Ateshian, G. A., Morrison, B., and Hung, C. T. (2010). Modeling of active transmembrane transport in a mixture theory framework. *Ann. Biomed. Eng.*, 38(5):1801–1814.

Aureli, M., Kopman, V., and Porfiri, M. (2010). Free-locomotion of underwater vehicles actuated by ionic polymer metal composites. *IEEE-ASME T. Mech.*, 15(4):603–614.

Aureli, M. and Porfiri, M. (2013). Nonlinear sensing of ionic polymer metal composites. *Continuum Mech. Therm.*, 25:273–310.

Bard, A. J. and Faulkner, L. R. (2001). *Electrochemical Methods: Fundamentals and Applications.* John Wiley & Sons, Inc., Hoboken, NJ, Second edition.

Bardella, L. (2008). Reliability of first-order shear deformation models for sandwich beams. *J. Mech. Mater. Struct.*, 3(7):1187–1206.

Bardella, L. and Mattei, O. (2014). On explicit analytic solutions for the accurate evaluation of the shear stress in sandwich beams with a clamped end. *Compos. Struct.*, 112:157–168. Corrigendum: Compos. Struct., 116:849, 2014.

Bardella, L. and Tonelli, D. (2012). Explicit analytic solutions for the accurate evaluation of the shear stresses in sandwich beams. *J. Eng. Mech.*, 138(5):502–507. Erratum: J. Eng. Mech., 138(10):1302, 2012.

Bassett, C. A. L. (1967). Biologic significance of piezoelectricity. *Calcif. Tissue Int.*, 1(1):252–272.

Bates, E. (2015). Ion channels in development and cancer. *Ann. Rev. Cell Dev. Biol.*, 31:231–247.

Beane, W. S., Morokuma, J., Adams, D. S., and Levin, M. (2011). A chemical genetics approach reveals H,K-ATPase-mediated membrane voltage is required for planarian head regeneration. *Chem. Biol.*, 18(1):77–89.

Bert, C. W. (1973). Simplified analysis of static shear factors for beams of nonhomogeneous cross section. *J. Compos. Mater.*, 7:525–529.

Binggeli, R. and Weinstein, R. C. (1986). Membrane potentials and sodium channels: hypotheses for growth regulation and cancer formation based on changes in sodium channels and gap junctions. *J. Theor. Biol.*, 123(4):377–401.

Biot, M. A. (1941). General theory of three-dimensional consolidation. *J. Appl. Phys.*, 12(2):155–164.

Blackiston, D. J., McLaughlin, K. A., and Levin, M. (2009). Bioelectric controls of cell proliferation: ion channels, membrane voltage and the cell cycle. *Cell Cycle*, 8(21):3527–3536.

Bluhm, J., Serdas, S., and Schröder, J. (2016). Theoretical framework of modeling of ionic EAPs within the Theory of Porous Media. *Arch. Appl. Mech.*, 86(1-2):3–19.

Boldini, A., Bardella, L., and Porfiri, M. (2020). On structural theories for ionic polymer metal composites: balancing between accuracy and simplicity. *J. Elast.*, 141:227–272.

Boldini, A. and Porfiri, M. (2020). Multiaxial deformations of ionic polymer metal composites. *Int. J. Eng. Sci.*, 149:103227.

Borukhov, I., Andelman, D., and Orland, H. (2000). Adsorption of large ions from an electrolyte solution: a modified Poisson-Boltzmann equation. *Electrochim. Acta*, 46:221–229.

Bowen, R. M. (1980). Incompressible porous media models by use of the theory of mixtures. *Int. J. Eng. Sci.*, 18(9):1129–1148.

Boyce, M. C. and Arruda, E. M. (2000). Constitutive models of rubber elasticity: a review. *Rubber Chem. Technol.*, 73(3):504–523.

Branco, P. C. and Dente, J. (2006). Derivation of a continuum model and its electric equivalent-circuit representation for ionic polymer–metal composite (IPMC) electromechanics. *Smart Mater. Struct.*, 15(2):378.

Carpi, F., Anderson, I., Bauer, S., Frediani, G., Gallone, G., Gei, M., Graaf, C., Jean-Mistral, C., Kaal, W., Kofod, G., et al. (2015). Standards for dielectric elastomer transducers. *Smart Mater. Struct.*, 24(10):105025.

Carrico, J. D., Traeden, N. W., Aureli, M., and Leang, K. (2015). Fused filament 3D printing of ionic polymer-metal composites (IPMCs). *Smart Mater. Struct.*, 24(12):125021.

Cha, Y., Aureli, M., and Porfiri, M. (2012). A physics-based model of the electrical impedance of ionic polymer metal composites. *J. Appl. Phys.*, 111:124901.

Cha, Y. and Porfiri, M. (2014). Mechanics and electrochemistry of ionic polymer metal composites. *J. Mech. Phys. Solids*, 71:156–178.

Cha, Y., Verotti, M., Walcott, H., Peterson, S. D., and Porfiri, M. (2013). Energy harvesting from the tail beating of a carangiform swimmer using ionic polymer metal composites. *Bioinspir. Biomim.*, 8(3):036003.

Chen, Z., Tan, X., Will, A., and Ziel, C. (2007). A dynamic model for ionic polymer–metal composite sensors. *Smart Mater. Struct.*, 16(4):1477–1488.

Cheney, N., Clune, J., and Lipson, H. (2014). Evolved electrophysiological soft robots. In *14th Int. Conf. on Synthesis and Simulation of Living Systems*, pages 222–229, Cambridge, MA. MIT Press.

Chernet, B. and Levin, M. (2013a). Endogenous voltage potentials and the microenvironment: bioelectric signals that reveal, induce and normalize cancer. *J. Clin. Exp. Oncol.*, S1.

Chernet, B. T. and Levin, M. (2013b). Transmembrane voltage potential is an essential cellular parameter for the detection and control of tumor development in a xenopus model. *Dis. Model. Mech.*, 6(3):595–607.

Chernet, B. T. and Levin, M. (2014). Transmembrane voltage potential of somatic cells controls oncogene-mediated tumorigenesis at long-range. *Oncotarget*, 5(10):3287.

Chester, S. A. and Anand, L. (2010). A coupled theory of fluid permeation and large deformations for elastomeric materials. *J. Mech. Phys. Solids*, 58:1879–1906.

Chorsi, M. T., Curry, E. J., Chorsi, H. T., Das, R., Baroody, J., Purohit, P. K., Ilies, H., and Nguyen, T. D. (2019). Piezoelectric biomaterials for sensors and actuators. *Adv. Mater.*, 31(1):1802084.

Coste, B., Mathur, J., Schmidt, M., Earley, T. J., Ranade, S., Petrus, M. J., Dubin, A. E., and Patapoutian, A. (2010). Piezo1 and Piezo2 are essential components of distinct mechanically activated cation channels. *Science*, 330(6000):55–60.

Coussy, O. (2004). *Poromechanics*. John Wiley & Sons, Hoboken, NJ.

Dallos, P. and Fakler, B. (2002). Prestin, a new type of motor protein. *Nat. Rev. Mol. Cell Biol.*, 3(2):104.

De Tommasi, D., Puglisi, G., and Saccomandi, G. (2015). Multiscale mechanics of macromolecular materials with unfolding domains. *J. Mech. Phys. Solids*, 78:154–172.

Del Bufalo, G., Placidi, L., and Porfiri, M. (2008). A mixture theory framework for modeling the mechanical actuation of ionic polymer metal composites. *Smart Mater. Struct.*, 17(4):045010.

Djamgoz, M. (2014). Biophysics of cancer: cellular excitability (celex) hypothesis of metastasis. *J. Clin. Exp. Oncol. S1*, 005.

Dorfmann, A. and Ogden, R. W. (2005). Nonlinear electroelasticity. *Acta Mech.*, 174:167–183.

Dorfmann, L. and Ogden, R. W. (2017). Nonlinear electroelasticity: material properties, continuum theory and applications. *Proc. Math. Phys. Eng. Sci.*, 473(2204):20170311.

Farinholt, K. and Leo, D. J. (2004). Modeling of electromechanical charge sensing in ionic polymer transducers. *Mech. Mater.*, 36(5-6):421–433.

Flory, P. J. (1942). Thermodynamics of high polymer solutions. *J. Chem. Phys.*, 10(1):51–61.

Fraldi, M., Palumbo, S., Carotenuto, A. R., Cutolo, A., Deseri, L., and Pugno, N. (2019). Buckling soft tensegrities: Fickle elasticity and configurational switching in living cells. *J. Mech. Phys. Solids*, 124:299–324.

Frostig, Y., Baruch, M., Vilnay, O., and Shelnman, I. (1992). High-order theory for sandwich-beam behavior with transversely flexible core. *J. Eng. Mech.*, 118(5):1026–1043.

Gao, J., Sun, X., Moore, L. C., White, T. W., Brink, P. R., and Mathias, R. T. (2011). Lens intracellular hydrostatic pressure is generated by the circulation of sodium and modulated by gap junction coupling. *J. Gen. Physiol.*, 137(6):507–520.

Gei, M., Springhetti, R., and Bortot, E. (2013). Performance of soft dielectric laminated composites. *Smart Mater. Struct.*, 22(10):104014.

Goodenough, D. A. and Paul, D. L. (2009). Gap junctions. *CSH Perspect. Biol.*, 1(1):a002576.

Gramse, G., Dols-Pérez, A., Edwards, M., Fumagalli, L., and Gomila, G. (2013). Nanoscale measurement of the dielectric constant of supported lipid bilayers in aqueous solutions with electrostatic force microscopy. *Biophys. J.*, 104(6):1257–1262.

Gurtin, M. E., Fried, E., and Anand, L. (2010). *The Mechanics and Thermodynamics of Continua.* Cambridge University Press, Cambridge, UK.

Guz, N., Dokukin, M., Kalaparthi, V., and Sokolov, I. (2014). If cell mechanics can be described by elastic modulus: study of different models and probes used in indentation experiments. *Biophys. J.*, 107(3):564–575.

Hamilton, E. S., Schlegel, A. M., and Haswell, E. S. (2015). United in diversity: mechanosensitive ion channels in plants. *Ann. Rev. Plant Biol.*, 66:113–137.

Haswell, E. S., Phillips, R., and Rees, D. C. (2011). Mechanosensitive channels: what can they do and how do they do it? *Structure*, 19(10):1356–1369.

Hille, B. (1984). *Ion Channels of Excitable Membranes.* Sinauer Associates, Inc., Sunderland, MA.

Hoffmann, E. K., Lambert, I. H., and Pedersen, S. F. (2009). Physiology of cell volume regulation in vertebrates. *Physiol. Rev.*, 89(1):193–277.

Holzapfel, G. A. (2000). *Nonlinear Solid Mechanics: A Continuum Approach for Engineering.* John Wiley & Sons, Hoboken, NJ.

Hong, W., Zhao, X., and Suo, Z. (2010). Large deformation and electrochemistry of polyelectrolyte gels. *J. Mech. Phys. Solids*, 58:558–577.

Hong, W., Zhao, X., Zhou, J., and Suo, Z. (2008). A theory of coupled diffusion and large deformation in polymeric gels. *J. Mech. Phys. Solids*, 56(5):1779–1793.

Huang, H., Kwon, R. Y., and Jacobs, C. (2012). *Introduction to Cell Mechanics and Mechanobiology.* Garland Science, New York, NY.

Huggins, M. L. (1941). Solutions of long chain compounds. *J. Chem. Phys.*, 9(5):440–440.

Hui, T., Cho, W., Fong, H., Yu, M., Kwan, K., Ngan, K., Wong, K., Tan, Y., Yao, S., Jiang, H., et al. (2019). An electro-osmotic microfluidic system to characterize cancer cell migration under confinement. *J. R. Soc. Interface*, 16(155):20190062.

Huyghe, J. M. and Janssen, J. (1997). Quadriphasic mechanics of swelling incompressible porous media. *Int. J. Eng. Sci.*, 35(8):793–802.

Ingber, D. (2003). Mechanobiology and diseases of mechanotransduction. *Ann. Med.*, 35(8):564–577.

Ingber, D. E. (2006). Cellular mechanotransduction: putting all the pieces together again. *FASEB J.*, 20(7):811–827.

Jiang, H. and Sun, S. X. (2013). Cellular pressure and volume regulation and implications for cell mechanics. *Biophys. J.*, 105(3):609–619.

Jo, C., Pugal, D., Oh, I.-K., Kim, K. J., and Asaka, K. (2013). Recent advances in ionic polymer-metal composite actuators and their modeling and applications. *Prog. Polym. Sci.*, 38(7):1037–1066.

Jourawski, D. (1856). Remarques sur la résistance d'un corps prismatique et d'une pièce composée en bois ou en tôle de fer à une force perpendiculaire à leur longeur. *Annales des Ponts and Chaussées*, 12:328–351.

Kamm, R. D., Bashir, R., Arora, N., Dar, R. D., Gillette, M. U., Griffith, L. G., Kemp, M. L., Kinlaw, K., Levin, M., Martin, A. C., et al. (2018). Perspective: The promise of multi-cellular engineered living systems. *APL Bioeng.*, 2(4):040901.

Kilic, M. S., Bazant, M. Z., and Ajdari, A. (2007a). Steric effects in the dynamics of electrolytes at large applied voltages. I. Double-layer charging. *Phys. Rev. E*, 75:021502.

Kilic, M. S., Bazant, M. Z., and Ajdari, A. (2007b). Steric effects in the dynamics of electrolytes at large applied voltages. II. Modified Poisson-Nernst-Planck equations. *Phys. Rev. E*, 75:021503.

Kim, K. J. and Shahinpoor, M. (2003). Ionic polymer-metal composites: II. Manufacturing techniques. *Smart Mater. Struct.*, 12:65–79.

Kim, S., Laschi, C., and Trimmer, B. (2013). Soft robotics: a bioinspired evolution in robotics. *Trends Biotechnol.*, 31(5):287–294.

Krajcinovic, D. (1972). Sandwich beam analysis. *J. Appl. Mech.*, 39(3):773–778.

Krajcinovic, D. (1975). Sandwich beams with arbitrary boundary conditions. *J. Eng. Ind. Trans. ASME*, 97(3):873–880.

Krishna, R. and Wesselingh, J. (1997). The Maxwell-Stefan approach to mass transfer. *Chem. Eng. Sci.*, 52(6):861–911.

Lanir, Y. (2009). Mechanisms of residual stress in soft tissues. *J. Biomech. Eng.*, 131(4):044506.

Lee, S.-G., Park, H.-C., Pandita, S. D., and Yoo, Y. (2006). Performance improvement of IPMC (ionic polymer metal composites) for a flapping actuator. *Int. J. Control Autom.*, 4(6):748–755.

Leichsenring, P., Serdas, S., Wallmersperger, T., Bluhm, J., and Schröder, J. (2017). Electro-chemical aspects of IPMCs within the framework of the theory of porous media. *Smart Mater. Struct.*, 26(4):045004.

Lekka, M. (2016). Discrimination between normal and cancerous cells using AFM. *BioNanoSci.*, 6(1):65–80.

Leronni, A. (2020). Modeling the mechanobioelectricity of cell clusters. *Biomech. Model. Mechanobiol.*

Leronni, A. and Bardella, L. (2019). Influence of shear on sensing of ionic polymer metal composites. *Eur. J. Mech. A-Solid.*, 77:103750.

Leronni, A. and Bardella, L. (2021). Modeling actuation and sensing in ionic polymer metal composites by electrochemo-poromechanics. *J. Mech. Phys. Solids*, 148:104292.

Leronni, A., Bardella, L., Dorfmann, L., Pietak, A., and Levin, M. (2020). On the coupling of mechanics with bioelectricity and its role in morphogenesis. *J. R. Soc. Interface*, 17(167):20200177.

Levin, M. (2014). Molecular bioelectricity: how endogenous voltage potentials control cell behavior and instruct pattern regulation in vivo. *Mol. Biol. Cell*, 25(24):3835–3850.

Levin, M., Pezzulo, G., and Finkelstein, J. M. (2017). Endogenous bioelectric signaling networks: exploiting voltage gradients for control of growth and form. *Annu. Rev. Biomed. Eng.*, 19:353–387.

Levin, M., Pietak, A. M., and Bischof, J. (2019). Planarian regeneration as a model of anatomical homeostasis: recent progress in biophysical and computational approaches. In *Semin. Cell Dev. Biol.*, volume 87, pages 125–144, Amsterdam, Netherlands. Elsevier.

Levin, M., Thorlin, T., Robinson, K. R., Nogi, T., and Mercola, M. (2002). Asymmetries in H^+/K^+-ATPase and cell membrane potentials comprise a very early step in left-right patterning. *Cell*, 111(1):77–89.

Li, L., Li, C., Zhang, Z., and Alexov, E. (2013). On the dielectric “constant” of proteins: smooth dielectric function for macromolecular modeling and its implementation in DelPhi. *J. Chem. Theory Comput.*, 9(4):2126–2136.

Liu, H., Xiong, K., and Wang, M. (2019). A gradient model for Young’s modulus and surface electrode resistance of ionic polymer–metal composite. *Acta Mech. Solida Sin.*, 32(6):754–766.

Love, A. E. H. (1927). *A Treatise on the Mathematical Theory of Elasticity.* Cambridge University Press, Cambridge, UK, Fourth edition.

MacMinn, C. W., Dufresne, E. R., and Wettlaufer, J. S. (2016). Large deformations of a soft porous material. *Phys. Rev. Appl.*, 5(4):044020.

Malvern, L. (1969). *Introduction to the Mechanics of a Continuous Medium.* Prentice-Hall, Englewood Cliffs, NJ.

Mammoto, T. and Ingber, D. E. (2010). Mechanical control of tissue and organ development. *Development*, 137(9):1407–1420.

Martinac, B. (2004). Mechanosensitive ion channels: molecules of mechanotransduction. *J. Cell Sci.*, 117(12):2449–2460.

Mathews, J. and Levin, M. (2018). The body electric 2.0: recent advances in developmental bioelectricity for regenerative and synthetic bioengineering. *Curr. Opin. Biotech.*, 52:134–144.

Mattei, O. and Bardella, L. (2016). A structural model for plane sandwich beams including transverse core deformability and arbitrary boundary conditions. *Eur. J. Mech. A-Solid.*, 58:172–186.

McCaig, C. D., Rajnicek, A. M., Song, B., and Zhao, M. (2005). Controlling cell behavior electrically: current views and future potential. *Physiol. Rev.*, 85(3):943–978.

Melnikov, A. and Ogden, R. W. (2016). Finite deformations of an electroelastic circular cylindrical tube. *Zeitschrift für angewandte Mathematik und Physik*, 67(6):140.

Moeendarbary, E., Valon, L., Fritzsche, M., Harris, A. R., Moulding, D. A., Thrasher, A. J., Stride, E., Mahadevan, L., and Charras, G. T. (2013). The cytoplasm of living cells behaves as a poroelastic material. *Nat. Mater.*, 12(3):253–261.

Mustard, J. and Levin, M. (2014). Bioelectrical mechanisms for programming growth and form: taming physiological networks for soft body robotics. *Soft Robot.*, 1(3):169–191.

Nardinocchi, P., Pezzulla, M., and Placidi, L. (2011). Thermodynamically based multiphysic modeling of ionic polymer metal composites. *J. Intel. Mat. Syst. Str.*, 22(16):1887–1897.

Nemat-Nasser, S. (2002). Micromechanics of actuation of ionic polymer-metal composites. *J. Appl. Phys.*, 92:2899–2915.

Nemat-Nasser, S. and Li, J. Y. (2000). Electromechanical response of ionic polymer-metal composites. *J. Appl. Phys.*, 87(7):3321–3331.

Nemat-Nasser, S., Zamani, S., and Tor, Y. (2006). Effect of solvents on the chemical and physical properties of ionic polymer-metal composites. *J. Appl. Phys.*, 99(10):104902.

Nguyen, T. D., Deshmukh, N., Nagarah, J. M., Kramer, T., Purohit, P. K., Berry, M. J., and McAlpine, M. C. (2012). Piezoelectric nanoribbons for monitoring cellular deformations. *Nat. Nanotechnol.*, 7(9):587–593.

Nguyen, T. D., Mao, S., Yeh, Y.-W., Purohit, P. K., and McAlpine, M. C. (2013). Nanoscale flexoelectricity. *Adv. Mater.*, 25(7):946–974.

Nodargi, N. A., Bisegna, P., and Caselli, F. (2017). Effective computational modeling of erythrocyte electro-deformation. *Meccanica*, 52(3):613–631.

Nuccitelli, R. (2003). A role for endogenous electric fields in wound healing. *Curr. Top. Dev. Biol.*, 58(2):1–26.

Ogden, R. W. (1984). *Non-Linear Elastic Deformations.* Ellis Horwood, Chichester, UK.

Onsager, L. (1931). Reciprocal relations in irreversible processes. I. *Phys. Rev.*, 37(4):405.

Overbeek, J. T. (1956). The Donnan equilibrium. *Prog. Biophys. Biophys. Chem.*, 6(1):57–84.

Page, K. A., Shin, J. W., Eastman, S. A., Rowe, B. W., Kim, S., Kusoglu, A., Yager, K. G., and Stafford, G. R. (2015). In situ method for measuring the mechanical properties of Nafion thin films during hydration cycles. *ACS Appl. Mater. Inter.*, 7(32):17874–17883.

Pai, V. P., Lemire, J. M., Chen, Y., Lin, G., and Levin, M. (2015). Local and long-range endogenous resting potential gradients antagonistically regulate apoptosis and proliferation in the embryonic CNS. *Int. J. Dev. Biol.*, 59(7-9):327–340.

Pai, V. P., Pietak, A., Willocq, V., Ye, B., Shi, N.-Q., and Levin, M. (2018). HCN2 rescues brain defects by enforcing endogenous voltage pre-patterns. *Nat. Commun.*, 9(1):998.

Panteghini, A. and Bardella, L. (2017). Structural theory and finite element modelling of linear elastic sandwich beams subject to severe boundary conditions. *Eur. J. Mech. A-Solid.*, 61:393–407.

Pelesko, J. A. and Bernstein, D. H. (2003). *Modeling MEMS and NEMS.* Chapman & Hall/CRC Press, Boca Raton, FL.

Peyronnet, R., Tran, D., Girault, T., and Frachisse, J.-M. (2014). Mechanosensitive channels: feeling tension in a world under pressure. *Front. Plant Sci.*, 5:558.

Pezzulo, G. and Levin, M. (2016). Top-down models in biology: explanation and control of complex living systems above the molecular level. *J. R. Soc. Interface*, 13(124):20160555.

Pfeifer, R. and Bongard, J. (2006). *How the Body Shapes the Way We Think: A New View of Intelligence.* MIT Press, Cambridge, MA.

Phillips, R., Theriot, J., Kondev, J., and Garcia, H. (2012). *Physical Biology of the Cell.* Garland Science, New York, NY.

Pietak, A. and Levin, M. (2016). Exploring instructive physiological signaling with the BioElectric Tissue Simulation Engine. *Front. Bioeng. Biotechnol.*, 4:55.

Pietak, A. and Levin, M. (2017). Bioelectric gene and reaction networks: computational modelling of genetic, biochemical and bioelectrical dynamics in pattern regulation. *J. R. Soc. Interface*, 14(134):20170425.

Porfiri, M. (2008). Charge dynamics in ionic polymer metal composites. *J. Appl. Phys.*, 104(10):104915.

Porfiri, M. (2009). Influence of electrode surface roughness and steric effects on the nonlinear electromechanical behavior of ionic polymer metal composites. *Phys. Rev. E*, 79:041503.

Porfiri, M., Leronni, A., and Bardella, L. (2017). An alternative explanation of back-relaxation in ionic polymer metal composites. *Extreme Mech. Lett.*, 13:78–83.

Porfiri, M., Sharghi, H., and Zhang, P. (2018). Modeling back-relaxation in ionic polymer metal composites: The role of steric effects and composite layers. *J. Appl. Phys.*, 123(1):014901.

Pugal, D., Jung, K., Aabloo, A., and Kim, K. J. (2010). Ionic polymer-metal composite mechanoelectrical transduction: review and perspectives. *Polym. Int.*, 59(3):279–289.

Pugal, D., Kim, K. J., and Aabloo, A. (2011). An explicit physics-based model of ionic polymer-metal composite actuators. *J. Appl. Phys.*, 110(8):084904.

Pugal, D., Stalbaum, T., Palmre, V., and Kim, K. J. (2015). Modeling ionic polymer metal composites with COMSOL: Step-by-step guide. In *Ionic Polymer Metal Composites (IPMCs)*, pages 185–214. The Royal Society of Chemistry, London, UK.

Punning, A., Kim, K. J., Palmre, V., Vidal, F., Plesse, C., Festin, N., Maziz, A., Asaka, K., Sugino, T., Alici, G., et al. (2014). Ionic electroactive polymer artificial muscles in space applications. *Sci. Rep.*, 4:6913.

Quarteroni, A. (2009). *Numerical Models for Differential Problems*, volume 2. Springer, Berlin, Germany.

Rubinstein, I. (1990). *Electro-diffusion of Ions*. SIAM, Philadelphia, PA.

Rus, D. and Tolley, M. T. (2015). Design, fabrication and control of soft robots. *Nature*, 521(7553):467.

Satterfield, M. B., Majsztrik, P. W., Ota, H., Benziger, J. B., and Bocarsly, A. B. (2006). Mechanical properties of Nafion and titania/Nafion composite membranes for polymer electrolyte membrane fuel cells. *J. Polym. Sci. Pol. Phys.*, 44:2327–2345.

Schäfer, M. (2006). *Computational Engineering: Introduction to Numerical Methods*. Springer, Berlin, Germany.

Schicker, D. and Wallmersperger, T. (2013). Modeling and simulation of the chemo-electro-mechanical behavior of ionic polymer-metal composites. *J. Appl. Phys.*, 114(16):163709.

Shahinpoor, M. (2011). Biomimetic robotic Venus flytrap (Dionaea muscipula Ellis) made with ionic polymer metal composites. *Bioinspir. Biomim.*, 6(4):046004.

Shahinpoor, M. (2015a). Fundamentals of ionic polymer metal composites (IPMCs). In *Ionic Polymer Metal Composites (IPMCs)*, pages 1–60. The Royal Society of Chemistry, London, UK.

Shahinpoor, M. (2015b). Ionic polymer metal composites (IPMCs) optimal manufacturing. In *Ionic Polymer Metal Composites (IPMCs)*, pages 61–147. The Royal Society of Chemistry, London, UK.

Shahinpoor, M. and Kim, K. J. (2001). Ionic polymer-metal composites: I. Fundamentals. *Smart Mater. Struct.*, 10:819–833.

Shahinpoor, M. and Kim, K. J. (2004). Ionic polymer-metal composites: III. Modeling and simulation as biomimetic sensors, actuators, transducers and artificial muscles. *Smart Mater. Struct.*, 13:1362–1388.

Shahinpoor, M. and Kim, K. J. (2005). Ionic polymer-metal composites: IV. Industrial and medical applications. *Smart Mater. Struct.*, 14:197–214.

Shishvan, S., Vigliotti, A., and Deshpande, V. (2018). The homeostatic ensemble for cells. *Biomech. Model. Mechanobiol.*, 17(6):1631–1662.

Silberstein, M. N. and Boyce, M. C. (2010). Constitutive modeling of the rate, temperature, and hydration dependent deformation response of Nafion to monotonic and cyclic loading. *J. Power Sources*, 195(17):5692–5706.

Silver, B. B. and Nelson, C. M. (2018). The bioelectric code: reprogramming cancer and aging from the interface of mechanical and chemical microenvironments. *Front. Cell Dev. Biol.*, 6:21.

Silver, B. B., Wolf, A. E., Lee, J., Pang, M.-F., and Nelson, C. M. (2020). Epithelial tissue geometry directs emergence of bioelectric field and pattern of proliferation. *Mol. Biol. Cell*, 31:1691–1702.

Simo, J. C. and Pister, K. S. (1984). Remarks on rate constitutive equations for finite deformation problems: computational implications. *Comput. Methods Appl. Mech. Eng.*, 46(2):201–215.

Stroka, K. M., Jiang, H., Chen, S.-H., Tong, Z., Wirtz, D., Sun, S. X., and Konstantopoulos, K. (2014). Water permeation drives tumor cell migration in confined microenvironments. *Cell*, 157(3):611–623.

Sundelacruz, S., Levin, M., and Kaplan, D. L. (2008). Membrane potential controls adipogenic and osteogenic differentiation of mesenchymal stem cells. *PLOS One*, 3(11):e3737.

Sundelacruz, S., Levin, M., and Kaplan, D. L. (2009). Role of membrane potential in the regulation of cell proliferation and differentiation. *Stem Cell Rev. Rep.*, 5(3):231–246.

Suresh, S. and Mortensen, A. (1998). *Fundamentals of Functionally Graded Materials*. Maney Publishing, Leeds, UK.

Tiwari, R. and Kim, K. J. (2010). Effect of metal diffusion on mechanoelectric property of ionic polymer-metal composite. *Appl. Phys. Lett.*, 97:244104.

Tixier, M. and Pouget, J. (2020). Validation of a model for an ionic electro-active polymer in the static case. *Smart Mater. Struct.*, 29(8):085019.

Topolov, V. Y., Bisegna, P., and Bowen, C. R. (2013). *Piezo-Active Composites: Orientation Effects and Anisotropy Factors*, volume 185 of *Springer Series in Materials Science*. Springer, Berlin, Germany.

Trivedi, D., Rahn, C. D., Kier, W. M., and Walker, I. D. (2008). Soft robotics: Biological inspiration, state of the art, and future research. *Appl. Bionics Biomech.*, 5(3):99–117.

Tsukita, S., Furuse, M., and Itoh, M. (2001). Multifunctional strands in tight junctions. *Nat. Rev. Mol. Cell Bio.*, 2(4):285–293.

Turing, A. M. (1952). The chemical basis of morphogenesis. *Philos. T. Roy. Soc. B*, 237(641):37–72.

Vanag, V. K. and Epstein, I. R. (2009). Cross-diffusion and pattern formation in reaction-diffusion systems. *Phys. Chem. Chem. Phys.*, 11(6):897–912.

Vandenberg, L. N. and Levin, M. (2013). A unified model for left–right asymmetry? Comparison and synthesis of molecular models of embryonic laterality. *Dev. Biol.*, 379(1):1–15.

Verhulst, F. (2005). *Methods and Applications of Singular Perturbations*, volume 50 of *Texts in Applied Mathematics.* Springer, Berlin, Germany.

Verkman, A. and Mitra, A. K. (2000). Structure and function of aquaporin water channels. *Am. J. Physiol. Renal Physiol.*, 278(1):F13–F28.

Volpini, V. and Bardella, L. (2021). Asymptotic analysis of compression sensing in ionic polymer metal composites: the role of interphase regions with variable properties. *Math. Eng.*, 3(2):1–31.

Volpini, V., Bardella, L., Rodella, A., Cha, Y., and Porfiri, M. (2017). Modelling compression sensing in ionic polymer metal composites. *Smart Mater. Struct.*, 26(3):035030.

Wallmersperger, T., Leo, D. J., and Kothera, C. S. (2007). Transport modeling in ionomeric polymer transducers and its relationship to electromechanical coupling. *J. Appl. Phys.*, 101:024912.

Wei, H.-C. and Su, G.-D. J. (2012). Design and fabrication of a large-stroke deformable mirror using a gear-shape ionic-conductive polymer metal composite. *Sensors*, 12:11100–11112.

Wiggins, P. and Phillips, R. (2004). Analytic models for mechanotransduction: gating a mechanosensitive channel. *Proc. Natl. Acad. Sci. USA*, 101(12):4071–4076.

Wolpert, L. (1969). Positional information and the spatial pattern of cellular differentiation. *J. Theor. Biol.*, 25(1):1–47.

Yang, J. (2005). *An Introduction to the Theory of Piezoelectricity*, volume 9 of *Advances in Mechanics and Mathematics*. Springer, Berlin, Germany.

Yang, M. and Brackenbury, W. J. (2013). Membrane potential and cancer progression. *Front. Physiol.*, 4:185.

Yellin, F., Li, Y., Sreenivasan, V. K., Farrell, B., Johny, M. B., Yue, D., and Sun, S. X. (2018). Electromechanics and volume dynamics in nonexcitable tissue cells. *Biophys. J.*, 114(9):2231–2242.

Yu, Y. Y. (1959). A new theory of elastic sandwich plates - One dimensional case. *J. Appl. Mech.*, 26:415–421.

Zangrilli, U. and Weiland, L. M. (2015). Prediction of the ionic polymer transducer sensing of shear loading. *Smart Mater. Struct.*, 20(9):094013.

Zhang, H., Dehghany, M., and Hu, Y. (2020). Kinetics of Polyelectrolyte Gels. *J. Appl. Mech.*, 87(6):061010.

Zhu, Z., Asaka, K., Chang, L., Takagi, K., and Chen, H. (2013). Multiphysics of ionic polymer-metal composite actuator. *J. Appl. Phys.*, 114(8):084902.

Zhu, Z., Chang, L., Horiuchi, T., Takagi, K., Aabloo, A., and Asaka, K. (2016). Multi-physical model of cation and water transport in ionic polymer-metal composite sensors. *J. Appl. Phys.*, 119:124901.

Zhu, Z., Chen, H., Chang, L., and Li, B. (2011). Dynamic model of ion and water transport in ionic polymer-metal composites. *AIP Adv.*, 1(4):040702.